JULY 2017

Ph.D. in Civil Engineering

FATEN IBRAHIM MUSSA

UNIVERSITY OF GAZİANTEP

GRADUATE SCHOOL OF

NATURAL & APPLIED SCIENCES

EXPERIMENTAL AND NUMERICAL ANALYSIS OF THERMAL BEHAVIOR OF COMPOSITE BRIDGE GIRDERS

Ph.D. THESIS

IN

CIVIL ENGINEERING

BY

FATEN IBRAHIM MUSSA

JULY 2017

Experimental and Numerical Analysis of Thermal Behavior of Composite Bridge Girders

Ph.D. Thesis

in

Civil Engineering

University of Gaziantep

Supervisor

Assoc. Prof. Dr. Nildem TAYŞİ

Co-Supervisor

Assist. Prof. Dr. Sallal ABID

by

Faten Ibrahim MUSSA

July 2017

REPUBLIC OF TURKEY
UNIVERSITY OF GAZİANTEP
GRADUATE SCHOOL OF NATURAL & APPLIED SCIENCES
CIVIL ENGINEERING DEPARTMENT

Name of the thesis: Experimental and Numerical Analysis of Thermal Behavior of Composite Bridge Girders

Name of the student: Faten Ibrahim MUSSA

Exam date: 31.07.2017

Approval of the Graduate School of Natural and Applied Sciences

Prof. Dr. Ahmet Necmeddin YAZICI
Director

I certify that this thesis satisfies all the requirements as a thesis for the degree of Doctor of Philosophy.

Prof. Dr. Abdulkadir ÇEVİK
Head of Department

This is to certify that we have read this thesis and that in our consensus opinion it is fully adequate, in scope and quality, as a thesis for the degree of Doctor of Philosophy.

Co-Supervisor
Assist. Prof. Dr. Sallal ABID

Supervisor
Assoc. Prof. Dr. Nildem TAYŞİ

Examining Committee Members:	Signature
Prof. Dr. Mustafa ÖZAKÇA	----------
Assoc. Prof. Dr. Nildem TAYŞİ	----------
Assoc. Prof. Dr. A. Hamza TANRIKULU	----------
Assist. Prof. Dr. A. İlker AKGÖNEN	----------
Assist. Prof. Dr. M. Tolga GÖĞÜŞ	----------

I hereby declare that all information in this document has been obtained and presented in accordance with academic rules and ethical conduct. I also declare that, as required by these rules and conduct, I have fully cited and referenced all material and results that are not original to this work.

Faten Ibrahim MUSSA

ABSTRACT

Experimental and Numerical Analysis of Thermal Behavior of Composite Bridge Girders

MUSSA, FATEN IBRAHIM
Ph.D. in Civil Engineering
Supervisor: Assoc. Prof. Dr. Nildem TAYŞİ
Co-Supervisor: Assist. Prof. Dr. Sallal ABİD
July 2017

164 pages

Due to their permanent external exposure, bridge structures are under the continuous exposure to the temporal thermal loads. These loads are mainly due to the temporal fluctuation of solar radiation and air temperature. In this research, experimental and FE studies were directed to investigate the thermal behavior of composite girders under the variation of solar radiation and air temperature. This research is divided into four parts. In the first, an experimental work including two composite girder segments, T-Beam and I-Beam, was conducted. The segments were instrumented with thermocouples, strain gages and weather sensors. In the second part, a thermo-mechanical FE analysis was conducted using COMSOL for the two segments, which was verified using the experimental temperature records. Using the verified FE model, a parametric study was conducted in the third part to evaluate the effect of the girder's size. The fourth part was directed to evaluate the long-term temperature variations in Turkey. In this part, the verified FE model in addition to weather history records for more than 50 years of 10 Turkish cities were utilized. The experimental results showed that the temperature variation in concrete parts was higher than in steel for the two segments. Comparisons between the experimental and FE temperatures revealed that the FE models could capture the temperatures accurately. The parametric study disclosed that the thickness of the top concrete flange was the most effective geometrical parameter. The extreme temperature analysis showed that based on the vertical temperature gradients, Turkey can be divided into two regions.

Keywords: Composite I-girder; concrete encased steel girder; solar radiation; thermal load, temperature distribution, temperature gradient.

ÖZET

KOMPOZİT KÖPRÜ KİRİŞLERİNİN DENEYSEL VE NÜMERİK ISIL ANALİZİ

MUSSA, FATEN İBRAHIM
Doktora Tezi, İnşaat Mühendisliği Bölümü
Tez Yöneticisi: Doç. Dr. Nildem TAYŞİ
Yardımcı Tez Yöneticisi: Yrd. Doç. Dr. Sallal ABİD
Temmuz 2017

164 sayfa

Sürekli dış hava olaylarına açık olan köprü yapıları değişken ısıl yüklere maruz kalmaktadırlar. Bu yükler esas olarak güneş radyasyonunun ve hava sıcaklığının zamanla değişkenliğinden kaynaklanmaktadır. Bu araştırmada, güneş radyasyonunun ve hava sıcaklığının değişimi altındaki kompozit köprülerin ısıl davranışlarını incelemek üzere deneysel ve sonlu elemanlar çalışmaları yürütülmüştür. Bu araştırma dört kısımdan oluşmaktadır. İlk aşamada, T-kiriş ve I-kiriş olmak üzere iki kompozit köprü parçası ile deneysel bir çalışma gerçekleştirilmiştir. Köprü parçaları, termokapıllar, gerinim ölçerler ve hava sensörleri ile donatılmıştır. İkinci bölümde ise deneysel sıcaklık kayıtları kullanılarak her iki köprü için termo-mekanik sonlu elemanlar analizi COMSOL programı kullanılarak gerçekleştirilmiştir. Köprü boyutlarının etkisini değerlendirmek için doğruluğu onaylanmış sonlu elemanlar modeli kullanarak, üçüncü bölümde bir parametrik çalışma yapılmıştır. Dördüncü bölüm ise Türkiye'deki uzun vadeli sıcaklık değişimlerini değerlendirmeye yöneliktir. Bu bölümde, Türkiye'deki 10 şehrin 50 yılı aşkın hava durumu kayıtlarına ek olarak doğrulanmış sonlu elmanlar modeli kullanılmıştır. Deneysel sonuçlar, her iki köprü için de, beton kısımlardaki sıcaklık değişiminin çelikten yüksek olduğunu göstermiştir. Deneysel ve sonlu elemanlar analizi arasındaki karşılaştırmalardan, sonlu elemanlar modellerinin sıcaklıkları doğru bir şekilde yakalayabileceğini ortaya koymaktadır. Parametrik çalışma, en etkili geometrik parametrenin, üst beton tabliyesinin kalınlığı olduğunu ortaya koymaktadır. Aşırı sıcaklık analizi, düşey sıcaklık değişimlerine dayanarak Türkiye'nin iki bölgeye ayrılabileceğini göstermektedir.

Anahtar Kelimeler: Kompozit I kiriş; beton kaplı çelik köprü; güneş radyasyonu; ısıl yük, sıcaklık dağılımı, sıcaklık değişimi.

To who I believing in waiting for him (the savior of the world),

To my precious country, which I lived in it and lived in my heart (Iraq),

To My Parents,

To My Big Families

ACKNOWLEDGEMENT

I am extremely grateful to my country, Gaziantep University, my family and friends gave me a lot of support during my time in Turkey and encouraged me in my work, of which the outcome is this thesis. My sincerest thanks go to all of them but I also want to address some people in particular.

First of all, I would like to place on record my limited thanks and praise against countless blessings of ALLAH Almighty. Without his care and guidance, I am nothing.

I am grateful and would like to thank my supervisor, Assoc. Prof. Dr. Nildem Turkey, deeply with the appreciation for her support during this thesis. I would like to express my sincerest gratitude and appreciation to my brother and supervisor, Assist. Prof. Dr. Sallal ABID, for his unlimited guidance, patience, support and dealing fraternal during this research really without him I cannot achieved this study. Thank you for all the support, freedom and patience to build up this thesis.

I would like to acknowledge the Iraqi Ministry of Higher Education (MOHE-IRAQ) for its financing to me and giving me the opportunity to study for a Ph.D.

I must acknowledge the assistance of the Scientific and Technical Council of Turkey.

Many thanks to Gaziantep University/ Civil Engineering Department for embracing me during the implementation of the work part of this thesis.

Special thanks to Prof. Dr. Mustafa ÖZAKÇA, who I learned much from him and for his unlimited support.

I would also like to special thanks to Prof. Dr. Abdulkadir ÇEVİK who always encourages me. Prof. Dr. Hamza Tanrıkulu, Assist. Prof. Dr. A. İlker AKGÖNEN and Assist. Prof. Dr. M. Tolga GÖĞÜŞ for their comments on the thesis and for agreeing to be on my Ph.D. committee.

Finally, I would like to thank my mother and father for their continued du'aa, without their continuous standing with me, I would not have finished this thesis.

TABLE OF CONTENTS

Page

LIST OF TABLES

Page

LIST OF FIGURES

Page

LIST OF SYMBOLS/ABBREVIATIONS

A	the apparent direct normal solar flux at the outer edge of the earth's atmosphere.
A	the area.
A_i	the individual area that surrounds the thermocouple.
AAE	the Average Absolute Error
B	the apparent atmosphere extinction coefficient.
c	the specific heat capacity in J/kg°C.
C_s	the Stefan-Boltzmann constant = $5.67\times10^{-8}\ W/m^2\ K^4$.
E	the modulus of elasticity.
h	denotes to the height of the cross-section.
h_c	the convection coefficient of heat transfer $W/m^2\ K$.
h_{web}	the depth of the web.
I	refers to the moment of inertia.
I_b	beam radiation on the horizontal surface.
I_{bn}	beam radiation on a tilted surface.
I_d	diffuse radiation on the horizontal surface.
I_{DN}	the intensity of solar radiation during average clear day.
I_{dn}	diffuse radiation on a tilted surface.
I_r	reflected solar radiation.
I_s	the total solar radiation incident normal to the surface of the girder.
I_{sn}	solar radiation on an inclined surface.
l_x, l_y, l_z	the directions cosines of the unit out-word normal to the boundary surface.

k_x, k_y, k_z	thermal conductivities in x, y and z-direction respectively, W/m℃.
L	length (mm).
MAE	the Maximum Absolute Error
Q	the amount of heat per unit volume generated inside the concrete by cement hydration (W/m^3).
q	is the boundary heat input or loss per unit area in W/m^2.
q_c	heat convection between the girder and the environment.
q_r	heat irradiation to the surrounding environment.
q_s	solar radiation from the sun.
r_g	ground reflectivity value of the surrounding surface.
T	the temperature at any point (x, y, z) at any time.
ΔT	the linear gradient.
T_i	the thermocouple temperature, ***i*** time step.
T (x, z)	the temperature difference a function of the (x) and (z) directions.
T_m	the uniform meancomponent.
T_o	nonlinear gradient related to the self-equilibrating stresses (eigenstresses)
T_s	the temperature of the girder surface.
T_α	the ambient air temperatures.
v	wind speed.
w_{bot}	the width of the bottom flange from the web.
w_{bot}	the width of the top flange overhang.
X_{FE}	the finite element predicted temperature.
X_{Exp}	the experimentally recorded temperature of each particular thermocouple at the same time step.
y_c	the centroid location.
α	coefficient of thermal expansion (mm/mm/℃).

α_s	the solar altitude angle.
β_T	inclined angle of the bottom flange.
ε	the emissivity coefficient of the surface.
γ	the surface azimuth angle.
γ_s	the solar azimuth angle.
δ	the tilted angle between the surface and the horizontal plane.
θ	incident angle
θ_z	zenith angle.
ρ	the density in kg/m^3.
n	the number of time steps.

CHAPTER 1

INTRODUCTION

1.1 General

Due to the daily and seasonally frequent changing of the environmental thermal loads (solar radiation, air temperature and wind speed), bridges are subjected to undesirable deformations and stresses. The solar radiation causes the temperature to vary nonlinearly through the depth and the width of the girders. Such variation leads to additional stresses (equilibrating stresses) to prevent the nonlinear deformation of the girder cross-section. The thermal equilibrating stresses can cause the cracking in concrete where it can be as effective as the static gravity loads. Moreover, the average temperature of the whole structure changes during the day and night cycles causing longitudinal movements or continuity stresses based on the end conditions of the bridge [1].

To understand the temperature gradient distributions and the consequent thermo-mechanical effects, many researches were carried out during the last three decades on several types and several parts of bridge structures. In general, the field long-tern studies are mostly fully sponsored as long-term Structural Health Monitoring (SHM) projects. The long term SHM systems include the instrumentation of the bridge girders, and other parts, by many types of sensors. Due to the high cost of bridge instrumentation, smaller size experimental girders were used by many previous studies [2-9] to evaluate the effect of the variations of solar radiation and air temperature on temperature gradient distributions and the consequent thermal response of bridge structures. Other studies [10-20] used analytical, numerical, and statistical techniques for this purpose.

1.2 Basic Concept

The heat transfers and flows in any grey body in three means. On the surfaces exposed to the surrounding environment, radiation and convection control the heat gain and loss to or from these surfaces. From surfaces to interiors and vice versa, the heat transfers via the heat conduction, which differs from material to another depending on the properties of the material. The main source of heat on the earth is the sun. Solar radiations reach the surfaces either directly or indirectly. A fraction of the incident solar radiation reflected into the atmosphere depending on the color and texture of the surfaces, while another fraction is absorbed as heat. Convection between the exposed surfaces and the air leads to the cooling of the bridge surfaces during the dark hours of the day. The degree of convection depends on wind speed and the difference in temperature between the surfaces and the surrounding air. The conduction of heat from exterior surfaces to the interior parts of the sections or vice versa depends on two primary thermal properties of the material in addition to the density, these are the specific heat and the thermal conductivity. Another important heat source is the absorption of the reflected radiation from the ground and other neighbor objects. The absorbed heat is also dissipated from concrete surfaces (during the cold dark hours) to the atmosphere via the long wave radiation, which is considered as a cooling load added to the convection cooling [21-25].

During the day, the temperature changes rapidly in the atmosphere. However, due to the weak thermal conductivity of concrete, the temperature inside the cross section changes slowly, while in the exposed steel sections, the opposite holds. Consequently, the temperature distributions in the cross section are non-linear and depend on many characteristics as the thermal properties, the geometry, the type and color of the surfaces, time of the season and the position of the bridges from the sun movement.

After sunrise, the air is heated due to solar radiation and its temperature is gradually increased. The variation in the air temperature produces uniform distributions of temperature in the bridge. On the other hand, the direct solar radiation leads to a significant change in the heat of the bridge surfaces, which leads to rapid changes in their temperatures. In the same time, the interior layers of concrete keep colder as the heat is slowly conducted from the exposed surfaces to the interiors. Thus, during the sunny hours (day hours before, during, and after midday), temperature gradients occur between the hot surfaces and the cold interiors. Such temperature gradients are

termed as positive gradients. If these gradients are calculated along the central vertical axis of the girder or through the webs, then they are termed as vertical temperature gradients. On the other hand, horizontal temperature gradients are those calculated laterally along the centerline of the horizontal parts of the superstructure such as the top slab or the flanges [26].

After sunset, the exterior surfaces are cooled quickly due to the effects of the convection and the long-wave radiation, while the interiors still hot. Thus, and again due to the weak thermal conductivity of concrete, reversed temperature gradients occur with cold surfaces and hot interiors. Such temperature gradients occur after sunset to sunrise and termed as negative temperature gradients.

In composite girders, the thermal conductivity of steel is much higher than of concrete. Moreover, the thicknesses of steel sections are extremely smaller than of concrete sections. Hence, minimal temperature gradients occur within the steel sections. Across the concrete sections however, significant temperature gradients occur. Another note is that the overall temperatures of the exposed steel sections become much higher during the day and much lower during the night compared to the concrete parts due to the same reasons. Thus, the temperature gradient distributions in composite girders are significantly different from those of concrete girders [27].

1.3 Objectives of the Research

This research implemented at the Gaziantep University campus (Latitude 37° 2' 22" N and longitude 37° 19' 2" E) in Turkey to study the thermal behavior of two different composite girder segments. The work presented in this thesis composes of four main parts. An experimental work, a finite element modeling study, a parametric study and an extreme analysis study. The main objectives of the work presented in this thesis are:

- Experimentally investigating the effect of solar radiation, air temperature, and wind speed on the temperature and temperature gradients distributions and thermal strains of composite girders. The experimental work includes the casting of two composite girder segments; a concrete slab on steel beam (T-Beam) and a concrete-encased-steel beam (I-Beam). The two segments were

instrumented with thermocouples, strain gages, air temperature probe, wind speed anemometer and solar radiation pyranometer.

- Conducting a thermo-mechanical finite element study using the COMSOL finite element package [28] to solve heat flow in the two composite girder segments under the effects of the different boundary condition, including the convection, solar radiation, reflected radiation and re-radiation. The FE thermal analysis investigates the temperature and temperature gradient distributions in addition to thermal strains and thermal stresses due to these gradients.

- Verifying the FE element model using temperature records from the two experimental segments and studying the influence of the size of the girder bridge on the thermal behavior using the verified FE model. In addition to the overall sizing of the girders, the effect of the thickness of concrete flanges or top slab and the height of the girder are also investigated.

- Conducting an extreme analysis to evaluate the long-term temperature gradient variations in composite girders in Turkey. For this aim, the verified FE model of the T-beam is used in conjugate with weather records of more than 50 years for 10 Turkish cities distributed along the seven Turkish regions. From this analysis, the possible extreme vertical and lateral temperature gradients are investigated for the adopted cities, and hence, design gradients can be introduced.

1.4 Layout of the Study

This dissertation consists of eight chapters to accomplish the problem of the study.

Chapter two summarizes the available literature review on the effect of environmental thermal loads on temperature and temperature gradients in bridge girders, especially composite girders, in addition to the consequent structural effects. The chapter also reviews some of the available international design code provisions on this subject.

Chapter three describes the experimental work, construction, setup and instrumentation of the two composite girder segments, while the records of the experimental work from the two segments are presented and discussed in chapter four. These results include the environmental records (air temperatures, wind speed and solar radiation) and temperature records from the different thermocouples installed in the different parts of the two girders, in addition to strain measurements.

In chapter five, a summary of the formulation of the temporal FE thermo-mechanical analysis and an overview of the temperature effects, provisions of AASHTO LRFD [29] is introduced, followed by an explanation of the conduction of this analysis using COMSOL. The verification of the FE thermal analysis is also presented in this chapter. Chapter six presents the FE parametric study, which is composed of three parts. The first investigates the combined effect of the girder depth and the thickness of its flanges and web. The second evaluates the effect of the girder depth by using fixed thicknesses for the web and flanges. The third part investigates the effect of the thickness of the web and flanges for a fixed depth of the section.

In chapter seven, the Turkish State Meteorological Service [30] data of temperature and solar radiation are used for more than 50 years, since 1960 to 2013 to estimate the extreme temperature and temperature gradients in composite girders. The analysis includes six different months, which are April, June, July, October, November, and December for two selected cities. Based on the verified COMSOL FE model, the maximum vertical and horizontal temperature gradients of composite bridge girder in ten cities for six months are obtained and compared in this chapter. Finally, the most important conclusions of the four parts of this study are presented in chapter eight in addition to recommendations for future required studies.

CHAPTER 2

LITERATURE REVIEW

2.1 General

From the early years of the 60th of the previous century, large studies were carried out to understand the effect of temperature related by the bridge problems. Field tests and numerical solutions were made to improve the understanding of the thermal behavior of bridges under environmental thermal loads. Generally, researchers have studied the thermal behavior devoted to composite box girder bridges. While the composite I-girder bridges are rare.

A detailed current survey of the literature published on the thermal gradient analysis in composite bridges girder is presented in this chapter. In addition, some current design codes provisions are reviewed.

2.2 Thermal Behavior of Composite Girder Bridges

In the earlier decades very large studies were conducted about temperature impacts on concrete bridges. One of the most significant studies in composite girder bridges is thermal effects. These effects have important impacts as dead or live load influence. But, only some investigations were devoted to composite steel-concrete bridges. On the other hand, in composite girder bridge, the temperature distributions are different due to various properties and cross sections. Hence, the shear connections in a composite girder bridge must be designed correctly to able of resisting thermal stresses.

2.2.1 Experimental and field data of thermal effects

Naruoka et al. [13], in 1957 checked a temperature at a simply supported bridge with reinforced deck slab-on-steel girders of the Shigita Bridge in Japan in July. The researchers have obtained a typical vertical temperature distribution during the study

period. Also, the results of the field tests showed that the distribution is linear in the concrete deck slab and almost constant in the steel girder. Furthermore, the researcher found that the maximum difference in temperature between the top and bottom of the concrete deck slab around 22 °C, in addition, the thermal gradient in the black surface is very steep.

Zuk [16], in 1961 discussed linear temperature gradients in statically determinate composite bridges by revealing accurate derivation of thermoelastic stresses and deformations. He assumed that slab and beam were considered separate and free to deform independently. Actual stresses and deformations could then be built by elementary beam theory. Later in 1965, Zuk [14] extended this work to handle the vertical temperature gradients as a function of depth in a composite bridge across the Hardware River in North Carolina. The outcomes pointed that the vertical temperature distribution is almost linear in the concrete part with very small variation through the depth of the steel girder. In addition, the researcher found that the temperature differences in concrete deck between the top and bottom ranged from 11 to 19 °C during the day and -2 to 4 °C during the night.

Brewanger and Symko [31], in 1976 illustrated from experimental and analytical steady-state of temperature distributions generated in cross-sectional planes of a composite steel-concrete single span for bridges. By using the theory of heat transfer in solids, the researchers predicted temperature distributions throughout the cross section from known surface temperature. On the other hand, the study included an improvement of finite solutions for steady-state of temperature distributions according to the known boundary conditions. Also, the evaluation of the strains and stresses were involved. Which reflected relatively small concrete slab stress when related to their allowable stress. While, the temperature stress in the steel beam is very large to consider in the design of these bridges. But, the empirical strains are linear in the composite section with the computed FE strains to give little higher stress. Finally, they found a temperature and stress distributions are nonlinear with linear strains in the FEs.

In 1977, Thepchatri et al. [32] conducted a series of an experimental and analytical study on three bridges of different sections in the Austin area: a post-tensioned concrete slab bridge, a composite post-tensioned bridge, and a composite steel girder

bridge. The researchers proceeded to determine thermal effects. In these studies, diurnal variation in air temperature, solar radiation and wind speed were chosen to express extreme winter and summer climatic conditions. The researchers made a comparison between available field data and the analytical result. This comparison of temperature distributions obtained a proper correlation. Also, the Center for Highway Research conducted several general conclusions resulted from these studies.

Chan et al. [33], in 1990 studied thermal stresses of three composite box girder bridges during the two-year period continuously of collection temperature data. From the three bridges, data of the extreme temperatures and temperature differentials in the box girder sections were examined. By using a FE method, thermal stresses were obtained from the measured temperature differential data. The results of this study gave thermal effects in compression in steel 92 and 3.8 MPa in tension in the concrete. Finally, the researchers suggested many scams to reduce temperature differences in the composite box girders.

Fu et al. [34], in 1990 determined the analytical results gained from a parametric study on the thermal behavior, according to the experimental study of three different species of composite bridge structures subjected to the thermal load. The parameters investigators were including the diurnal ambient air temperature, intensity of solar radiation, slabbing overhang-to-slab depth ratio and heat-transfer coefficient. These composite concrete-steel bridges were a single and double-cell box girder and a plate-girder. The researchers computed temperature distributions and temperature induced stresses identical to a given geographic location and anticipated environmental conditions. The outcomes of this study prove that a steady state thermal condition never exists in a bridge structure. The intensity of solar radiation and ambient air temperature are both time-dependent.

In 1991, Pentas et al. [35] carried out an investigating for temperatures and temperature distributions into a composite bridge in Louisiana. Researchers found that the maximum average girder temperature closely follows the ambient temperature and the maximum average slab temperatures followed a similar trend. But at higher temperature solar radiation will magnify the slab temperatures in a somewhat linear manner. Also, they suggested two relationships to predict maximum average slab temperatures dependent on slab temperature and ambient temperature.

According to their observations, a vertical temperature profile will be developed. Furthermore, they introduce equations to suggest the temperatures at three points through the depth of the section: top of a deck, deck-girder junction, and mid- depth of the girder. By this equation, the temperature profile is linear between these points and constant below the center of the girder.

Mootry and Roeder [36], in 1992 made a large study of thermal effects at 11 different locations in the United States for typical bridges of three cross sections: concrete box girder, concrete T-beam, and composite steel I-girder. Maximum and minimum effective bridge temperatures for every section were determined. These were compared to AASHTO [37] specified temperature ranges. Generally, the results showed that concrete bridges undergo mean temperatures which sometimes exceed the AASHTO recommended range while mean temperatures for the steel bridges were completely within the recommended range.

In 2004, Im and Chang [38] observed a steel-concrete composite box girder bridge by thermocouples during more 6-years in the south of Seoul. The study focused on a three parameters of the thermal load which is involved: effective temperature, vertical and horizontal temperature difference. According to the hourly data measured the researchers revealed that the horizontal temperature differences are no longer negligible since they are of the same order of magnitude as the vertical temperature differences in the winter months. On the other hand, they indicated that all the thermal load parameters of hourly maximum and hourly minimum values obey to the Gumbel distribution.

Římal et al. [39], carried out an empirical study on the performance of a composite box-girder railway bridge subjected to the environmental thermal effects (solar radiation, air temperature and wind speed) in Kralovske Porici Bridge. The measurement of the temperature fields and the temperature gradients in the bridge structure was made under extreme summer and winter temperature conditions. The researchers found that the temperature and time pattern along the cross-section height takes a general form not approaching the majority of the current standard design of composite steel-concrete bridges. Also, they referred to the temperature, time pattern along the concrete slab cross-section may be considered as linear.

In 2009, Zhang Tao [40] implemented an experimental work for composite I-girder bridge. He presented the characteristic of the temperature field, and examined the relation between the ambient and structural temperature field by a mathematical model. And suggested a design temperature profile. Dimensions of the section of plate girder are 380 × 560 cm^2, a concrete plate deck supported on three I-main beam and I-cross beam sections of 40 and 25 cm depth respectively. This study pointed that heating by the solar radiation made the concrete deck as a heat source and raises the temperature of the steel plates which aren't exposed to direct sunlight. And because of the non-uniformity of the temperatures in concrete deck and steel girder, large internal thermal stresses are developed if any thermal deformation is restrained. Also, he found that the variation of the steel girder is faster than the concrete girder due to thermal properties of the material. In addition, the temperature distribution in the concrete deck is nonlinear, the temperature difference is maximized. the researcher concluded that the vertical temperature distribution caused by the solar radiation is not homogeneity, and the temperature difference changes a little with the ambient environment change. He also showed that under the solar radiation, the shear connection is easy to damage.

In 2009, Francesca [41] studied the long-term behavior of composite steel-concrete bridge beams subjected to static loads, shrinkage, and thermal gradients. Diurnal and seasonal temperature variations are taken into account. From experimental work, the researcher adopted in his analysis a linear elastic law for the steel beam and a linear viscoelastic behavior for a concrete slab. He also found that, when the temperature gradients present non-linear distributions along the vertical axis of the section, further self-equilibrated stresses arise in the composite section, even if simply supported systems are considered. These stresses have to be added to those generated by permanent and static loads and the ones induced by shrinkage of the concrete slab. Finally, the researcher point that, in the service stage, the steel beam does not present stresses of any significance, as its cross-section is designed in order to limit vertical displacement while the concrete slab can be subjected to cracking phenomena.

In 2013, Zhou and Yi [42] studied a thermal load by representation the three types of bridges that are a concrete bridge, steel-concrete composite bridge, and steel bridge. Based on field measurement results, the researchers adopted the finite difference

method and FE method in the numerical analysis. According to the different heat transfer coefficients of steel and concrete make a nonlinear thermal gradient along the vertical axis of the cross section. The researchers found that from the investigation of thermal load in three types of bridges by the theoretical model, numerical analysis, and field measurement refer to progressing remarkable results.

2.2.2 Theory and computational evaluation of thermal load

In 1977, Emanuel and Hulsey [43] worked out a new numerical solution to compute the differential heat flow equation of FE method for different composite bridge decks. They divided cross section into constant heat flow elements. In this study, the main environmental factors studied: solar radiation, shade, temperature and wind speed.

Emanuel and Lewis [44], in 1981 carried out a simulation for a prior study of the environmental stress on the slab force. The researchers made correlation results of strain and deflection with theoretical values, which reflects agreement results between the experimental and theoretical values. This, in turn, provided a reasonable method for predicted the thermal behavior of composite bridge and can be used with actual temperature profiles, material properties, and substructure stiffness characteristics.

Dilger et al. [45], in 1981 developed a computer program able to predict the temperature distribution in the cross-section of a composite steel box-girder bridge. Researchers demonstrated that a very high temperature differences develop as a result of the different thermal properties of the two materials and the stresses caused by thermal effects are higher in continuous structures. Also, the study found that under the worst conditions, temperature differences of up to 70 °C may develop. On the other hand, they suggested that to reduce the differences between steel and concrete in temperature by many means: painting the steel box with a bright color, providing a long cantilevering deck, and sloping the webs of the box.

Berwanger [46], in 1983 studied a numerical procedure for the solution of transient temperature variations in composite slab–beam highway bridges. By using higher order triangular FEs, the bridge deformations calculated. Also, strain and stresses are

determined by using small deflection theory. According to the FE thermoelastic analysis method, continuous composite slab-beams bridges can be solved.

Xia et al. [47], in 2011 checked the temperature pattern of a structure by a thermodynamic direct approach on a simple rectangular concrete slab. The researcher found that the mechanical model can accurately forecast the structural temperature field. Because of, the mechanical model deals with the temperature effect on the thermal reliance with young's modulus and its gradient in the structure considering a composite structure whose components have different young's moduli.

2.3 Temperature Gradients of Bridges

During daytime, especially in summer, a net gain of energy occurs, resulting in a rise in temperature through the structure such that the top surface becomes warmer than the soffit. Because of the poor thermal conductivity of concrete, this rise in temperature results in temperature gradients within the bridge structure. These gradients are denoted as positive gradients. Conversely, the net loss of heat which occurs, typically, during winter nights, results in a reduction of temperature in the structure, thereby creating negative gradients of temperature with warmer soffit than the top. The resulted deformations from temperature gradients, when restrained, produce stresses in the structure. To calculate the resulted stresses, these gradients must be calculated. The temperature gradients are governed by the heat flow through the body and are functions of the density, specific heat and thermal conductivity of the material.

In 1970, and based on measurements taken from three bridges in Britain, Maher [48] suggested a linear temperature distribution through the top slab of the bridge. In 1972, Priestly [49] analyzed the effect of different available suggested thermal gradient models and compared the results with available measured data. Among these suggested gradients is proposed by Maher. Another one proposed by the Ministry of Works of New Zealand [50] in which temperature varies with depth as second, fourth and sixth-degree parabolas. Based on his study, Priestly found that the sixth-degree parabola gives the most accurate temperature distribution and thus was recommended for superstructure depths between 1200 and 1500 mm as shown in Figure 2.1.

In 1976, Priestly [10] proposed a revised temperature gradient to that suggested in 1972. It has consisted of three individual parts. In the first part, the temperature was assumed to decrease nonlinearly from a maximum at the top surface of the deck slab to a depth of 1200 mm, with the nonlinear variation represented by a fifth-degree parabola. The second part applied only to a top slab of a box girder, in which temperature was assumed to decrease linearly. The third part assumed a linear variation of temperature over the bottom 200 mm of the cross section.

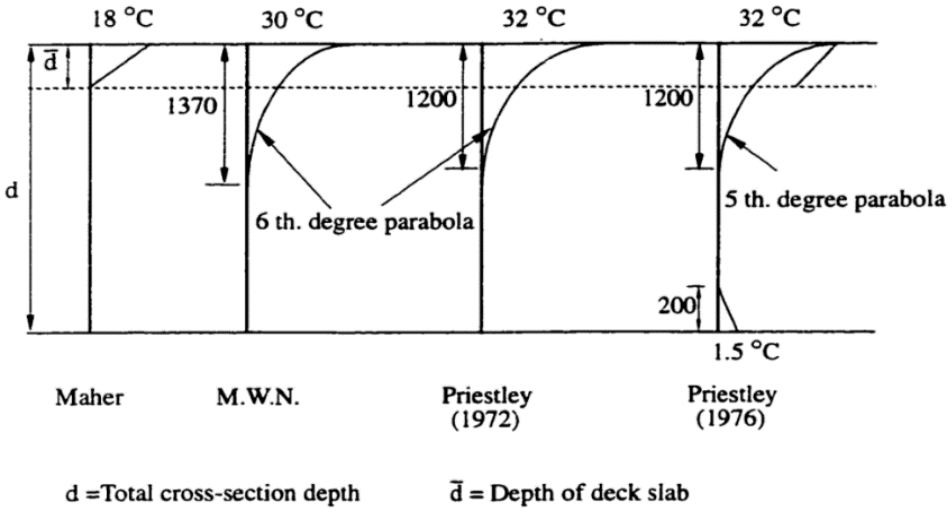

Figure 2.1 Temperature gradients suggested by Priestly [51].

In 1983, Dilger et al. [51] carried out measurements on the Muskwa River Bridge, a composite steel box girder bridge. They found that a large temperature difference of 41 ℃ occurred between the concrete deck and the steel box exposed to the sunlight. This temperature difference developed in less than two hours. Also, temperature difference alone would have been large enough to cause cracking of the concrete deck. The maximum and average recorded crack width was 0.22 and 0.09 mm respectively.

Elbadry and Ghali [52], in 1986 studied the temperature variations produced by weather conditions over the cross section of a bridge structure which are generally nonlinear and which induce stresses of substantial magnitude in both the longitudinal and transverse directions. They discussed the variables that affect thermal stresses and used a computer program to predict the temperature distribution and the corresponding self-equilibrating stresses over the bridge cross sections of data related to the bridge location and weather conditions. They found that the tensile stresses

due to temperature could be high enough to cause concrete cracking in different parts of the box girder bridges.

Chang and Im, in 2000 [53] studied the thermal behavior of composite box girder bridges. Their study is based on field measurements of a newly constructed composite box girder bridge in South Korea. The authors carried out a two-dimensional FE analysis, which has good agreement with the field records. They compared their results with the BS 5400 [54], and AASHTO LRFD [29] recommended temperature gradients. The researchers concluded that the design temperature distribution with a uniform differential between the concrete slab and the steel girder is unsuitable for representing the thermal effects in design purpose.

In 2002, Au et al. [55] conducted a study of thermal behavior of composite bridges in Hong Kong. The results of this study demonstrated that the temperature distribution in bridge depends essentially on the solar radiation, ambient air temperature and wind speed. Also, the researchers suggested that a fifth-order equation of the design temperature profile for better estimation of thermal properties of the material and file coefficients in tropical regions, which is very similar to the one proposed by Priestley [49].

In 2007, Stuart et al. [56] found that in-plane shear strain in the slab acting as a flange in the composite girder under the applied bending causes the longitudinal displacements. This shear lag can result in an incorrect calculation of the displacement and extreme fiber stresses when using only the basic theory of bending beam. A parametric study was carried based on FE analysis of bridges selected by a statistical method (namely, the design of experimental concepts. Effective width values at the critical sections were calculated from stresses obtained from FE models).

2.4 Solar Models Literature

Emanuel and Hulsely, in 1978 [57] analyzed a composite girder bridge based on Columbia weather conditions. They studied two extreme conditions; the first is the maximum ambient air temperatures and their corresponding solar flux on July 20th, while, the second is the minimum ambient air temperature and their corresponding solar flux on January 18th. They proposed formulas to estimate the solar heat flux

corresponding to the maximum and minimum air temperature for horizontal surfaces. Their formulas depend on many variables, among which are; the solar heat incident to the horizontal surface, a day of the year, daytime (hour), sunrise and sunset hours, a length of sunlight hours, turbidity of the atmosphere, and the solar constant I_{SC}.

In 1998, Kuehn et al. [58] gave a simple equation to estimate the intensity of solar radiation during average clear day, and this can be expressed as:

$$I_{DN}=Ae^{-B/sinB} \quad (2.1)$$

Where the coefficients A and B are empirical to be determined from the measurements of I_{DN} made on the typical clear day. A is the apparent direct normal solar flux at the outer edge of the earth's atmosphere. B is the apparent atmosphere extinction coefficient. The numerical values of A and B vary throughout the year because of seasonal changes in the dust and water vapor content of the atmosphere and because of changing the earth-sun distance. The author gave recommended tabular values for coefficient A and B for the twenty-first days of each month.

2.5 Current Design Codes

Many design codes were used around the world; however, in this section, the temperature distribution and the thermal design provisions of the widely used codes will be reviewed.

1. AASHTO Standard Specification of Highway Bridges (2007) [59],
2. AASHTO LRFD Bridge Design Specifications (2012) [60],
3. AASHTO Guide Specifications of Horizontally Curved Highway Bridges (2003) [61],
4. Eurocode, CEN ENV 1991-1-5 (2003) [62] and
5. British Standard BS 5400 (1978) [54].

2.5.1 US Code

Three important provisions of the American Association of State Highway and Transportation Official (AASHTO) standards will be discussed in the following subsection.

2.5.1.1 AASHTO Standard Specification for Highway Bridges (2007)

The AASHTO Standard Specification for Highway Bridges (2007) [59] provided thermal gradients or temperature differentials through the depth of the bridge, which stated that for mineral structures and for concrete structure, the range of bridge temperature should be taken generally as 0 ~ 120 ^{o}F under moderate climate and -30 ~ 120 ^{o}F for cold climate for steel while taken 10 ~ 80 ^{o}F under moderate climate and 0 ~ 80 ^{o}F for cold climate for concrete. So, AASHTO [59] put a limit for design massive concrete members or metallic structures in moderate and cold climates.

2.5.1.2 AASHTO LRFD Bridge Design Specifications

AASHTO LRFD [60] Bridge Design Specifications supply more detailed on thermal loading than AASHTO Stander Specification [59]. There are two officials way in LRFD Specifications can be used to calculate the thermal movement associated with the uniform temperature change. The first procedure in the LRFD Specification similar to recommended temperature ranges in moderate and cold climates in the AASHTO Standard Specification. Table of the AASHTO LRFD [60] temperature ranges includes the superstructure and the climate (moderate and cold) at degrees Fahrenheit. By using this manner the temperature range is multiplied by the thermal coefficient of expansion of the material and the length of the member being designed. The second procedure selected a maximum and minimum design bridge temperature, from a thermal contour map of the United States. Which provided various maps for concrete and composite superstructure.

2.5.1.3 AASHTO Specifications of Horizontally Curved Highway Bridges

Generally, the limitations of the thermal effects in the AASHTO Guide Specifications for Horizontally Curved Steel Girder Highway Bridges (2003) act according to the recommendations of the AAHSTO Standard Specification, with the addition of temperature differential between the deck and girders, which states: “ A

uniform temperature difference of 25 degrees Fahrenheit between the deck and the girders shall be considered when the width of the deck is less than one-fifth of the longest span. The load effects due to the temperature differential shall be added to the effects due to the temperature changes specified in AASHTO".

Extra comments with respect to the tendency of bearing guides are included in the commentary of the Guide Specification.

2.5.2 Eurocode (CEN ENV)

In Eurocode 1 [62], the requires of a steel-concrete composite bridge for thermal effects be evaluated by the uniform temperature component and the temperature difference components. Generally, the uniform temperature component correlated with minimum and maximum shade air temperature that depends on the site of mean sea level, which shall be derived from national maps of isotherms for each country. Furthermore, the vertical temperature difference component includes either the nonlinear component by using the normal procedure or linear component using the simplified procedure. Eurocode 1 illustrated that for important structures the thermal analysis must be used.

2.5.3 British Standard BS 5400

In BS 5400-1-1978 [55] code, the uniform temperature component and difference components estimate the thermal actions. The maximum and minimum uniform temperatures are obtained from the maximum and the minimum shade air temperatures and the types of bridge cross section. This code used two maps of isotherm in order to select the maximum and minimum shade air temperatures depends on the site of mean sea level and asphalt depth of bridges. Linear temperature distributions are assumed to consider the effects of vertical temperature difference. BS 5400-1-1978 [55] code gives the shapes of positive and negative temperature distributions according to the cross section type for steel-concrete composite bridges.

2.6 Conclusions from the Literature Review

From the review literature, and according to the current literature survey, it can be concluded that:

- In general, the researches on composite I-steel girder bridge subjected to the thermal load behavior by experimental work very little and not cover many parameters.

- The numerical modeling under the effect of elevated temperatures is still not fully covered.

So, it can be noted that, for the thermal behavior of composite I-steel girder bridges, complete works with field measurements and numerical studies are RARE.

CHAPTER 3

THE EXPERIMENTAL TEST SET UP

3.1 Generally

In this study, an experimental work carried out to examine the environmental thermal loads under influence of ambient air temperature, solar radiation and wind speed on the thermal behavior of two different composite I-steel girder segments at the Gaziantep University campus (Latitude 37° 2' 22" N and 37° 19' 2" E).

3.2 Instruments and Equipment

In general, sensors include thermocouples, strain gages, air temperature probe, wind speed anemometer and solar radiation pyranometer are illustrated in this section. While, measurement units include the data logger and the connecting parts.

3.2.1 Air temperature probe and sensor mounts

The air temperature probe is an instrument used for observing the ambient air temperature in the study field. The 108-temperature probe is proposed to use a thermistor to measure temperature [63].This type of probe is designed accurately to measure a variety of applications of air, soil and water temperature fields. Figure 3.1 shows a radiation shield to amount the 108-probe and limit solar radiation loading for air temperature. Also, this type of probe effective in temperature range of -5 to +95 ^{o}C. The polynomial linearization accuracy typically < ±0.5 °C at the -5 to +90 °C range, also interchangeability error typically < ±0.2 °C over 0 to 70 °C range increasing to ±0.3 °C at 95 °C.

The 108-probes must be housed inside a 41303-5A radiation shield if open to sunlight. To attach the radiation shield directly to a tripod mast, tower mast, or tower leg, places the U-bolt in the side holes as shown in Figure 3.2.

Figure 3.1 The 108-probe requires one single-ended channel for measurement [63].

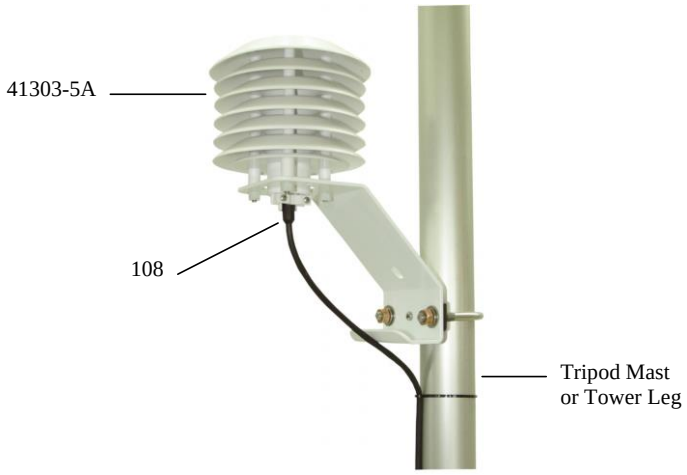

Figure 3.2 The 108-air temperature probe with solar shield [64].

3.2.2 Wind speed sensor

The three–cup NRG#40 anemometers [65] from NRG system will be used to measure wind speed as shown in Figure 3.3. This type of device recommended by Campbell Scientific. The sensor is able to read the wind speed ranging from 0 to 96 m/s (0 to 215 mph).

The accuracy of the NRG#40 is high because having three conical cups molded in one continuous piece; the estimated error is ± 0.14 m/s at 10 m/s. A rubber terminal boot is included. Cup rotation produces a sine wave voltage in a single coil by a four-pole magnet. Two sine wave cycles were generated for each revolution of the cups with the frequency directly proportional to wind speed.

Figure 3.3 The NRG#40 three- cup anemometers [65].

3.2.3 Solar radiation sensor

The CS300 used a silicon photovoltaic detector mounted in a cosine-corrected head to supply solar radiation measurements for solar, meteorological and hydrological applications [66].

Figure 3.4 shows the CS300 pyranometer provided by Campbell Scientific is used to monitor the global sun plus sky radiation in the experimental field. The CS300 measures a radiation range of 0 to 2000 W/m^2 with an accuracy of ±5% of daily total radiation. The dome-shaped head prevents water from accumulating on the sensor head.

Figure 3.4 The CS300 silicon pyranometer [66].

To reduce internal condensation, the sensor head is potted solid and the cable is shielded with a rugged Santoprene casing [66]. Figure 3.5 shows leveling fixture of CS300 pyranometer and Figure 3.6 shows holding of CS300 pyranometer and associated fixture to a holding arm [66].

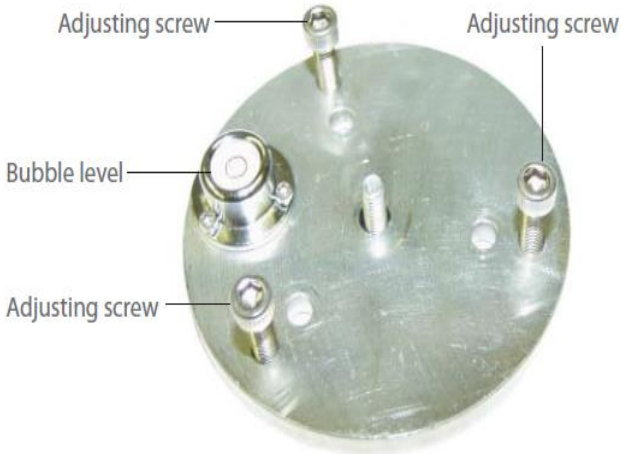

Figure 3.5 Leveling fixture of CS300 pyranometer [66].

Figure 3.7 shows the solar radiation system which includes a sensor of the air temperature probe, wind speed and solar radiation in the site.

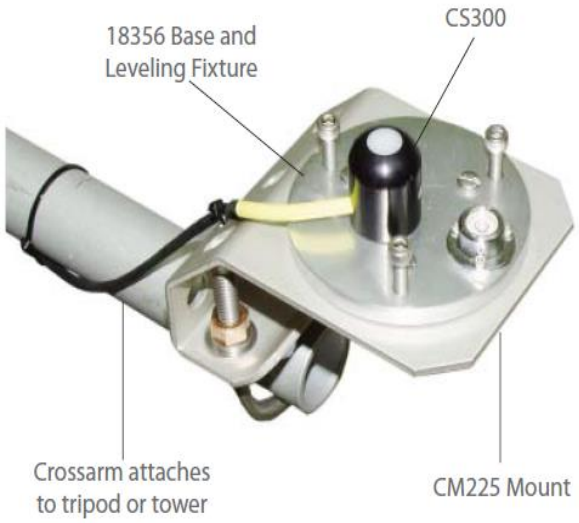

Figure 3.6 Holding of CS300 pyranometer and associated fixture to a holding arm.

Figure 3.7 The solar radiation system in the site.

3.2.4 Data acquisition system

The Campbell Scientific's products are used to compose the data acquisition system of the study. Figure 3.8 shows the data logger CR1000 which is the core of this system. CR1000 operated in a temperature range of -55 to +85 ℃. Also, the temperature sensor has built in the data logger to measure the temperature of the panel.

Three the AM16/32 multiplexers are employed to increase the number of sensors that can be measured by a data logger as shown in Figure 3.9. Also, Ethernet type NL115 and compact flash will be used to store data and directly download to PC as shown in Figure 3.10. These three products compose the main parts of the system. The data recording, timing, downloading and presentation will be controlled by the LoggerNet 4.1 software.

Figure 3.8 The data logger CR1000.

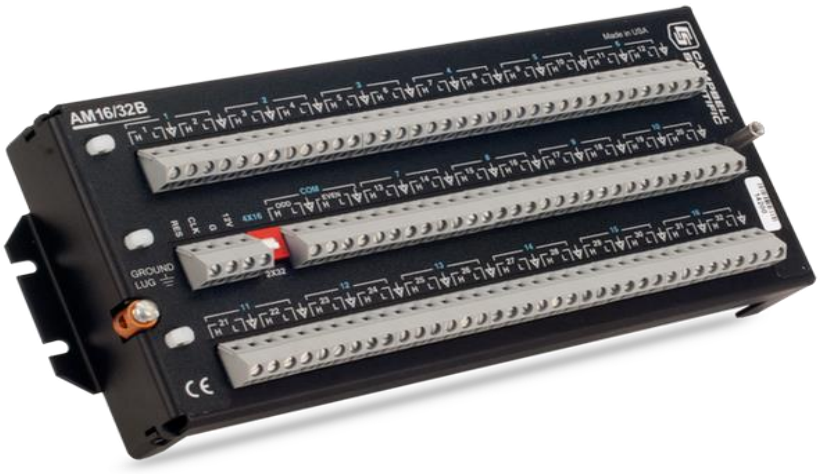

Figure 3.9 The AM16/32 channel multiplexers**.**

Figure 3.10 The L115 Ethernet/ compact flash module.

3.2.5 Thermocouples

A thermocouple is a sensor used to measure a temperature-time relationship. This composed of two legs of the wires of different metals welded together at one end as shown in Figure 3.11. The welded end produces a junction that leads to a voltage under any change in the temperature. By thermocouple reference tables the voltage can be correlated to a temperature reading.

There are several types of the thermocouples according to their characteristics. Types K, J, E and T are the most common types of thermocouples. In this study, thermocouple type T is used, which are made with a copper (positive) and a constantan (negative). Because copper has a much higher thermal conductivity than the alloys used in thermocouple constructions. This type is appropriate for measurements in the -200 to 370 ℃ range and has lowest error than other types, Table 3.1 shows the detail of the four common types of thermocouple.

Figure 3.11 The thermocouple type T.

Table 3.1 The detail of the four common types of thermocouple.

Type	Conductors		Temperature ℃		Accuracy (whichever is greater) Special limits of Error:
	(+) Leg	(-) Leg	Min	Max	
K	Chromel	Alumel	-270	1260	+/- 1.1 ℃ or 0.4%
J	Iron	Constantan	-210	760	
E	Chromel	Constantan	-270	870	+/-1.0 ℃ or 0.4%
T	Copper	Constantan	-200	370	+/- 0.5 ℃ or 0.4%

3.2.6 Vibrating Wire Strain Gages

By using a strain gages, the strain and the stresses in different directions can be checked. In this study, two types of strain gages are used. One for reinforced concrete and mass concrete structures and other for steel as shown in Figure 3.12 (a) and (b) respectively

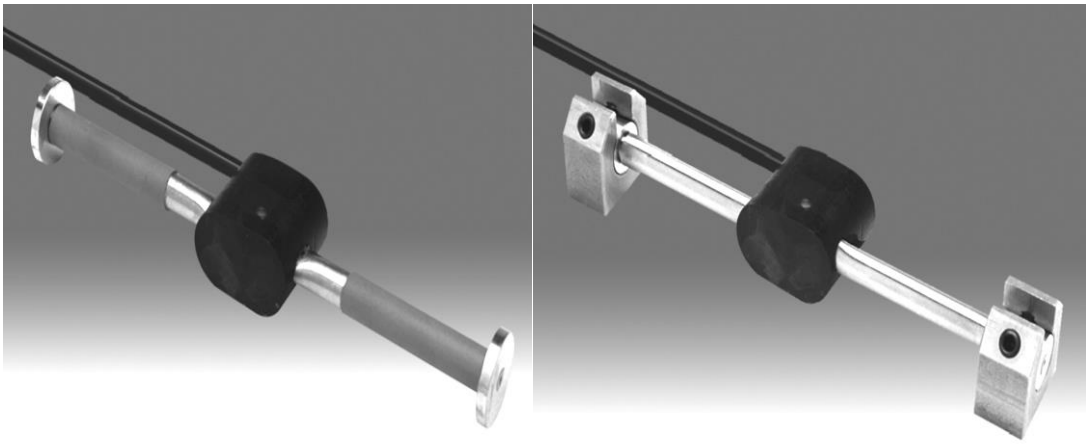

(a) (b)

Figure 3.12 Vibrating wire strain gage (a) for reinforced concrete and (b) for steel.

3.3 Experimental segments

Experimental works included casting two segments of composite girders. One segment was composite concrete I-steel girder (T-Beam) as shown in Figure 3.13. Another segment was composite encased concrete I-steel girder (I-Beam) as shown in Figure 3.14.

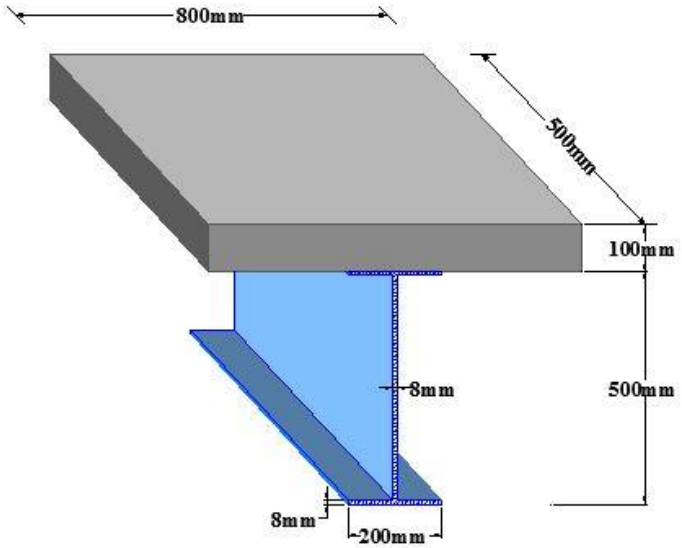

Figure 3.13 Composite concrete I-steel girder (T-Beam) segment.

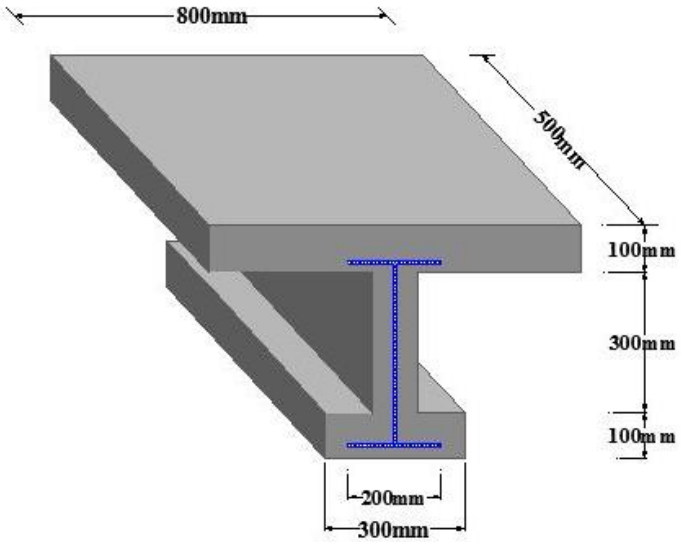

Figure 3.14 Composite encased concrete I-steel girder (I-Beam) segment.

3.4 The Composite Concrete I-Steel Girder Segment

Figure 3.13 shows detailed dimensions of the T-Beam segment. I-steel girder depth is 500 mm, width of the flange is 200 mm and the thickness is 8 mm for the steel

part. The segment I-Beam has the same dimensions of I-steel girder except 400 mm depth as shown in Figure 3.14.

Figure 3.15 shows, top view of concrete deck 500 × 800 mm and thicknesses are 100 mm for the two segments. Steel reinforcements are 10 mm diameter bars with 100 mm spacing.

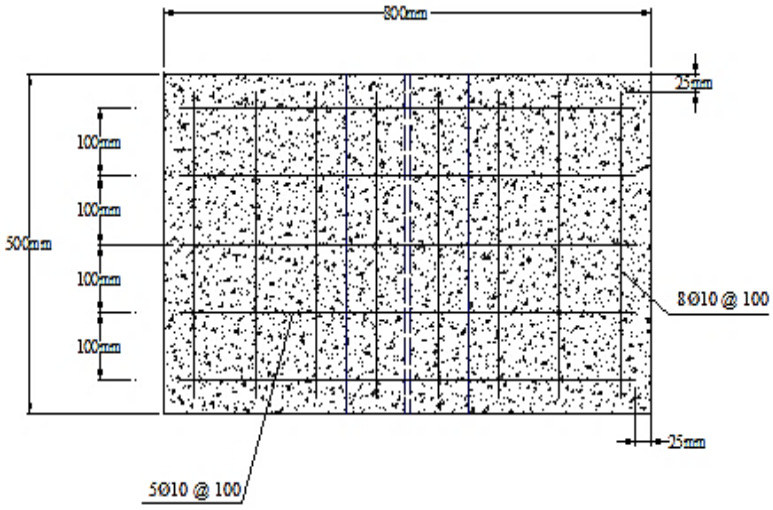

Figure 3.15 Cross-section and steel reinforcement of concrete deck.

3.5 Experimental Work of composite Girder Segments

In the first step of the experimental work thermocouples and strain gages are installed into the two segments. Figures 3.16 to 3.19 show the T-Beam and the I-Beam segments before and after concrete casting into the site.

Figure 3.16 The T-Beam specimen before casting.

Figure 3.17 The T-Beam specimen after casting.

Figure 3.18 The I-Beam specimen before casting.

Figure 3.19 The I-Beam specimen after casting.

3.5.1 Position of Thermocouples

For segment T-Beam, the total number of used thermocouples was 14. Seven thermocouples are installed for both concrete (TC) and steel (TS). Figure 3.20 shows the locations of thermocouples which installed in the T-Beam specimen. While, 15 thermocouple used in I-Beam segment. The location of 12 thermocouples in concrete (TC) and 3 thermocouples in steel (TS) are shown in Figure 3.21.

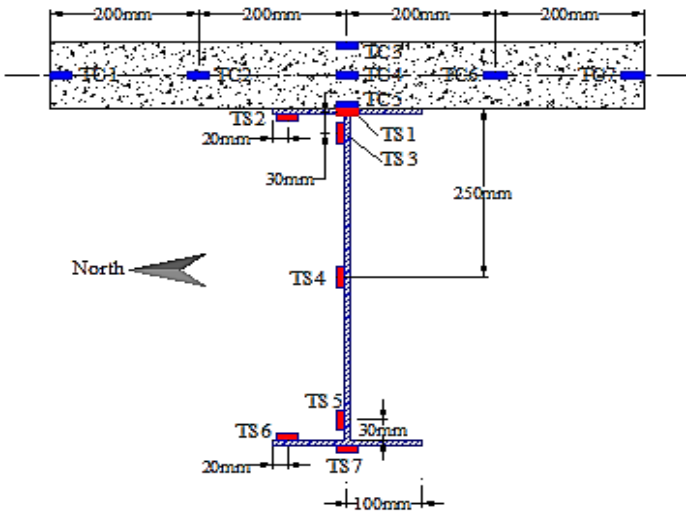

Figure 3.20 The locations of thermocouples installed in T-Beam segment.

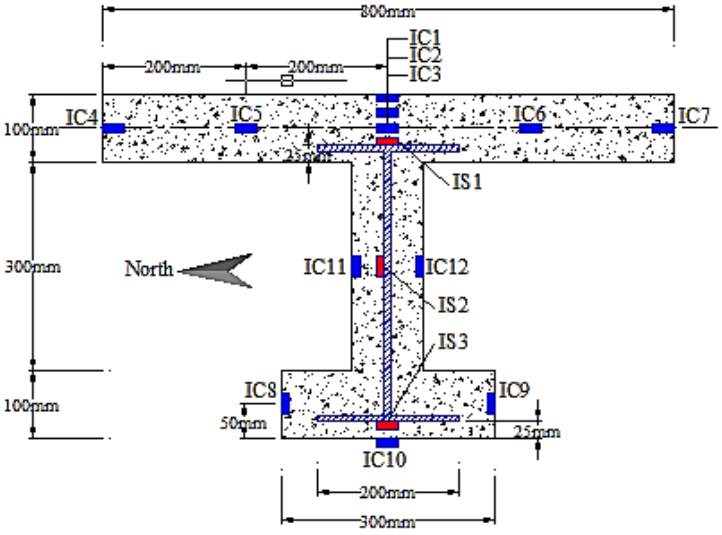

Figure 3.21 The locations of thermocouples installed in I-Beam segment.

3.6 Position of Strain Gages

In this study, for the T-Beam segment two different types of strain gages are used for steel and concrete materials. The position of these strain gages are shown in Figure 3.22(a) and (b).

For the I-Beam specimen, two strain gages of the same type installed in the concrete materials. Figure 3.23(a) and (b) shows the strain gages in the orthogonal position.

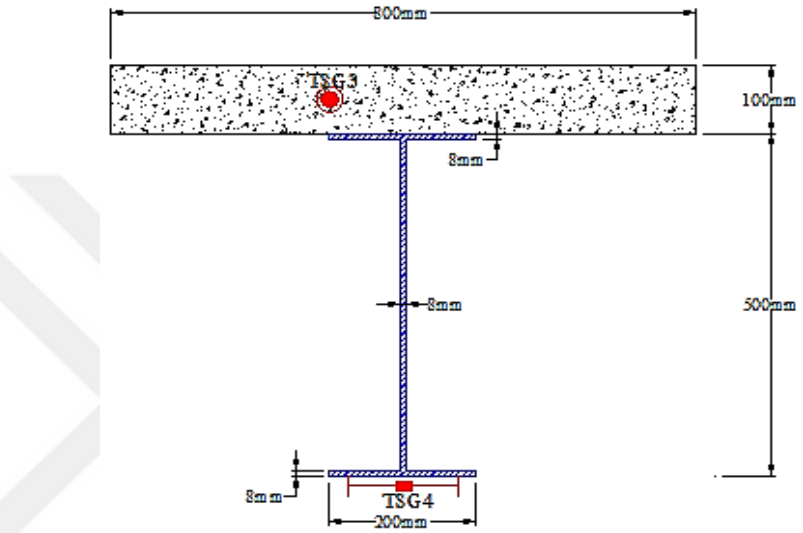

(a)

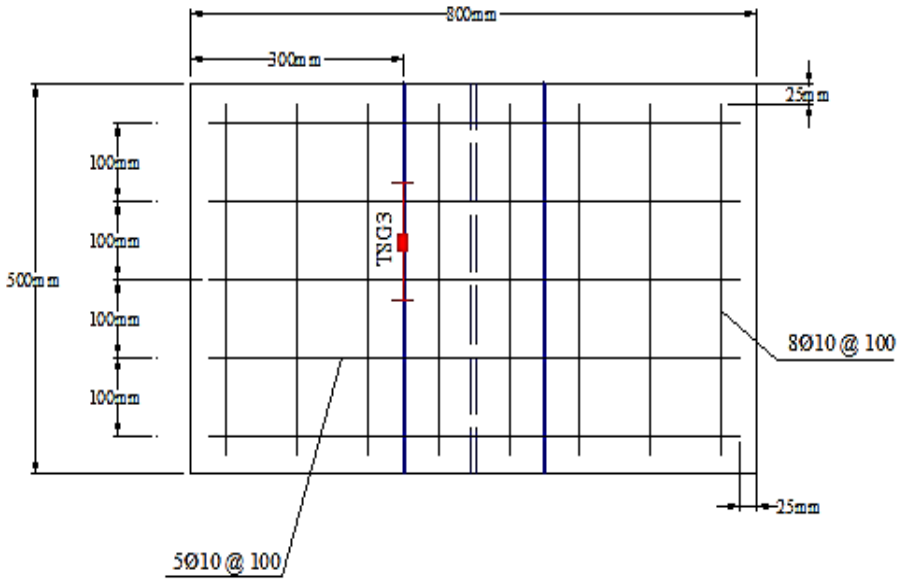

(b)

Figure 3.22 The position of strain gages in T-Beam segment (a) cross section and (b) top view.

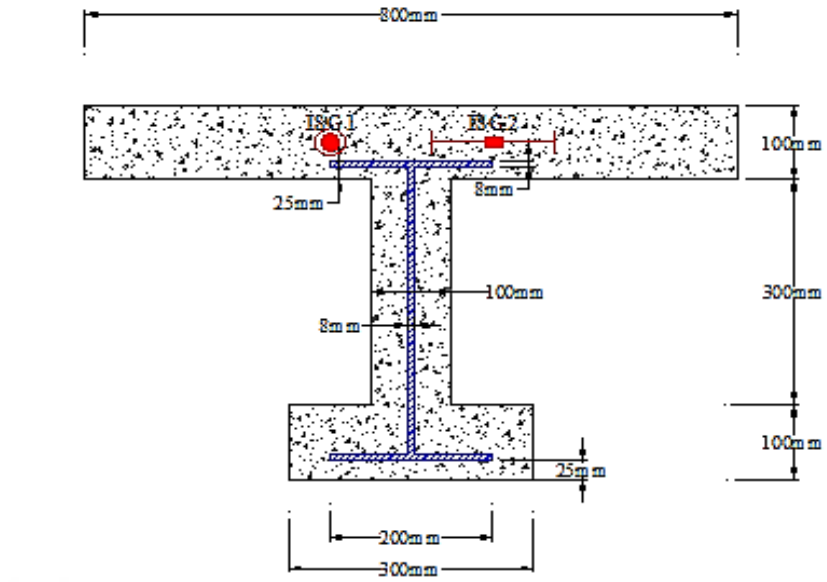

(a)

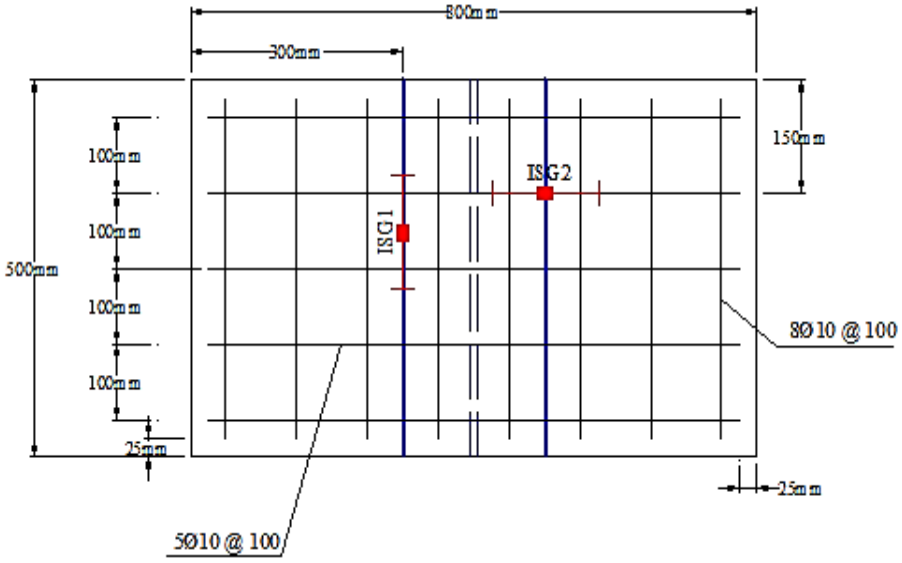

(b)

Figure 3.23 The position of strain gages in I-Beam segment (a) cross section, and (b) top view.

Figures 3.24 and 3.25 show clearly all sensor and measurement devices set up on the site before casting the two segments.

Figure 3.24 Sensor and measurement devices set up in the T-Beam specimen.

Figure 3.25 Sensor and measurement devices set up in I-Beam specimen.

CHAPTER 4

THE EXPERIMENTAL RESULTS

4.1 General

In this chapter, the results of the experimental two segments of composite concrete-steel girders, T-Beam and I-Beam segments will be discussed in details during the test period. The test period extended from 21-December-2015 to 22-February-2016. The results include the environmental records such as the air temperatures, wind speed and solar radiation. The results of the recorded data of thermocouples in the different parts have been addressed for T-Beam and I-Beam segments in the cold season during the annual thermal cycle (December, January and February).

Moreover, in this chapter, the temperature distributions and vertical and lateral temperature gradients along the two segments in different parts will be presented for frozen, cold and sunny days of the same period.

4.2 The Environmental Records

The data collected from the environmental sensors that explained in chapter three will be discussed in this section. The air temperature, solar radiation and wind speed are demonstrated graphically.

Figure 4.1 shows the hourly air temperature variation and the daily air maximum, minimum and difference (max-min) temperatures from 21-December-2015 to 22-February-2016. Where, the maximum recorded air temperature during the selected period was 23.0 ℃ in 18-February-2016 at 3:00 PM, while the minimum recorded air temperature was -9.9 ℃ in 28-January-2016 at 3:00 AM. The maximum daily temperature difference (max-min) was 18.6 ℃ in 25-December-2015 and the minimum daily temperature difference was 1.4 ℃ in 13-January-2016.

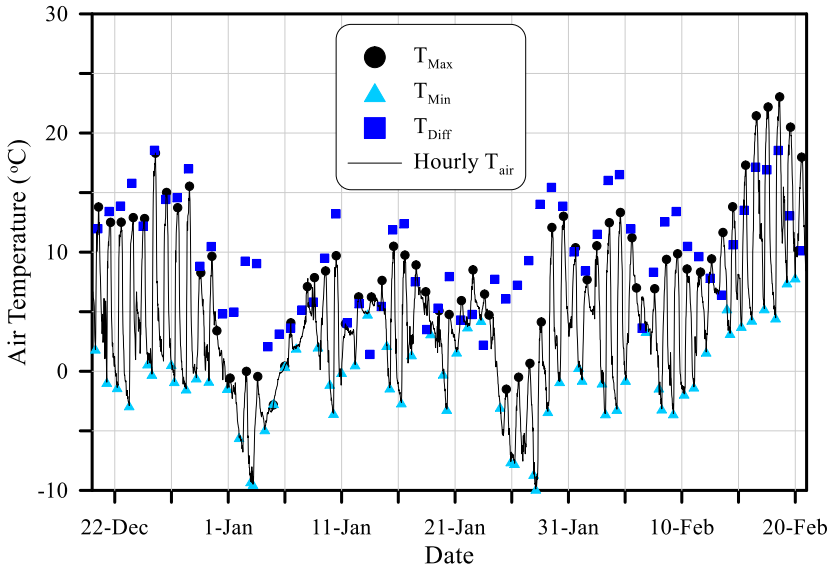

Figure 4.1 Hourly air temperatures and daily maximum, minimum, and difference (max-min) air temperatures from 21-December-2015 to 22-February-2016.

Figure 4.2 illustrates hourly and daily maximum solar radiation intensities from 21-December-2015 to 22-February-2016. The maximum recorded solar radiation intensity during the examined period was 870 W/m^2 in 10-February-2016 at 11:30 AM.

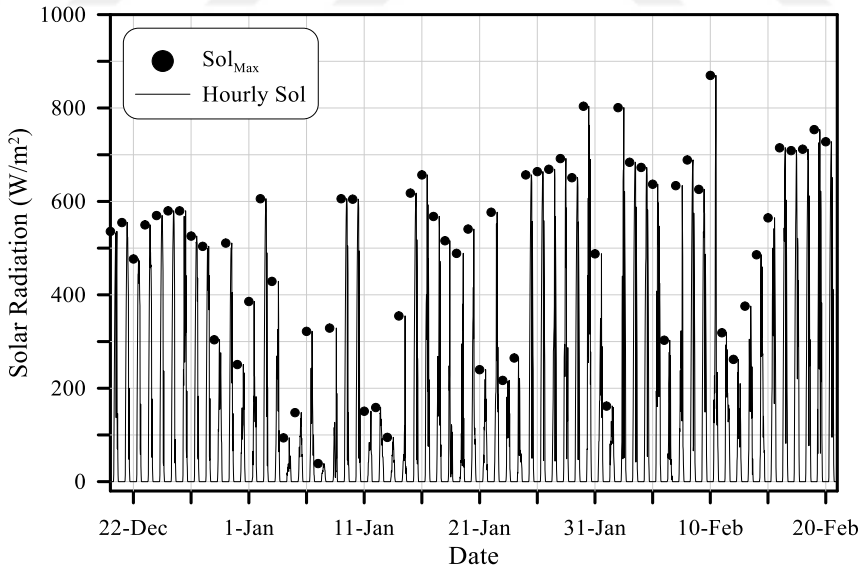

Figure 4.2 Hourly and daily maximum solar radiation intensities from 21-December-2015 to 22-February-2016.

Figure 4.3 shows the hourly wind speed from 21-December-2015 to 22-February-2016. The maximum recorded wind speed in the selected period was 5.049 m/s in 25-January-2016 at 2:00 PM, while the minimum recorded wind speed was 0 m/s,

which is a frequent minimum value, occurred before sunrise and before/after one hour of sunset. The daily average wind speed for the examined period was 0.095 m/s.

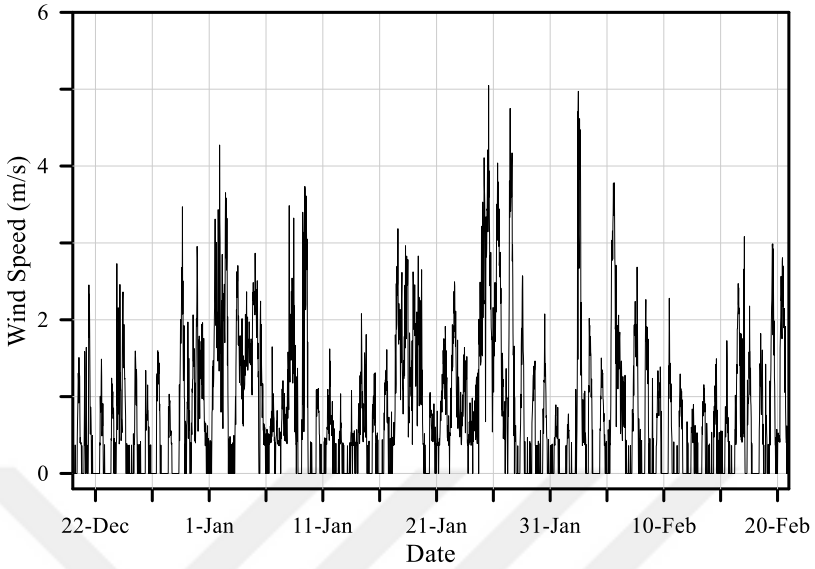

Figure 4.3 Hourly wind speed from 21-December-2015 to 22-February-2016.

4.3 Results of the T-Beam during the Test Period

The fluctuated temperature with time during the cold season will be presented in this section. The hourly maximum, minimum, different (max-min), the average temperature of the 14 thermocouples and the mean temperature are studied. The hourly average temperatures of thermocouples in concrete and steel parts are discussed separately. The hourly and daily maximum and minimum temperature differences at different locations in the segment are studied.

Figure 4.4 shows the hourly maximum temperatures of the 14 thermocouples, where the highest recorded hourly maximum temperature was 36.41 ℃ on 18-February-2016 at 2:00 PM at the location of TC1.

Figure 4.5 illustrates the hourly minimum temperatures of the 14 thermocouples. The lowest recorded hourly minimum temperature was -9.39 ℃ in 28-January-2016 at 4:30 AM at the location of TS6. The variations in the maximum and minimum temperatures reflect the influence of the location of the thermocouple. Where TC1 at the extreme edge of the concrete deck and the TS6 at the edge of the bottom flange of I-steel girder exhibited the maximum and minimum temperatures, which is

directly attributed to their locations from sun movement and hence the received quantity of solar radiation.

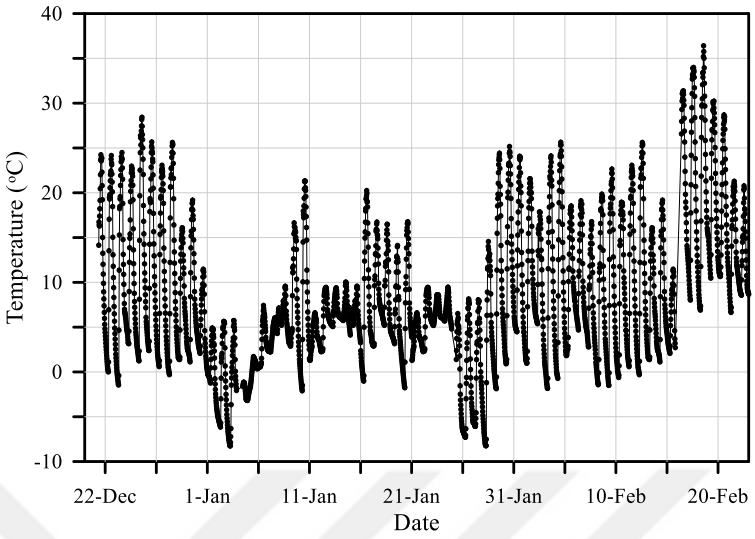

Figure 4.4 Hourly maximum temperatures of 14 thermocouples from 21-December-2015 to 22-February 2016 for the T-Beam segment.

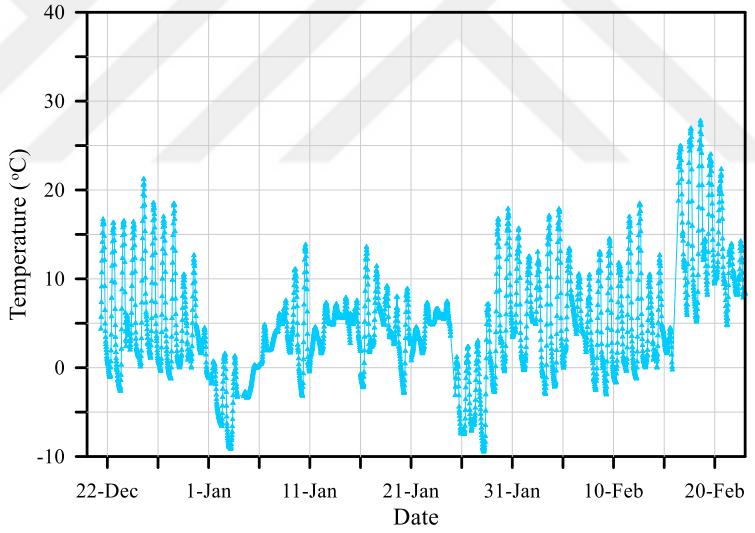

Figure 4.5 Hourly minimum temperatures of 14 thermocouples from 21-December-2015 to 22-February 2016 for the T-Beam segment.

Figure 4.6 shows the hourly temperature difference (maximum-minimum) of the 14 thermocouples, where the maximum difference was 15.13 ℃ in 25-December-2015 at 10:00 AM and the minimum value was 0.02 ℃ in 4-January-2016 at 10:30 PM.

Figure 4.7 shows the hourly average temperatures of the 14 thermocouples from 21-December-2015 to 22-February 2016. The maximum recorded hourly average temperature was 30.3 ℃ in 18-February-2016 at 2:00 PM, while the minimum

recorded hourly average temperature was -8.6 ℃ in 28-January-2016 at 5:00 AM. The average of the hourly average temperature during the examined period was 6.5 ℃.

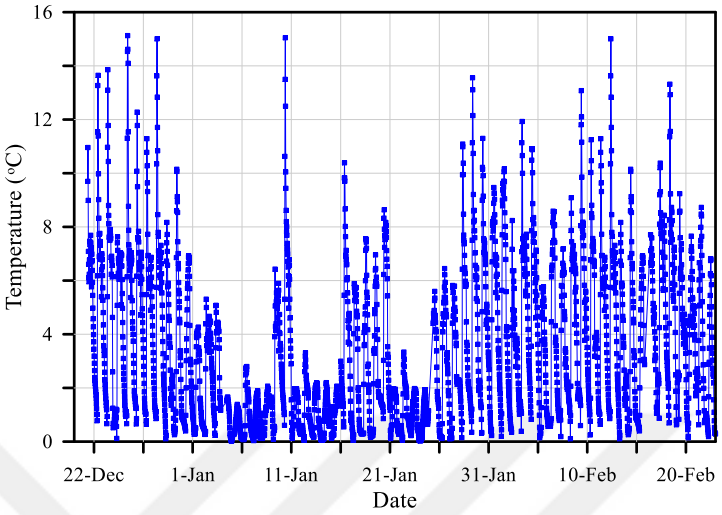

Figure 4.6 Hourly temperature differences (max-min) of 14 thermocouples from 21-December-2015 to 22-February 2016 for the T-Beam segment.

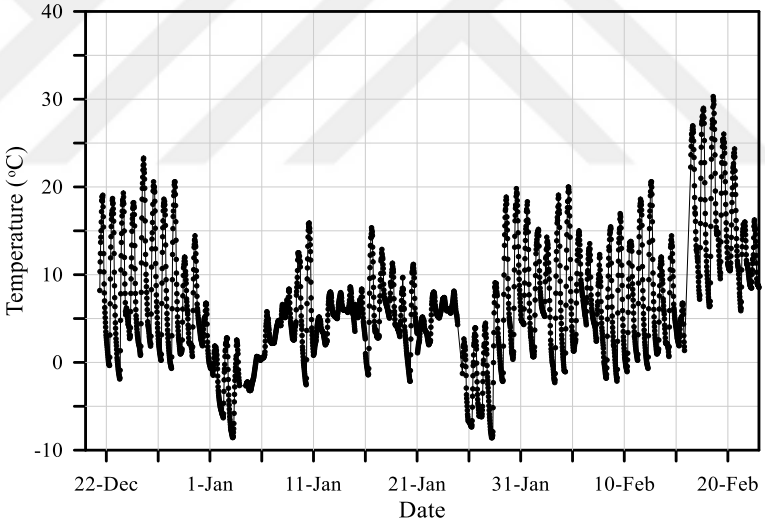

Figure 4.7 Hourly average temperatures of 14 thermocouples from 21-December-2015 to 22-February 2016 for the T-Beam segment.

Figure 4.8 presents the hourly average temperatures of the seven thermocouples fixed in concrete during the studied period. The maximum value for the average temperature was 31.0 ℃ in 18-February-2016 at 2:30 PM, while the minimum recorded value of the average temperature was -8.4 ℃ in 3-January-2016 at 5.30 AM. The average value of the hourly average temperature of the seven concrete thermocouples during the examined period was 6.6 ℃. The fluctuation of the

average temperature of the seven concrete thermocouples is almost identical with that of the average temperature of the 14 thermocouples.

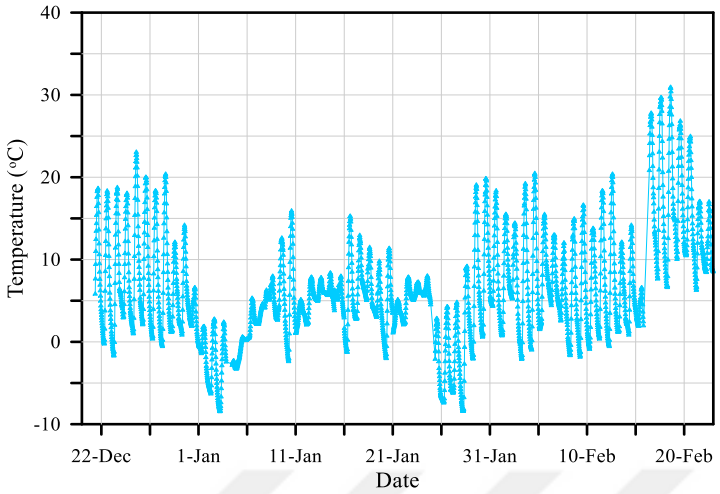

Figure 4.8 Hourly average temperatures of the seven concrete thermocouples from 21-December-2015 to 22-February 2016 for the T-Beam segment.

Figure 4.9 shows the hourly average temperature of the seven thermocouples fixed on the steel section of the segment from 21-December-2015 to 22-February 2016. The hourly average temperatures of the thermocouple were limited between 30.0 ℃ in 18-February-2016 at 2:00 PM to -9.0 ℃ in 28-January-2016 at 4:30 AM. The Average value for the hourly average temperature of the steel thermocouples during the examined period was 6.4 ℃.

Figure 4.10 illustrates the hourly mean temperatures of thermocouples during the studied period. The mean temperature is the area based average temperature of the beam, which is calculated as the sum of the temperatures of each thermocouple multiplied by its surrounding area divided by the total area of the beam section, which is calculated by:

$$Mean(T) = \frac{\sum T_i \times A_i}{\sum A_i} \quad (4.1)$$

Where T_i is the thermocouple temperature, i is the number of the thermocouple, and A_i is the individual area that surrounds the thermocouple.

The maximum value of the mean temperature was 30.9 ℃ in 18-Faburay-2016 at 2:30 PM. The minimum recorded value was -8.4 ℃ in 3-January-2016 at 5:30 AM.

In the design of thermal movements, the maximum and the minimum mean temperatures are used.

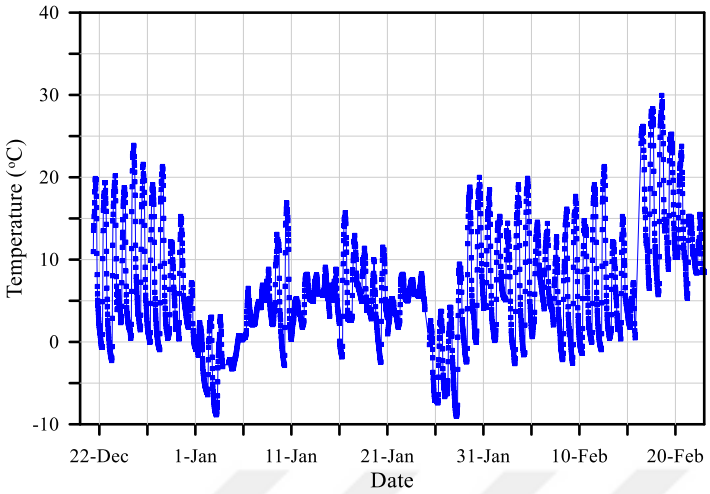

Figure 4.9 Hourly average temperatures of the seven steel thermocouples from 21-December-2015 to 22-February 2016 for the T-Beam segment.

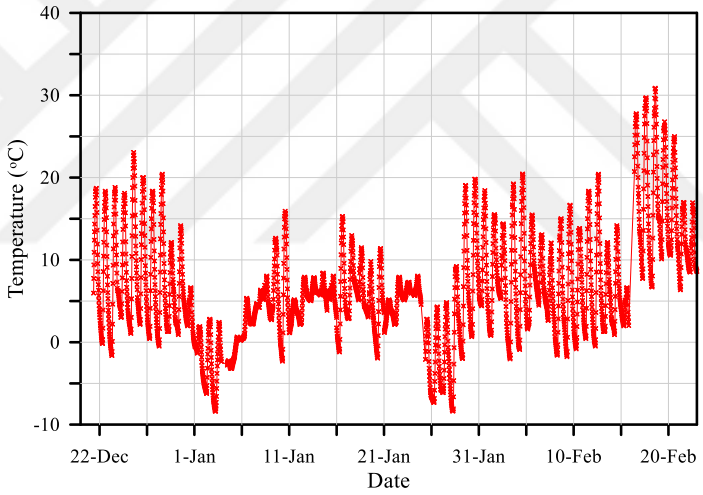

Figure 4.10 Hourly mean temperatures of thermocouples from 21-December-2015 to 22-February 2016 for the T-Beam segment.

The thermocouples were installed at different places distributed as vertical and horizontal grids in/on the concrete slab and the steel girder to evaluate the temperature variations along the vertical and lateral sections. Figures 4.11 to 4.19 study the hourly variation and the daily maximum and minimum temperature differences at different locations of the segment from 21-December-2015 to 22-February 2016.

Figures 4.11 to 4.16 show the temperature differences between the thermocouples along the vertical centerline of the girder. The visualization of these temperature

differences gives better understanding for the aforementioned distribution of the vertical temperature gradient. The maximum temperature along the vertical centerline occurs at the top surface thermocouple (TC3) during the hot hours of the day, which composes the positive temperature gradients. On the other hand, after several cooling hours, the temperature of this thermocouple becomes the lowest (in the concrete slab) along the vertical center line, which leads to the distributions of the negative vertical temperature gradients. Therefore, TC3 is compared in this section with the concrete-slab mid-thickness thermocouple (TC4), the thermocouple installed at the bottom face of the concrete slab (TC5), the central thermocouple of the steel section (TS4), and the thermocouple TS7, which is installed at the lower face of the bottom flange of the steel section. In addition, the temperature of TC3 is compared at each time step with the maximum and minimum temperatures of the thermocouples installed along the vertical centerline of the girder, hence the maximum and minimum temperatures of thermocouples TC3, TC4, TC5, TS1, TS3, TS4, TS5 and TS7.

Figure 4.11 shows the hourly variation and the daily maximum and minimum temperature differences between TC3 and the TC4 during the studied period. This temperature difference shows the temperature variation along the top half of the concrete slab. The hourly and daily maximum temperature differences ranged from 0.3 to 3.1 ℃, while the hourly and daily minimum temperature difference ranged from -1.5 to -0.03 ℃.

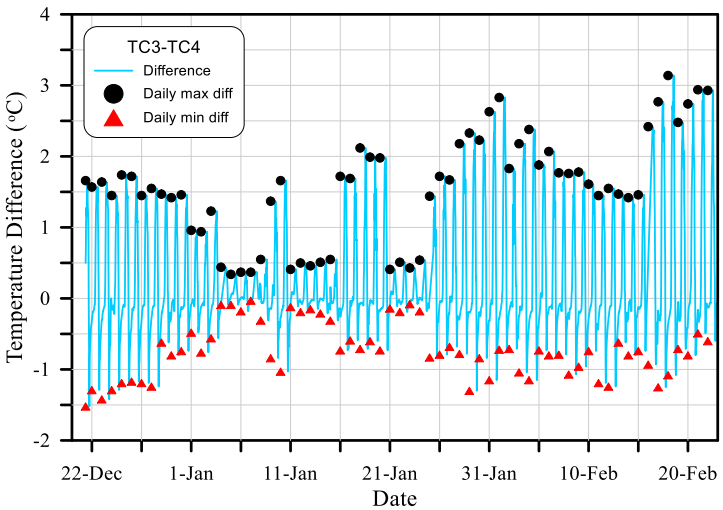

Figure 4.11 Hourly variation and daily maximum and minimum temperature differences (TC3-TC4) from 21-December-2015 to 22-February-2016 for the T-Beam segment.

Figure 4.12 shows the hourly variation and the daily maximum and minimum temperature differences between the thermocouples TC3 and the TC5 from 21-December-2015 to 22-February-2016. This difference shows the variation of temperature between the top and bottom surfaces of the concrete slab. The maximum difference value ranged from 0.4 to 5.5 ℃, and the minimum difference value was in the range of 0.3 to -2.4 ℃.

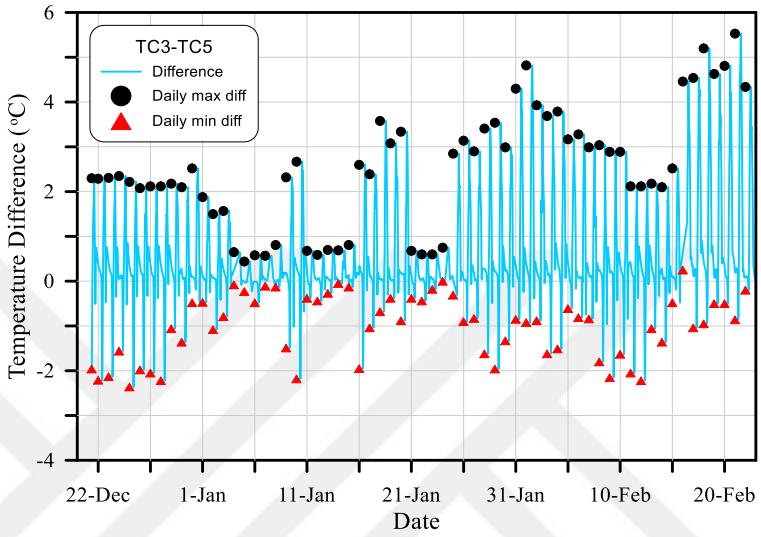

Figure 4.12 Hourly variation and daily maximum and minimum temperature differences (TC3-TC5) from 21-December-2015 to 22-February 2016 for the T-Beam segment.

Figure 4.13 illustrates the hourly variation and the daily maximum and minimum temperature differences between the TC3 and the central steel thermocouple TS4 during the examined period. The maximum recorded difference was from -0.01 to 7.0 ℃, while the minimum temperature difference ranged from -12.8 to -0.3 ℃.

Figure 4.14 shows the hourly variation and the daily maximum and minimum temperature differences between TC3 and TS7 during the studied period. This temperature difference shows the gradient between the top and bottom surfaces of the composite girder. The maximum recorded temperature differences were from 0.0 to 7.1 ℃, while the minimum temperature differences were from -0.3 to -12.1 ℃.

Figure 4.15 illustrates hourly variation and the daily maximum and minimum differences between TC3 and the minimum temperature of the girder during the examined period. The maximum difference temperature was from 0.4 to 7.1 ℃, while the minimum temperature difference ranged from 0.0 to 0.5 ℃. The

comparison between the results of the temperature difference of (TC3-Min) with the differences with other thermocouples (TC4, TC5, TS4 and TS7) show that higher temperature differences were recorded between the TC3 and the minimum temperature.

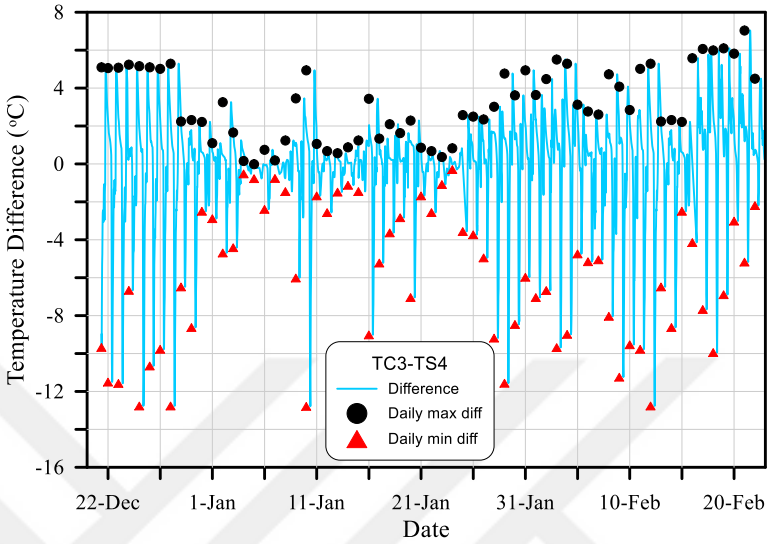

Figure 4.13 Hourly variation and daily maximum and minimum temperature differences (TC3-TS4) from 21-December-2015 to 22-February 2016 of the T-Beam segment.

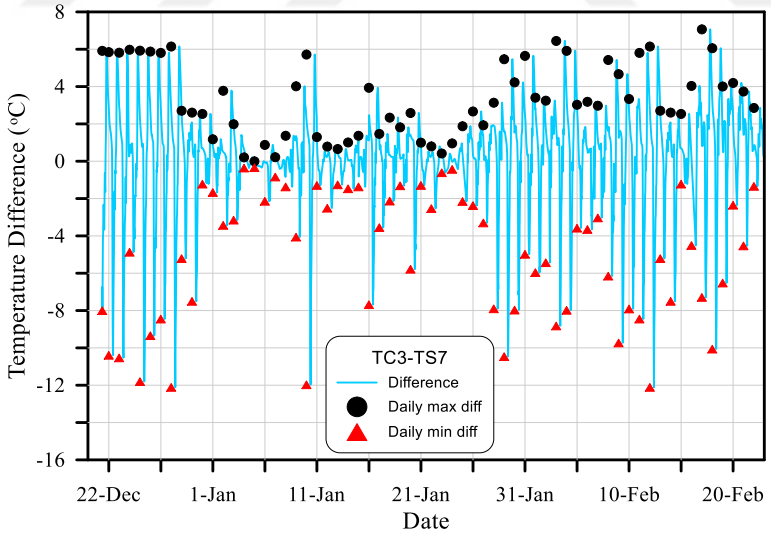

Figure 4.14 Hourly variation and the daily maximum and minimum temperature difference (TC3-TS7) from 21-December-2015 to 22-February 2016 of the T-Beam segment.

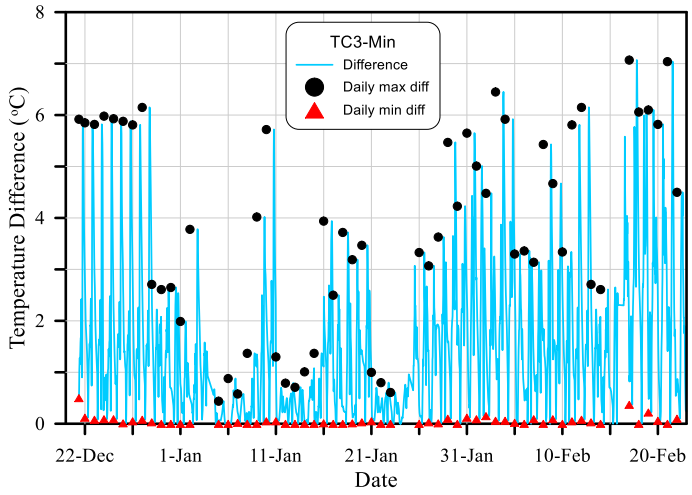

Figure 4.15 Hourly variation and the daily maximum and minimum temperature differences (TC3-Min) from 21-December-2015 to 22-February 2016 for the T-Beam segment.

Figure 4.16 visualizes the hourly variation and daily maximum and minimum temperature differences between TC3 and the maximum temperature (TC3-Max) during the studied period. The maximum recorded values of this difference were from -0.3 to 0.0 ℃ and the minimum values ranged from -12.8 to -0.8 ℃.

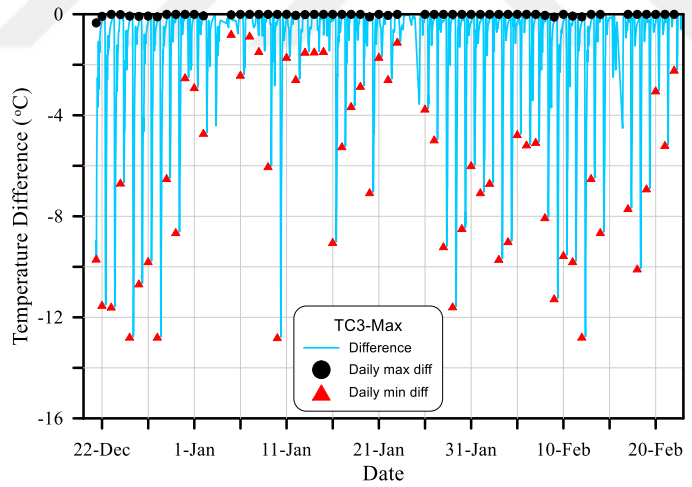

Figure 4.16 Hourly variation and daily maximum and minimum temperature differences (TC3-Max) from 21-December-2015 to 22-February 2016 for the T-Beam segment.

After reviewing the difference temperatures between the thermocouples along the vertical centerline of the composite girder that composes the vertical temperature gradient distributions, the differences between the temperatures of the thermocouples along the horizontal direction are shown in Figures 4.17 to 4.19. The lateral

temperature gradients occurs along the width of the top concrete slab, therefore thermocouples were installed along the horizontal centerline of the concrete slab to evaluate this gradient. These are TC1, TC2, TC4, TC6 and TC7 from north to south.

Figure 4.17 shows the hourly variation and the daily maximum and minimum temperature differences of the thermocouple southern edge thermocouple TC7 and the slab's central thermocouple TC4 from 21-December-2015 to 22-February 2016. This temperature difference shows the lateral temperature gradient at the southern edge of the top concrete slab. The maximum value of the difference of (TC7-TC4) ranged from 1.3 to 9.3 ℃, while the minimum value ranged from 0.06 to -2.5 ℃.

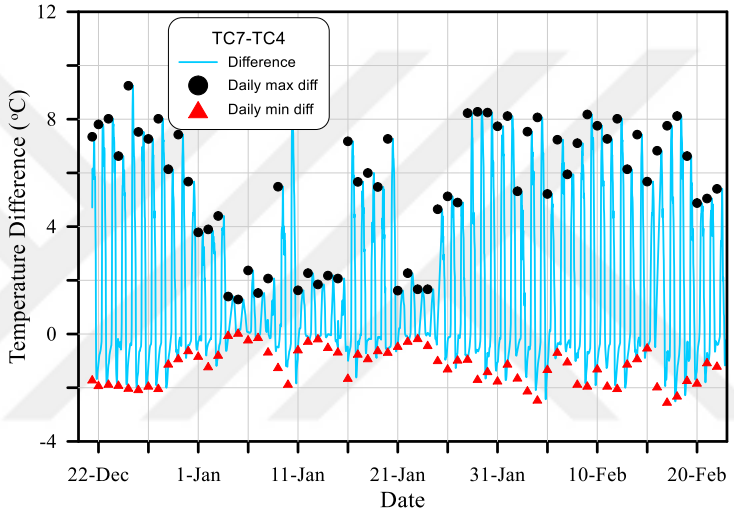

Figure 4.17 Hourly variation and daily maximum and minimum temperature differences (TC7-TC4) from 21-December-2015 to 22-February 2016 for the T-Beam segment.

Figure 4.18 shows the hourly variation and daily maximum and minimum temperature differences between TC7 and TC1 from 21-December-2015 to 22-February 2016. TC1 is the northern edge thermocouple. Thus the temperature difference (TC7-TC1) shows the lateral temperature gradient between the southern edge and the northern edge of the concrete slab. The maximum value of the difference of (TC1-TC7) ranged from 1.4 to 9.2 ℃, while the minimum value of the difference was between -0.01 and 0.4 ℃. When comparing the results of the temperature differences (TC7-TC4) and (TC7-TC1), the maximum difference values were in the range of 0.02 to 0.06 ℃ (very close), yet the minimum difference values ranged from -2.5 to 0.31 ℃.

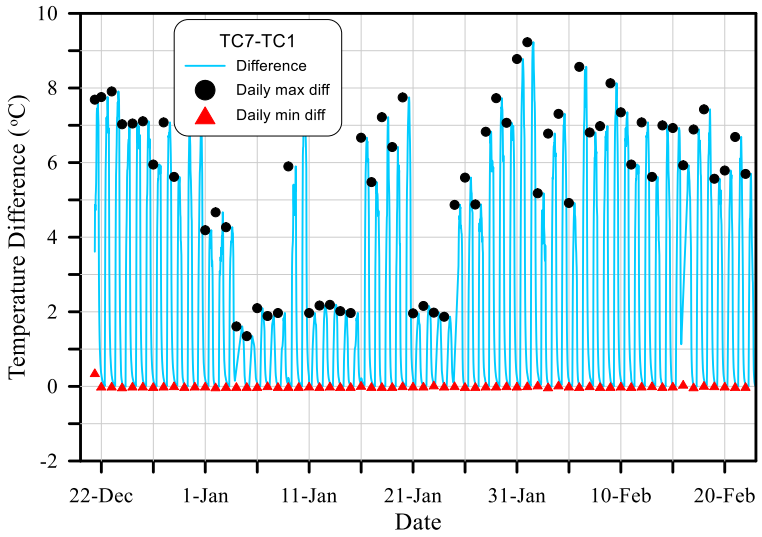

Figure 4.18 Hourly variations and daily maximum and minimum temperature differences (TC7-TC1) from 21-December-2015 to 22-February 2016 for the T-Beam segment.

Figure 4.19 shows the hourly variation and the daily maximum and the minimum temperature differences between the northern edge thermocouple TC1 and the central thermocouple TC4 from 21-December-2015 to 22-February 2016. The maximum difference (TC1-TC4) ranged between 2.6 and -0.3 ℃, while minimum difference ranged from -0.34 to -4.8 ℃. The comparison between the results of the difference of (TC1-TC4) with the results of the difference of (TC7-TC4) shows that the values of the maximum and minimum differences of (TC7-TC4) were higher.

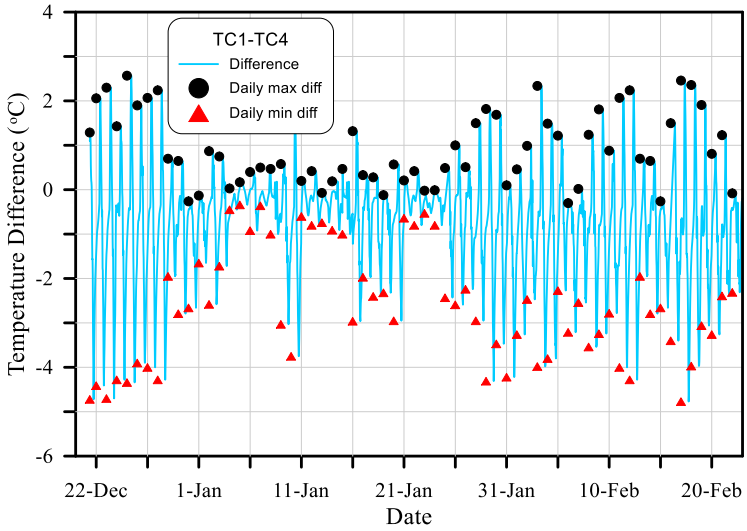

Figure 4.19 Hourly variation and the daily maximum and minimum temperature difference (TC1-TC4) from 21-December-2015 to 22-February 2016 for the T-Beam segment.

This is an expected result, as it is expected that the temperature of the southern edges of the girder are higher than that of the northern edge. This is due to the sun movement in winter and hence the quantity of the received solar radiation by both edges. In winter, the sun rises from south-east moves to the south of the equator and sets at the south-west. This means that along the full day hours, the southern edges are exposed to solar radiation, while northern edges are mostly shaded. Thus, the temperature at the southern edge thermocouple is generally higher that all other points along the slab

4.4 Results of the I-Beam during the Test Period

The results of the I-Beam segment are discussed briefly in this section. Fifteen thermocouples were installed in the girder segment, 12 thermocouples were distributed in the concrete section and three thermocouples were installed on the steel beam.

Figures 4.20 to 4.22 show the hourly maximum, minimum and difference (max-min) temperatures of thermocouples from 21-December-2015 to 22-February 2016. The highest maximum hourly temperature value was 36.5 ℃ at thermocouple IC4 in 18-February-2016 at 2:00 PM and the lowest value was -7.3 ℃ in 3-January-2016 at 6:00 AM at thermocouple IS2.

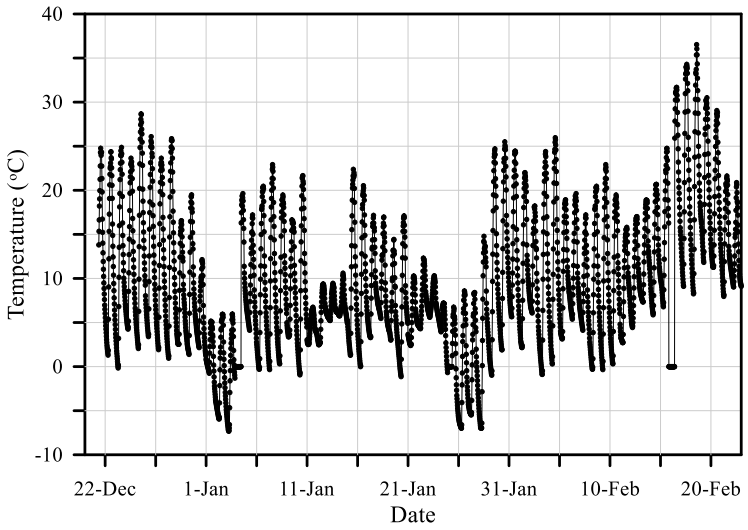

Figure 4.20 Hourly maximum temperatures of thermocouples from 21-December-2015 to 22-February 2016 for the I-Beam.

The highest value of the hourly minimum temperature of the 15 thermocouples was 24.3 ℃ in 21-December-2015 at 1:00 PM at IC4 and the lowest value was -8.4 ℃ in 28-January-2016 at 4:30 AM at IC7. For the hourly difference (max-min) temperature of thermocouples, the highest value was 13.3 ℃ in 1-January-2016 at 1:30 PM and the lowest value was 0.0 ℃ on many days.

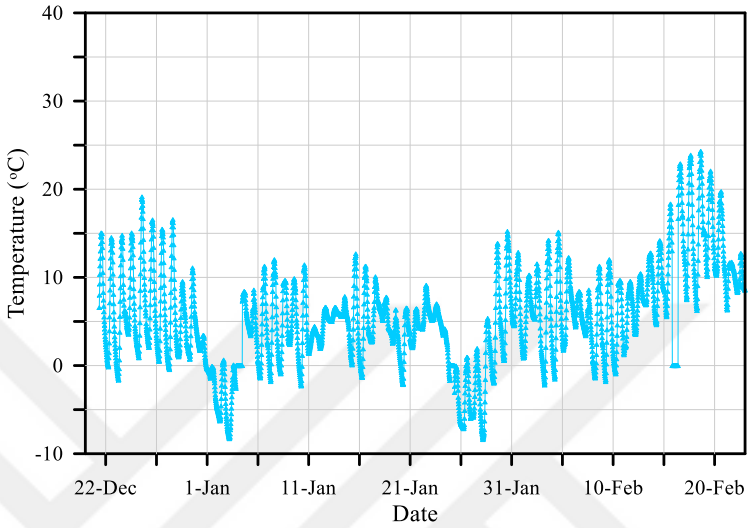

Figure 4.21 Hourly minimum temperature of thermocouples from 21-December-2015 to 22-February 2016 for the I-Beam.

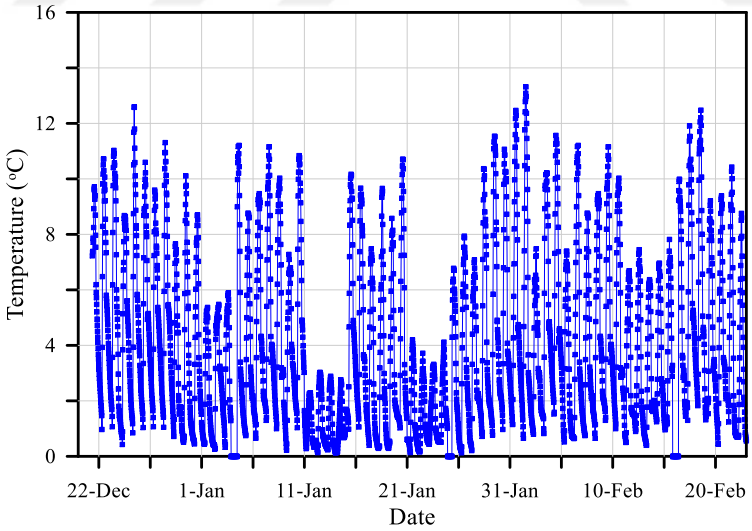

Figure 4.22 Hourly difference (max-min) temperature of thermocouples from 21-December-2015 to 22-February 2016 for the I-Beam segment.

Figures 4.23 to 4.25 illustrate the hourly average temperature for all of the 15 thermocouples, the 12 concrete thermocouples, and the 3 steel thermocouples, respectively, from 21-December-2015 to 22-February 2016. The maximum hourly average temperature value for the 15 thermocouples was 28.4 ℃, while the minimum

value was -7.6 ℃. For the 12 concrete thermocouples, the maximum recorded average temperature was 29.0 ℃ and the minimum was -7.6 ℃. The maximum average temperature of the 3 steel thermocouples was 26.7 ℃, while the minimum value was -7.4 ℃. The maximum and minimum values took place in 18-February-2016 and 3-January-2016 respectively.

Figure 4.26 shows the hourly mean temperature of the 15 thermocouples from 21-December-2015 to 22-February-2016. The maximum and minimum values of mean temperature were 28.7 and -7.6 ℃, respectively.

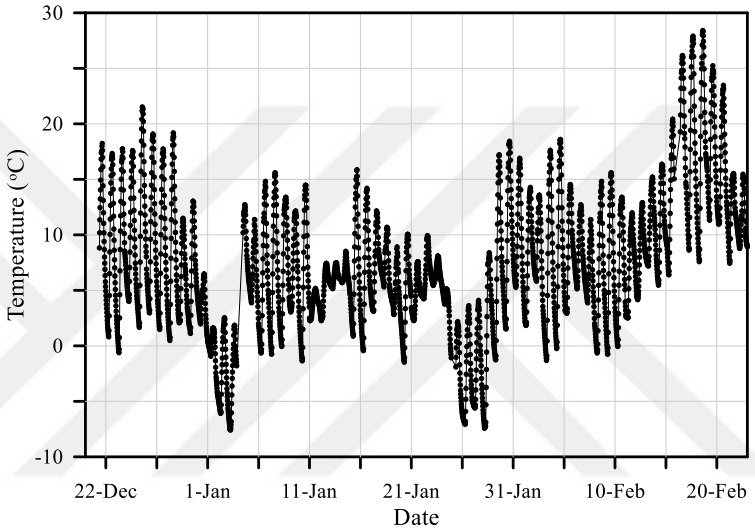

Figure 4.23 Hourly average temperature of the 15 thermocouples from 21-December-2015 to 22-February 2016 for the I-Beam segment.

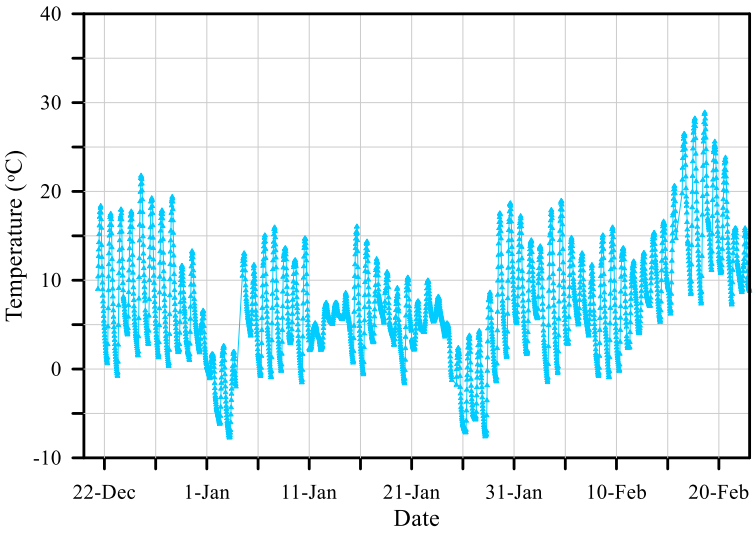

Figure 4.24 Hourly average temperature of the 12 concrete thermocouples from 21-December-2015 to 22-February 2016 for the I-Beam segment.

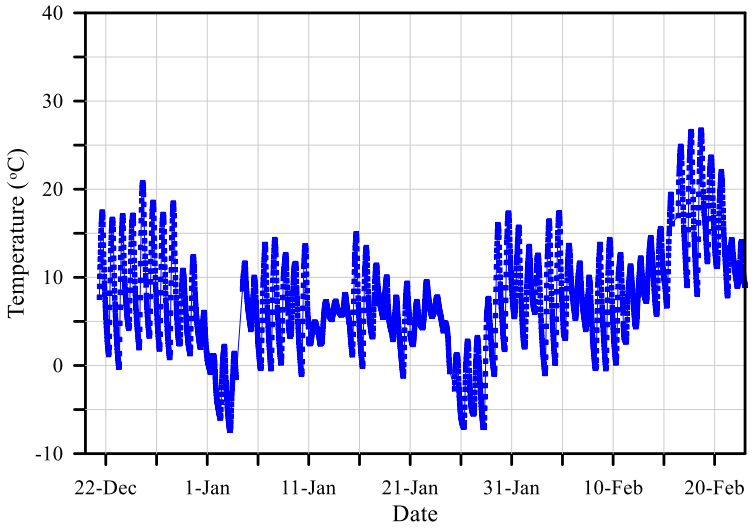

Figure 4.25 Hourly average temperature of the 3 steel thermocouples from 21-December-2015 to 22-February 2016 for the I-Beam segment.

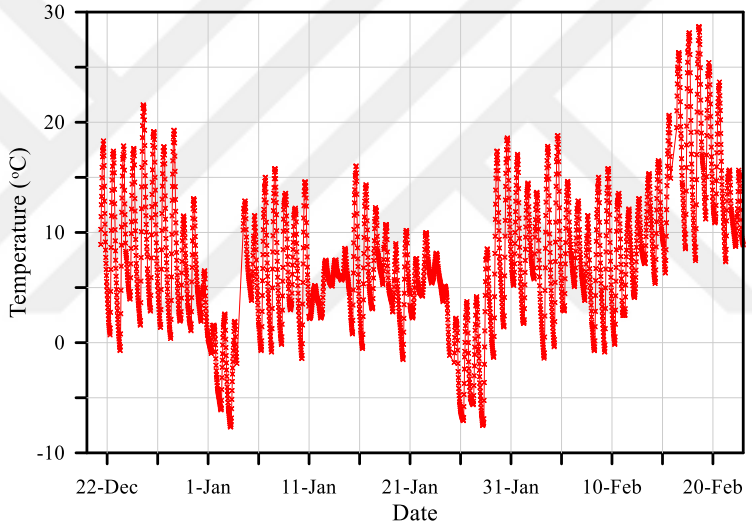

Figure 4.26 Hourly mean temperature of thermocouples from 21-December-2015 to 22-February 2016 for the I-Beam segment.

The difference in temperature between the thermocouples installed along the vertical centerline of the composite girder was calculated to study the vertical temperature gradient. Figures 4.27 to 4.29 show the hourly variation and daily maximum and minimum temperature differences between the thermocouple IC1 and the thermocouples IC2, IC3 and IC10 during the study period. The maximum temperature difference value of (IC1-IC2), (IC1-IC3) and (IC1-IC10) were 3.11, 5.7 and 6.66 ℃. The corresponding minimum values were -1.4, -2.2 and -1.25 ℃, respectively. The thermocouple IC1 was considered as it is the top surface's thermocouple, hence, to which the gradients along the vertical axis of the girder are

calculated. IC2 is the thermocouple installed in the top concrete flange, 25 mm below the top surface (25 mm below IC1); while IC3 is the thermocouple installed at the center of the top concrete flange (50 mm blow the top surface). On the other hand, IC10 is the girder's bottom surface's thermocouple (installed on the bottom surface of the bottom concrete flange). Therefore, the differences of IC1 with IC2 and IC3 show the temperature gradient within the top concrete flange, while its difference with IC10 show the general linear gradient between the top and bottom surfaces of the girder.

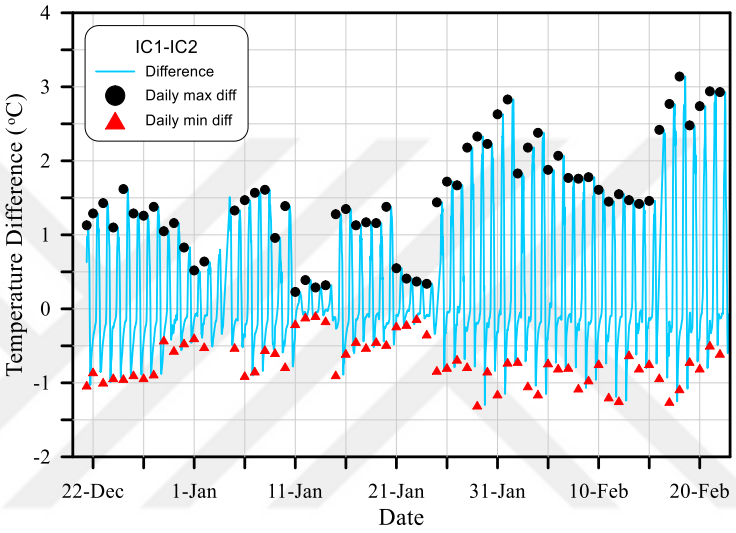

Figure 4.27 Hourly variation and daily maximum and minimum temperature differences of (IC1-IC2) from 21-December-2015 to 22-February 2016 for the I-Beam segment.

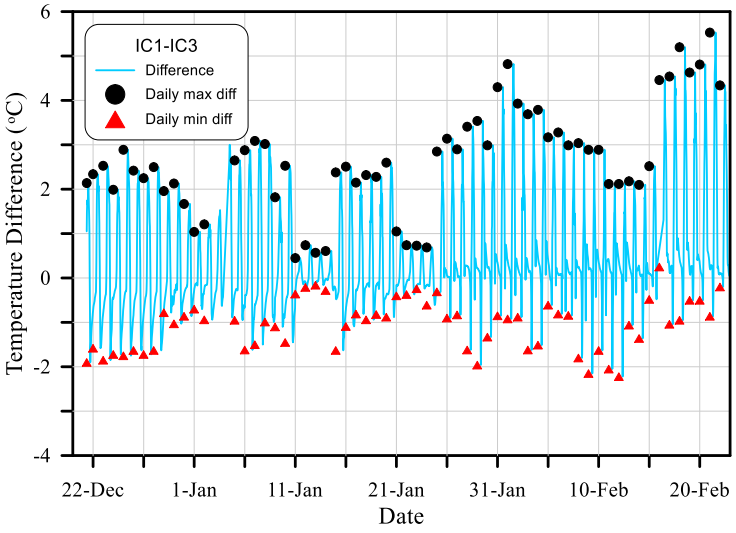

Figure 4.28 Hourly variation and daily maximum and minimum temperature differences of (IC1-IC3) from 21-December-2015 to 22-February 2016 for the I-Beam segment.

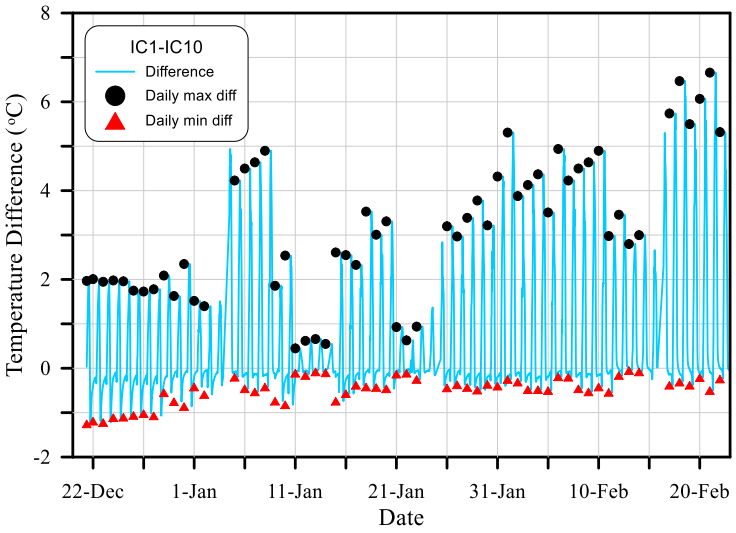

Figure 4.29 Hourly variation and daily maximum and minimum temperature differences (IC1-IC10) from 21-December-2015 to 22-February 2016 for the I-Beam.

Figure 4.30 illustrates hourly variation and the daily maximum and the minimum temperature differences of IC1 and IS2 thermocouples from 21-December-2015 to 22-February 2016. IS2 is the thermocouple installed on the central web of steel girder inside the concrete. The maximum value of the daily maximum temperature difference was 7.6 ℃, while the minimum value of the daily minimum temperature difference was -3.6 ℃.

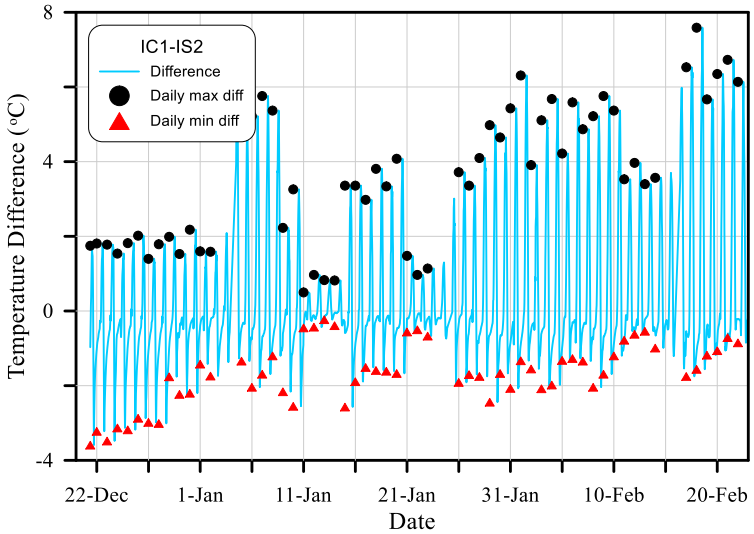

Figure 4.30 Hourly variation and daily maximum and minimum temperature differences of (IC1-IS2) from 21-December-2015 to 22-February 2016 for the I-Beam segment.

The hourly maximum and minimum temperatures of all thermocouples along the vertical centerline of the composite girder were calculated to better understand the temperature gradient along this line. These thermocouples are the concrete thermocouples IC1, IC2, IC3 and IC10 in addition to the three steel thermocouples IS1, IS2 and IS3. Figure 4.31 shows the hourly variation and the daily maximum and the minimum temperature difference between IC1 and the minimum temperature from 21-December-2015 to 22-February 2016. The values ranged from 7.6 to 0.0 ℃.

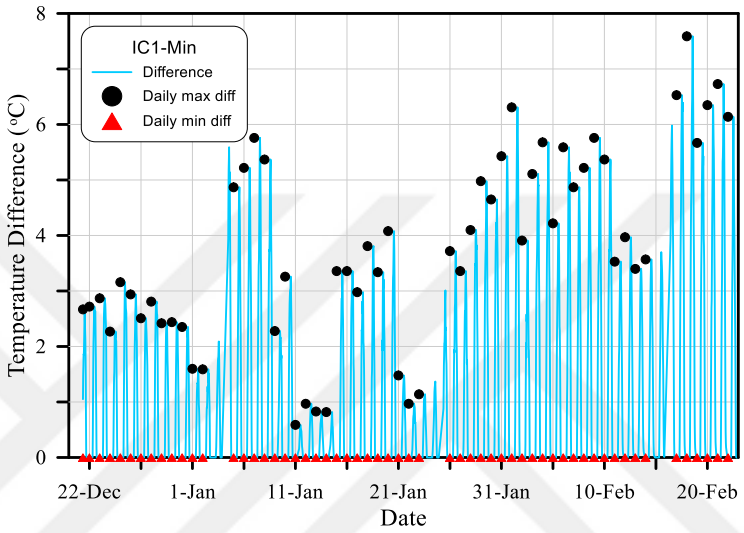

Figure 4.31 Hourly variation and daily maximum and minimum temperature differences of (IC1-Min) from 21-December-2015 to 22-February 2016 for the I-Beam segment.

While Figure 4.32 shows the difference between the IC1 and the maximum temperature for the same period. The maximum and minimum values were 0.0 and -3.6 ℃ respectively. These values reveal that the top surface thermocouple IC1 records the highest temperature in some times (midday) and the minimum in others (after midnight), while in other times, the maximum and minimum temperatures are recorded by other thermocouples.

The lateral temperature gradient is evaluated along the centerline of the top flange of the composite girder, hence along the concrete section only. The lateral gradient is evaluated by taking temperature differences of the edge thermocouples (IC4 and IC7) and the central thermocouple IC3. Note that the thermocouples installed along the horizontal centerline of the top flange from North to South are IC4, IC5, IC3, IC6 and IC7 with a fixed spacing of 200 mm. Thus, the southern edge thermocouple is IC7, while the northern edge thermocouple is IC4.

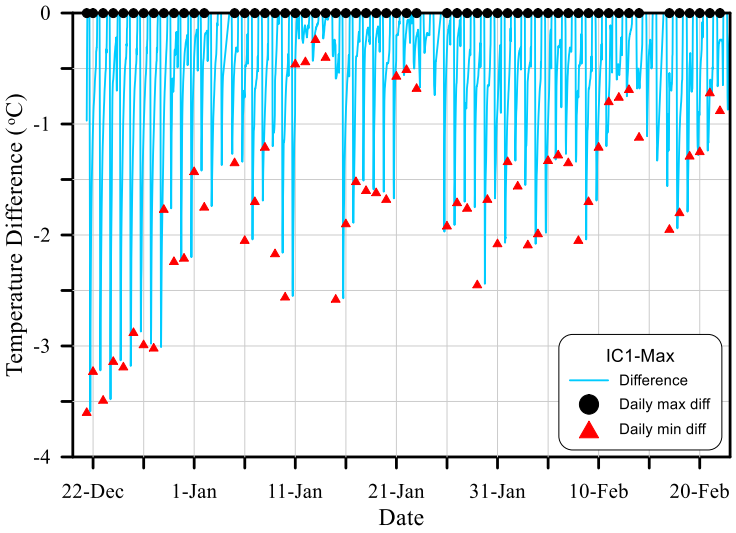

Figure 4.32 Hourly variation and daily maximum and minimum temperature differences of (IC1-Max) from 21-December-2015 to 22-February 2016 for the I-Beam segment.

As discussed in the lateral gradient of the T-beam, during the cold season, the sun moves from sunrise to sunset along the day to the south of the equator. Thus, the solar radiation received by the southern surfaces is much higher than those received by the northern ones. Therefore, it is clear in Figures 4.33, 4.34 and 4.35 that the maximum lateral temperature gradients all occur at the southern edge, where the maximum temperatures were recorded at thermocouple IC7. Figure 4.33 shows temperature differences between the southern edge thermocouple IC7 and the central thermocouple IC3. The maximum value of the difference was 12.41 ℃ and the minimum value was -4.11 ℃.

On the other hand, Figure 4.34 illustrates the temperature difference between the southern edge thermocouple IC7 and the northern edge thermocouple IC4 during the tested period. The maximum recorded value for this difference was 10.1 ℃ and the minimum recorded value was -0.04 ℃. These values reveal that along the full day fours, the highest temperatures were recorded at the southern edge, hence the daily lateral gradient jump occurs there compared to other thermocouples. Comparing the difference values from Figures 4.33 and 4.34, it is clear that the maximum lateral gradients occur between the southern edge and the center of the slab.

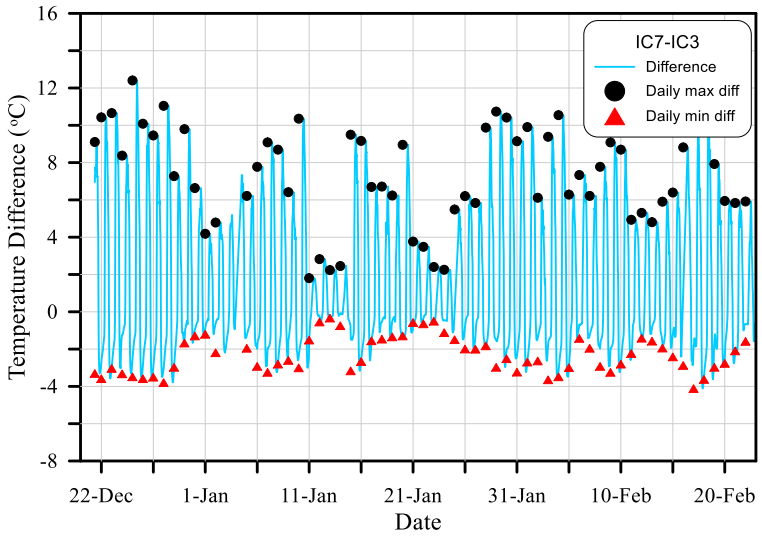

Figure 4.33 Hourly variation and the daily maximum and minimum temperature differences of (IC7-IC3) from 21-December-2015 to 22-February 2016 for the I-Beam segment.

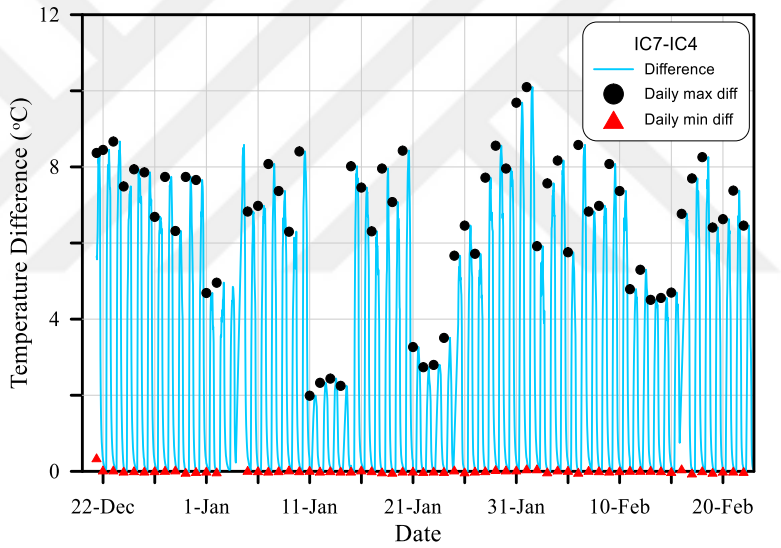

Figure 4.34 Hourly variation and the daily maximum and minimum temperature differences of (IC7-IC4) from 21-December-2015 to 22-February 2016 for the I-Beam segment.

Figure 4.35 shows the difference of temperature between IC4 and IC3 thermocouples during the study period. The maximum difference result was 4.5 ℃ and the minimum result was -5.08 ℃. This again reveals that the gradient at the northern edge (compared to the center of the flange) is much lower than the temperature gradient at the southern edge.

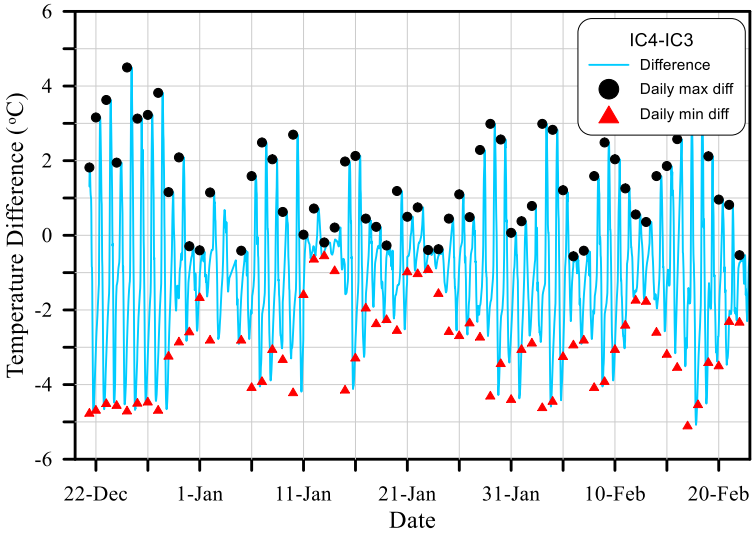

Figure 4.35 Hourly variation and the daily maximum and minimum temperature differences of (IC4-IC3) from 21-December-2015 to 22-February 2016 for the I-Beam segment.

4.5 Frozen, Cold and Sunny Days

From the two winter months period, days were selected and categorized into three distinguished categories. These are the Frozen, Cold and Sunny days.

The first category, Frozen day, refers to the day within which the temperature of the air was lower than zero during the full 24 hours. From the data of the tested period, seven days were recorded as frozen days. The frozen days are 1 to 4-January-2016 and 25 to 27-January-2016.

Cold day refers to any day having a daily minimum air temperature less than zero. However, to optimize this term for most severe conditions, only those days having daily air temperature difference not be less than 15 ℃ ($Tair_{max}$–$Tair_{min}$≥15 ℃) were considered as cold days. According to the above mentioned two conditions, six days can be considered as cold days. These six days are 23, 25 and 28-December-2015, 29-January-2016, in addition to 3 and 4-February-2016.

Three conditions must be satisfied for a day to be termed as a Sunny day. The first term is that temperature of air must be higher than zero along the 24 hours, while the second term is that the daily air temperature difference should not be less than 15 ℃ ($Tair_{max}$–$Tair_{min}$≥15 ℃). The third condition of sunny days is that the daily maximum of hourly solar radiation should be greater than 700 W/m^2. During the two months of

the test, only three days can be distinguished as Sunny days, these are 16 to 18-February-2016.

For better and optimized presentation of the recorded environmental, temperature and strain readings, only one day from each category was chosen for data presentation and comparison purposes. These three days and their recorded environmental data are shown in Table 4.1.

Table 4.1 Environmental data of the chosen Frozen, Cold and Sunny days.

Condition	**Frozen Day**	**Cold Day**	**Sunny Day**
Date	**2-Jan-2016**	**4-Feb-2016**	**18-Feb-2016**
Max. Air. Temperature (^{o}C)	0	13.3	23
Min. Air. Temperature (^{o}C)	-9.25	-3.2	4.5
Air Temperature Difference (^{o}C)	9.25	16.5	18.5
Max. Hourly Solar Radiation (W/m^{2})	606	673	712
Average Wind Speed (m/sec)	1.46	0.43	0.44

4.5.1 Environmental records of the Frozen, Cold and Sunny days

The hourly air temperatures during the 24 hours for the three tested days are shown in Figure 4.36. Maximum hourly air temperature recorded for the Frozen, Cold and Sunny day were 0.0, 13.3 and 23.0 ℃ respectively. The minimum air temperature on the same days was -9.25, -3.2 and 4.5 ℃ respectively.

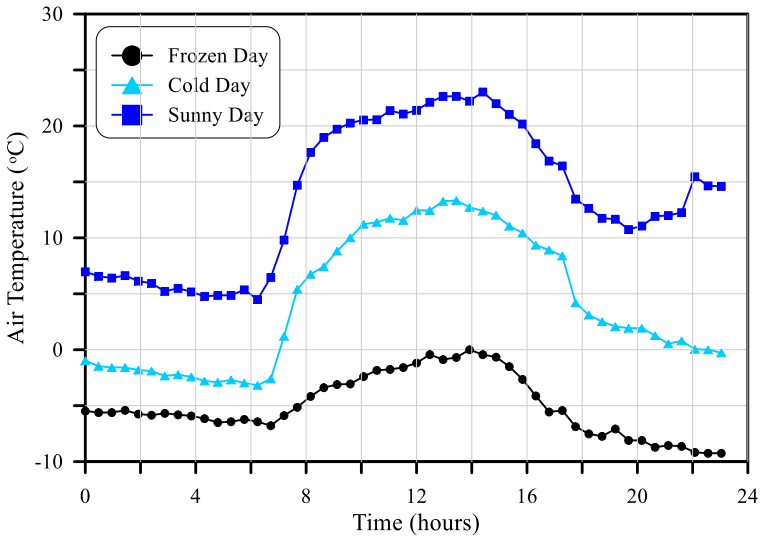

Figure 4.36 Hourly air temperatures during the 24 hours in 2-January (Frozen), 4-February (Cold), and 18-February (Sunny).

Figure 4.37 illustrates the hourly solar radiation intensities during the 24 hours on (2-January (Frozen), 4-February (Cold) and 18-February (Sunny)). The maximum value of the hourly solar radiation intensities recorded for the three examined days was 606, 673 and 712 W/m^2 on Frozen, Cold and Sunny day respectively

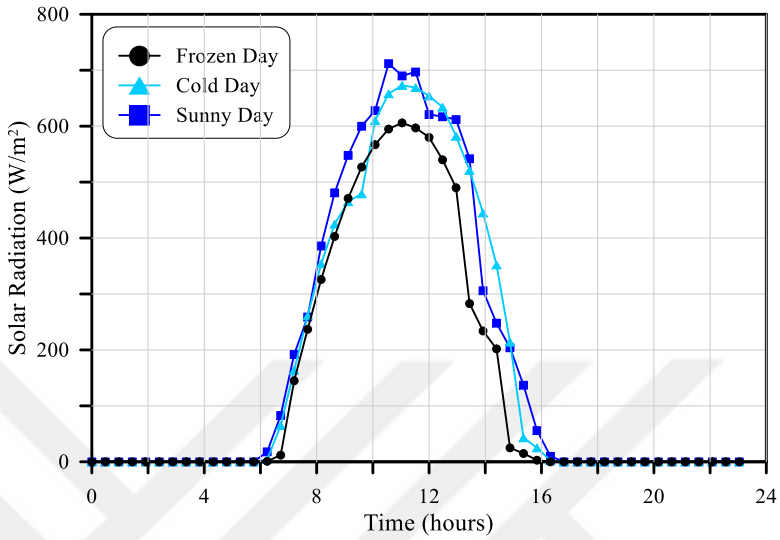

Figure 4.37 Hourly solar radiation intensities during the 24 hours in 2-January (Frozen), 4-February (Cold), and 18-February (Sunny).

4.5.2 T-Beam results of the Frozen, Cold and Sunny days

As stated previously, three days were selected from the three different conditions to evaluate the temperature distributions of the different thermocouples, the hourly maximum, and the hourly mean temperature of all thermocouples during these days. The three days are 2-January (Frozen), 4-February (Cold) and 18-February (Sunny). In addition, the hourly variations of the temperature gradients are also presented along the 24 hours of the presented days.

4.5.2.1 T-Beam temperatures of the Frozen, Cold and Sunny days

The hourly temperatures of thermocouples TC1, TC3, TC4, TC5, TS1, TS4 and TS7 during the 24 hours of 2-January (Frozen), 4-February (Cold) and 18-February (Sunny) are shown in Figures 4.38 to 4.44, respectively, while, the maximum and mean temperature of all thermocouples during the same selected days are shown in Figures 4.45 and 4.46 respectively.

Figure 4.38 shows the hourly temperatures of thermocouple TC1 during the 24 hours in 2-January (Frozen), 4-February (Cold) and 18-February (Sunny). The recorded maximum hourly temperature values were 5.64, 25.64 and 36.41 ℃ for Frozen, Cold and Sunny days, respectively. On the other hand, the recorded minimum hourly temperatures of this thermocouple were -7.23, -1.1 and 6.36 ℃, respectively.

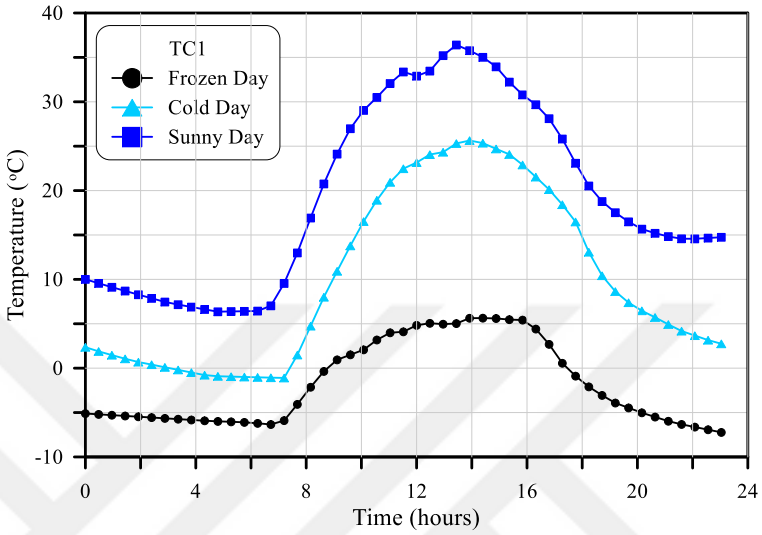

Figure 4.38 Hourly temperatures of thermocouple TC1 during the 24 hours in 2-January (Frozen), 4-February (Cold), and 18-February (Sunny) for the T-Beam segment.

Figure 4.39 illustrates the hourly temperatures of thermocouple TC3 during the 24 hours of the three tested days. The recorded maximum hourly temperature were 3.2, 21.4 and 32.5 ℃ in the Frozen, Cold and Sunny days respectively, while their corresponding minimum hourly temperatures were -6.68, -0.97 and 6.7 ℃ respectively. When comparing the results of the TC1 and TC3 thermocouples, it is noted that the maximum values of temperature was higher for TC1 than for TC3, while the minimum temperature was lower for TC1 than TC3. This result is an expected one as TC1 is a surface thermocouple, while TC3 is an interior one. Hence, TC1 heated faster during the day hours and cooled faster during the night hours.

Figure 4.40 represents the hourly temperatures of thermocouple TC4 for the 24 hours of 2-January (Frozen), 4-February (Cold) and 18-February (Sunny). The maximum hourly temperatures were 2.5, 19.8 and 30.3 in 2-January, 4-February, and 18-February, respectively, while the minimum hourly temperatures for the same sequence of days were -6.47, -0.8 and 6.8, respectively. As TC4 is an internal thermocouple, its daily maximum temperatures in the three tested days were lower

than those of TC1 and TC3. The solar radiation received by internal is minimal compared to that received by the edge and the top surface.

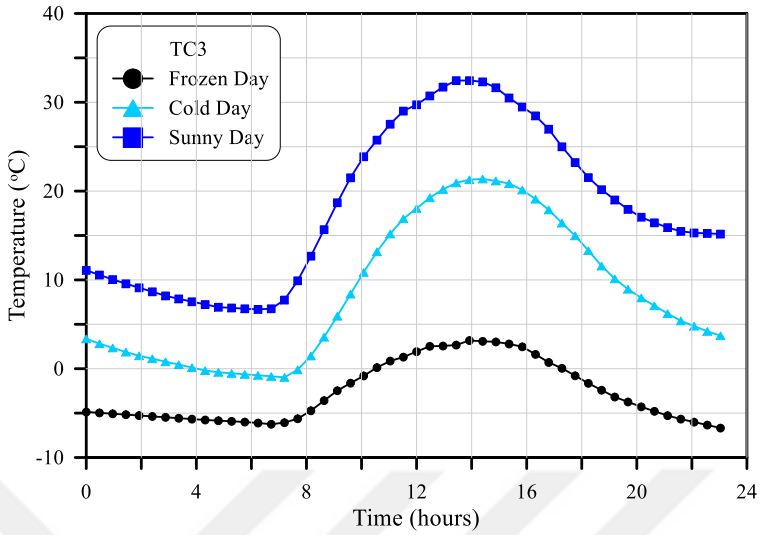

Figure 4.39 Hourly temperatures of thermocouple TC3 during the 24 hours in 2-January (Frozen), 4-February (Cold), and 18-February (Sunny) for the T-Beam segment.

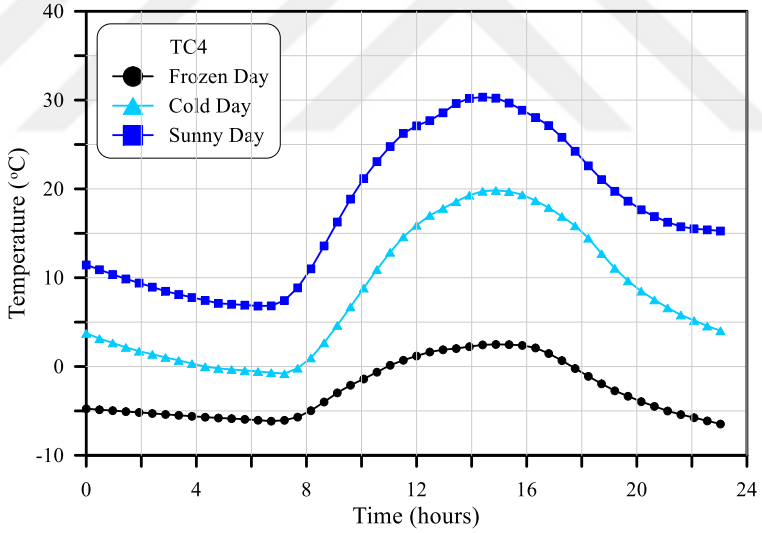

Figure 4.40 Hourly temperatures of thermocouple TC4 during the 24 hours in 2-January (Frozen), 4-February (Cold), and 18-February (Sunny) for the T-Beam segment.

The hourly temperatures variation of thermocouple TC5 during the 24 hours in the three selected days is shown in Figure 4.41. The recorded maximum values were 2.2, 18.4 and 28.2 ℃ in the Frozen, Cold, and Sunny days, respectively, while the minimum values were -6.96, -0.84 and 6.7 ℃, respectively.

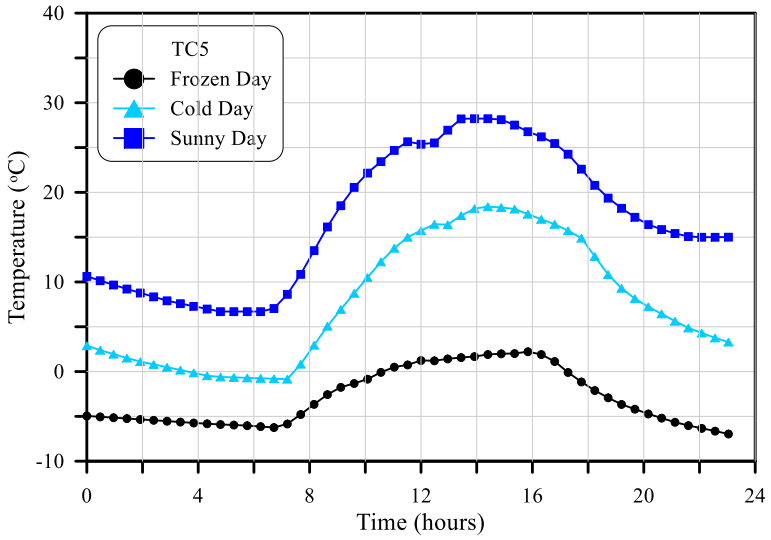

Figure 4.41 Hourly temperatures of thermocouple TC5 during the 24 hours in 2-January (Frozen), 4-February (Cold), and 18-February (Sunny) for the T-Beam segment.

Figure 4.42 illustrates the hourly temperatures of thermocouple TS1 for the 24 hours of the Frozen, Cold, and Sunny days. The daily maximum temperatures were 2.2, 18.3 and 28.14 ℃ in 2-January, 4-February, and 18-February, respectively, the corresponding minimum temperatures were -7.05 , -0.86 and 6.62 ℃, respectively.

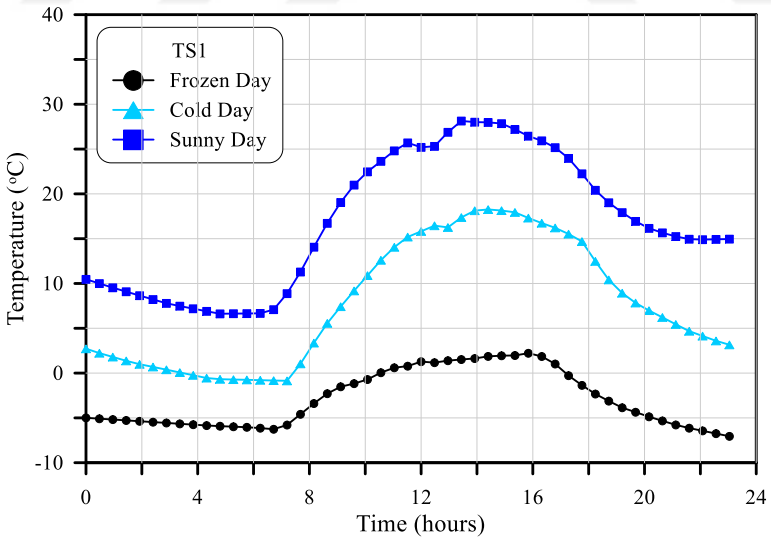

Figure 4.42 Hourly temperatures of thermocouple TS1 during the 24 hours in 2-January (Frozen), 4-February (Cold), and 18-February (Sunny) for the T-Beam segment.

The hourly temperature variation of thermocouple TS4 during the 24 hours of the three tested days is shown in Figure 4.43. Where, the daily maximum hourly temperatures were 4.53, 19.73 and 28.74 ℃ in the Frozen, Cold, and Sunny days,

respectively, while the daily minimum hourly temperatures were -8.34, -1.76 and 5.54 ℃, respectively. The maximum temperature of TS4 was higher than those of TC1 because of its location. Similarly, the minimum temperatures were lower than those of TC1 for the same reason. The thermocouple TS4 is located at the central depth of the steel beam. Thus it is installed on a vertical surface, and hence receives high solar radiation than that of the top surface (TC1) during the cold season. Although TS4 is installed on the northern surface, this was not as effective as steel is highly conductive metal and the thickness of the web is only few millimeters.

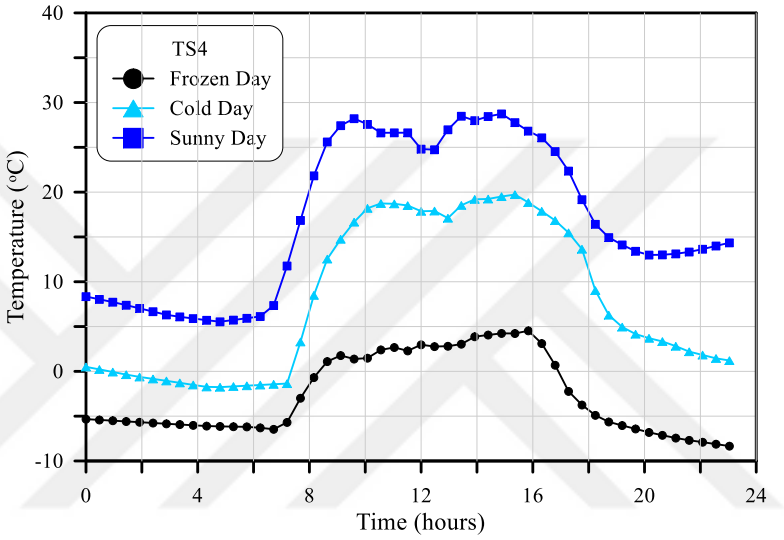

Figure 4.43 Hourly temperatures of thermocouple TS4 during the 24 hours in 2-January (Frozen), 4-February (Cold), and 18-February (Sunny) for the T-Beam segment.

Figure 4.44 presents the hourly temperature variation of thermocouple TS7 for the 24 hours on the three selected days. TS7 is the girder's bottom surface's thermocouple (at the bottom surface of the bottom flange of the steel section). The daily maximum values were 3.46, 21.64 and 32.13 ℃ in 2-January, 4-February, and 18-February, respectively, while the minimum values were -8.67, -2.04 and 5.26 ℃, respectively. It should be noted that this thermocouple is highly affected by the reflected radiation (albedo).

The hourly variation of the maximum temperatures of all thermocouple during the 24 hours of 2-January (Frozen), 4-February (Cold), and 18-February (Sunny) are shown in Figure 4.45. The maximum values in the three selected days were 5.64, 21.64 and 32.13 ℃, respectively, while the minimum values were -6.28, -0.71 and 6.91 ℃, respectively.

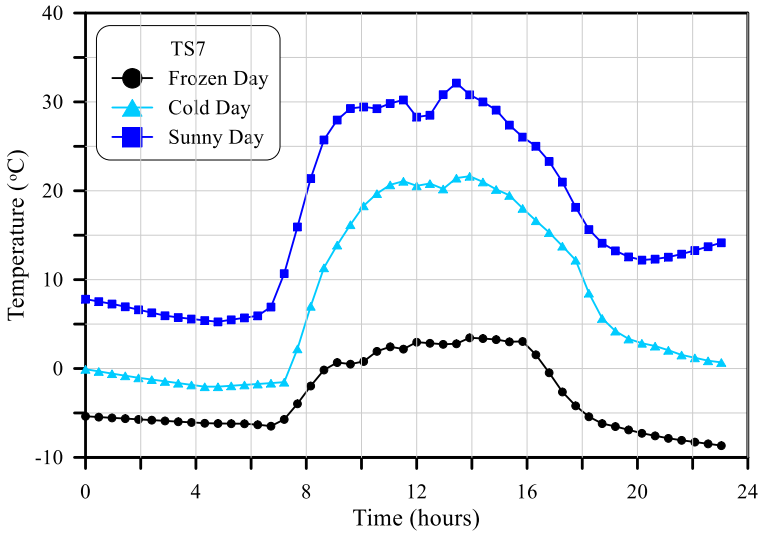

Figure 4.44 Hourly temperatures of thermocouple TS4 during the 24 hours in 2-January (Frozen), 4-February (Cold), and 18-February (Sunny) for the T-Beam segment.

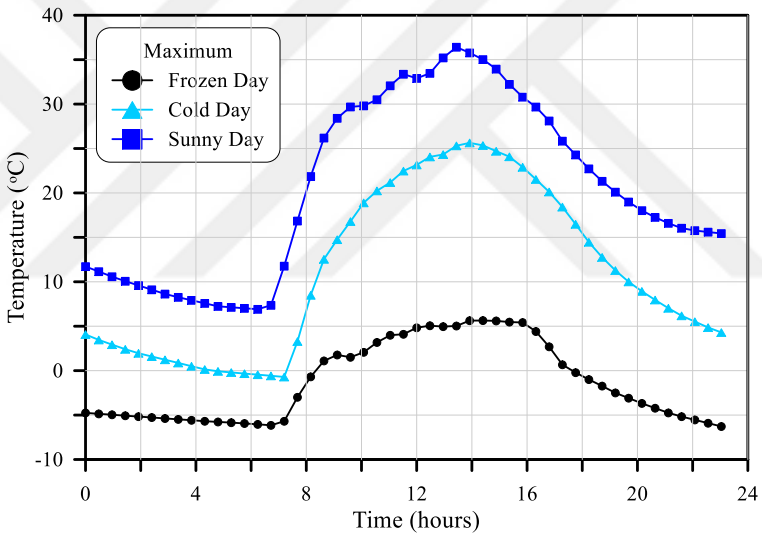

Figure 4.45 Maximum temperature of all thermocouple during the 24 hours in 2-January (Frozen), 4-February (Cold), and 18-February (Sunny) for the T-Beam segment.

Figure 4.46 shows the hourly variation of the mean temperatures of all thermocouples during the 24 hours in 2-January (Frozen), 4-February (Cold) and 18-February (Sunny). The highest recorded mean temperatures were 2.81, 20.45 and 30.87 ℃ in the Frozen, Cold and Sunny days, respectively, while the lowest mean temperatures were -6.76, -0.88 and 6.71 ℃, respectively.

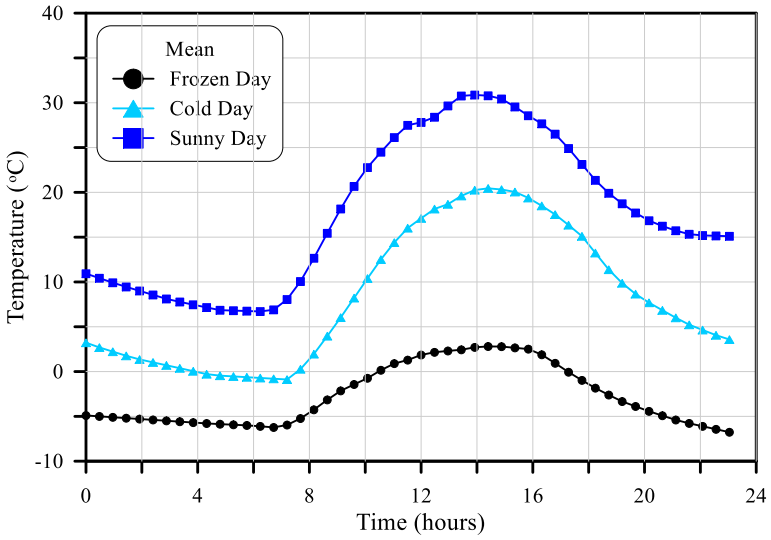

Figure 4.46 Mean temperature of all thermocouple during the 24 hours in 2-January (Frozen), 4-February (Cold), and 18-February (Sunny) for the T-Beam segment.

4.5.2.2 T-Beam temperature differences of the Frozen, Cold and Sunny days

The maximum vertical temperature gradient is calculated by subtracting the minimum temperature along the vertical centerline of the composite girder from all temperatures of the thermocouples along this line. These thermocouples from top to bottom are TC3, TC4, TC5, TS1, TS3, TS4, TS5 and TS7.

Similarly, the lateral temperature gradient is calculated by subtracting the minimum temperature of the thermocouples installed along the horizontal centerline of the top concrete slab from the temperatures of all these thermocouples. The thermocouples that were used for the calculation of lateral temperature gradient from north to south are TC1, TC2, TC4, TC6 and TC7.

However, for easier presentation of gradient data, the difference of (TC3-TS4) is considered here for the vertical gradient, while the temperature difference (TC7-TC4) is considered here for the lateral gradients. In this section, the maximum vertical and lateral temperature gradients were studied during the 24 hours of 2-January (Frozen), 4-February (Cold) and 18-February (Sunny). The ranges of vertical and lateral temperature gradients for the three examined days are presented in Table 4.2.

Figure 4.47 shows the variation of the vertical temperature gradient by calculating the difference between TC3 and TS4 during the 24 hours of 2-January (Frozen), 4-February (Cold) and 18-February (Sunny). The minimum values of vertical temperature gradient for the three days were -4.69, -8.98 and -9.94 in the Frozen,

Cold and Sunny days, respectively, which were occurred around 9:00 AM. On the other hand, the corresponding maximum gradient values were 3.29, 5.29 and 5.99 ℃ at 7:00, 7:30 and 1:00 PM, respectively.

Figure 4.48 graphs the lateral temperature gradient by (difference between TC7 and TC4) during the 24 hours of 2-January (Frozen), 4-February (Cold) and 18-February (Sunny). The minimum and maximum lateral temperature gradients are listed in Table 4.2. The minimum values for the three days were occurred at 8:00, 8:00 and 7:30 PM, respectively, while the maximum values for these days were occurred at 9:30, 11:30 and 10:00 AM, respectively.

Table 4.2 Temperature gradient ranges of the chosen Frozen, Cold, and Sunny days for the T-Beam segment.

Condition	**Frozen Day**	**Cold Day**	**Sunny Day**
Date	**2-Jan-2016**	**4-Feb-2016**	**18-Feb-2016**
Vertical Gradient Range (°C)	-4.69 to 3.26	-8.98 to 5.29	-9.94 to 5.99
Lateral Gradient Range (°C)	-1.19 to 3.90	-2.43 to 8.07	-2.28 to 8.12

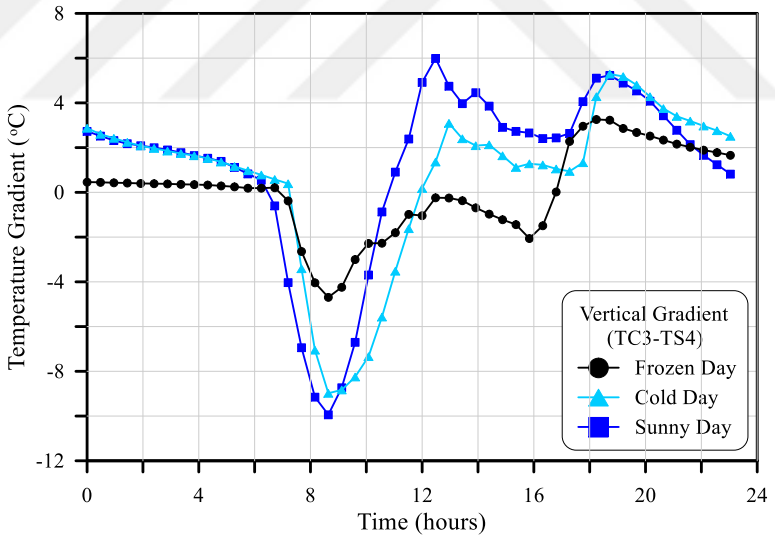

Figure 4.47 Vertical temperature gradient (TC3-TS4) during the 24 hours of 2-January (Frozen), 4-February (Cold), and 18-February (Sunny) for the T-Beam segment.

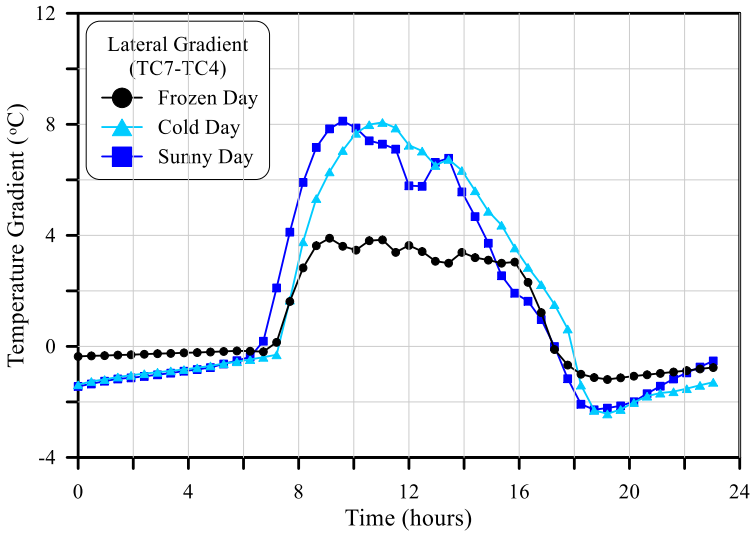

Figure 4.48 Lateral temperature gradient (TC1-TC4) during the 24 hours of 2-January (Frozen), 4-February (Cold), and 18-February (Sunny) for the T-Beam segment.

4.5.2.3 T-Beam vertical and lateral temperature distributions of the Frozen, Cold, and Sunny days

Figures 4.49 to 4.51 study the vertical temperature distributions for the T-Beam segment at five different time steps in the three tested days. The temperature distributions consider all thermocouples listed along the vertical centerline of the girder, as stated in the previous section. The figures show that the temperature at top and bottom surfaces of the segment decreased before sunrise and after sunset at the time steps 4:00 AM and 6:00 PM.

The temperature distributions are almost nonlinear along the interior part of the girder. It is noted in the three figures that at 8:00 AM, the temperature of the steel section increased noticeably compared to the concrete slab. This is mainly due to the high solar radiation received by the vertical surfaces due to the high inclination angles of sunrays at this time. Similar, but less noticeable behavior is noticed at 4:00 PM. On the other hand, the temperature is almost constant along the girder at 4:00 AM due to the long cooling hours which neutralize the day heating effect.

During the hot hours (1:00 PM and 4:00 PM), the temperature of the top surface increases due to the receiving of considerable amount of energy from solar radiation. Although, in most cases, the temperature of the top surface still not the highest along the vertical axis except in the sunny day. This can be attributed to two reasons; the

inclination of sunrays in winter (high solar inclination angles) and the high thermal conductivity of steel compared to concrete. After sunset, as in the distribution at 6:00 PM, due to the higher thermal conductivity of steel, the steel section cooled faster than the concrete section as it is clear in Figures 4.49, 4.50 and 4.51.

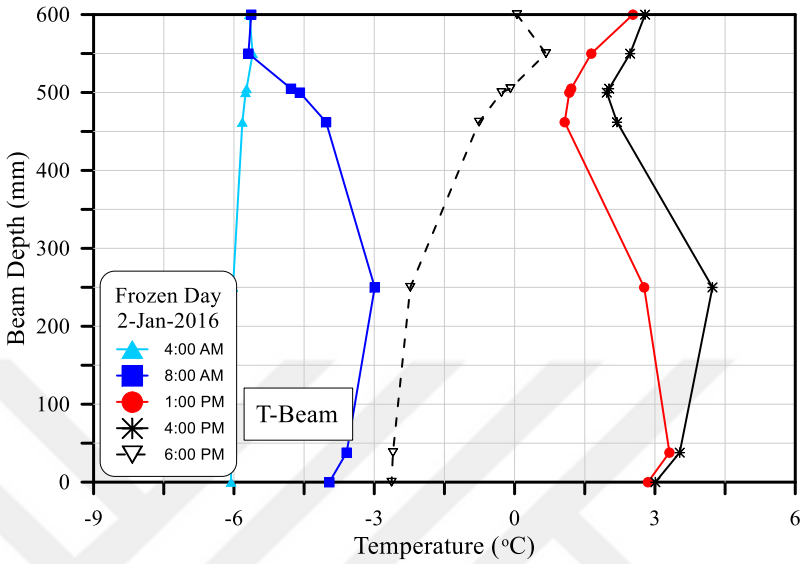

Figure 4.49 Vertical temperature distributions at different times in 2-January-2016 (Frozen) for the T-Beam segment.

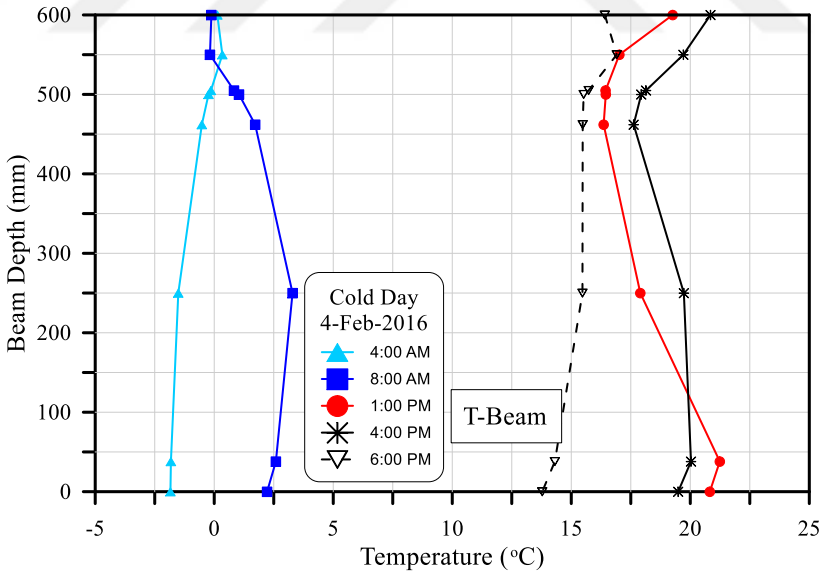

Figure 4.50 Vertical temperature distributions at different times in 4-February-2016 (Cold) for the T-Beam segment.

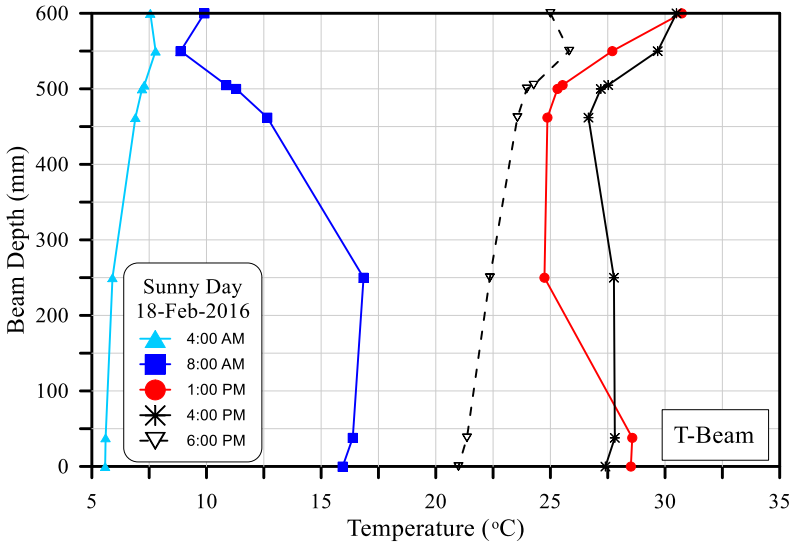

Figure 4.51 Vertical temperature distributions at different times in 18-February-2016 (Sunny) for the T-Beam segment.

Figures 4.52 to 4.54 study the lateral temperature distributions along the horizontal centerline of the concrete slab at five different times in the three tested days. The temperature distributions at five different time steps of the day were constant along interior part of the concrete flange at (TC2, TC4 and TC6) for the three selected days. The variation of temperature occurred at the exterior thermocouples at the northern and southern edges of the concrete slab reflecting significant variations at 1:00 and 4:00 PM for three tested days.

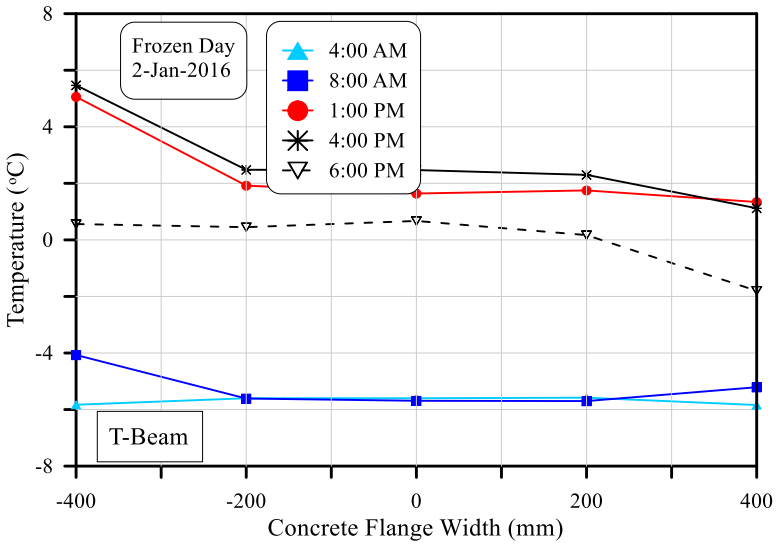

Figure 4.52 Lateral temperature distributions at different times in 2-January-2016 (Frozen) for the T-Beam segment.

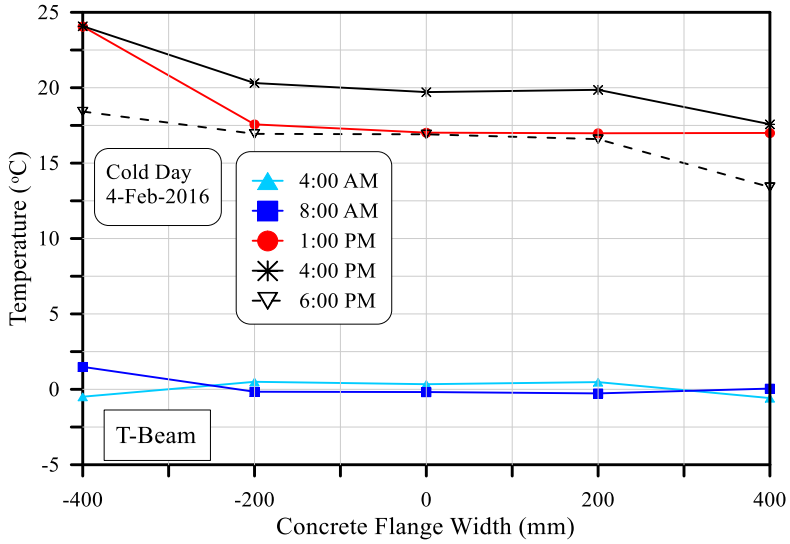

Figure 4.53 Lateral temperature distributions at different times in 4-February-2016 (Cold) for the T-Beam segment.

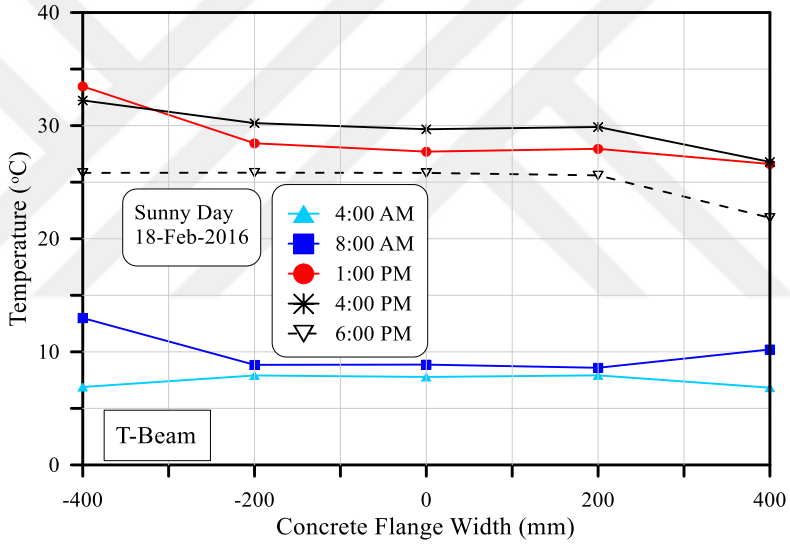

Figure 4.54 Lateral temperature distributions at different times in 18-February-2016 (Sunny) for the T-Beam segment.

4.5.3 I-Beam results of the Frozen, Cold and Sunny days

In this section, the temperatures and temperature gradient distributions of the I-beam composite girder segment are analyzed in the same manner as in the previous section for the T-beam.

4.5.3.1 I-Beam temperatures of the Frozen, Cold and Sunny days

Figure 4.55 shows the hourly temperatures of thermocouple IC1 during the 24 hours on the three tested days. The maximum hourly temperatures of thermocouple were

2.88, 20.44 and 31.49 ℃ in the Frozen, Cold and Sunny days, respectively, at 2:30 PM, while corresponding minimum values were -6.09 ℃ at 7:00 AM, -0.18 ℃ at 6:30 AM and 7.66 ℃ at 6:30 AM, respectively.

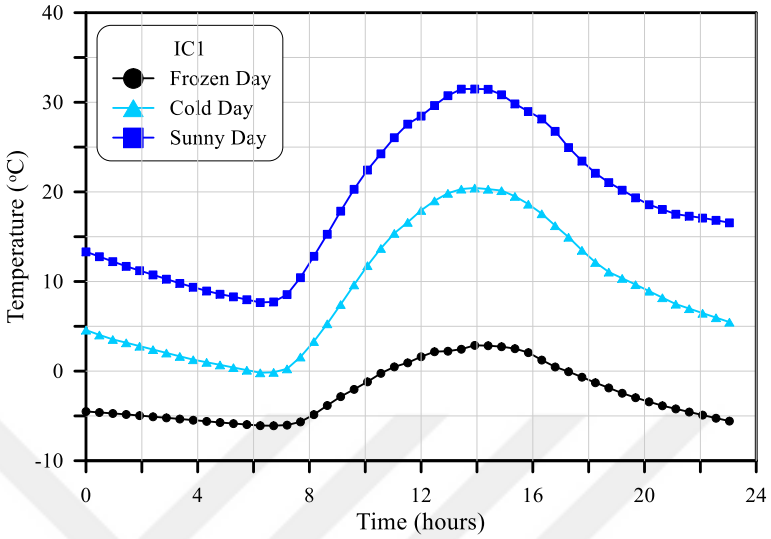

Figure 4.55 Hourly temperatures of thermocouple IC1 during the 24 hours of 2-January (Frozen), 4-February (Cold), and 18-February (Sunny) for the I-Beam segment.

Figure 4.56 illustrates the hourly temperature variation of thermocouple IC3 during the 24 hours of the selected days. The maximum recorded values of temperature were 2.05, 18.59 and 28.92 ℃ in the Frozen, Cold and Sunny days, respectively, at 3:30 PM. The minimum values were -5.98 ℃ at 7:30 AM, 0.16 ℃ at 7:00 AM, and 7.98 ℃ at 7:00 AM, respectively. The maximum temperatures of IC3 were lower than those of IC1, while the minimum values were higher than IC1. This is an expected result as IC1 is the top surface's thermocouple, while IC3 is an interior thermocouple that is installed 25 mm deeper in the concrete slab. Thus, IC1 is heated faster during the hot hours due to solar radiation and cooled faster due to cold air during the cold hours of the day.

Figure 4.57 shows the hourly temperature variation of thermocouple IC7 during the 24 hours of the three tested days. The maximum recorded values were 5.95 ℃ at 3:00 PM, 25.97 ℃ at 2:00 PM, and 36.53 ℃ at 2:00 PM in the Frozen, Cold and Sunny days, respectively. The minimum recorded values in IC4 were -6.95 ℃ at 12:00 AM, -1.5 ℃ at 6:30 AM, and 6.27 ℃ at 6:30 AM, respectively. As it is a

surface thermocouple, the maximum hourly temperature for IC7 was higher than the IC3, but the minimum hourly temperature for IC3 was higher.

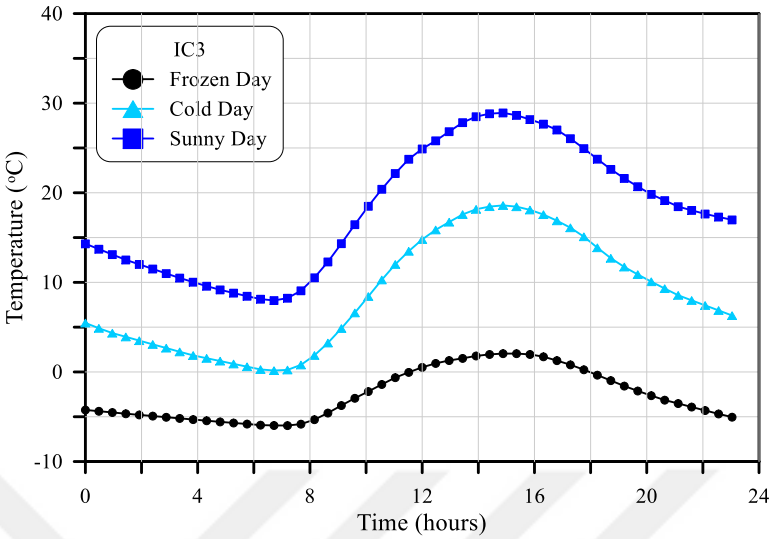

Figure 4.56 Hourly temperatures of thermocouple IC3 during the 24 hours in 2-January (Frozen), 4-February (Cold), and 18-February (Sunny) for the I-Beam segment.

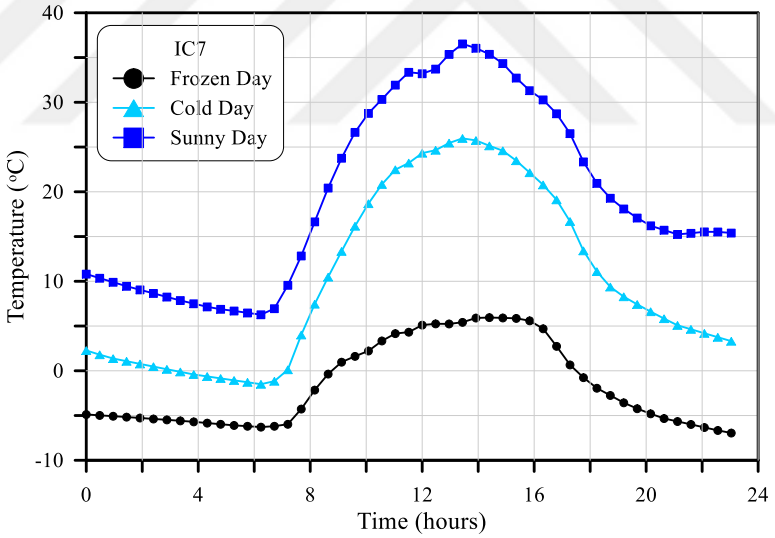

Figure 4.57 Hourly temperatures of thermocouple IC7 during the 24 hours in 2-January (Frozen), 4-February (Cold), and 18-February (Sunny) for the I-Beam segment.

Figure 4.58 presents the hourly temperature of thermocouple IC4 during the 24 hours of the three tested days. The maximum values of hourly temperature were 1.43 ℃ at 3:00 PM, 18.07 ℃ at 2:30 PM and 28.27 ℃ at 2:00 PM in the Frozen Cold and Sunny days, respectively. On the other hand, the minimum values were -7.14 ℃ at 12:00 AM, -1.54 ℃ at 6:30 AM and 6.25 ℃ at 6:30 AM, respectively.

Comparing the temperatures of IC1, IC7 and IC4, it is clear that the southern edge thermocouple IC7 exhibited higher temperatures than the top surface's thermocouple IC1 and the northern edge thermocouple IC4. This was discussed in the previous section and was attributed to solar altitude angles during the cold season.

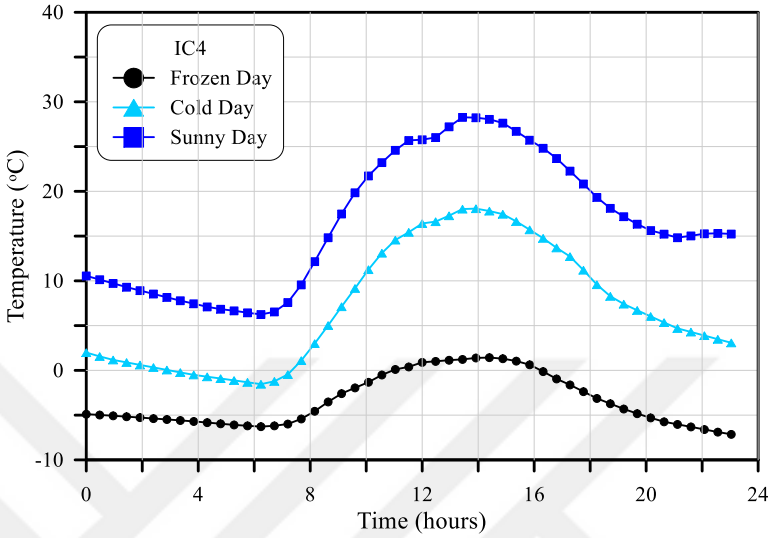

Figure 4.58 Hourly temperatures of thermocouple IC4 during the 24 hours in 2-January (Frozen), 4-February (Cold), and 18-February (Sunny) for the I-Beam segment.

Figure 4.59 shows the hourly temperatures of thermocouple IC10 during the 24 hours of the selected days. The maximum hourly temperature values were 1.67 ℃ at 3:00 PM, 16.88 ℃ at 3:00 PM, and 25.68 ℃ at 3:30 PM in the Frozen, Cold and Sunny days, respectively. The minimum recorded hourly temperatures were -6.04 ℃ at 6:30 AM, 0.04 ℃ at 6:30 AM and 7.87 ℃ at 6:30 AM, respectively. The maximum and minimum hourly temperatures for IC10 was lower than the IC1 and IC3 noting that IC10 is the bottom surface's thermocouple, where solar radiation is mostly received as reflected radiation from the ground.

Figure 4.60 illustrates the hourly temperatures of thermocouple IS2 during the 24 hours for the three tested days. IS2 is the thermocouple installed on the web of the steel section at the central depth of the girder. The maximum recorded values were 2.58 ℃ at 4:30 PM, 17.24 ℃ at 4:30 PM and 26.42 ℃ at 5:00 PM in the Frozen, Cold, and Sunny days, respectively. The minimum hourly temperatures were -5.95 ℃ at 7:00 AM, 0.31 ℃ at 7:00 AM and 8.17 ℃ at 7:00 AM, respectively.

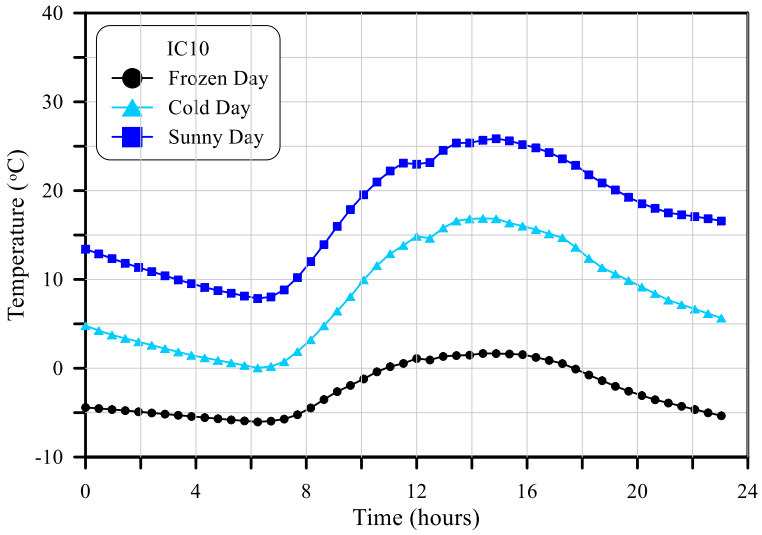

Figure 4.59 Hourly temperatures of thermocouple IC10 during the 24 hours of 2-January (Frozen), 4-February (Cold), and 18-February (Sunny) for the I-Beam segment.

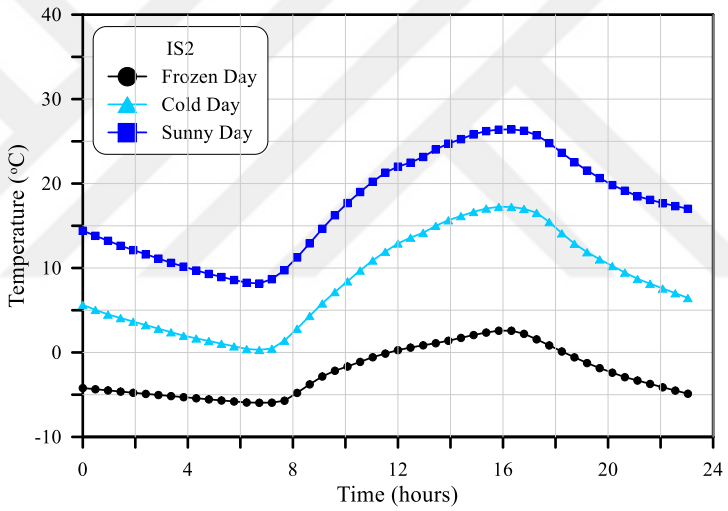

Figure 4.60 Hourly temperatures of thermocouple IS2 during the 24 hours of 2-January (Frozen), 4-February (Cold), and 18-February (Sunny) for the I-Beam segment.

Figure 4.61 shows the maximum hourly temperatures for all thermocouples during the 24 hours. The maximum recorded values were 5.95 ℃ at 3:00 PM, 25.97 ℃ at 2:00 PM, and 36.53 ℃ at 2:00 PM in the Frozen, Cold and Sunny days, respectively. On the other hand, their corresponding minimum values were -5.93 ℃ at 7:00 AM, 0.31 ℃ at 7:00 AM, and 8.26 ℃ at 6:30 AM, respectively.

Mean temperature of all thermocouples during the 24 hours on three selected days are shown in Figure 4.62. The maximum values of the mean temperature during the three days (Frozen, Cold and Sunny) were 2.59, 18.78 and 28.69 ℃ at 3:30 PM,

respectively. The corresponding the minimum mean temperature values were -6.09, -0.37 and 7.64 ℃ at 6:30 AM, respectively.

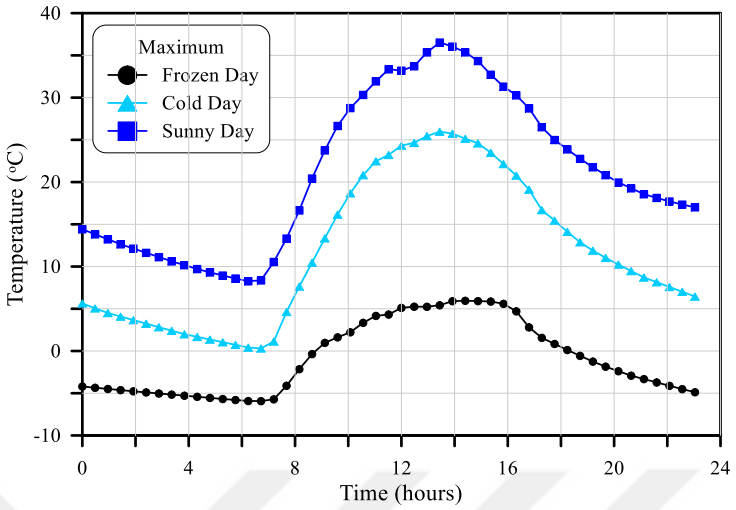

Figure 4.61 Maximum temperature of all thermocouples during the 24 hours in 2-January (Frozen), 4-February (Cold), and 18-February (Sunny) for the I-Beam segment.

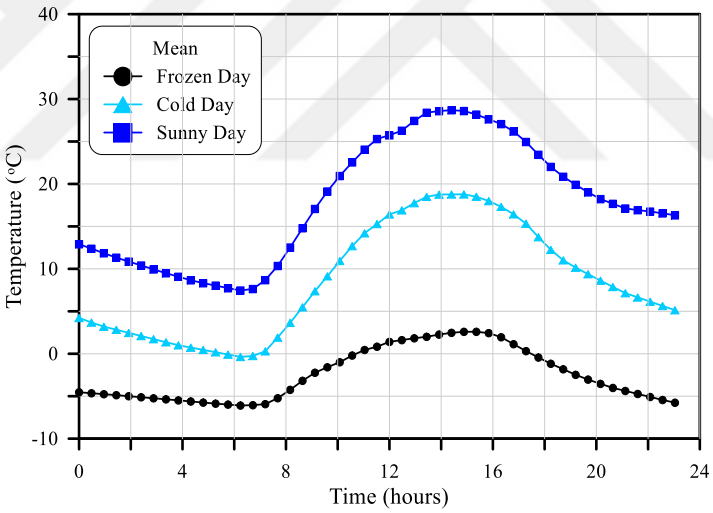

Figure 4.62 Mean temperature of all thermocouples during the 24 hours on 2-January (Frozen), 4-February (Cold), and 18-February (Sunny) for the I-Beam segment.

4.5.3.2 I-Beam temperature differences of the Frozen, Cold and Sunny days

The hourly variation of the maximum vertical and lateral temperature gradients during the 24 hours on three selected days (2-January (Frozen), 4-February (Cold) and 18-February (Sunny)) are discussed in this section. As discussed for the T-beam composite girder in the previous section, the vertical gradient was considered as the

difference between top surface's thermocouple IC1 and the central steel thermocouple IS2. For lateral gradient, the difference between two of the concrete slab thermocouples was considered. These are the southern edge thermocouple IC7 and the concrete slab's central thermocouple IC4. Table 4.3 shows the range of the recorded vertical and lateral temperature gradients during the chosen days in 2-January (Frozen), 4-February (Cold) and 18-February (Sunny).

Table 4.3 Temperature gradient ranges of the chosen days for the I-Beam segment.

Condition	**Frozen day**	**Cold day**	**Sunny day**
Date	**2-Jan-2016**	**4-Feb-2016**	**18-Feb-2016**
Vertical Gradient Range (°C)	-1.74 to 1.59	-1.98 to 5.68	-1.56 to 7.59
Lateral Gradient Range (°C)	-2.19 to 4.79	-3.48 to 10.55	-3.62 to 10.27

Figure 4.63 illustrates the hourly variation of the vertical temperature gradient during the 24 hours on the three chosen days. The maximum values of this gradient were 1.59 ℃ at 1:00 PM, 5.68 ℃ at 1:30, and 7.59 ℃ at 1:30 in the Frozen, Cold and Sunny days, respectively. The corresponding minimum values were -1.74 ℃ at 5:30 PM, -3.48 ℃ at 7:00 PM and -.62 ℃ at 7:00 PM, respectively.

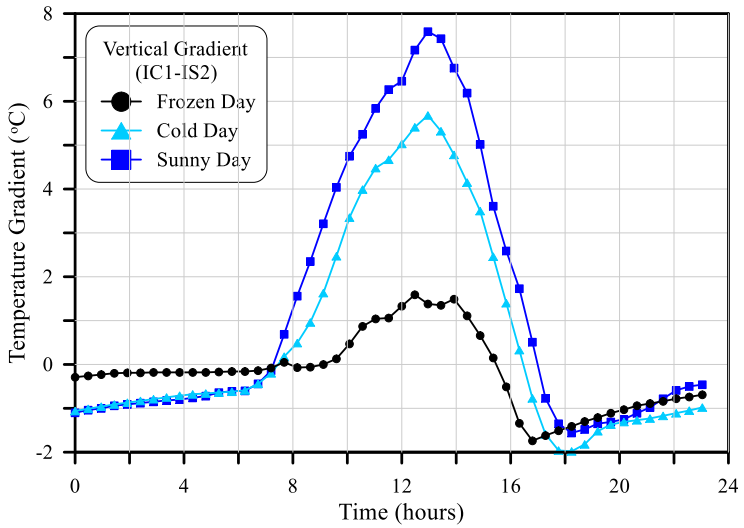

Figure 4.63 Vertical temperature gradient (IC1-IS2) during the 24 hours in 2-January (Frozen), 4-February (Cold), and 18-February (Sunny) for the I-Beam segment.

Figure 4.64 shows the hourly variation of the lateral temperature gradient during the 24 hours in the three tested days. The maximum recorded values of the lateral gradient were 4.79 ℃ at 11:30 AM, 10.55 ℃ at 11:00 AM, and 10.27 ℃ at 10:30 in

the Frozen, Cold and Sunny days, respectively. In the same order, the minimum values were -2.19 ℃ at 11:30 PM, -3.48 ℃ at 11:30 PM and -3.62 ℃ at 11:00 PM, respectively.

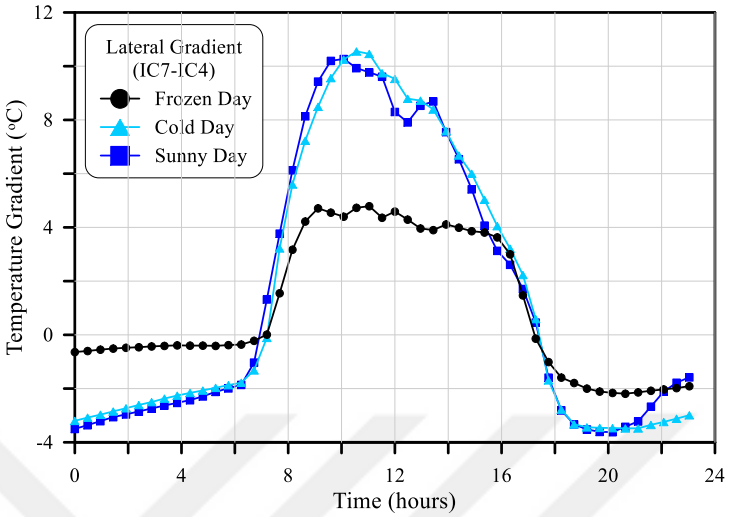

Figure 4.64 Lateral temperature gradient (IC7-IC4) during the 24 hours in 2-January (Frozen), 4-February (Cold), and 18-February (Sunny) for the I-Beam segment.

4.5.3.3 I-Beam vertical and lateral temperature distributions of the Frozen, Cold and Sunny days

Figures 4.65 to 4.67 illustrate the vertical temperature distributions at different times in 2-January-2016 (Frozen day), 4-February-2016 (Cold day) and 18-February-2016 (Sunny day) for the I-Beam segment. The results of the three tested days show that the vertical temperature distribution with the highest temperatures occurred at 4:00 PM for Frozen, Cold and Sunny day at depth 500 mm. Unlike the T-beam composite girder, the distribution of 8:00 AM is also almost nonuniform. At 4:00 AM with minor temperature increases at the top and bottom surfaces the distribution is also almost uniform. In the I-beam on the other hand, the thermocouples of the steel section are installed in concrete. Thus, needs much more time for heating. Hence, the web temperature still cold during the morning shining hours.

As shown in Figures 4.65, 4.66 and 4.67, the noticeable positive vertical temperature gradients occurred between 1:00 PM and 4:00 PM. After which, the distribution changes to the negative gradient distribution as shown in the distribution at 6:00 PM. The gradient distribution at 1:00 PM can be used for vertical positive gradient considerations in cold seasons. As shown in the three figures, the temperature

gradient is evident to occur across the top flange thickness, with highest temperature at the top surface and lowest temperature at the central depth of the composite girder. The temperature at the bottom surface small and there is no temperature increase there as that at 8:00 AM. The gradient at the top surface of the 1:00 PM distribution is the highest in the sunny day and the lowest in the frozen day. Note that the small increase at the top surface is more noticeable in the sunny day, while it is not noticeable in the frozen day. This is directly attributed to the amount of received radiations and the cloud cover variation between the three days.

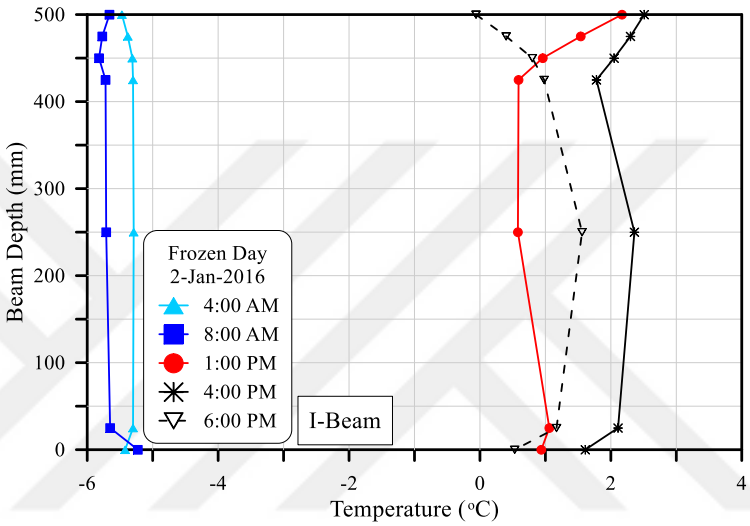

Figure 4.65 Vertical temperature distributions at different times in 2-January-2016 (Frozen) for the I-Beam segment.

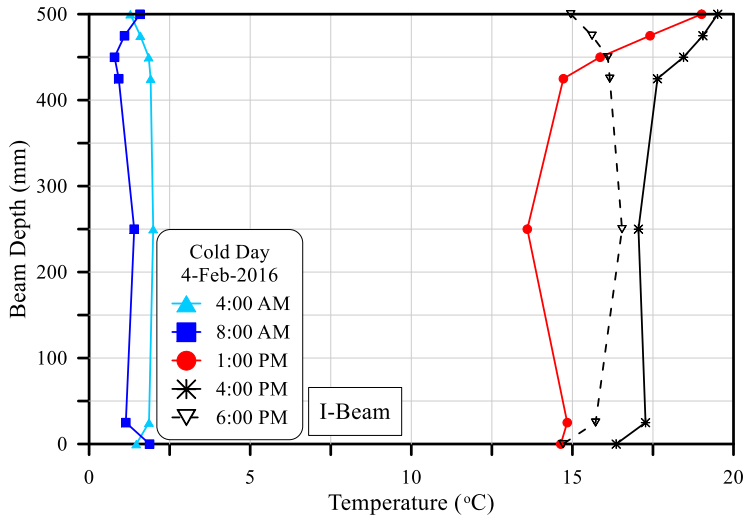

Figure 4.66 Vertical temperature distributions at different times in 4-February-2016 (Cold) for the I-Beam segment.

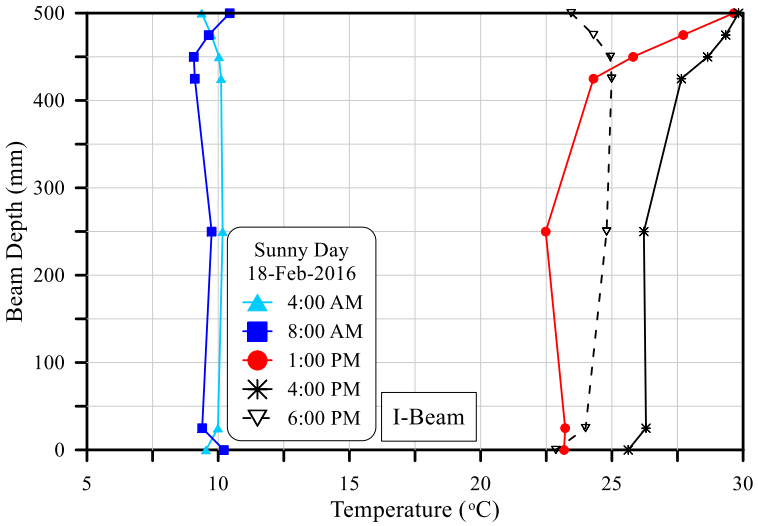

Figure 4.67 Vertical temperature distributions at different times in 18-February-2016 (Sunny) for the I-Beam segment.

Figures 4.68 to 4.70 show the lateral temperature distributions along the horizontal centerline of the top concrete flange at different time steps in the three chosen days. It is clear the distributions at 4:00 AM and 6:00 PM are almost neutralized along the full width of the top flange. At 8:00 AM, the increase of temperature at the southern thermocouple due to the received radiation from sunrise to 8:00 AM leas to the shown temperature gradient at the southern edge. However, the overall temperature of the flange still low. After five heating hours, the overall temperature of the top flange increased as shown in the temperature distributions at 1:00 PM. Moreover, the gradient at the southern edge becomes higher as shown in Figures 4.68 to 4.70.

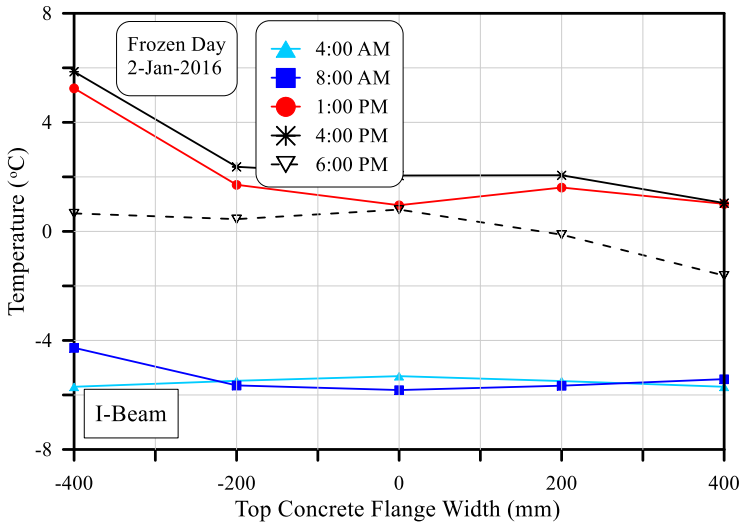

Figure 4.68 Lateral temperature distributions of top-concrete flange at different times in 2-January-2016 (Frozen) for the I-Beam segment.

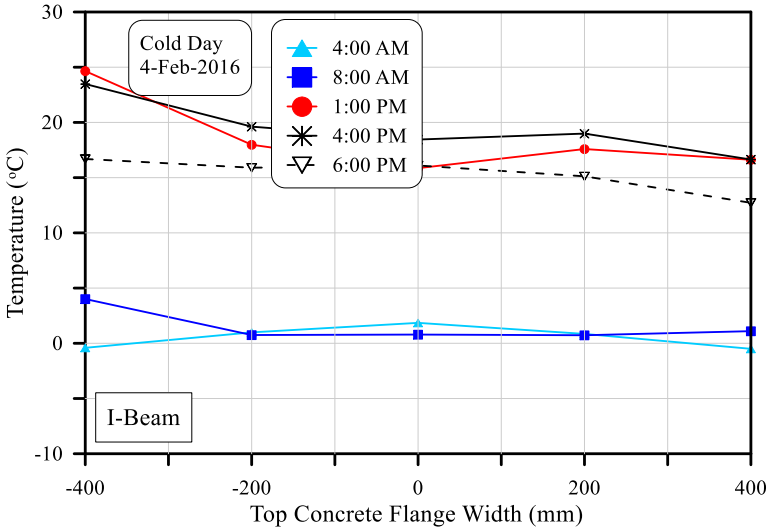

Figure 4.69 Lateral temperature distributions of top-concrete flange at different times in 4-February-2016 (Cold) for the I-Beam segment.

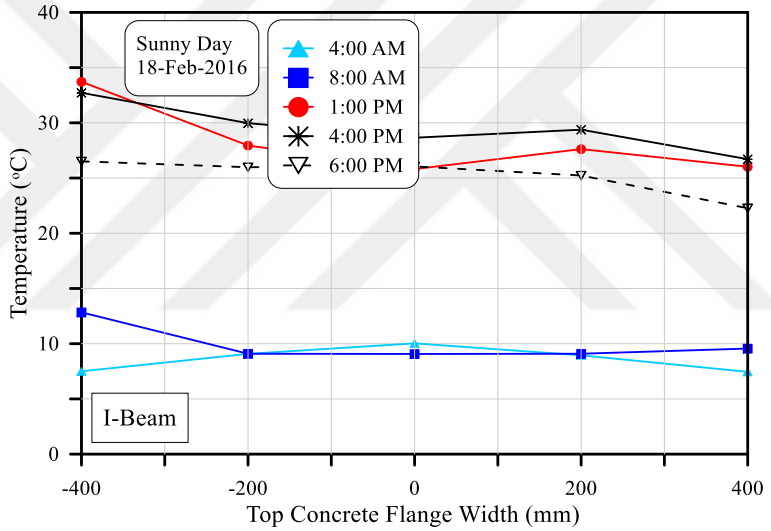

Figure 4.70 Lateral temperature distributions of top-concrete flange at different times in 18-February-2016 (Sunny) for the I-Beam segment.

4.6. Thermal strains for I-Beam Segment

Figure 4.71 shows the hourly variation of the strains measured from the two strain gages that were embedded at the central depth of the top flange of I-Beam segment. The strains were measured as the change of the strains from an initial strain reading. This reading was the strain value at the start time of the period, which is at the midnight (00:00) on the first day of 21-December-2016. The data logger was supplied with a compatible strain analyzer, which uses a spectral interpolation method to measure the resonant frequency. The recorded frequency at each time step

was then converted to micro strains after subtracting the frequency at the starting time (initial frequency) and multiplying by conversion factors provided by the manufacturer.

The nonlinear temperature distributions shown in Figures 4.65 to 4.67 cause free nonlinear thermal strains that try to deform the section nonlinearly. However, the actual thermal strain distribution is linear because the section should keep plane after deformation. As a result, equilibrating thermal strains form. These thermal strains are compression along the hotter regions and tension along the colder regions. As shown in Figure 4.71, the strains increased from zero at the starting time to tensile strains during the cooling hours where the vertical temperature gradient was negative. Starting from the first shining hours, the thermal strains changed from tension toward compression as the temperature of the top surface increased. The compression strains increased during the day hours reaching maximum daily values during the midday hours. After which, the thermal strains reversed toward zero strain as the temperature of the top flange decreased. This cycle is repeated for the next 9 days, but with different strain values depending on the temperature gradient distributions of these days compared to the starting time.

During the last 10 days of December, the recorded maximum compression and tensile strains were approximately 110 and 40 micro-strains, respectively. It is worth to remind that these strains are change of strains from the initial strain values.

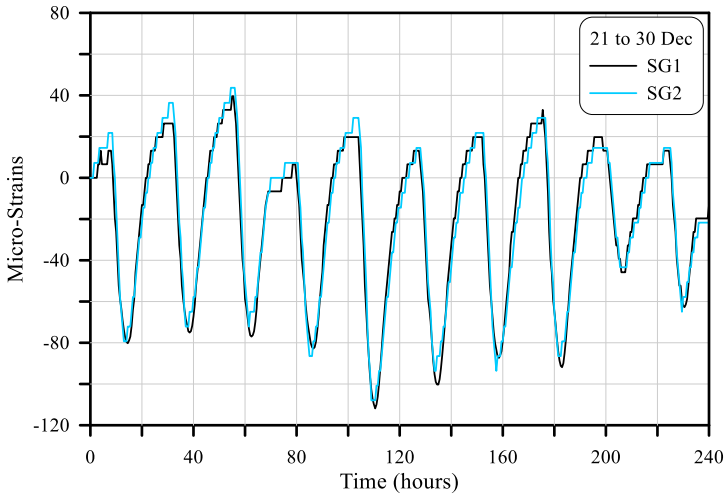

Figure 4.71 Ten days variation of thermal strains from 21 to 30-December-2016 of I-Beam segment.

.

CHAPTER 5

FINITE ELEMENT ANALYSIS OF HEAT TRANSFER

5.1 General

Externally exposed structures, such as bridges, continuously lose and gain heat by three main mechanisms of heat transfer. Conduction to and from the surroundings through the section's thicknesses, convection with the ambient air, and solar radiation and irradiation from the bridge surfaces. Figure 5.1 shows the environmental actions on the bridge. In contrast, the variations of heat produce variations in temperature distribution, in addition, the effects of condition restraints of the bridge structure, all these lead to creating thermal stresses. Therefore, make use of a numerical technique to predict the thermal behavior of bridges gives clear process. Among the different available numerical analysis, two methods, namely, the finite difference and the FE methods [67].

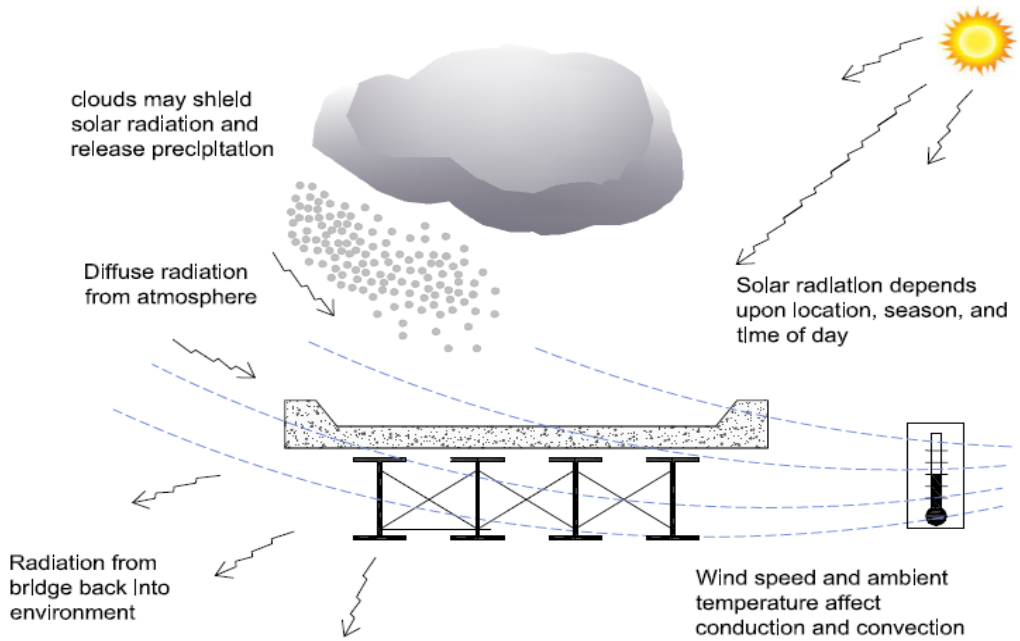

Figure 5.1 Environmental actions on the bridge [67].

Analysis of heat flow in a body is generally a three-dimensional problem. In the bridge with constant cross-section properties over a long length, it can be assumed that the temperature is constant over the bridge length, but varies through the depth and within the thickness of the cross section. However, in composite girder bridges, the temperature varies from one section to another as well as within each cross section of material in both the vertical and horizontal directions. Therefore, a three dimensions analysis is required.

An overview of the formulation of the FE method used to solve the heat flow equation with time and the thermal stresses is presented.

5.2 Basic Equations of Heat Transfer

The basic equations of heat transfer, namely the differential equation of heat flow in three dimensions in a solid presented by Carslaw and Jaeger [68] is:

$$\frac{\partial}{\partial x}\left(k_x \frac{\partial T}{\partial x}\right) + \frac{\partial}{\partial y}\left(k_y \frac{\partial T}{\partial y}\right) + \frac{\partial}{\partial z}\left(k_z \frac{\partial T}{\partial z}\right) = \rho c \frac{\partial T}{\partial t} \quad (5.1)$$

Where: k_x, k_y, k_z are thermal conductivities in x, y and z-direction. Thermal conductivity is a material property, describing the ability to conduct heat, can be defined as "the quantity of heat transmitted through a unit thickness of a material - in a direction normal to a surface of unit area - due to a unit temperature gradient under steady state conditions", the unit of k is W/m℃. T is the temperature at any point (x, y, z) at any time, t, ρ is the density in kg/m^3, c is the specific heat capacity in J/kg℃.

In 1980, Dilger and Ghali [69] added the term Q for the heat generated inside the body. So Eq. 5.1 becomes:

$$\frac{\partial}{\partial x}\left(k_x \frac{\partial T}{\partial x}\right) + \frac{\partial}{\partial y}\left(k_y \frac{\partial T}{\partial y}\right) + \frac{\partial}{\partial z}\left(k_z \frac{\partial T}{\partial z}\right) + Q = \rho c \frac{\partial T}{\partial t} \quad (5.2)$$

Where, Q is the amount of heat per unit volume generated inside the concrete by cement hydration (W/m^3). So Q considered only during the early age of concrete and equal to zero on the other stage.

For a bridge, it is a common assumption that the temperature along the length is constant. This lead to simplified equation 5.1 and 5.2 to:

$$\frac{\partial}{\partial x}\left(k_x \frac{\partial T}{\partial x}\right) + \frac{\partial}{\partial y}\left(k_y \frac{\partial T}{\partial y}\right) = \rho c \frac{\partial T}{\partial t} \quad (5.3)$$

$$\frac{\partial}{\partial x}\left(k_x \frac{\partial T}{\partial x}\right) + \frac{\partial}{\partial y}\left(k_y \frac{\partial T}{\partial y}\right) + Q = \rho c \frac{\partial T}{\partial t} \quad (5.4)$$

5.2.1 Boundary conditions

The boundary equations associated with heat flow equation can be expressed in the following form [49]:

$$k_x \frac{\partial T}{\partial x} l_x + k_y \frac{\partial T}{\partial y} l_y + k_z \frac{\partial T}{\partial z} l_z + q = 0 \quad (5.5)$$

Where: l_x, l_y, l_z are the directions cosines of the unit out-word normal to the boundary surface. q is the boundary heat input or loss per unit area in W/m^2. For isotropic, homogeneous and temperature-independent materials $k_x = k_y = k_z = k$ = constant, then Eq. (5.2) can be written as:

$$k\left(\frac{\partial^2 T}{\partial x^2} + \frac{\partial^2 T}{\partial y^2} + \frac{\partial^2 T}{\partial z^2}\right) + Q = \rho c \frac{\partial T}{\partial t} \quad (5.6)$$

And Eq. (5.5) can be written as:

$$k\left(\frac{\partial T}{\partial x} l_x + \frac{\partial T}{\partial y} l_y + \frac{\partial T}{\partial z} l_z\right) + q = 0 \quad (5.7)$$

The value of q is the sum of three basic components of heat transfer mechanisms: heat convection q_c between the girder and the environment, heat irradiation q_r to the surrounding environment, and solar radiation q_s from the sun [68, 69]. This sum varies with time and the position considered on the boundary surface *s* and is given as [49]:

$$q = q_c + q_s + q_r \quad (5.8)$$

5.2.1.1 Convection (q_c)

The movement of air over the girder surface and the differences between the temperature of the bridge surface and the ambient air lead to heat transfer by convection q_c which can be calculated by the following expression [70]:

$$q_c = h_c(T_s - T_\alpha) \quad (5.9)$$

Where: T_s is the temperature of the girder surface, T_α is the ambient air temperatures, that is dependent on position and time t. h_c is the convection coefficient of heat transfer W/m^2 K, which is a function of wind speed, surface roughness and the geometric configuration of the structure. It can be calculated by using the empirical equations in ASHRAE 2005 [71]:

$$h_c = 5.6 + 4.0v \quad \text{for } v \leq 5 \text{ m/s} \tag{5.10}$$

$$h_c = 7.2v^{0.78} \quad \text{for } v > 5\ m/s \tag{5.11}$$

Where v is wind speed and 5.6 W/m^2 K for average surface roughness without the effects of wind.

5.2.1.2 Solar radiation (q_s)

The heat gain due to solar radiation received by an exposed surface can be expressed as:

$$q_s = \alpha I_s \tag{5.12}$$

Where: α is the absorption coefficient of the surface which depends on the nature of the surface. I_s is the total solar radiation incident normal to the surface of the girder at time t. The total solar radiation, I_s, striking a surface consists of three components: beam radiation I_b, diffuse radiation I_d, and reflected solar radiation I_r.

$$I_s = I_b + I_d + I_r \tag{5.13}$$

Where I_b refers to the solar radiation originates from the direct beam, intense, and parallel sun's rays striking the horizontal surface. While I_d is derived from the scattering of the beam component by dust, fog, clouds, smoke, and other particles suspended in the atmosphere [72]. Finally, I_r refers to reflected solar radiation on the surface due to other surrounding surfaces. Hence, it depends on the reflective properties of the surrounding surfaces and the total radiation striking the horizontal plane.

Generally, most weather stations report only solar radiation incident on a horizontal plane. So, the calculation of solar radiation incident on a tilted surface of the girder is required. According to orientation, location and the geometry of the girder, solar radiation on an inclined surface calculated by using the following equations [73]:

$$I_{sn} = I_{bn} + I_{dn} + I_r \quad (5.14)$$

$$I_{bn} = I_b \left(\frac{\cos\theta}{\cos\theta_z}\right) \quad (5.15)$$

$$I_{dn} = I_d \left(\frac{1+\cos\delta}{2}\right) \quad (5.16)$$

$$I_r = r_g (I_b + I_d) \left(\frac{1-\cos\delta}{2}\right) \quad (5.17)$$

So Eq. (5.13) becomes:

$$I_{sn} = I_b \left(\frac{\cos\theta}{\cos\theta_z}\right) + I_d \left(\frac{1+\cos\delta}{2}\right) + r_g (I_b + I_d) \left(\frac{1-\cos\delta}{2}\right) \quad (5.18)$$

Where I_b, I_d on the horizontal surface, I_{bn}, I_{dn} on a tilted surface, θ_z and θ zenith and incident angle respectively, δ is the tilted angle between the surface and the horizontal plane, and r_g ground reflectivity value of the surrounding surface normally equal to 0.2 for the surface without snow.

5.2.1.3 Irradiation (q_r)

q_r is the heat transfer from the heated surface to the surrounding atmosphere by long wave radiation. Irradiation heat transfer can be expressed as [74]:

$$q_r = \varepsilon C_s (T_s^4 - T_\alpha^4) \quad (5.19)$$

Where: C_s is the Stefan-Boltzmann constant = $5.67\times10^{-8}\ W/m^2\ K^4$ and ε is the emissivity coefficient of the surface. While T_s and T_α the temperature at the surface of the girder, and ambient air temperature respectively.

Diurnal ambient air temperature $T_\alpha(t)$ variation follows a sinusoidal daily cycle between the minimum T_{min} and maximum T_{max} temperatures [75]:

$$T_\alpha(t) = \frac{1}{2}(T_{min} + T_{max}) + \frac{1}{2}(T_{min} - T_{max}).\sin[(t-9)\frac{\pi}{12}] \quad (5.20)$$

On the other hand, many researchers pointed to the importance of determined the shadow depth, which depends on the time and the inclined angle of the surface. Which has a significant impact on the solar radiation [74-76]. In 2012, Lee [77] accounted in the calculation of solar radiation, the effect of the shadow casts on the web and bottom flange of the girder by the top flange as shown in Figure 5.2. The

shadow depth on the web d and the shadow extends along the inclined bottom flange of the girder d_T obtained to the following equation [78]:

$$d = w_{top} \frac{\tan \alpha_s}{\cos(\gamma_s - \gamma)} \tag{5.21}$$

$$d_T = \frac{(d - h_{web})/ w_{bot}}{\cos \beta_T} \tag{5.22}$$

Where: w_{top} is the width of the top flange overhang, $\alpha_s$is the solar altitude angle, γ_s refer to the solar azimuth angle, and γ is the surface azimuth angle. h_{web} denotes to the depth of the web, w_{bot} is the width of the bottom flange from the web, and β_T is the inclined angle of the bottom flange. Figure 5.2 shows all these details.

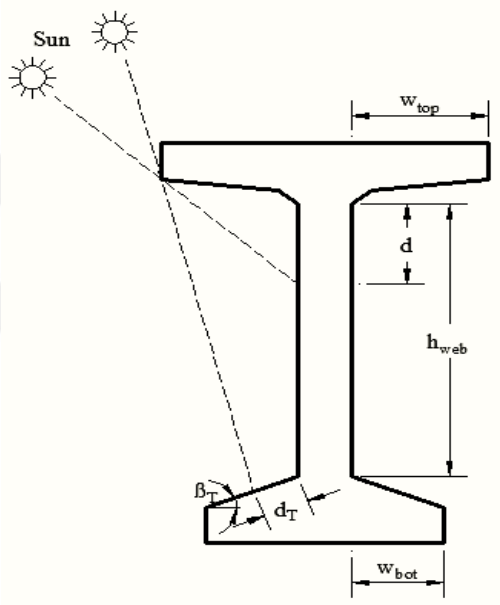

Figure 5.2 Shadow cast on the web and the bottom flange [78].

5.3 Thermal Stresses

In general, many researchers revealed by experimental works for significant influence of thermal stresses on bridge structures [28, 49, 69, 77]. These stresses are induced by variations in the uniform temperature and the thermal gradients across the section of the bridge. Therefore, several methods of analysis are used according to certified codes to study the effect of temperature changes on bridge superstructures. In this study, the composite I-steel girders are examined a section along the straight span in the y-axis is constant as shown in Figure 5.3. Thus, the temperature difference T (x, z) is a function of the (x) and (z) directions only.

Consequently, there are two types of thermal stress variation. Thermal stress varying along the longitudinal direction (z), and thermal stress that varies along the transverse direction (x). Types of thermal stresses and available methods of analysis are given in the following sections.

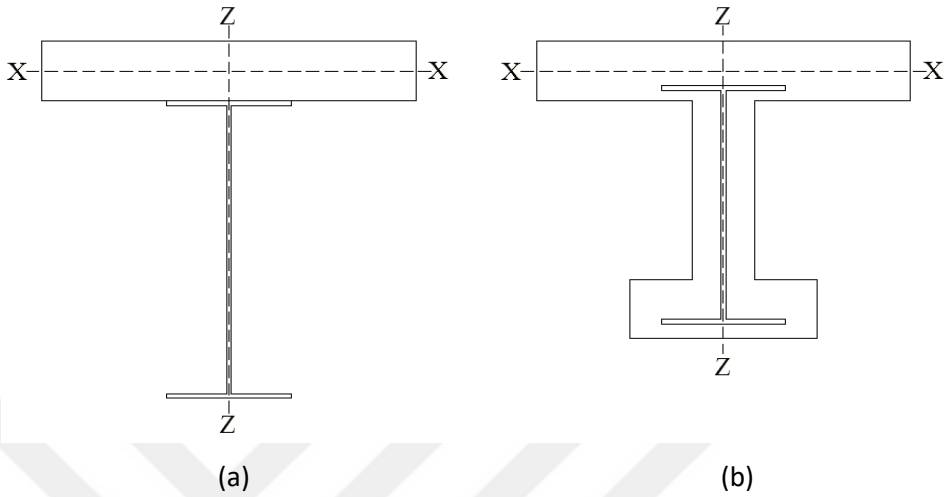

Figure 5.3 Composite concrete-steel girders: (a) T-Beam and (b) I-Beam

5.3.1 Longitudinal stresses

Longitudinal stresses are the thermal stresses that vary along the vertical axis, (z). If the structure is statically determinate and the temperature distribution is uniform or linear, no stresses are developed. But if the shapes are nonlinear over the cross section, then thermal stresses occur in both statically determinate and indeterminate structures. In the longitudinal direction, there are two types of thermal stresses, self-equilibrating and continuity stresses [79].

5.3.1.1 Self-equilibrating stresses

Self-equilibrating stresses are stresses produced from the nonlinear variation of temperature over the cross-section of the bridge superstructure. This variation tries to deform the subsequent fibers of the section of the superstructure. The deformation is proportional to the distance of each fiber from the centroid. If the section is allowed to deform freely, then the strain is termed as “free strain”, which equals the product of the temperature difference by the coefficient of thermal expansion (αT). In general, if the variation of temperature is linear, the free strain will be linear and deformations will occur in the cross section without creating stress. On the other

hand, if the variation of temperature is nonlinear, then strained fibers of the cross-section try to nonlinearly lie out of their plane section. As a result, the self-equilibrating stresses are produced to restore the deformed shape to extend in one plane (assure linear deformation). According to the Navier-Bernoulli hypothesis, that plane sections perpendicularly to the neutral axis before deformation stay plane and perpendicular to the neutral axis after deformation [80-82].

Thus, it is obvious that the self-equilibrating stresses (eigenstresses) exist if the temperature variations (gradient) nonlinear along the cross section, despite the support condition. This type of stresses can be determined by several techniques.

5.3.1.2 Continuity stresses

Continuity stresses are stresses induced in a multi-span statically indeterminate bridge. Generally, the variation in temperature over the cross-section induces support reactions and internal force in the girders. Hence, these forces lead to continuity stresses as deformations resulting from the change of temperature are restrained by the intermediate supports. To calculate the continuity stresses, there are many methods can be applied to analyses the structure depending on the degree of freedom.

The longitudinal stresses are the resultants of continuity stresses and the self-equilibrating stresses.

5.3.2 Transverse stresses

Transverse stresses are the thermal stresses that act along the transverse direction. In 1985, Imbson et al. [76] found that transverse thermal stresses can be as significant effect as those acts vertically along the depth of the section. Transverse stresses occur in sections like box-girders where temperature varies laterally along the top and bottom slabs and across the webs in addition to the vertical temperature variation [83, 84].

5.4 The AASHTO Specifications

As mentioned in the literature review, there are many codes deal with the effect of temperature, one of these codes is AASHTO LRFD [59]. In this section, an overview

of the temperature actions, provisions of AASHTO LRFD is introduced. The AASHTO [60] specification is one of the commonly used codes that take into account the effect of temperature changes in bridge structures. The included thermal effects are two-fold. The first is the change of the overall mean temperature of the superstructure of the bridge from time to another. The second thermal action is the existence of temperature gradient along the vertical depth of the superstructure and the consequent stresses.

5.4.1 AASHTO LRFD Design Methods for Uniform Temperature

AASHTO LRFD [29] introduces two design procedures for calculating thermal movement associated with uniform temperature, procedure A and procedure B. For concrete bridges with concrete or steel girders, these two procedures can be used. On the other hand, procedure A employed for all other bridge types and the code described it as the historic method.

Procedure A in AASHTO LRFD [29] specification is similar to that recommended in the AASHTO Standard Specification of Highway Bridges (2007) [59]. In this procedure, the climate of the USA is classified into two categories; moderate and cold climates, according to a number of freezing days as shown in Table 5.1 (AASHTO Table 3.12.2.1-1). If the number of freezing days is less than 14, the climate is considered as moderate, otherwise, the climate is considered as cold. Where freezing days can be considered when the average temperature is less than 0 ℃.

The minimum and maximum temperatures are given in Table 5.1 represent the minimum and maximum design temperatures. In this procedure the change in temperature the difference between the lower or the upper bound temperature from Table 5.1 and the temperature at which the bridge was constructed.

Table 5.1 Procedure (A) temperature ranges.

Climate	Steel or aluminum	Concrete	Wood
Moderate ℃	-18 to 50	-12 to 27	-12 to 24
Cold ℃	-35 to 50	-18 to 27	-18 to 24

On the other hand, procedure B uses the thermal contour maps of the United States for an average history of 70 years (with a minimum of 60 years) of data to determine the maximum and minimum design temperatures. AASTHO LRFD [29] gives several maps for concrete girder bridges with concrete decks and for steel girder bridges with concrete decks. The difference between the maximum design temperature and the minimum design temperature is multiplied by the coefficient of thermal expansion to obtain the thermal strain. The thermal strain is multiplied by the length to estimate the thermal movement as shown in the equation below.

$$\Delta_T = \alpha L\left(T_{MaxDesign} - T_{MinDesign}\right) \tag{5.23}$$

Where L is length (mm) and α is the coefficient of thermal expansion (mm/mm °C).

5.4.2 AASHTO LRFD Temperature Gradient

AASHTO LRFD discusses the effect of the temperature gradient on the depth of the superstructure of the bridge in section 4.6.6 [29]. As illustrated in Figure 5.4, there are three effects of the vertical temperature gradient: axial expansion, flexural deformation, and internal stress (self-equilibrating stresses).

Figure 5.4 shows three components of temperatures that compose the free temperature distribution. Where, T_m represents the uniform mean component, which reflects the expansion of the neutral axis of the member. ΔT refers to the linear gradient, which causes the curvature of the member. Finally, T_o is the nonlinear gradient that is related to the self-equilibrating stresses (eigenstresses).

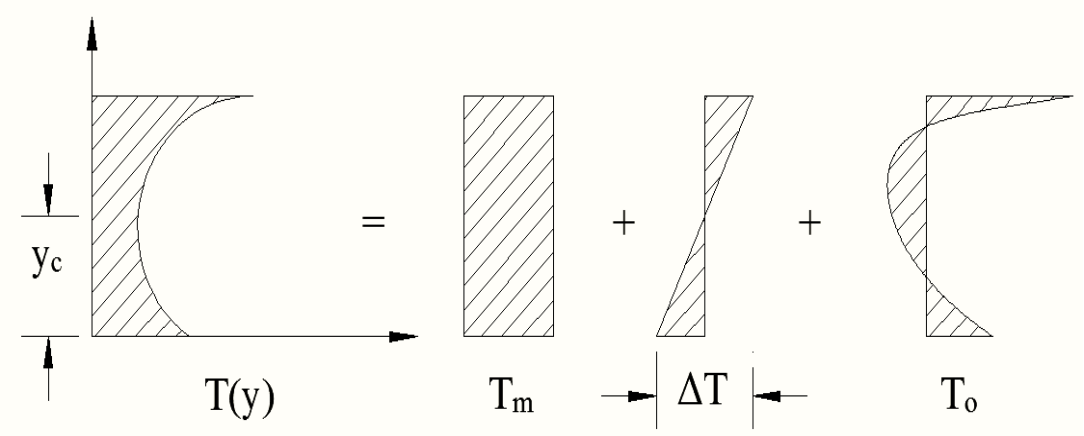

Figure 5.4 Components of the general nonlinear temperature gradient.

The three components can be extracted by the following three equations respectively:

$$T_m = \frac{1}{A} \int T \, dA \tag{5.24}$$

$$\Delta T = \frac{h}{I} \int T \, (y - y_c) \, dA \tag{5.25}$$

$$T_\circ = T - T_m - \frac{y}{h} \Delta T \tag{5.26}$$

Where A is the area, I refers to the moment of inertia, h denotes to the height of the cross-section, and y_c refers to the centroid location.

The actions that are produced by the three temperatures mentioned above are as follows, respectively.

$$\epsilon = \alpha \, T_m \tag{5.27}$$

$$\varphi = \alpha \frac{\Delta T}{h} \tag{5.28}$$

$$\sigma_\circ = E \, \alpha \, T_\circ \tag{5.29}$$

Where α is the coefficient of thermal expansion, and E refers to the modulus of elasticity.

These responses from equations (5.27) to (5.29) can be rearranged as follows for the composite steel girder section with concrete slab:

$$\epsilon = \frac{1}{A} \int \alpha \, T \, dA \tag{5.30}$$

$$\varphi = \frac{1}{I} \int \alpha \, T \, (y - y_c) dA \tag{5.31}$$

$$\sigma_\circ = E \, [\alpha \, T - \epsilon - \varphi \, (y - y_c)] \tag{5.32}$$

Where A and I are transformed by the modular ratio as α have different value at the interface between the steel and concrete.

5.5 The Finite Element Modeling Using COMSOL

In this study, the COMSOL Finite Element program [28] adopted to accomplish the analysis of the thermal transfer on the composite concrete-steel girder bridge segments. COMSOL includes two expressions of radiation interface. Surface-to-ambient radiation, and surface-to-surface radiation, which was used in this study to

deal with the heat transfer equation illustrated in section 5.2 with applied the boundary condition, and the structural boundary conditions discussed in section 5.3.

5.5.1 Element Type

All element types in COMSOL program were used to accomplish the meshing process which includes tetrahedral, triangular, edge and vertex element in both the concrete and the steel part. Where, the tetrahedral element used to mesh the volume of composite concrete girder for heat conduction. The triangular elements were appropriate to mesh boundary surface.

5.5.2 Mesh Size

Before computing the heat transfer analysis for the models, meshing process achieved by using fine size to more accurate results. Figures 5.5 and 5.6 show the T-Beam and I-Beam meshed segments. The 0.04354 m^3 volume of T-Beam segment is meshed by using more than 31000 elements, while for 0.07 m^3 volume of I-Beam is segment meshed by more than 78000 elements. Figures 5.7 and 5.8 show the mesh quality where the average mesh quality was 0.7 for the two segments which reflect a high quality of the mesh. Also, the figures show that almost the element quality exceeds 0.9.

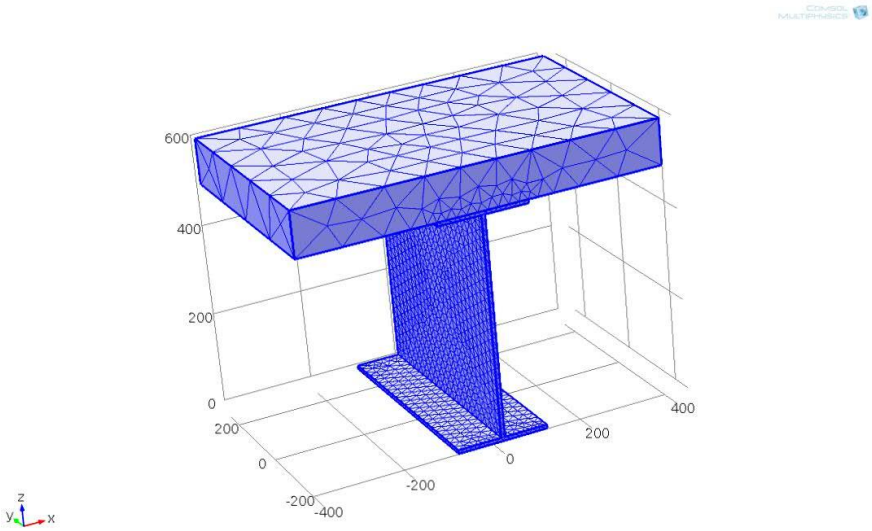

Figure 5.5 The mesh of the T-Beam segment.

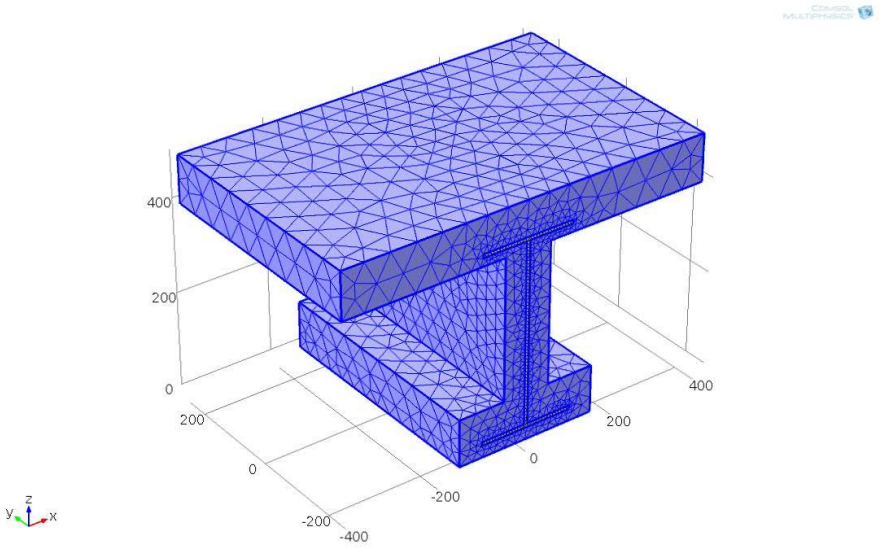

Figure 5.6 The mesh of the I-Beam segment.

5.5.3 Material thermal properties

The same material properties used in the heat transfer analysis for the two segments. A homogeneous, isotropic, and independent of time material are assumed in heat transfer process.

1. The material properties of the concrete:

- Concrete density $\rho = 2400\ kg/m^3$.
- Thermal conductivity $k = 1.5\ W/(m\ K)$.
- Specific heat capacity $c = 900\ J/(kg\ K)$.

2. The material properties of the steel:

- Steel density $\rho = 7850\ kg/m^3$.
- Thermal conductivity $k = 44.5\ W/(m\ K)$.
- Specific heat capacity.$c = 475\ J/(kg\ K)$.

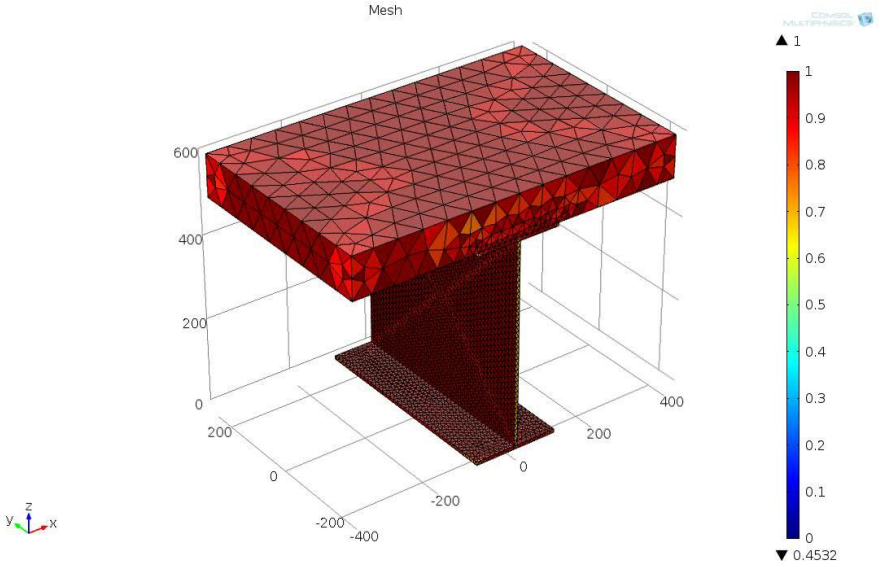

Figure 5.7 The quality of mesh's elements of T-Beam segment.

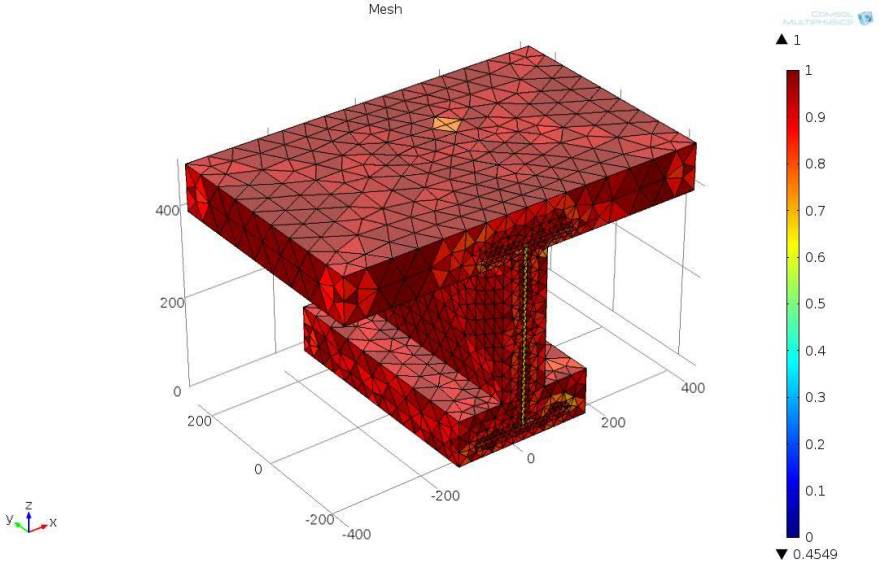

Figure 5.8 The quality of mesh's elements of T-Beam segment.

5.6 Verification of the Finite Element Models

As mentioned previously, COMSOL program is adopted. The verification purposes were achieved for the two segments. The maximum vertical temperature gradients for the three selected days are presented. The temperature variation at each thermocouple during the 24 hours are illustrated in the figures for Frozen, Cold and Sunny day in 2-Janurary-2016, 4-Febreuary-2016 and 18-February-2016 respectively to study the comparison between the recorded temperatures from the experimental

composite concrete bridge girder segments and the predicted temperatures from the FE thermal analysis.

5.6.1 The Temperature Daily Variation at Thermocouple of T-Beam Segment

Figures 5.9 to 5.22 show the daily variation between FE thermal analysis and the recorded experimental temperatures at thermocouples of T-Beam segment during the three selected days. The results of the 14 thermocouples installed in different places of the concrete (TC) and steel (TS) during the three selected days shown in these figures. The location of the thermocouples along the vertical and the horizontal section is shown in Figure 3.20.

The position of the thermocouples in concrete part (TC) is along the vertical and the horizontal section. But, for steel part, there are two thermocouples (TS) located along the vertical section which represented TS1 and TS7. TS2 and TS6 located 180 mm from the centerline of the vertical section on the north side. Also, there were three thermocouples are located 4 mm from the centerline of the vertical section, which are TS3, TS4 and TS5. These details are shown in Figure 3.20.

To examining the results and study the degree of the acceptability between the recorded and the predicted temperatures distributions, so the Average Absolute Error (AAE) and the Maximum Absolute Error (MAE) are calculated.

Where, AAE equals the 24 hours average of the absolute difference between experimental and FE temperatures of each particular thermocouple. MAE is the maximum absolute difference between experimental and FE temperatures of each particular thermocouple during the 24 hours which obtained by used statistical verification tools. AAE can be calculated by:

$$AAE = \frac{\Sigma|X_{FE} - X_{Exp}|}{n} \tag{5.33}$$

Where X_{FE} is the finite element predicted temperature, X_{Exp} is the experimentally recorded temperature of each particular thermocouple at the same time step, and n which is 48 for the day.

Figure 5.9 shows the results of the three selected days at thermocouple TC1. The figure visualises well agreement between the predicted and the recorded

temperatures results. Gaps between the predicted and experimental results accrue at a maximum temperature and the beginning/end of the day during the 24 hours. The AAE recorded for TC1 were 1.18, 1.25 and 1.5 ℃ in frozen, cold and sunny day respectively. While the MAE in corresponding days were 3.42, 3.62 and 4.18 ℃ respectively. For the AAE and MAE, the Frozen day (2-January-2016) recorded the lowest error and the Sunny day (18-February-2016) recorded the highest error. The general behavior of the variation temperatures with time was almost the same for experimental and FE results.

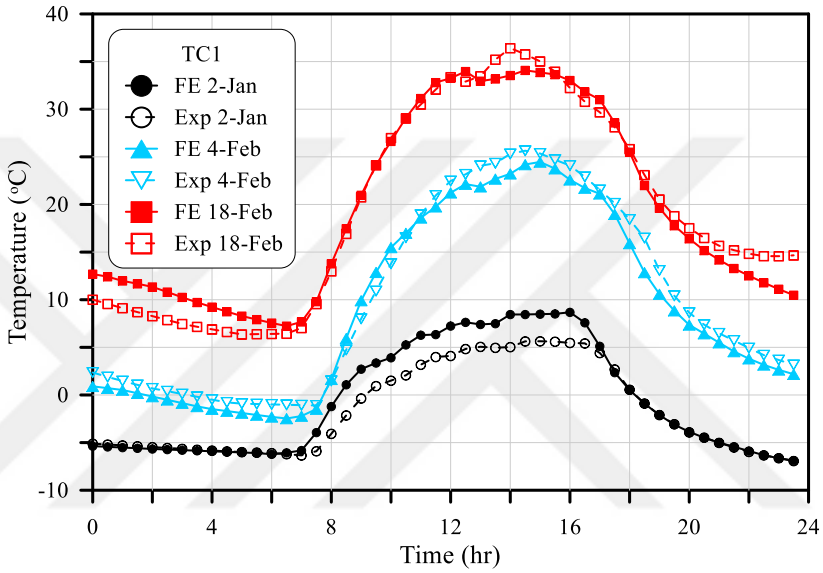

Figure 5.9 Hourly experimentally recorded and FE predicted temperatures at thermocouple TC1 for T-Beam segment.

The results at thermocouple TC2 also gave better agreement as shown in Figure 5.10. The AAE recorded were 0.7, 1.2 and 1.24 ℃ in the three selected days respectively. The MAE in the corresponding days was 1.87, 2.37 and 3.28 ℃ respectively. The lowest error recorded for the AAE and MAE was in the frozen day and the highest error recorded on a sunny day. The results of the two types of errors at thermocouple TC2 were lower than thermocouple TC1.

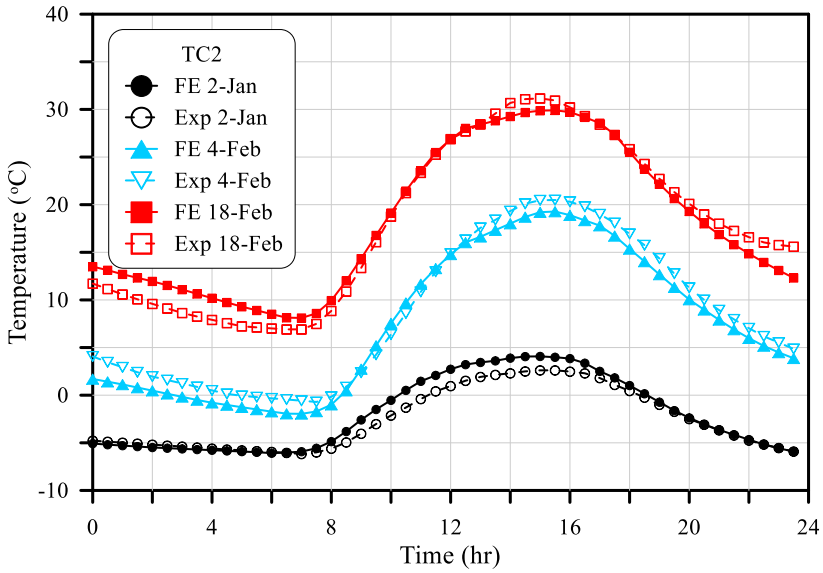

Figure 5.10 Hourly experimentally recorded and FE predicted temperatures at thermocouple TC2 for T-Beam segment.

Figure 5.11 demonstrate the results at thermocouple TC3 which gave a good agreement between the predicted and recorded temperature results. The AAE recorded were 0.76, 1.2 and 1.32 ℃ in the Frozen, Cold and Sunny day respectively. The MAE in the corresponding days was 2.26, 2.0 and 3.62 ℃ respectively. The AAE was lowest in the frozen day while the MAE was in the cold day. The highest errors were recorded on a sunny day. Recorded errors at TC3 were lower than the errors in thermocouple TC1.

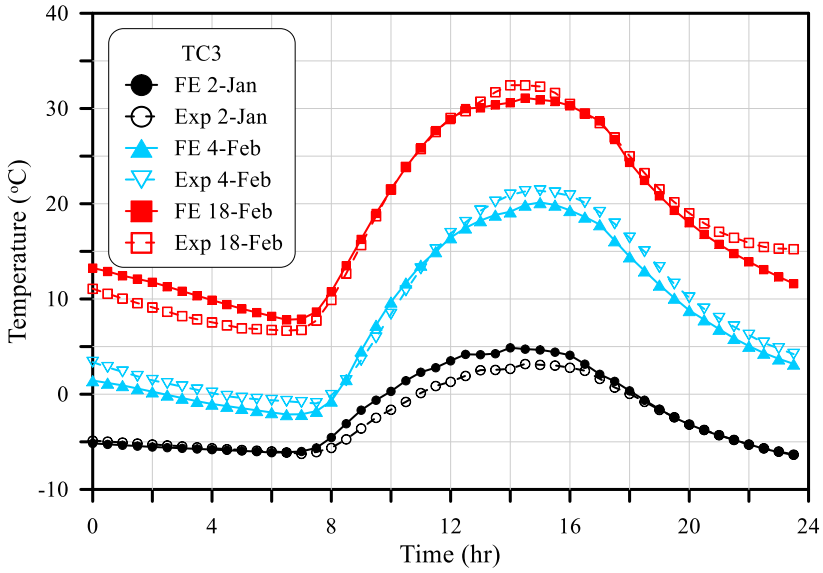

Figure 5.11 Hourly experimentally recorded and FE predicted temperatures at thermocouple TC3 for T-Beam segment.

Graphically, a good agreement of the results at the thermocouple TC4 as shown in Figure 5.12. The AAE recorded were 0.67, 1.16 and 1.26 ℃ in Frozen, Cold and Sunny day respectively. The MAE in corresponding days was 1.77, 2.11 and 3.39 ℃ respectively. As the previous thermocouple, for the AAE and MAE, the frozen day (2-January-2016) recorded the lowest error and the sunny day (18-February-2016) recorded the highest error. The two types of errors in the TC4 are the almost lowest than the TC1 and TC3.

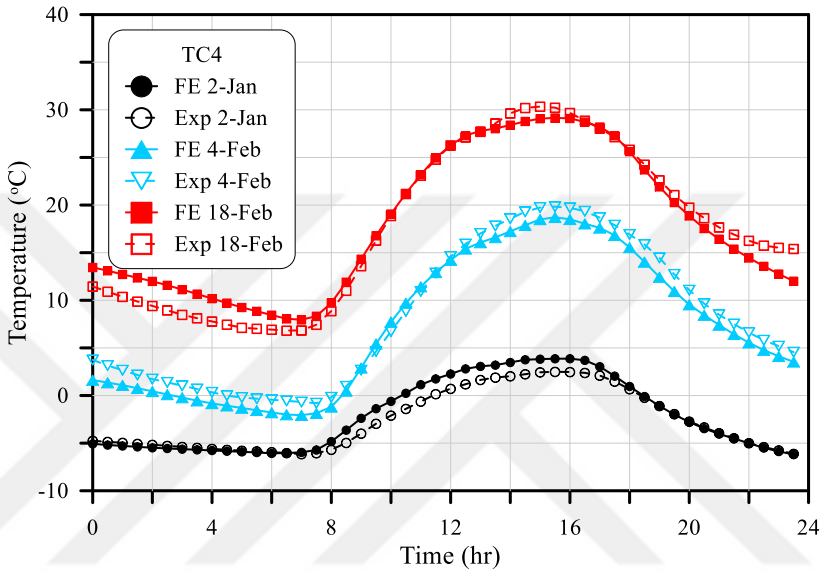

Figure 5.12 Hourly experimentally recorded and FE predicted temperatures at thermocouple TC4 for T-Beam segment.

Figure 5.13 shows the results of the three selected days at thermocouple TC5. The figure reflects a good agreement between the predicted and the recorded temperatures results. The AAE recorded for TC5 were 0.55, 1.08 and 1.34 ℃ in frozen, cold, and sunny day respectively. While the MAE in corresponding days were 1.84, 2.5 and 3.85 ℃ respectively. For the AAE and MAE, the Frozen day (2-January-2016) recorded the lowest error and the Sunny day (18-February-2016) recorded the highest error. Also, the general behavior of the variation temperatures with time was the same for experimental and FE results. Recorded errors at TC5 were almost lower than the errors in thermocouples TC1, TC3 and TC4.

The results at thermocouple TC6 as well gave better agreement as shown in Figure 5.14. The AAE recorded were 0.62, 1.19 and 1.27 ℃ in the tree selected days respectively. The MAE in the corresponding days was 1.78, 2.24 and 3.26 ℃

respectively. The lowest error recorded for the AAE and MAE was in the Frozen day and the highest error recorded on a Sunny day. The results of the two types of errors at thermocouple TC6 were almost lower than thermocouples TC1 and TC3.

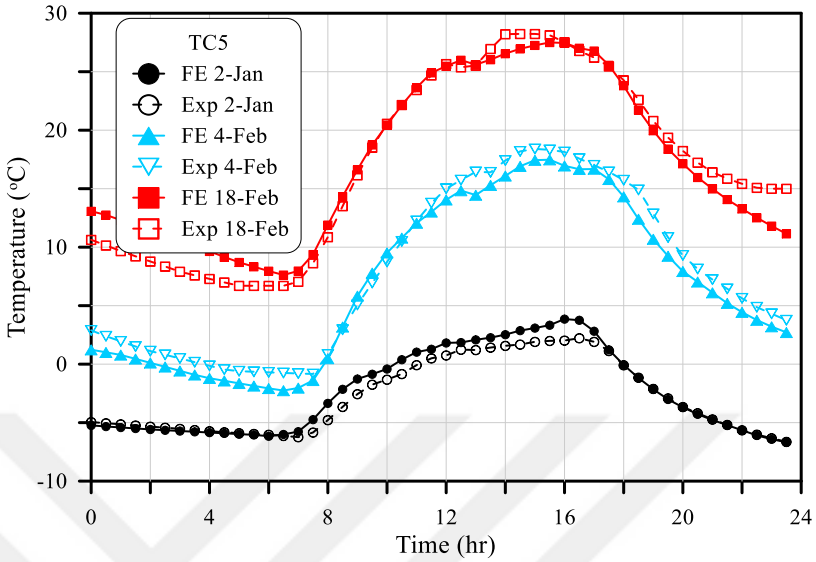

Figure 5.13 Hourly experimentally recorded and FE predicated temperatures at thermocouple TC5 for T-Beam segment.

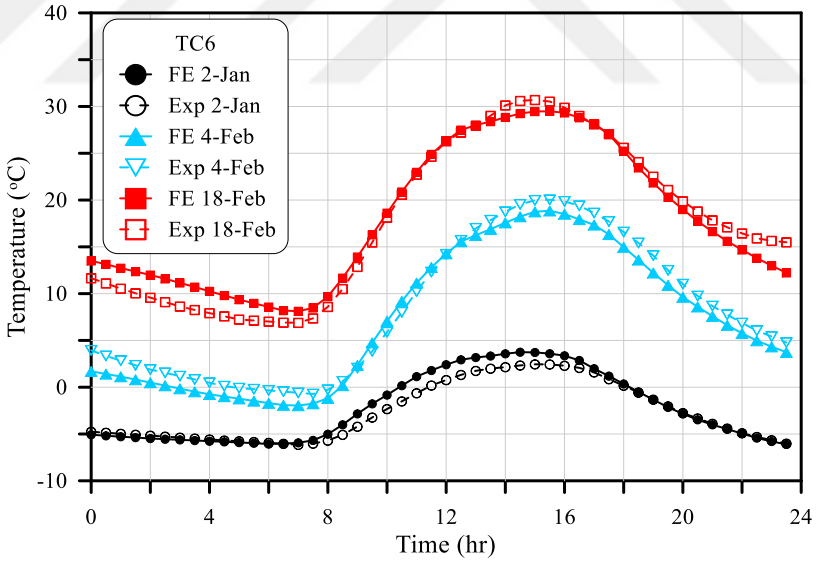

Figure 5.14 Hourly experimentally recorded and FE predicted temperatures at thermocouple TC6 for T-Beam segment.

Figure 5.15 shows the results of the three selected days at thermocouple TC7. The figure gave a better understanding between the predicted and the recorded temperatures results. The AAE recorded for TC7 were 0.42, 1.14 and 1.51 ℃ in Frozen, Cold and Sunny day respectively. While the MAE in corresponding days were 1.29, 2.39 and 4.21 ℃ respectively. For the AAE and MAE, the Frozen day (2-

January-2016) recorded the lowest error and the Sunny day (18-February-2016) recorded the highest error. Also, the general behavior of the variation temperatures with time was the same for experimental and FE results. Errors at TC7 were almost lower than the errors in thermocouple TC1.

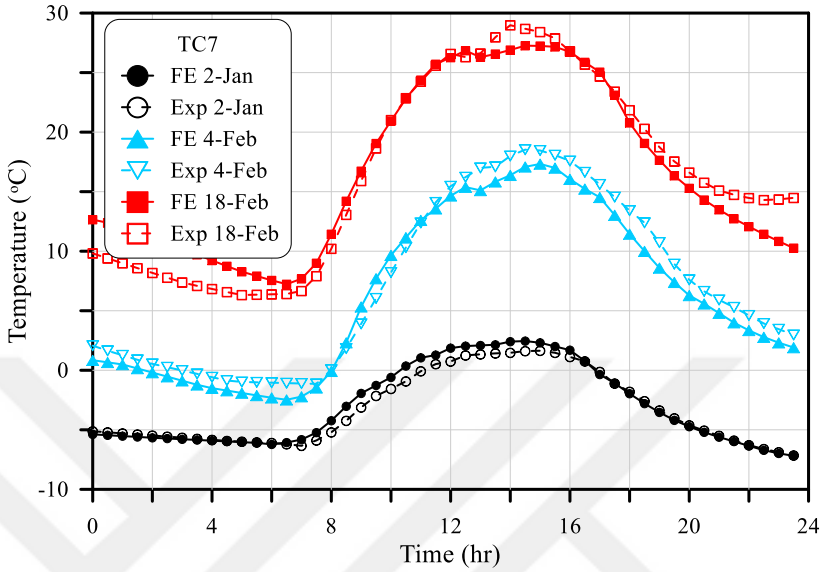

Figure 5.15 Hourly experimentally recorded and FE predicted temperatures at thermocouple TC7 for T-Beam segment.

Figure 5.16 shows the results of the frozen, cold, and sunny day at the thermocouple TS1, which fixed on steel part. The figure reflects a good agreement between the predicted and the recorded temperatures results. The AAE recorded for the TS1 were 0.53, 1.08 and 1.36 ℃ in the three selected days respectively. While, the MAE in corresponding days were 1.93, 2.66 and 3.96 ℃ respectively. As same as, in concrete part, for the AAE and MAE, the Frozen day (2-January-2016) recorded the lowest errors and the Sunny day (18-February-2016) recorded the highest errors. The general behavior of the variation temperatures with time was the same for experimental and FE results. The AAE was almost the same between the TS1 and the TC5. The MAE at the TS1 higher than the TC5.

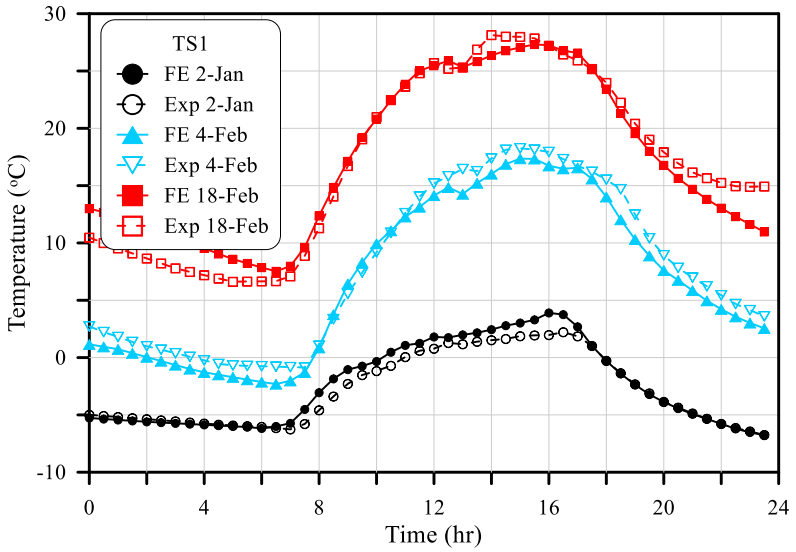

Figure 5.16 Hourly experimentally recorded and FE predicted temperatures at thermocouple TS1 for T-Beam segment.

Figure 5.17 shows the results of the selected days at the thermocouple TS2. The figure gives a better agreement between the predicted and the recorded temperatures results. The AAE recorded were 0.51, 1.09 and 1.33 ℃ in the Frozen, Cold and Sunny days respectively. The MAE in corresponding days was 1.57, 2.21 and 3.79 ℃ respectively. For the AAE and MAE, the Frozen day (2-January-2016) recorded the lowest errors and the Sunny day (18-February-2016) recorded the highest errors. Errors at the TS2 were almost lower than the errors in the thermocouple TS1.

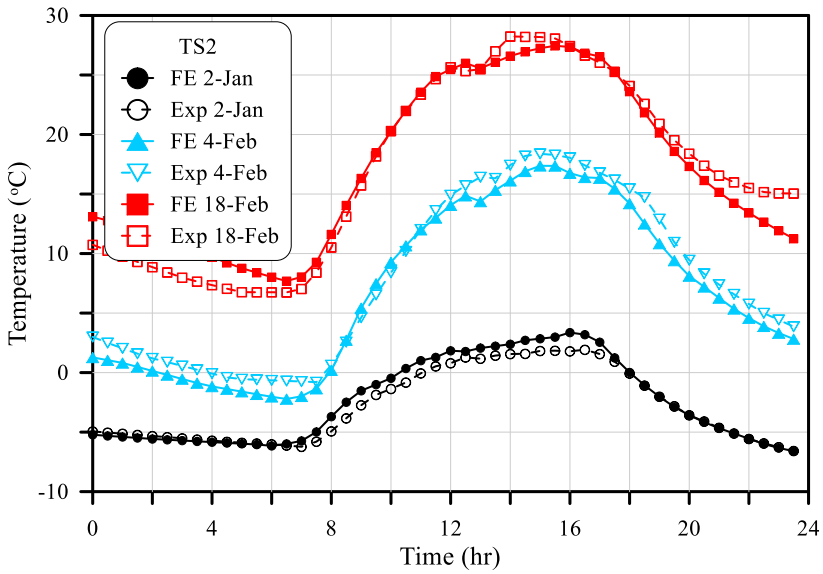

Figure 5.17 Hourly experimentally recorded and FE predicted temperatures at thermocouple TS2 for T-Beam segment.

The results at the thermocouple TS3 also gave a better agreement for the Frozen, Cold and Sunny days as shown in Figure 5.18. The AAE recorded were 0.58, 1.09 and 1.44 ℃ in the tree selected days respectively. The MAE in the corresponding days was 2.51, 3.36 and 4.25 ℃ respectively. As the previous thermocouples, the lowest error recorded for the AAE and MAE was on Frozen day and the highest error recorded on Sunny day. The results of the two types of errors at the thermocouple TS3 were almost higher than the thermocouples TS1 and TS2.

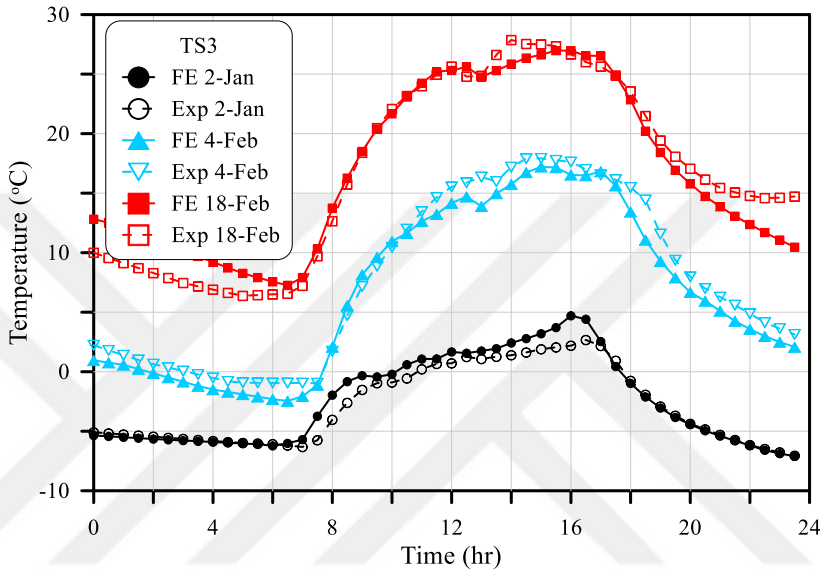

Figure 5.18 Hourly experimentally recorded and FE predicted temperatures at thermocouple TS3 for T-Beam segment.

Figure 5.19 shows the results of the selected days at the thermocouple TS4. The variation in figure almost still in the accepted range between the predicted and the recorded temperatures results. The AAE recorded were 1.07, 1.31, and 1.83 ℃ in the Frozen, Cold and Sunny days respectively. The MAE in corresponding days was 3.75, 5.59 and 5.29 ℃ respectively. For the AAE and MAE values, the Frozen day (2-January-2016) recorded the lowest errors values and the Sunny day (18-February-2016) recorded the highest errors values. Errors at the TS4 recorded a highest than the errors in thermocouples TS1, TS2 and TS3.

The results at the thermocouple TS5, as well, gave accepted range for the selected days as shown in Figure 5.20. The AAE recorded were 1.04, 1.39 and 2.02 ℃ in the Frozen, Cold and Sunny day respectively. The MAE in the corresponding days were 3.3, 5.19 and 5.57 ℃ respectively. The lowest error values recorded for the AAE and

MAE was in the frozen day and the highest error values recorded on a sunny day. The results of the two types of errors at the thermocouple TS5 were almost higher than the thermocouples TS1, TS2 and TS3.

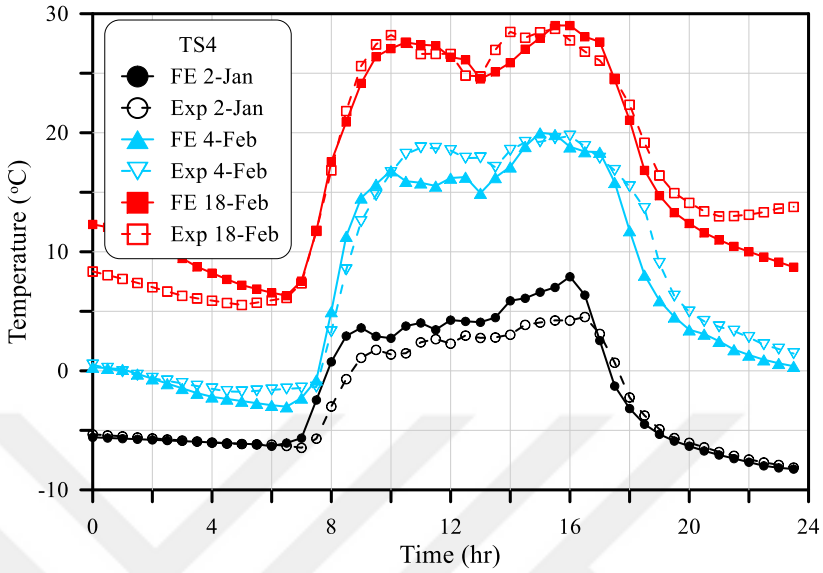

Figure 5.19 Hourly experimentally recorded and FE predicted temperatures at thermocouple TS4 for T-Beam segment.

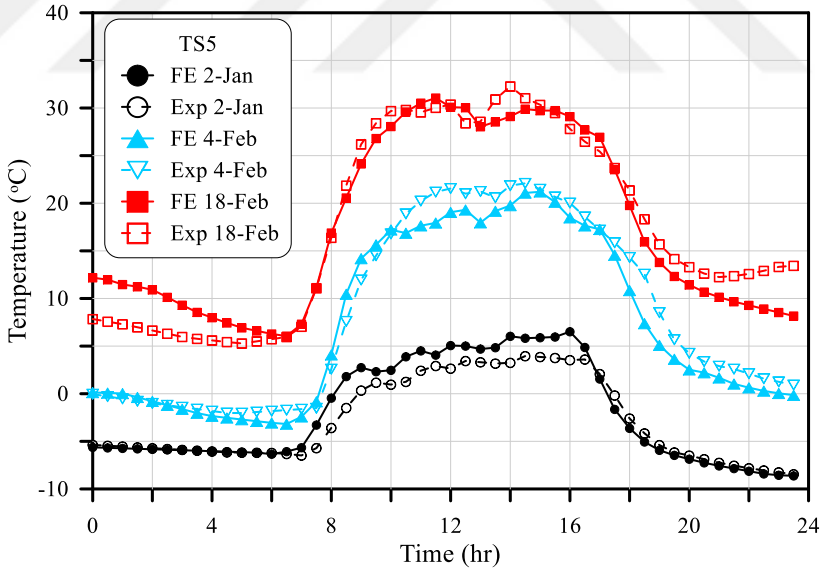

Figure 5.20 Hourly experimentally recorded and FE predicted temperatures at thermocouple TS5 for T-Beam segment.

Figure 5.21 shows the results of the selected days at the thermocouple TS6. The variation in figure almost still in the accepted range between the predicted and the recorded temperatures results. The AAE recorded were 0.75, 1.35 and 2.04 °C in the Frozen, Cold and Sunny days respectively. The MAE in corresponding days was 2.6,

4.6 and 5.61 ℃ respectively. For the AAE and MAE values, the Frozen day (2-January-2016) recorded the lowest errors values and the Sunny day (18-February-2016) recorded the highest errors values. Errors at the TS6 recorded the highest values than the errors in the thermocouples TS1, TS2 and TS3.

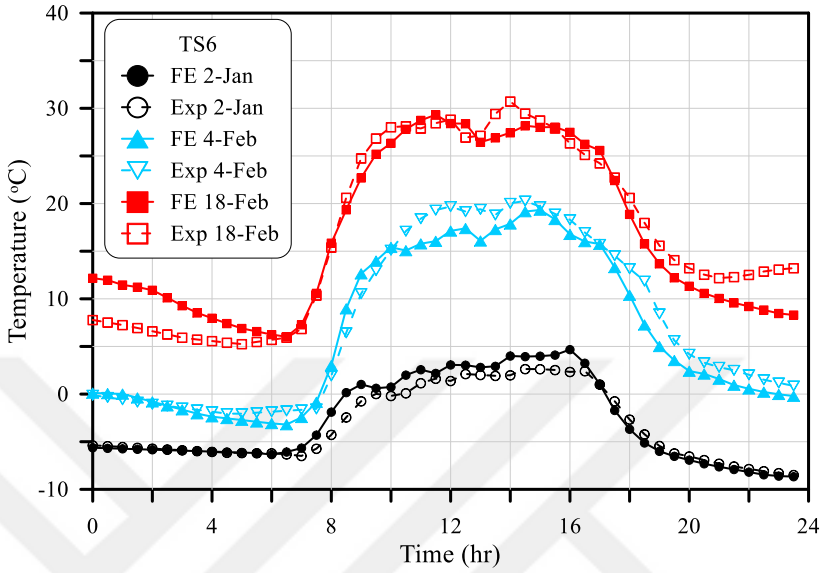

Figure 5.21 Hourly experimentally recorded and FE predicted temperatures at thermocouple TS6 for T-Beam segment.

The results at the thermocouple TS7 gave accepted range between the predicted and recorded results for the selected days as shown in Figure 5.22. The AAE values recorded were 0.92, 1.39 and 2.04 ℃ in the Frozen, Cold and Sunny day respectively. The MAE values in the corresponding days were 3.02, 4.87 and 5.59 ℃ respectively. The lowest error values recorded for the AAE and MAE was in the Frozen day and the highest error values recorded on a Sunny day. The results of the two types of errors at the thermocouple TS7 were almost higher than the thermocouples TS1, TS2, TS3 and TS6.

Table 5.1 shows the difference between the predicted and the recorded results of the selected days in 2-January-2016, 4-February and 18-February for the T-Beam segment. The AAE is ranged from 0.42 to 2.04 ℃, and the MAE ranged from 1.29 to 5.61 ℃. A good agreement and accepted values obtained from the percentage of errors reflect a good simulation and convergence between the FE thermal analysis and the temperature distributions in the experimental composite T-Beam bridge girder segment.

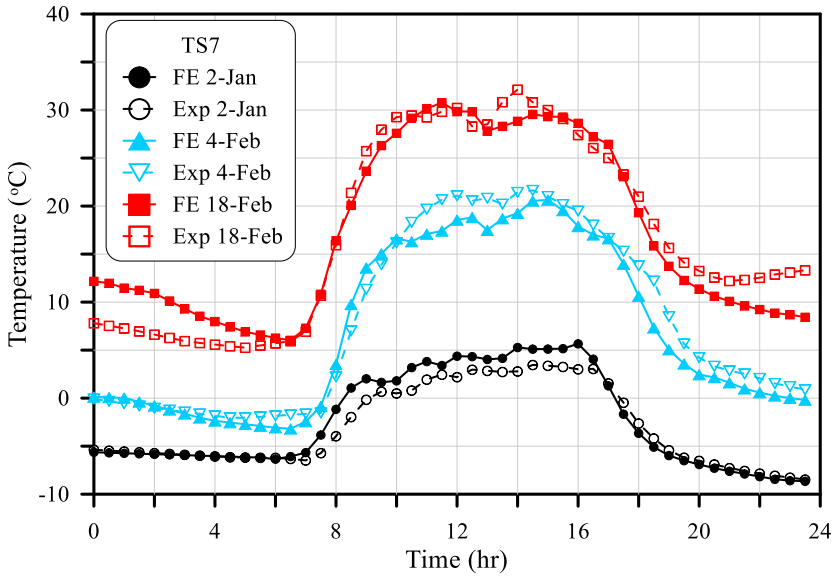

Figure 5.22 Hourly experimentally recorded and FE predicted temperatures at thermocouple TS7 for T-Beam segment.

Table 5.1 Average and maximum absolute errors between experimental and FE temperatures for all thermocouples of the T-Beam segment.

Thermocouple	2-Jan-2016 (Frozen day)		4-Fe-2016 (Cold day)		18-Feb-2016 (Sunny day)	
	AAE	MAE	AAE	MAE	AAE	MAE
TC1	1.18	3.42	1.25	3.62	1.50	4.18
TC2	0.70	1.87	1.20	2.37	1.24	3.28
TC3	0.76	2.26	1.20	2.00	1.32	3.62
TC4	0.67	1.77	1.16	2.11	1.26	3.39
TC5	0.55	1.84	1.08	2.50	1.34	3.85
TC6	0.62	1.78	1.19	2.24	1.27	3.26
TC7	0.42	1.29	1.14	2.39	1.51	4.21
TS1	0.53	1.93	1.08	2.66	1.36	3.96
TS2	0.51	1.57	1.09	2.21	1.33	3.79
TS3	0.58	2.51	1.09	3.36	1.44	4.25
TS4	1.07	3.75	1.31	5.59	1.83	5.29
TS5	1.04	3.30	1.39	5.19	2.02	5.57
TS6	0.75	2.60	1.35	4.60	2.04	5.61
TS7	0.92	3.02	1.39	4.87	2.04	5.59

5.6.2 The Temperature Daily Variation at Thermocouple of I-Beam Segment

Figures 5.23 to 5.37 illustrated the verification of daily variation between the FE thermal analysis and recorded experimental results at thermocouples of the I-Beam segment during the three selected days. As presented in section 3.4.1, the numbers of the thermocouples installed in the segment were 15 thermocouples. 12

thermocouples fixed in concrete part IC, and 3 thermocouples fixed on steel part IS. Figure 3.21 shows the locations of the thermocouples with details.

By the same scenarios studied in the previous section, Figures 5.19 to 5.30 show the results at the IC thermocouples, While, Figures 5.31 to 5.33 show the results at the IS thermocouples. To obtain the convergence between the FE thermal analysis and the recorded experimental results of temperatures distributions, the AAE and the MAE will be studied.

Figures 5.23 to 5.34 show the results of the Frozen, Cold and Sunny days at thermocouples IC. The values of the AAE at the IC4 thermocouple are almost greater than the IC5, the IC6 and the IC7. Also, the IC4 is almost lower than the IC1, the IC2 and the IC3. The AAE in the IC1 is higher than the IC10. Generally, the AAE for the IC thermocouples ranged from 0.3 to 2.1 ℃ at the thermocouples IC7 and IC11 respectively. While the MAE ranged from 0.89 to 5.59 ℃ also at the thermocouples IC7 and IC11 respectively. Table 5.2 reflect a good and accepted agreement for the I-Beam segment and interview a well simulated between the FE analysis and the experimental work at the thermocouple installed in concrete.

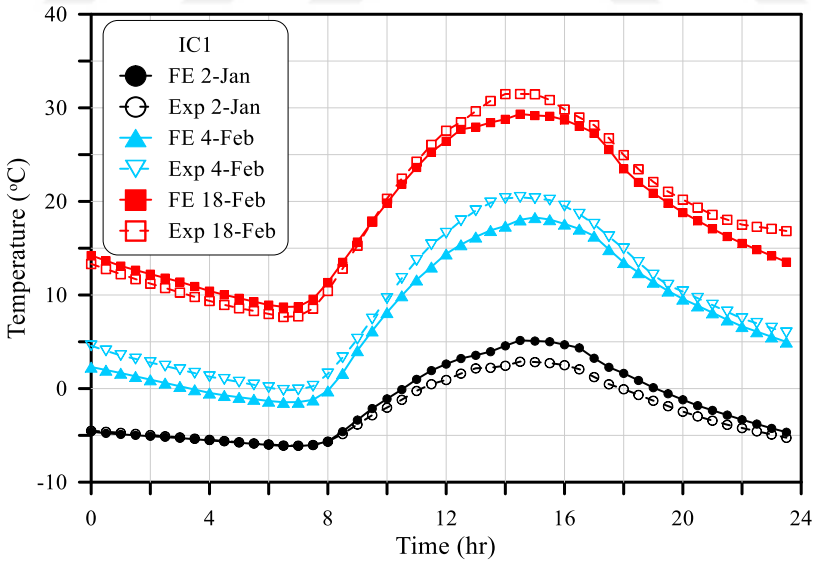

Figure 5.23 Hourly experimentally recorded and FE predicted temperatures at thermocouple IC1 for I-Beam segment.

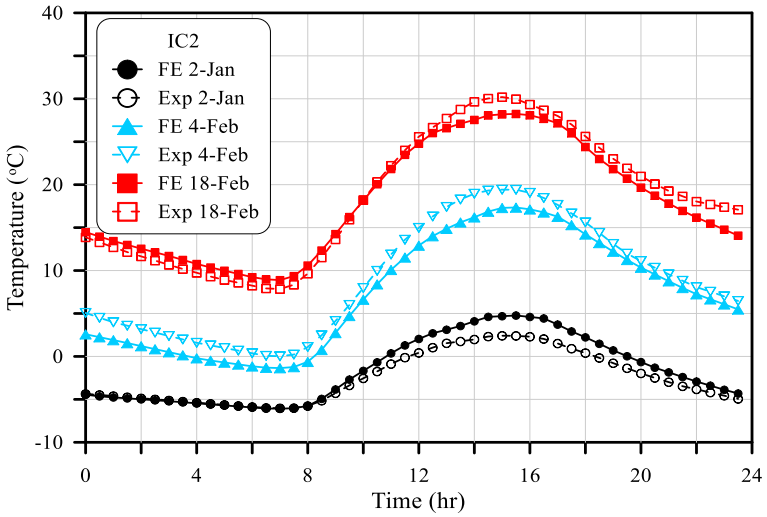

Figure 5.24 Hourly experimentally recorded and FE predicted temperatures at thermocouple IC2 for I-Beam segment.

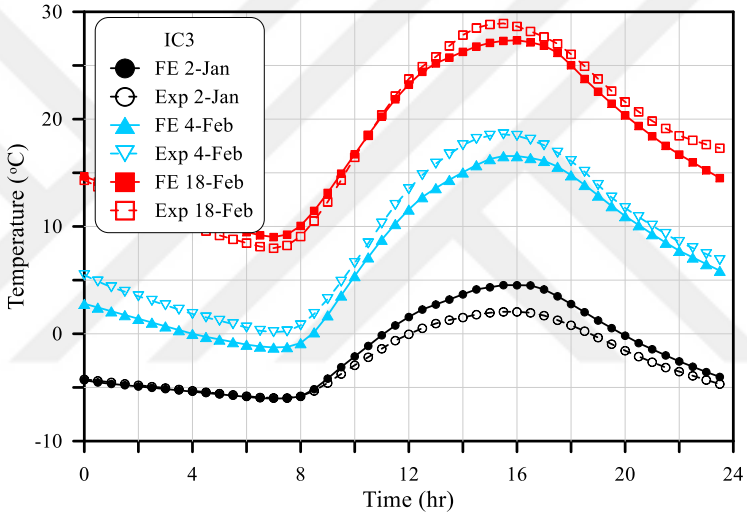

Figure 5.25 Hourly experimentally recorded and FE predicted temperatures at thermocouple IC3 for I-Beam segment.

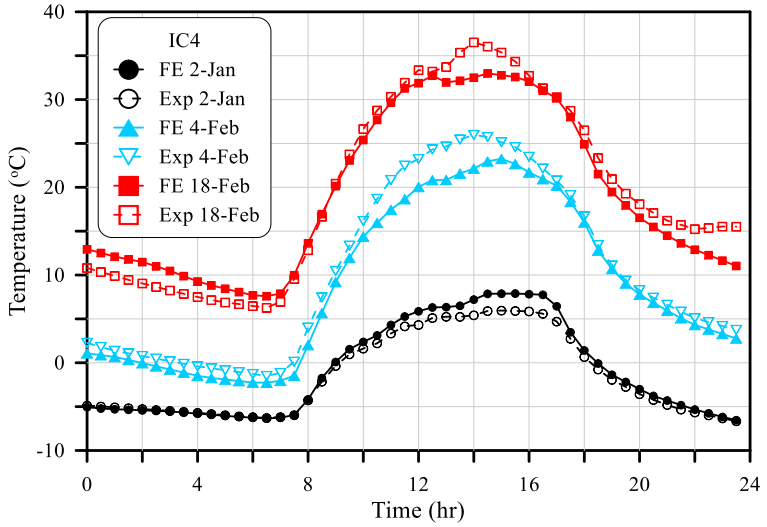

Figure 5.26 Hourly experimentally recorded and FE predicted temperatures at thermocouple IC4 for I-Beam segment.

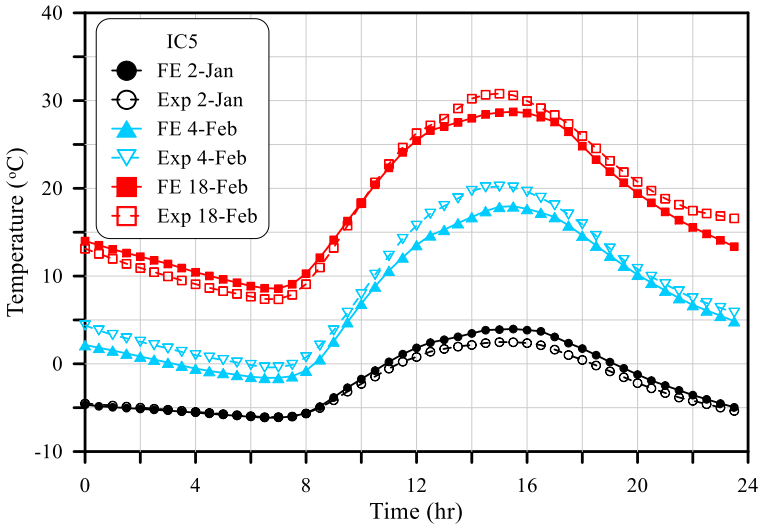

Figure 5.27 Hourly experimentally recorded and FE predicted temperatures at thermocouple IC5 for I-Beam segment.

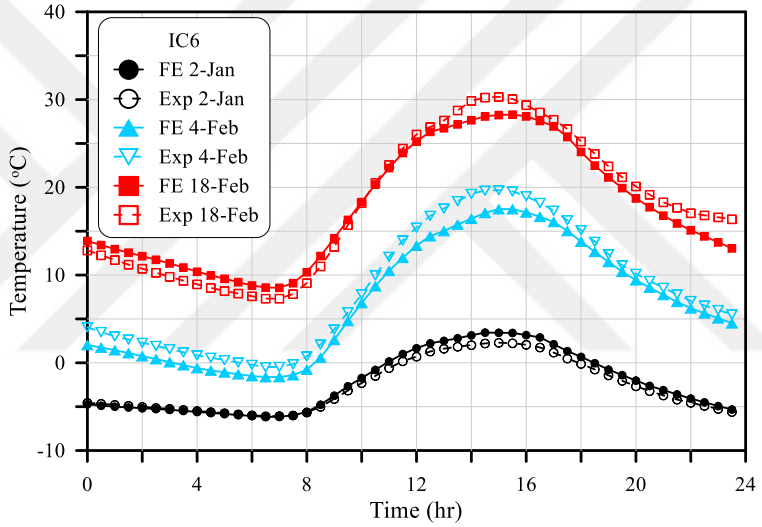

Figure 5.28 Hourly experimentally recorded and FE predicted temperatures at thermocouple IC6 for I-Beam segment.

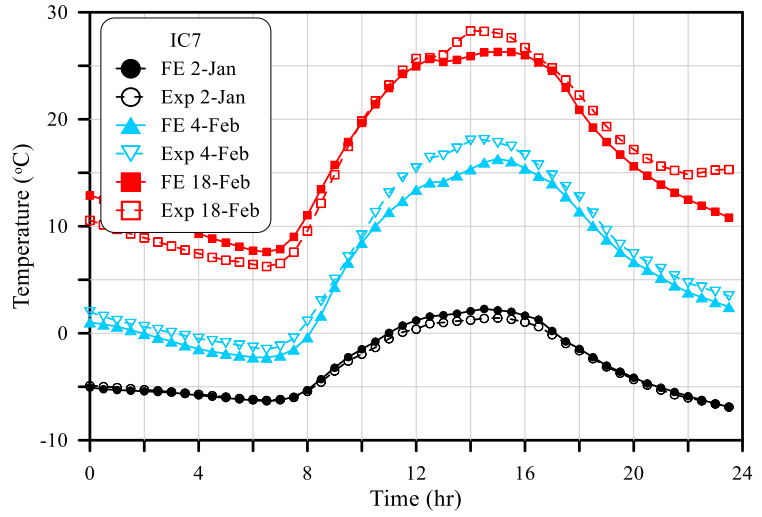

Figure 5.29 Hourly experimentally recorded and FE predicted temperatures at thermocouple IC7 for I-Beam segment.

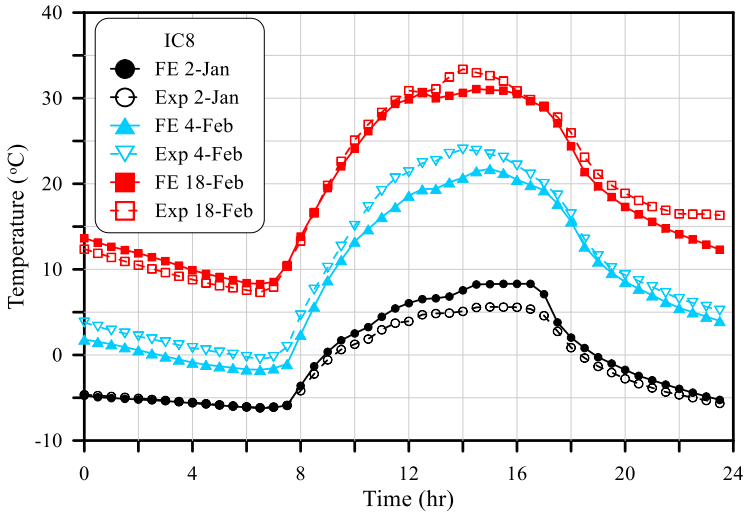

Figure 5.30 Hourly experimentally recorded and FE predicted temperatures at thermocouple IC8 for I-Beam segment.

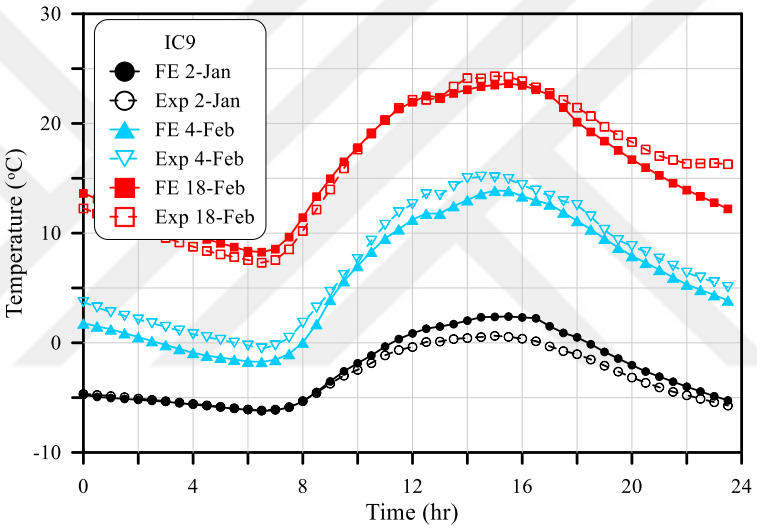

Figure 5.31 Hourly experimentally recorded and FE predicted temperatures at thermocouple IC9 for I-Beam segment.

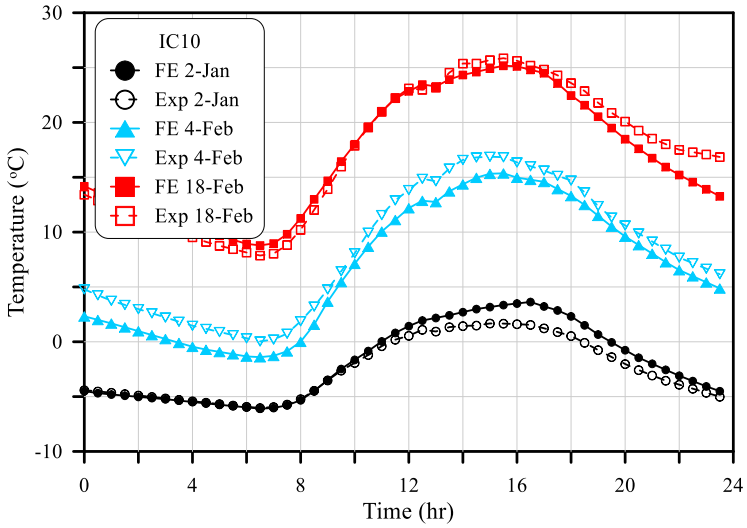

Figure 5.32 Hourly experimentally recorded and FE predicted temperatures at thermocouple IC10 for I-Beam segment.

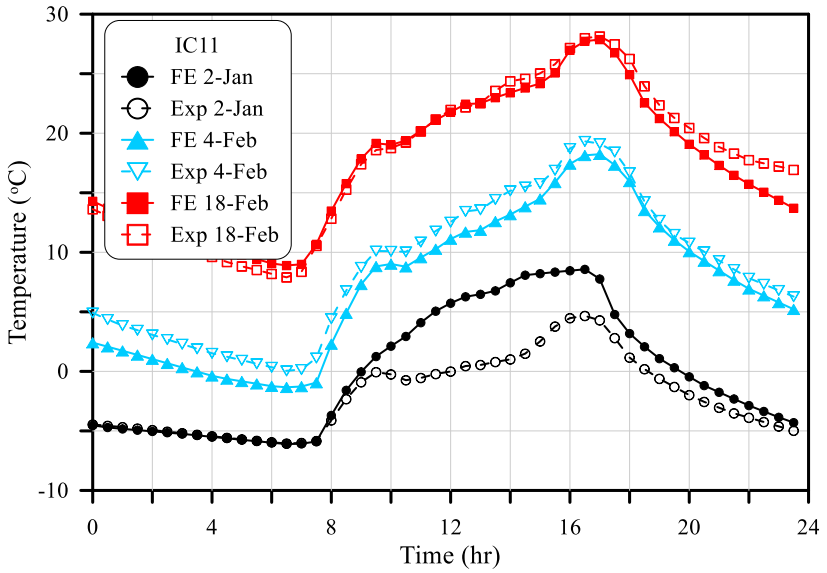

Figure 5.33 Hourly experimentally recorded and FE predicted temperatures at thermocouple IC11 for I-Beam segment.

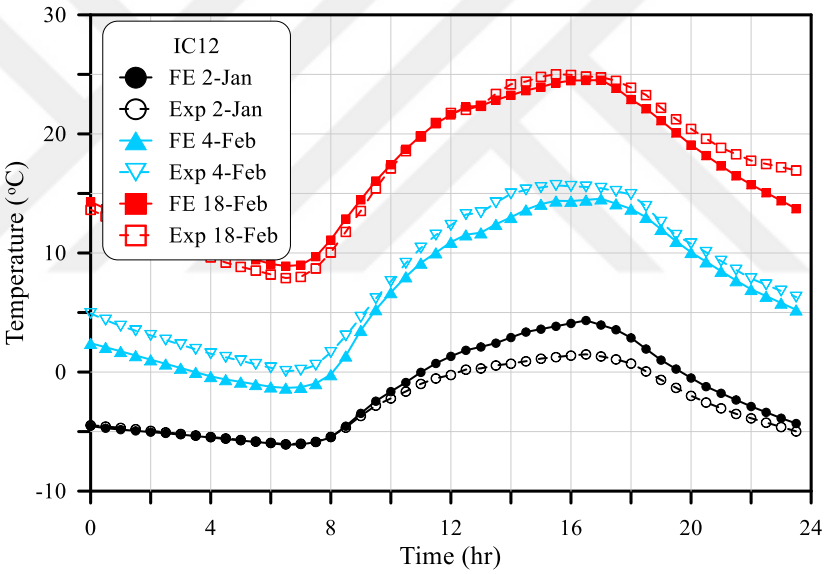

Figure 5.34 Hourly experimentally recorded and FE predicted temperatures at thermocouple IC12 for I-Beam segment.

Figures 5.35 to 5.37 show the results at thermocouples fixed in steel part IS. The AAE values ranged from 0.85 to 1.65 ℃ recorded at the thermocouple IS3. While the MAE values ranged from 2.27 to 3.53 ℃ recorded at the thermocouples IS3 and IS2 respectively. The Maximum differences between the predicted and experimental results take place at a maximum temperature and the beginning/end of the day during the 24 hours. As shown in Table 5.2 the results at thermocouples installed in steel part gave a good agreement.

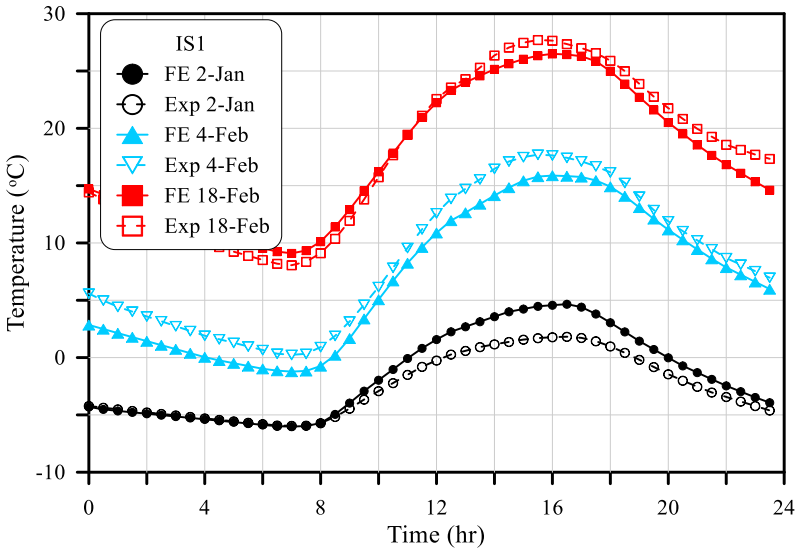

Figure 5.35 Hourly experimentally recorded and FE predicted temperatures at thermocouple IS1 for I-Beam segment.

The figure visualises well agreement between the predicted and the recorded temperatures results. Gaps between the predicted and experimental results accrue at a maximum temperature and the beginning/end of the day during the 24 hours. The AAE recorded for TC1 were 1.18, 1.25 and 1.5 ℃ in Frozen, Cold and Sunny day respectively. While the MAE in corresponding days were 3.42, 3.62 and 4.18 ℃ respectively. For the AAE and MAE, the Frozen day (2-January-2016) recorded the lowest error and the Sunny day (18-February-2016) recorded the highest error. The general behavior of the variation temperatures with time was almost the same for experimental and FE results.

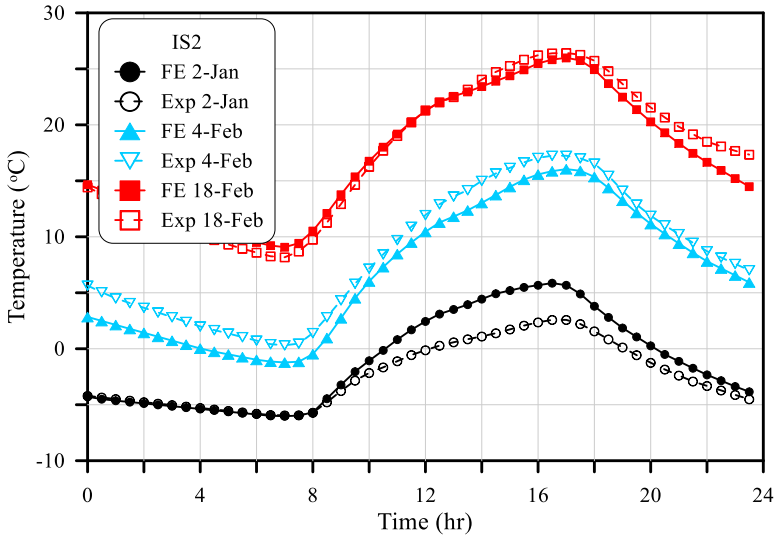

Figure 5.36 Hourly experimentally recorded and FE predicted temperatures at thermocouple IS2 for I-Beam segment.

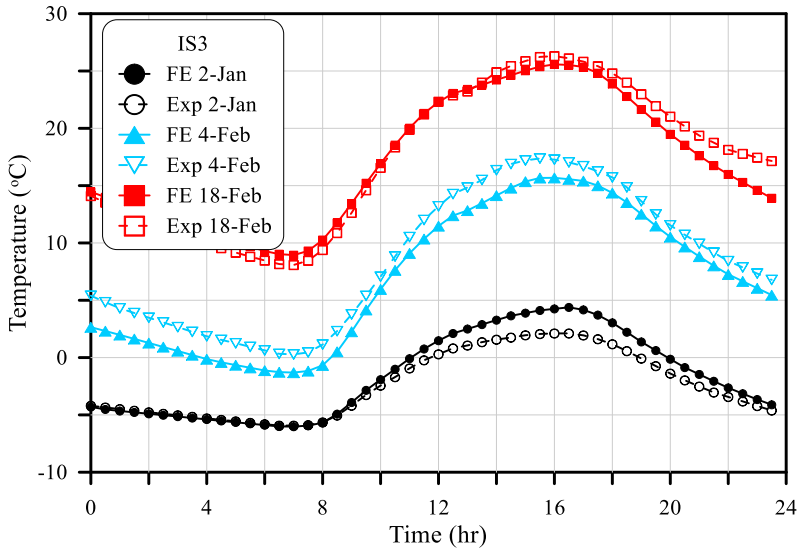

Figure 5.37 Hourly experimentally recorded and FE predicted temperatures at thermocouple IS3 for I-Beam segment.

Table 5.2 Average and maximum absolute errors between experimental and FE temperatures for I-Beam segment.

Thermocouple	2-Jan-2016 (Frozen day)		4-Fe-2016 (Cold day)		18-Feb-2016 (Sunny day)	
	AAE	MAE	AAE	MAE	AAE	MAE
IC1	0.93	2.29	1.63	2.95	1.28	3.31
IC2	0.96	2.39	1.63	2.75	1.16	3.02
IC3	1.01	2.55	1.62	2.67	1.06	2.79
IC7	0.30	0.89	1.15	2.69	1.58	4.49
IC6	0.52	1.23	1.46	2.83	1.33	3.31
IC5	0.65	1.58	1.53	2.98	1.30	3.22
IC4	0.66	2.16	1.48	3.88	1.69	4.47
IC9	0.76	2.09	1.32	2.00	1.14	4.07
IC8	1.01	2.94	1.70	3.34	1.26	4.02
IC10	0.72	2.09	1.55	2.46	1.01	3.58
IC12	1.01	2.85	1.42	2.50	0.93	3.21
IC11	2.01	5.59	1.44	2.50	0.89	3.22
IS1	1.10	2.84	1.57	2.73	0.99	2.73
IS2	1.33	3.53	1.55	2.80	0.86	2.85
IS3	0.85	2.27	1.65	2.75	0.94	3.24

CHAPTER 6

PARAMETRIC STUDY: SIZE EFFECT

6.1 General

The design temperature gradients of the bridge design codes are considered applicable for wide range of section sizes. However, that the size of the section matters and that the available design gradients may result in underestimated or overestimated stresses for large sections or special configuration sections. From this review, it can be said that the depth of the girder and the thickness of the flanges and web should have an influence on the temperature gradient distributions. In this chapter, a parametric study is carried out on the concrete-encased steel-beam girder to investigate the effect of the size of the girder using the verified FE model. This parametric study is subdivided into three studies.

Firstly, the overall section sizing is studied so that both section depth and member thicknesses are increased in similar rates keeping the same aspect ratios. This parametric study investigates the combined effect of the girder depth and the thickness of its flanges and web. The second parametric study, the effect of the girder depth is studied using fixed thickness of web and flanges, while the third investigates the effect of the thickness of the web and flanges for a fixed depth section. In all parts of the FE parametric study, the environmental data of 5-July-2015 were used.

6.2 Experimental, double, and triple size girders

Based on Figure 6.1, the dimensions of three FE girders are listed in Table 6.1. The first girder has the same dimensions of the experimental girder, while in the second and the third girders all dimensions were twice and tripled, respectively, keeping fixed geometrical aspect ratios. As shading effects depend on the aspect ratios of the

girder members, they were kept fixed at this stage to overcome any result confusion due to the different shading effects.

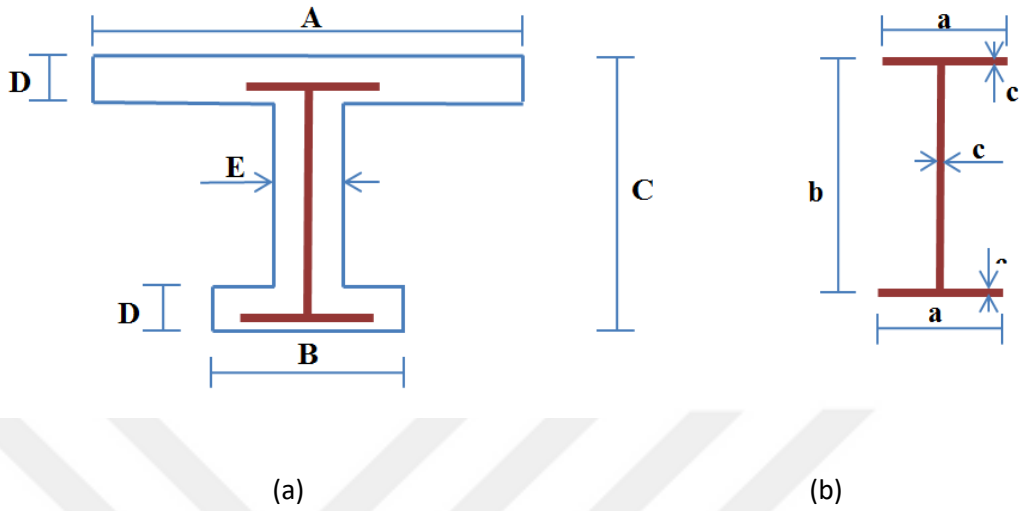

Figure 6.1 Dimensions of the FE sized: (a) composite girder and (b) steel part.

Table 6.1 Dimensions of the FE sized composite girder sections for the overall size effect parametric study.

Dimensions (mm)	**A**	**B**	**C**	**D**	**E**	**a**	**b**	**c**
Experimental	800	300	500	100	100	200	400	8
Double	1600	600	1000	200	200	400	800	16
Triple	2400	900	1500	300	300	600	1200	24

Figures 6.2 to 6.5 show comparisons of the 24-hour temperature variation at selected thermocouple locations. The selected locations are the center of the top concrete surface of the girder, the center of the bottom concrete surface of the girder, the central height of girder within the steel section, and the center of the northern concrete edge surface of the top flange, which are given in Figures 6.2, 6.3, 6.4 and 6.5 respectively.

As shown in Figure 6.2, the temperature differences between the three girders are quite acceptable during the 24 hours at the top-surface thermocouple. The maximum temperature difference at this point is 4.7 ℃, while the minimum difference is less than 0.2 ℃. As shown in Figure 6.2, the temperature difference starts increasing after

sunset and continues increasing during the night cooling hours to reach a maximum around the sunrise. During the sunshine hours, the opposite stands, where the temperature gap between the three girders decreases during this period. The explanation of this behavior is that for thicker flanges, higher heat is reserved during the day heating hours because of the higher concrete mass. Thus, longer night cooling hours are required to decrease the temperature of the surface. As a result, the smaller (experimental size) top surface cooled faster during the night hours showing lower temperatures than the larger girders, while it shows slightly higher temperatures during the mid-day hours.

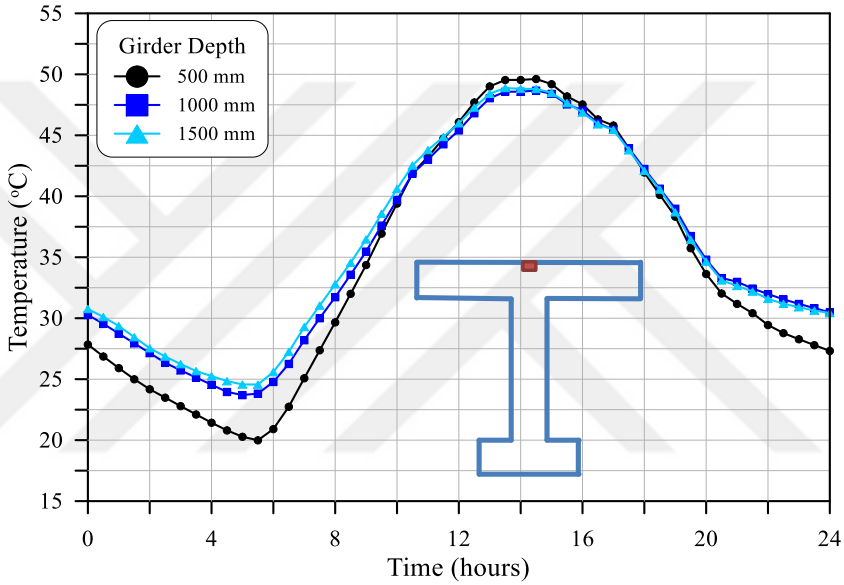

Figure 6.2 Size effect on 24-hours temperature distributions at top surface of the composite girder.

Figure 6.3 shows that similar behavior stands for the bottom surface thermocouple but with slightly different rates. The minimum and maximum temperature differences at this thermocouple are 0.8 and 4.8 ℃ respectively.

Figure 6.4 shows that the size of the girder has a larger impact on the temperature of the steel central-web thermocouple than on those at the top and bottom surfaces. As shown in the figure, the largest girder (triple size) shows the lowest daily temperature fluctuation, while the smallest one (experimental size) shows the highest fluctuation. In contrary to the top and bottom surfaces, the temperature difference is high during both the cold and the hot hours. The maximum temperature difference of this thermocouple during the 24 hours is 7.8 ℃. This is because the larger girders have

thicker webs, hence, smaller girders conduct more heat to the steel section during the day hours, and allow to faster reversed heat conduction during the night hours. As a result, the temperature of the steel section of smaller girders increases faster during the day and decreases faster during the night.

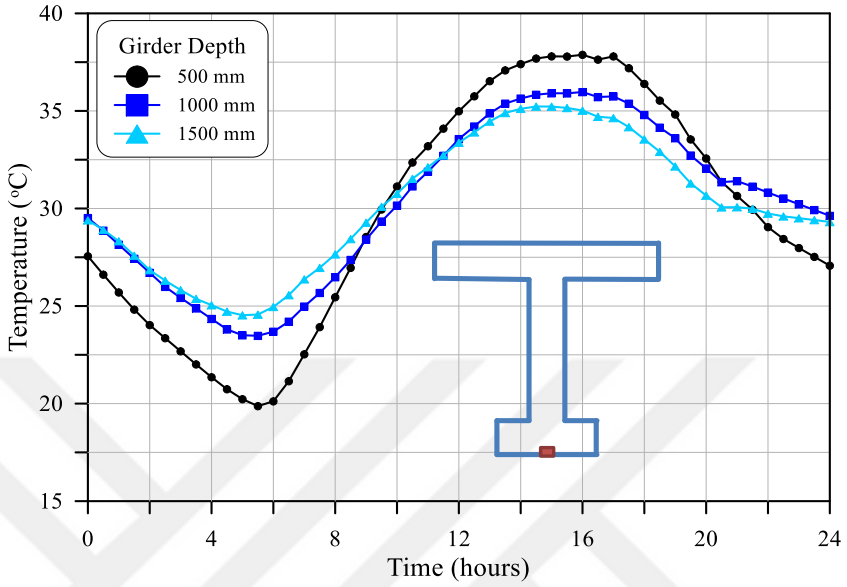

Figure 6.3 Size effect on 24-hours temperature distributions at bottom surface of the composite girder.

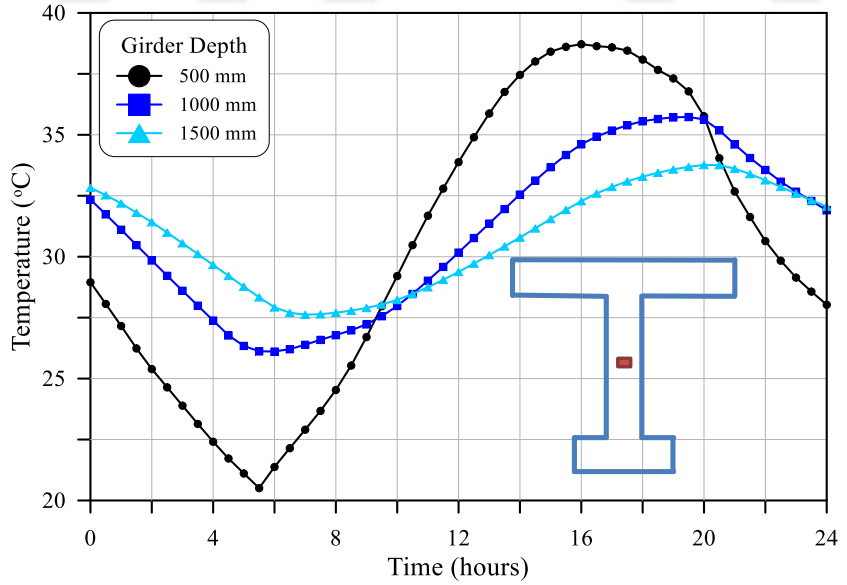

Figure 6.4 Size effect on 24-hours temperature distributions at the mid-height of the composite girder.

Figure 6.5 shows the temperature variation between the three girders at the top-flange edge thermocouple is also significant with a temperature difference ranges from 0.9 to 8.6 ℃ during the 24 hours.

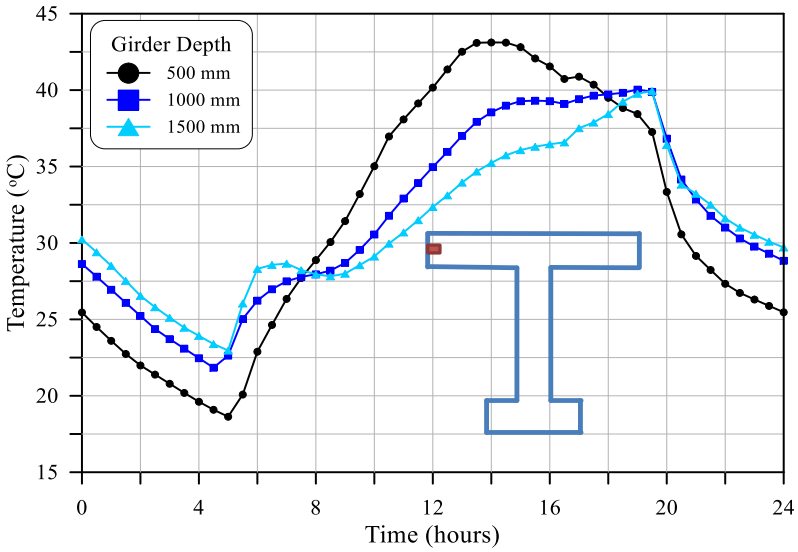

Figure 6.5 Size effect on 24-hours temperature distributions at the north edge of the composite girder.

In Figure 6.6, the distribution of the vertical temperature gradient is used to evaluate the effect of the size of the girder. The effects of temperature differences between the three girders discussed in Figures 6.2 to 6.5 are reflected here on the vertical temperature gradient distributions. The maximum temperature gradient occurs during the mid-day hours, where solar radiation and air temperature are around their daily highest records. At this time and as shown in Figure 6.2, the top surface temperature is almost the same for all girders (between 48 and 49 ℃) with slightly higher temperature for the smallest girder. On the other hand, the temperatures of the steel web are much lower for larger girders as shown in Figure 6.4.

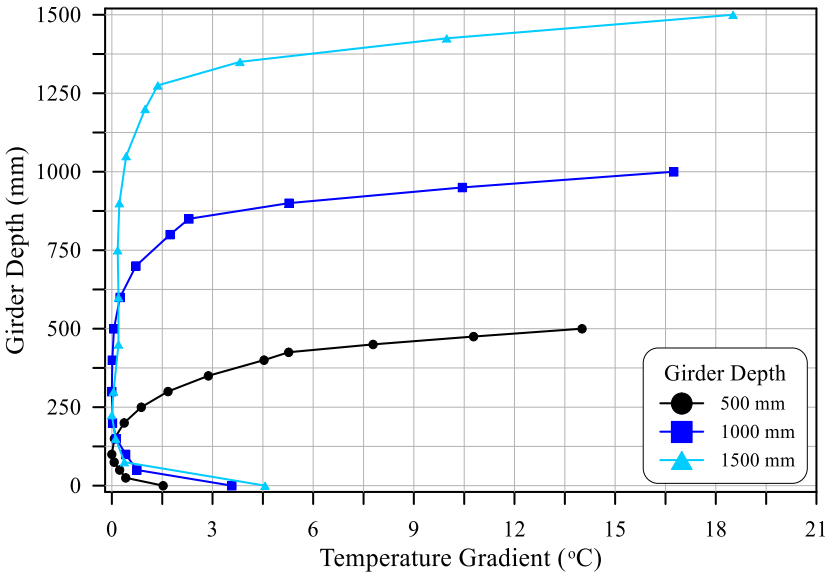

Figure 6.6 Size effect on vertical temperature gradient.

The lowest temperatures of the steel web of the experimental, double, and triple size girders at the time of maximum gradient (13:00) are 35, 31.3 and 29.9 ℃ respectively. This vertical temperature distribution leads to the increase of the vertical temperature gradient as the size of the girder increase as shown in 6.6 which are 14.0, 16.8 and 18.5 respectively. Figures 6.7 to 6.9 show the 3D temperature distributions at midday (12:00) for the three girders.

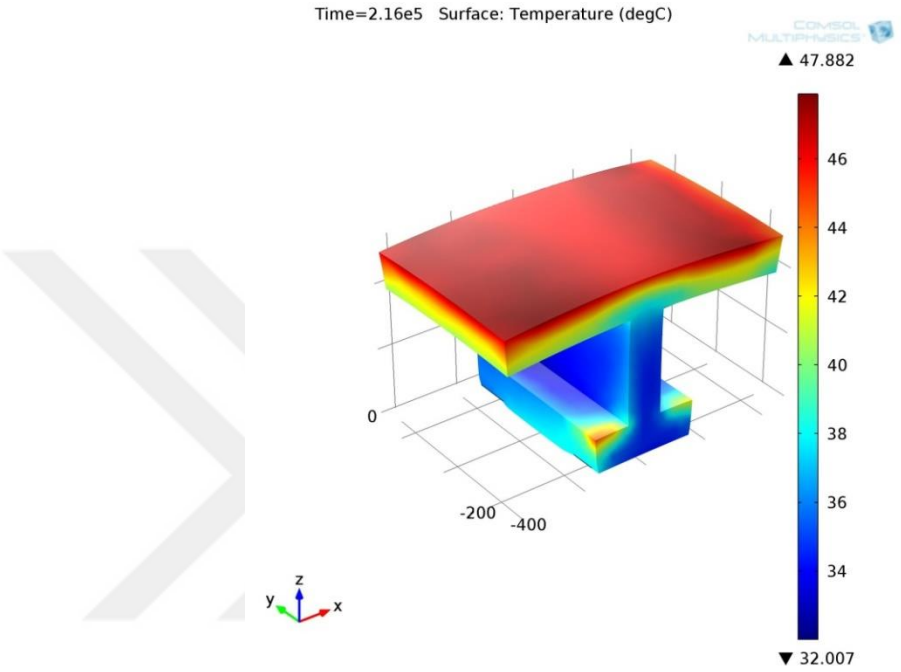

Figure 6.7 3D temperature distribution at midday (12:00) for the normal size girder.

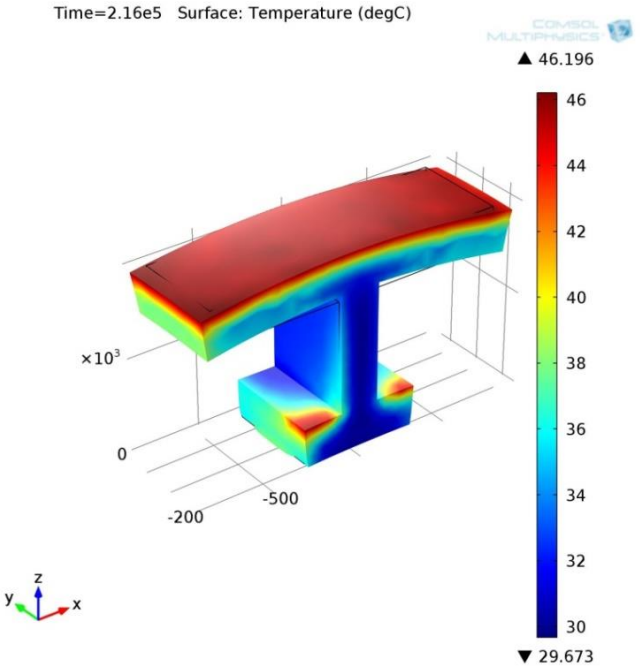

Figure 6.8 3D temperature distribution at midday (12:00) for the double size girder.

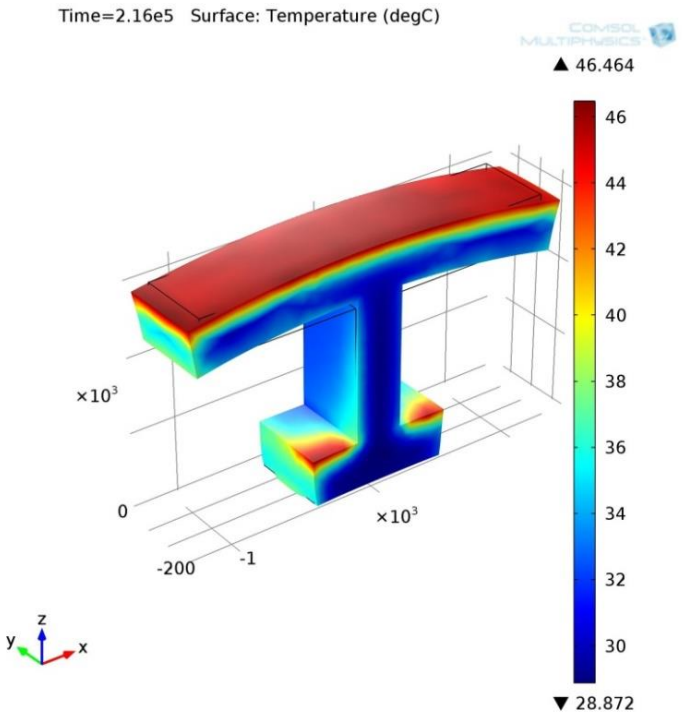

Figure 6.9 3D temperature distribution at midday (12:00) for the triple size girder.

6.3 Effect of the girder depth

In the previous section, it was shown that the size of the girder affects the temperature variations and temperature gradient distributions. The effect of the depth of the girder is discussed in this section. This FE parametric study compares between the same sized beams of the previous section but with fixed web and flanges thickness for all girders, which is 150 mm. Thus, the same dimensions are shown in Table 6.1, with different depths of 500, 1000 and 15000 mm but with D = E= 150 mm as prepared in Table 6.2.

Table 6.2 Dimensions of the FE sized composite girder sections for the girder depth effect parametric study

Dimensions (mm)	**A**	**B**	**C**	**D**	**E**	**a**	**b**	**c**
Experimental	800	300	500	150	150	200	400	8
Double	1600	600	1000	150	150	400	800	16
Triple	2400	900	1500	150	150	600	1200	24

Figures 6.10 to 6.13 show that for sections with variable depth and fixed member's thickness of 150 mm, the temperature variations between the 500, 1000 and 1500 mm depth girders are in general minimal and much smaller than those shown in

Figures 6.2 to 6.5. The maximum temperature differences between the three girders at the concrete top surface, concrete bottom surface, steel web, and concrete top-flange's edge are 0.8, 1.3, 1.7 and 2.1 ℃ respectively.

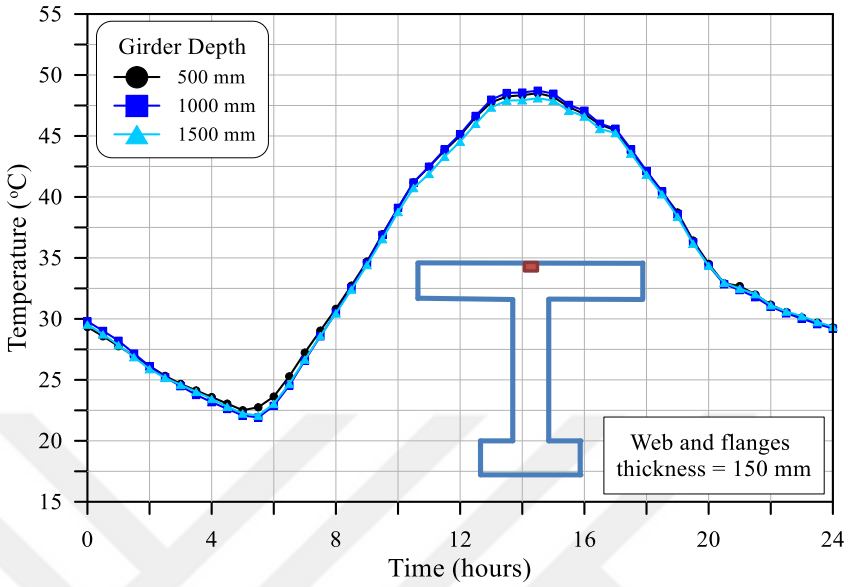

Figure 6.10 24-hours temperature distributions for different girder depths with 150 mm thick web and flanges at top surface of the composite girder.

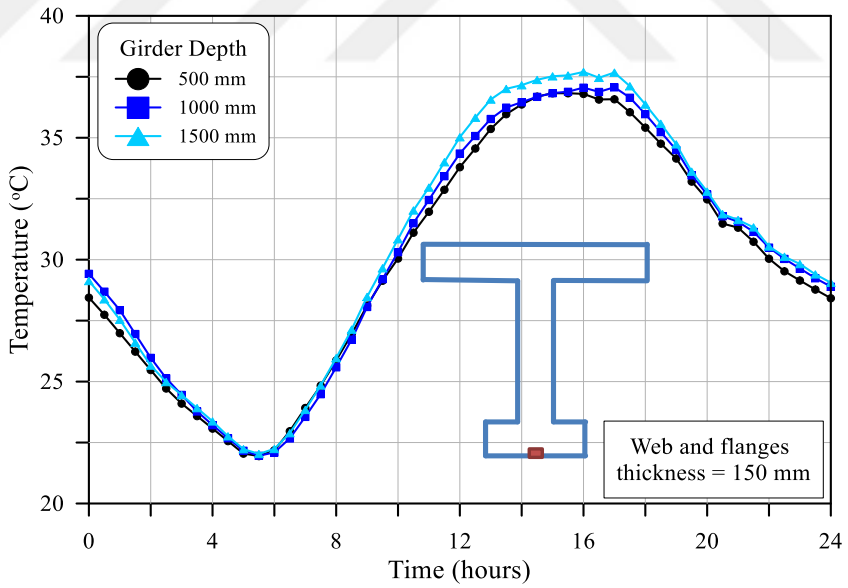

Figure 6.11 24-hours temperature distributions for different girder depths with 150 mm thick web and flanges at the bottom surface of the composite girder.

Similarly, Figure 6.14 shows that for the girders having depths of 500, 1000 mm and 1500 mm with constant web and flange thicknesses, the maximum vertical temperature gradients are quite the same, which are 14.8, 15.4 and 15.0 ℃ respectively. This leads to the conclusion that if the thicknesses of the girder's

members are kept constant, increasing the height and width of these members with the same aspect ratios has a minor effect on temperature and gradient distributions. Figures 6.7, 6.15 and 6.16 show the 3D temperature distributions at midday (12:00) for the three different depth girders (fixed thickness = 150 mm).

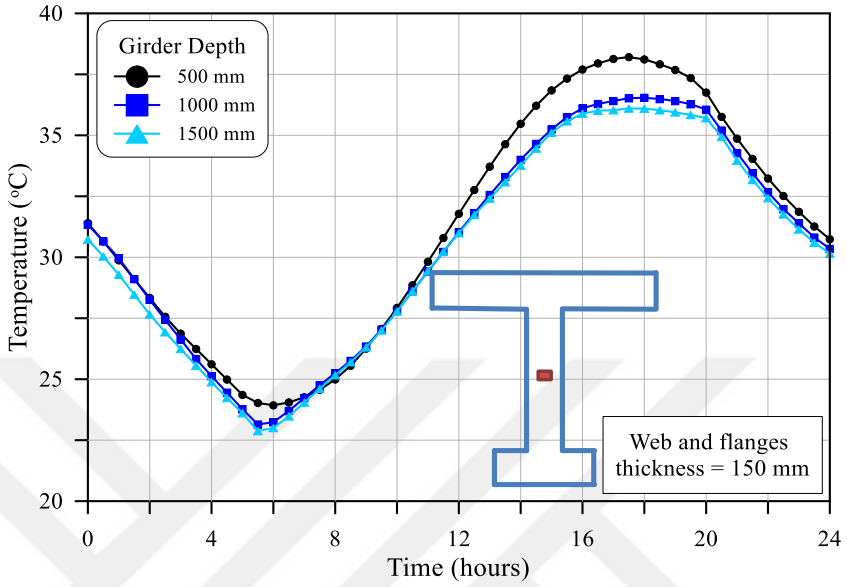

Figure 6.12 24-hours temperature distributions for different girder depths with 150 mm thick web and flanges at the mid-height of the composite girder.

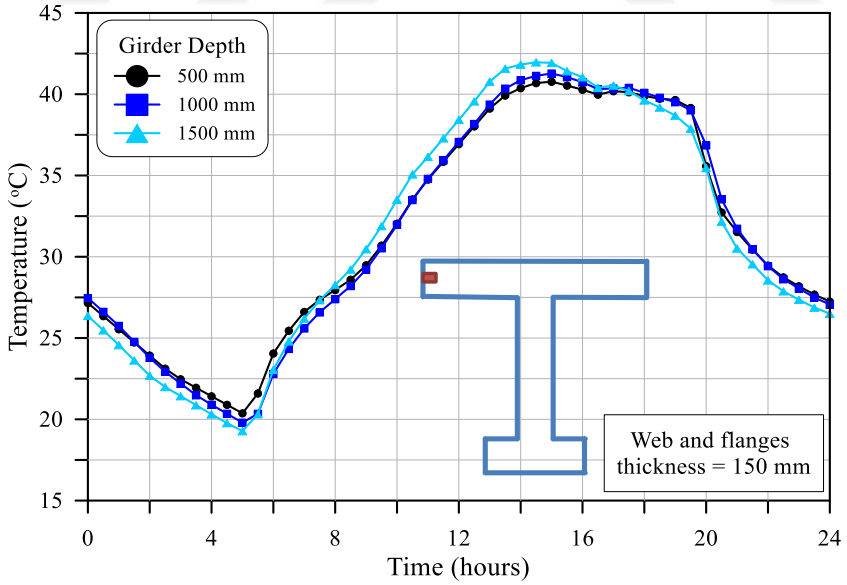

Figure 6.13 24-hours temperature distributions for different girder depths with 150 mm thick web and flanges at the north edge of the composite girder.

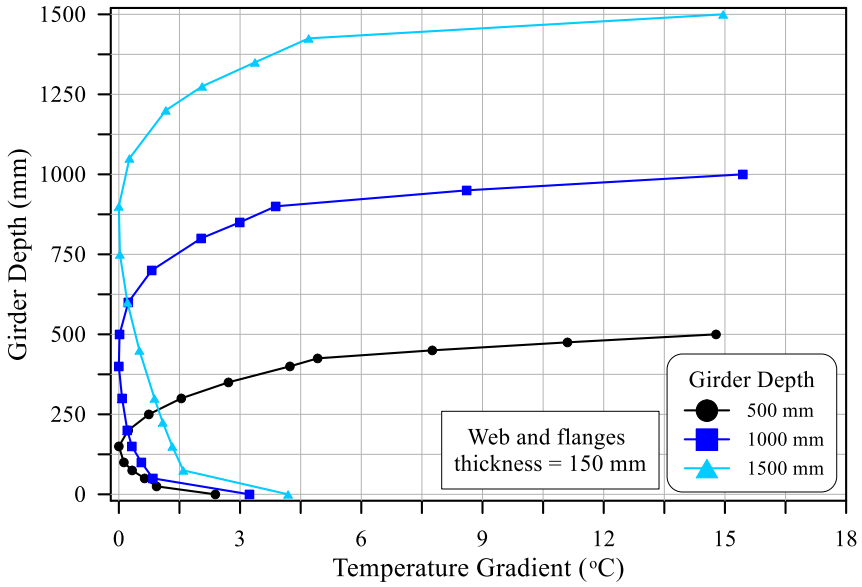

Figure 6.14 Vertical temperature gradients for different girder depths with 150 mm thick web and flanges.

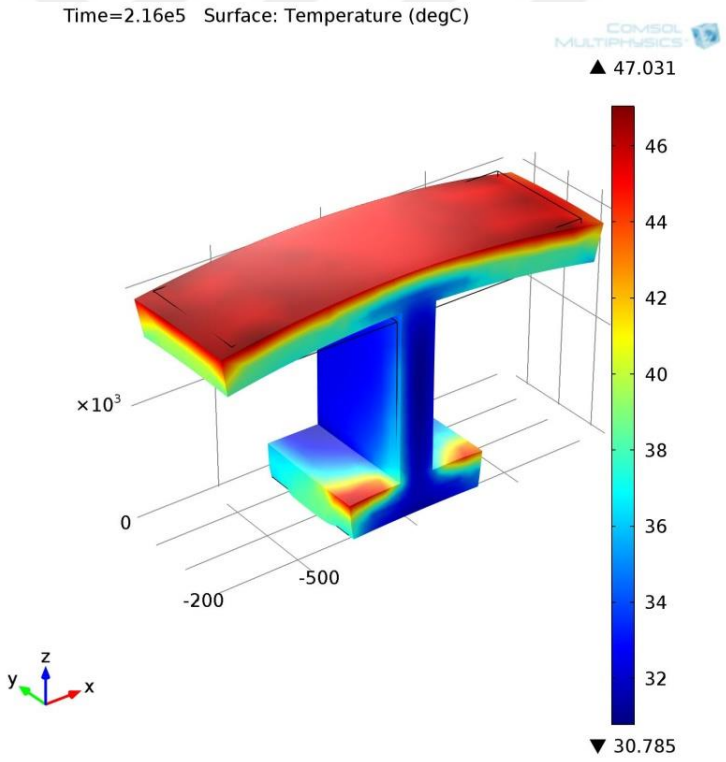

Figure 6.15 3D temperature distribution at midday (12:00) for the double size girder with web and flanges thickness of 150 mm.

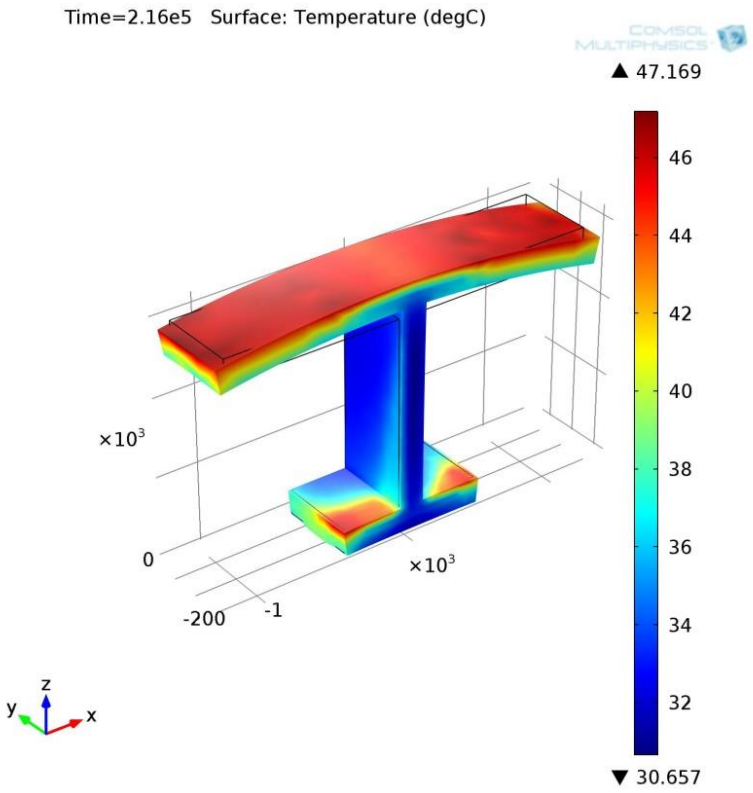

Figure 6.16 3D temperature distribution at midday (12:00) for the triple size girder with web and flanges thickness of 150 mm.

6.4 Effect of the web and flanges thickness

In this section, the particular effect of the thickness of the web and flanges is investigated. The effect of the thickness of the girder members is shown in Figures 6.17 to 6.20 and Figure 6.21. In these figures, all girders have the dimensions of the triple size girder shown in Table 6.1. However, the thickness of the flanges and the webs (D and E) is variable from 150 to 300 mm with a step of 50 mm as listed in Table 6.3.

Table 6.3 Dimensions of the FE sized composite girder sections for the overall size effect parametric study.

Dimensions (mm)	**A**	**B**	**C**	**D**	**E**	**a**	**b**	**c**
Case 1	2400	900	1500	150	150	600	1200	24
Case 2	2400	900	1500	200	200	600	1200	24
Case 3	2400	900	1500	250	250	600	1200	24
Case 4	2400	900	1500	300	300	600	1200	24

It is shown in Figures 6.17 and 6.18 that as the thickness increases from 150 to 300 mm, the temperature variations increase. This is more noticeable in Figure 6.19 and Figure 6.20 at the steel web and the edge of the top flange. The maximum temperature differences at the top surface, the bottom surface, the steel web, and the top-flange edge are 2.7, 3.0, 5.5 and 6.9 ℃ respectively. Comparing these values with those from sections 6.2 and 6.3, it is obvious that the greatest part of temperature variation can be attributed to the thickness of the concrete web and flanges.

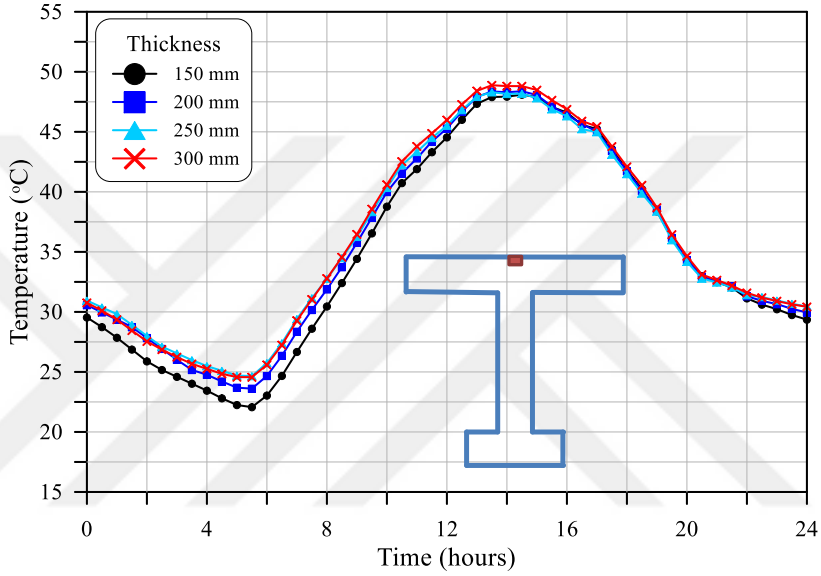

Figure 6.17 24-hours temperature distributions for different web and flanges thicknesses at top surface of the composite girder.

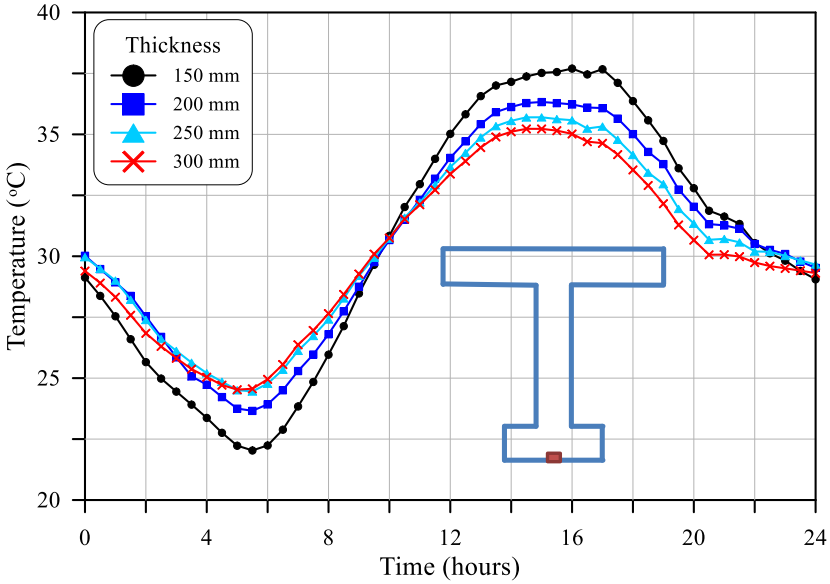

Figure 6.18 24-hours temperature distributions for different web and flanges thicknesses at bottom surface of the composite girder.

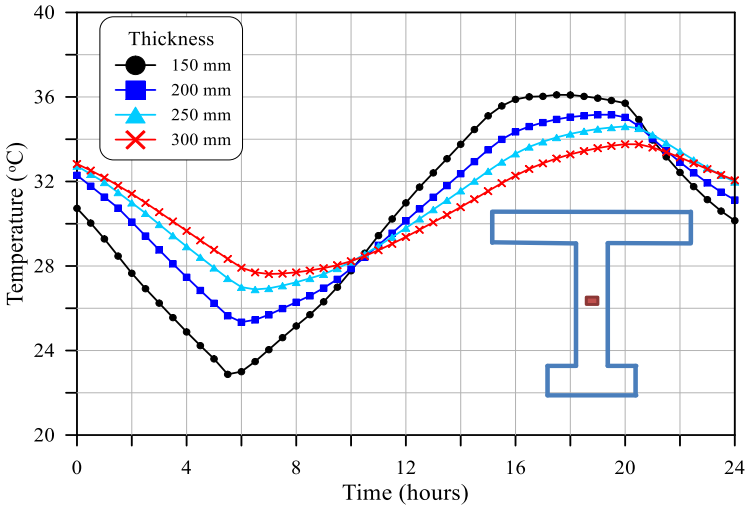

Figure 6.19 24-hours temperature distributions for different web and flanges thicknesses at the mid-height of the composite girder.

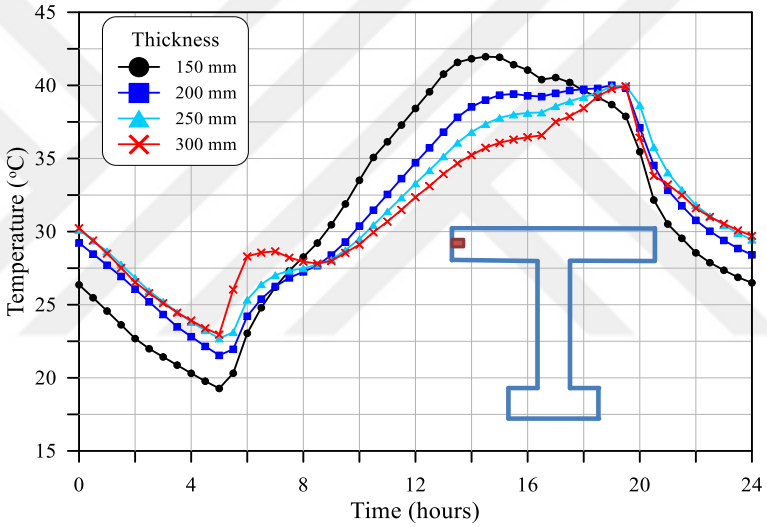

Figure 6.20 24-hours temperature distributions for different web and flanges thicknesses at the north edge of the composite girder.

Comparing the vertical temperature gradients of the four triple size girders with different thicknesses of concrete web and flanges, it is clear that the maximum gradient increases as the thickness increase. The maximum vertical temperature gradients of the triple size girders with thicknesses of 150, 200, 250 and 300 mm are 14.9, 16.7, 17.2 and 18.5 ℃ respectively as shown in Figure 6.21. This result confirms the conclusion that the thickness of the web and the flanges has a significant impact on temperature distributions and temperature gradients. Figures 6.16, 6.22, 6.23 and 6.9 show the 3D temperature distributions at midday (12:00) for the three different depth girders (fixed thickness = 150 mm) triple size girder with thicknesses of 150, 200, 250 and 300 mm respectively.

As a result of the three parametric studies and within the limits of the studied parameters, it can be concluded that the size of the girder affects the temperature and temperature gradient in girders subjected to solar radiation and air temperature. The results also showed that the thickness of the flanges and web has a more significant effect than that of the girder depth.

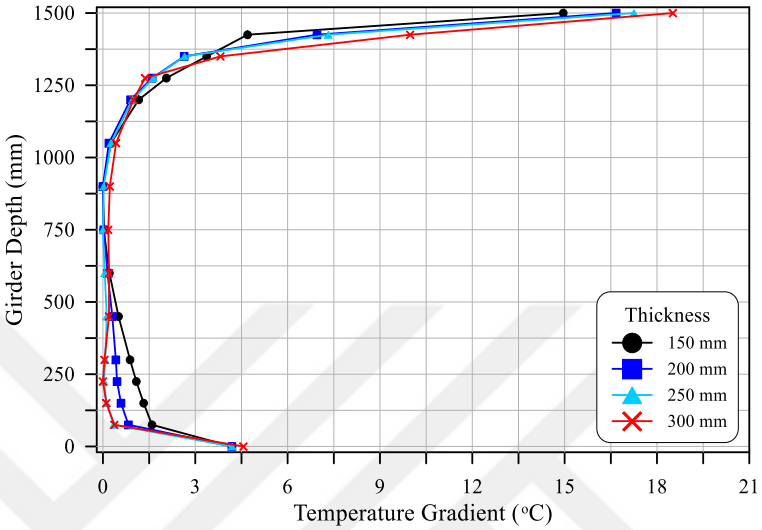

Figure 6.21 Vertical temperature gradients for different thicknesses of web and flanges.

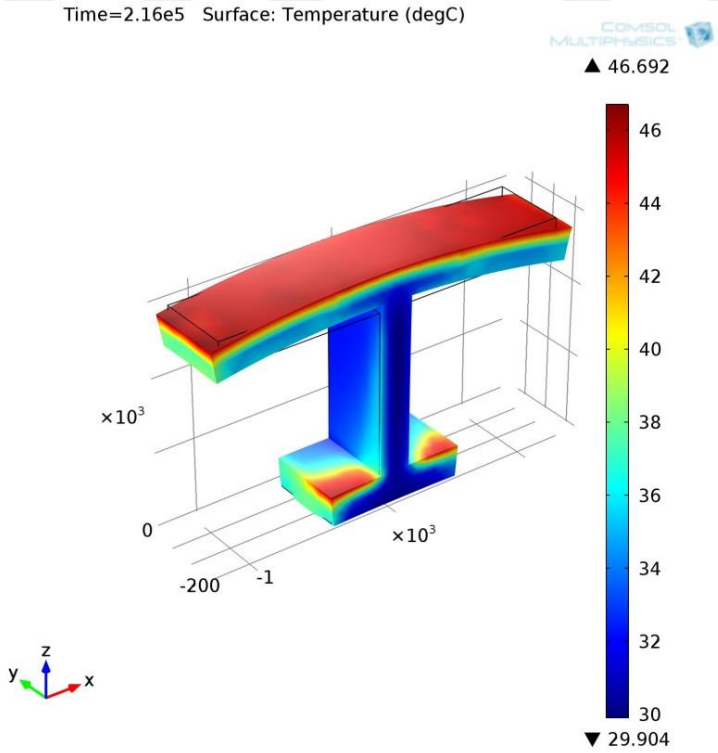

Figure 6.22 3D temperature distribution at midday (12:00) for the triple size girder with web and flanges thickness of 200 mm.

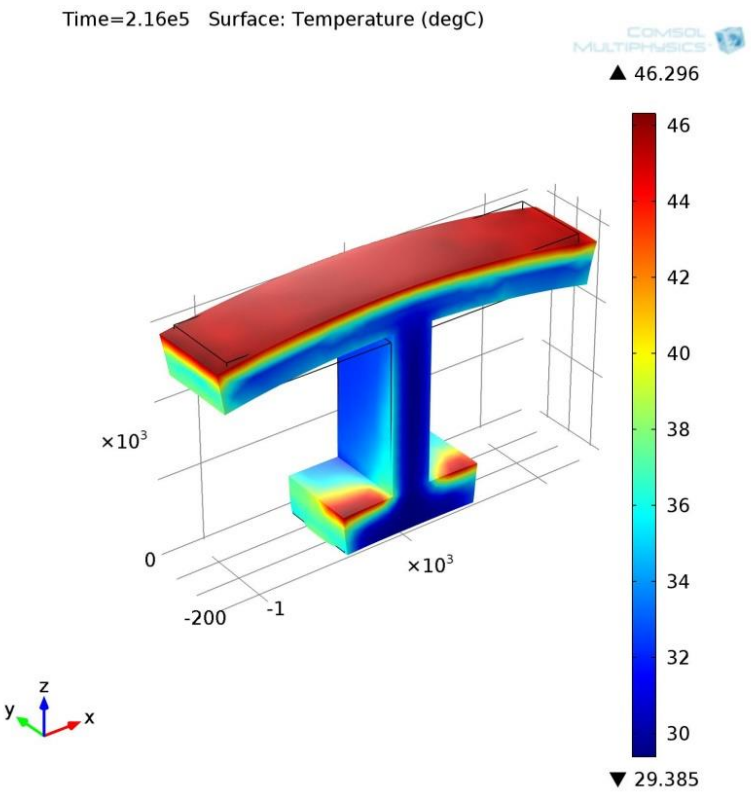

Figure 6.23 3D temperature distribution at midday (12:00) for the triple size girder with web and flanges thickness of 250 mm.

CHAPTER 7

TEMPERATURE GRADIENTS IN TURKEY

7.1 General

There are seven different regions in Turkey, so ten cities selected from several geographical locations to represent the entire Turkey area as shown in Figure 7.1. The COMSOL 4.3a finite element program [28] adopted to analysis the effect of air temperature and solar radiation on composite concrete-steel girders. The maximum vertical and horizontal temperature gradients of composite concrete-steel bridge girders in ten cities for six months obtained. According to the similarity of results between the two segments, hence the results for the T-Beam segment adopted in this study.

Figure 7.1 The location and regions of the selected cities.

7.2 The Regions and Geographical Location of the Selected Cities

The seven regions of Turkey divided into two groups. One group is coastal which represented four regions. The second is inland which includes the other three regions.

The coastal regions are the Mediterranean, the Black Sea, the Marmara, and the Aegean. The inland regions are the Central Anatolian, the Eastern Anatolian, and the Southeastern Anatolian. Ten cities were selected to make a detailed investigation and analysis for whole Turkey region: Adana, Ankara, Antalya, Çorum, Diyarbakır, İstanbul, İzmır, Samsun, Şanlıurfa and, Şırnak as shown in Figure 7.1. The regions and the geographical locations of the selected cities are given in Table 7.1.

Table 7.1 The selected cities and their regions and geographical location.

City	Region	Latitude	Longitude
Adana	Mediterranean	36.98 N	35.35 E
Antalya	Mediterranean	36.91 N	30.69 E
Ankara	Central Anatolian	39.95 N	32.88 E
Çorum	Black Sea	40.55 N	34.95 E
Diyarbakır	Southeastern Anatolian	37.89 N	40.20 E
İstanbul	Marmara	40.90 N	29.15 E
İzmir	Aegean	38.43 N	27.17 E
Samsun	Black Sea	41.28 N	36.30 E
Şanlıurfa	Southeastern Anatolian	37.13 N	38.77 E
Şırnak	Eastern Anatolian	37.52 N	42.46 E

7.3 The Long-Term Distributions of the Solar Radiation in Turkey

Figures 7.2 and 7.3 clarify the long-term distributions of monthly average solar radiation in June and December according to the data provided by the Turkish State Meteorological Service [30]. Figures 7.4 to 7.7 illustrated the long-term distributions for the maximum and minimum air temperatures in June and December. The data of the long-term was used to determine the difference in the expected temperature gradients and bridge temperature in the whole regions of Turkey.

Figures 7.2 and 7.3 show the long-term monthly average solar radiation in June and December respectively. Where, the lowest intensity of monthly average solar radiation occur in: the northern regions, the coastal areas along the north Black sea and the east of the Marmara region. The maximum differences in the data of up to 256 Cal/cm^2 ($W/m^2 = Cal/cm^2 \times 11.63$).

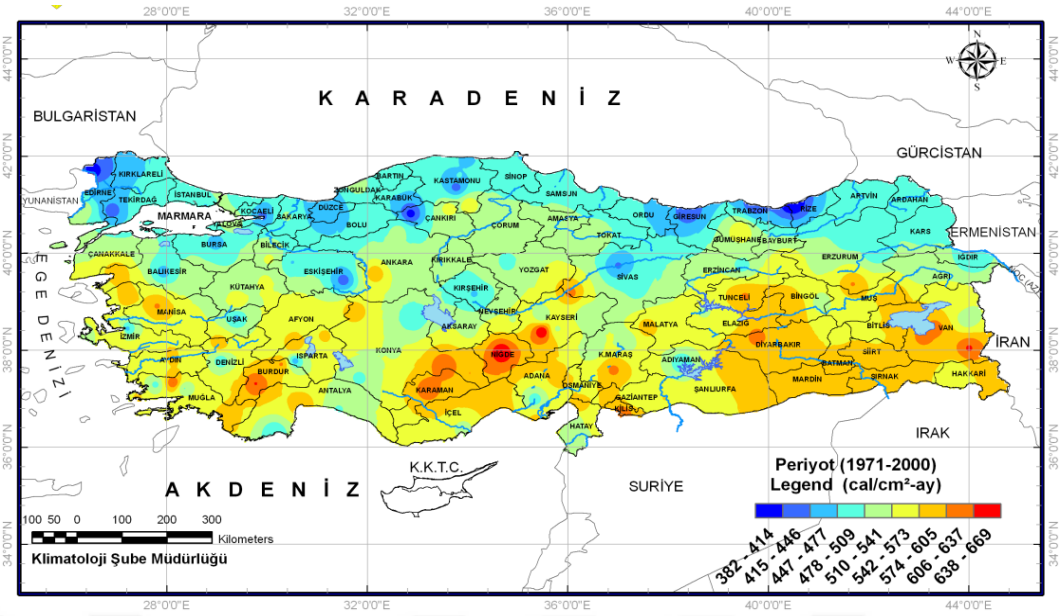

Figure 7.2 The long-term monthly average solar radiation of June [30].

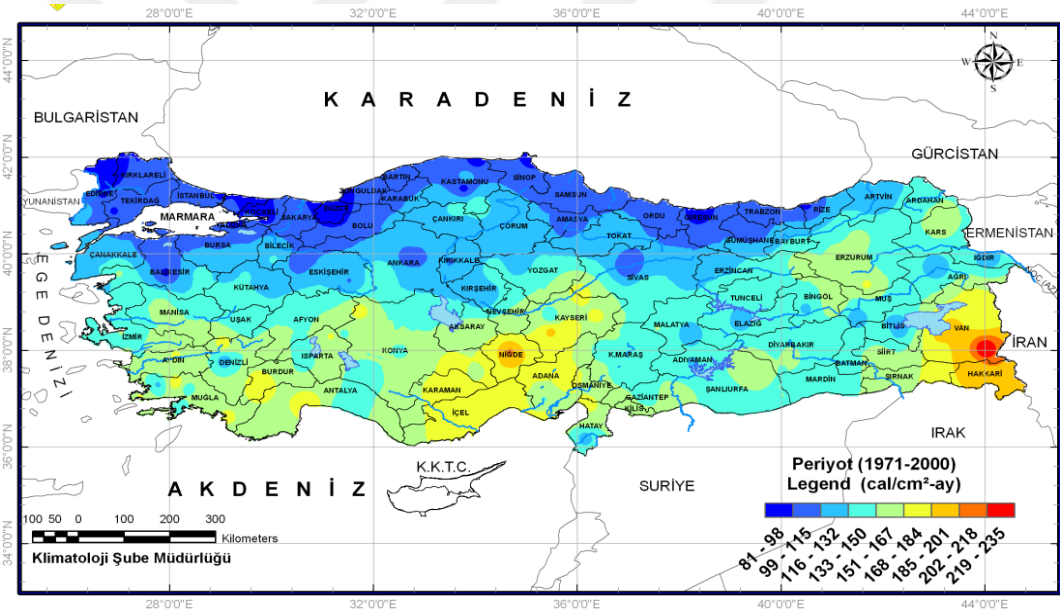

Figure 7.3 The long-term monthly average solar radiation of December [30].

Figure 7.4 explain the distribution of the maximum air temperature in a long-term for Turkey in June. The range of air temperatures was between 29 and 45 °C, and the highest distribution of the maximum air temperatures in the south and south-west of Turkey. The extreme daily maximum temperature was greater than 40 °C. While the maximum air temperature distribution in the long-term recorded in December was between 9 and 37 °C in Turkey.

Figure 7.5 illustrates the maximum air temperature distribution in December which was in the northeast area and the south-west area as the highest and lowest area in Turkey respectively.

Figure 7.4 The long-term maximum air temperature of June [30].

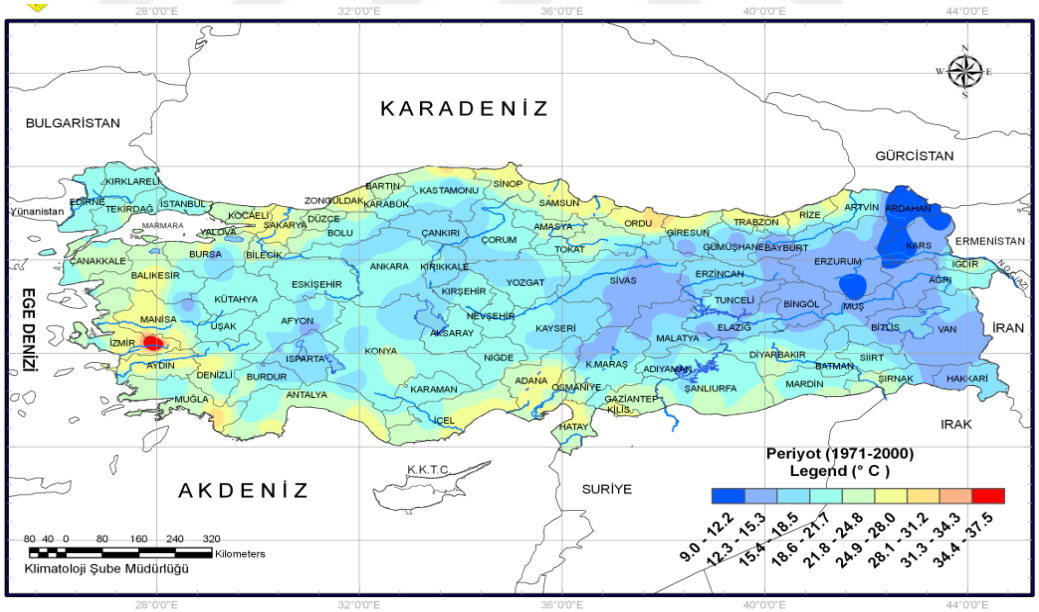

Figure 7.5 The long-term maximum air temperature of December [30].

The minimum air temperature for long-term in June was from -5 to 14 °C as shown in Figure 7.6. Southeastern Anatolian and coastal areas along the four seas show the highest value of minimum air temperatures, but the lower value of minimum air temperatures recorded in the eastern and central high altitude regions. While regions

like Çorum in the southern part of the Black Sea region recorded high value of daily maximum air temperatures and low value daily minimum air temperatures. The daily air temperature difference is higher in such regions.

Figure 7.7 shows the long-term of minimum air temperature distribution in December for whole Turkey. The minimum air temperature in complete Turkey between -44 to 5 °C.

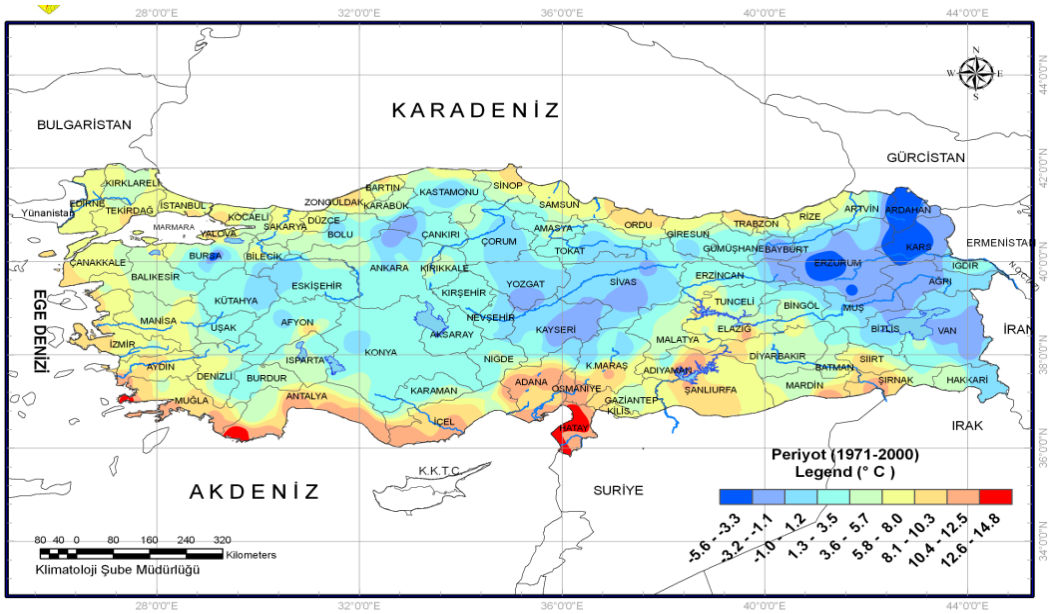

Figure 7.6 The long-term minimum air temperature of June [30].

Figure 7.7 The long-term minimum air temperature of December [30].

7.4 The Data Provided By Turkey Stat Meteorological Service

The data were provided by the Turkey State Meteorological Service [30] include temperature and solar radiation records for more than 50 years, since 1960 to 2013. This data are used to evaluate the extreme temperature and temperature gradients in composite concrete-steel girder bridges. The analysis was carried out for six different months they represent the four seasons of the year, which are April, June, July, October, November and December.

The selected day of each month reflects the maximum daily air temperature difference. Based on the long-term recorded daily maximum and average daily minimum air temperature, the maximum air temperature difference was calculated. Also, for each of these six months, the long-term maximum daily average of total global solar radiation was considered. The wind speed was taken as zero to maximize the temperatures and temperature gradients.

The data listed in Table 7.2 to 7.7 represented the daily air temperature and solar radiation for the ten cities in the six months. With regard to the solar radiation the daily maximum, minimum, and difference are calculated at horizontal surfaces in W/m^2.

Table 7.2 Solar radiation and air temperature in April.

City	Daily maximum hourly solar radiation W/m^2	Daily air temperature °C		
		Max.	Min.	Difference
Adana	938.66	35.6	11.6	24
Antalya	1023.9	32.5	14.5	18
Ankara	975.52	30.0	5.3	24.7
Çorum	865.27	30.4	3.8	26.6
Diyarbakır	989.59	35.3	7.8	27.5
İstanbul	816.43	32.9	8.7	24.2
İzmir	886.21	32.1	11.2	20.9
Samsun	858.29	37.0	7.7	29.3
Şanlıurfa	907.14	34.6	12.6	22
Şırnak	1041.7	29.0	8.1	20.9

Table 7.3 Solar radiation and air temperature in June.

City	Daily maximum hourly solar radiation W/m^2	Daily air temperature °C		
		Max.	Min.	Difference
Adana	960.87	40.8	18.5	22.3
Antalya	1075.1	35.8	18.6	17.2
Ankara	1002.74	35.3	11.6	23.7
Çorum	955.98	36.9	9.6	27.3
Diyarbakır	996.57	39.6	14.0	25.6
İstanbul	879.23	40.2	17.9	22.3
İzmir	935.05	38.7	18.0	20.7
Samsun	861.31	37.4	16.7	20.7
Şanlıurfa	921.09	44.0	19.3	24.7
Şırnak	1027.28	33.4	15.4	18

Table 7.4 Solar radiation and air temperature in July**.**

City	Daily maximum hourly solar radiation W/m^2	Daily air temperature °C		
		Max.	Min.	Difference
Adana	936.33	44	22.7	21.3
Antalya	1018.55	40.8	23.7	17.1
Ankara	996.11	40.8	16.6	24.2
Çorum	1004.83	42.6	13.4	29.2
Diyarbakır	1008.55	44.7	21.7	23
İstanbul	886.21	39.7	19.4	20.3
İzmir	921.09	42.6	22.4	20.2
Samsun	830.38	36.1	18.4	17.7
Şanlıurfa	955.98	46.8	25.0	21.8
Şırnak	1002.62	40.4	22.9	17.5

Table 7.5 Solar radiation and air temperature in October.

City	Daily maximum hourly solar radiation W/m^2	Daily air temperature °C		
		Max.	Min.	Difference
Adana	798.63	38	15.8	22.2
Antalya	818.98	34.9	17.5	17.4
Ankara	732.22	31.4	8.4	23
Çorum	683.84	33.0	6.8	26.2
Diyarbakır	753.62	31.0	8.2	22.8
İstanbul	655.93	34.2	13.5	20.7
İzmir	732.69	33.2	13.5	19.7
Samsun	648.95	38.4	14.0	24.4
Şanlıurfa	767.58	34.8	14.4	20.4
Şırnak	806.07	27.4	10.7	16.7

Table 7.6 Solar radiation and air temperature in November.

City	Daily maximum hourly solar radiation W/m^2	Daily air temperature °C		
		Max.	Min.	Difference
Adana	588.59	32.6	10.9	21.7
Antalya	641.04	28.9	11.7	17.2
Ankara	585.8	23.6	2.7	20.9
Çorum	551.26	25.0	2.3	22.7
Diyarbakır	690.82	24.3	3.7	20.6
İstanbul	537.30	27.2	9.9	17.3
İzmir	655.93	28.8	10.7	18.1
Samsun	516.37	28.8	8.0	20.8
Şanlıurfa	635	27.3	7.3	20
Şırnak	641.28	22.6	4.2	18.4

Table 7.7 Solar radiation and air temperature in December.

City	Daily maximum hourly solar radiation W/m^2	Daily air temperature °C		
		Max.	Min.	Difference
Adana	551.38	30.8	8.6	22.2
Antalya	567.54	26.8	11.5	15.3
Ankara	529.05	19.8	0.7	19.1
Çorum	565.22	18.0	-2.5	20.5
Diyarbakır	621.04	18.0	-1.2	19.2
İstanbul	516.37	25.5	7.4	18.1
İzmir	537.31	24.7	7.1	17.6
Samsun	411.7	26.9	5.7	21.2
Şanlıurfa	509.39	26.0	5.4	20.6
Şırnak	551.38	30.8	8.6	22.2

7.5 Temperature Gradients

In order to focus and clarify the results of the COMSOL 4.3a finite element program [28], two cities of Turkey selected: Samsun and Adana. Where, Samsun from the cold Black Sea region, and Adana from the hot south region. This section studies the maximum vertical and horizontal temperature gradients in the six selected months, the variation of the average, the maximum and the minimum temperatures.

Figures 7.8 and 7.9 show the temperature gradients in the 3D plot for the T-Beam segment in the six tested months for Adana and Samsun.

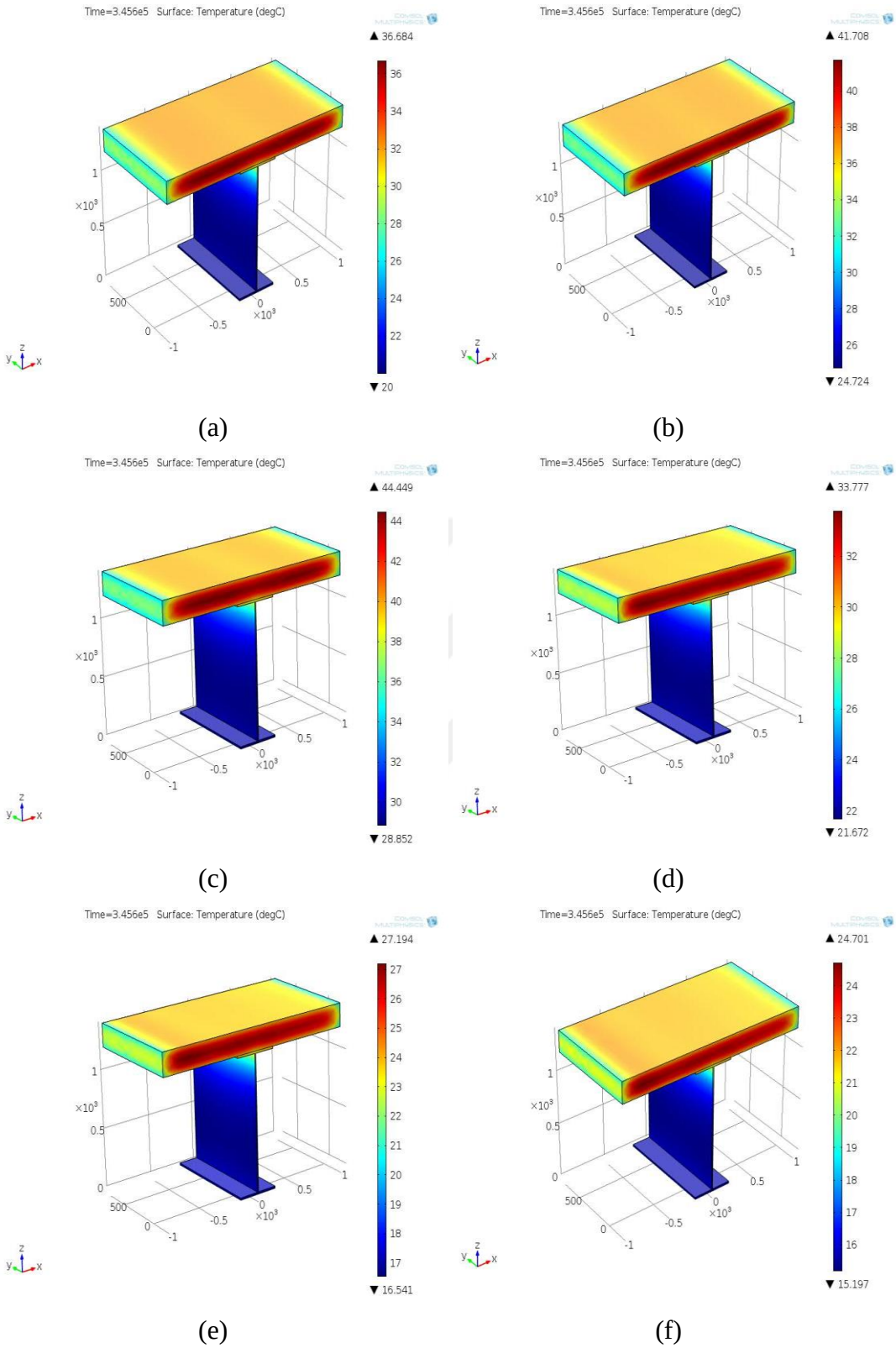

Figure 7.8 The temperature gradients in 3D plot for (T-Beam) to Adana in: (a) April, (b) June, (c) July, (d) October, (e) November and (f) December.

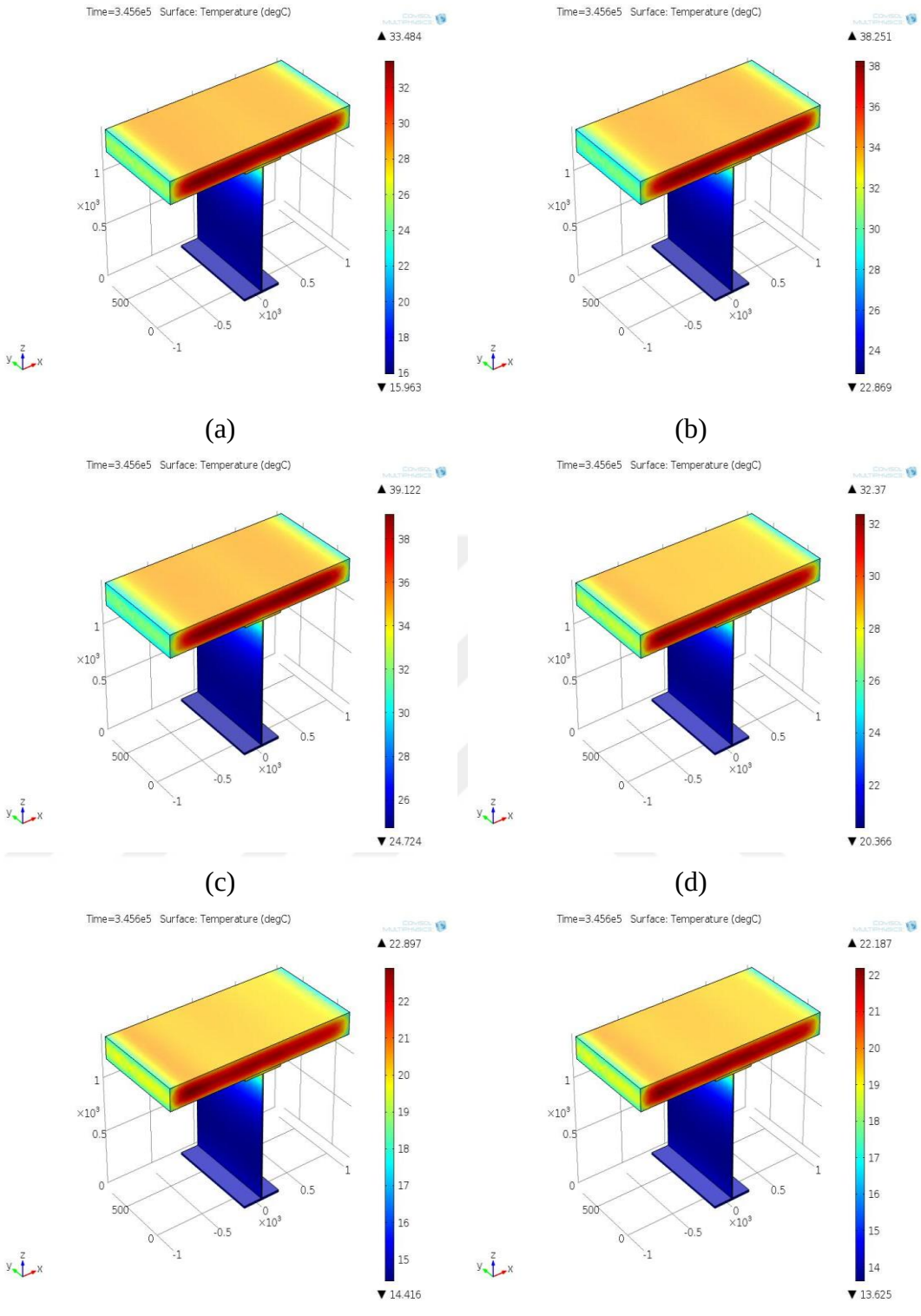

Figure 7.9 The temperature gradients in 3D plot for (T-Beam) to Samsun in: (a) April, (b) June, (c) July, (d) October, (e) November and (f) December.

7.5.1 Vertical Temperature Gradients

The results of the maximum vertical positive and negative temperature gradients for the two cities in the six tested months are shown in Figures 7.10 to 7.13. The vertical temperature gradients calculated along section Z-Z.

When studying the maximum positive gradient of the vertical section, it is clear that the variation in the concrete part is almost the same for both cities with the difference in values, but in the steel part, it is to some extent similar as shown in Figures 7.10 and 7.11. When a comparison between the results of the two cities, Adana showed higher temperature gradients than Samsun. Where the maximum value of Adana city was 15.05, 15.48, 14.49, 13.33, 13.11 and 12.25 °C in April, June, July, October, November and December respectively. The corresponding maximum value for Samsun was 11.41, 13.49, 12.79, 10.23, 9.14 and 8.83 °C.

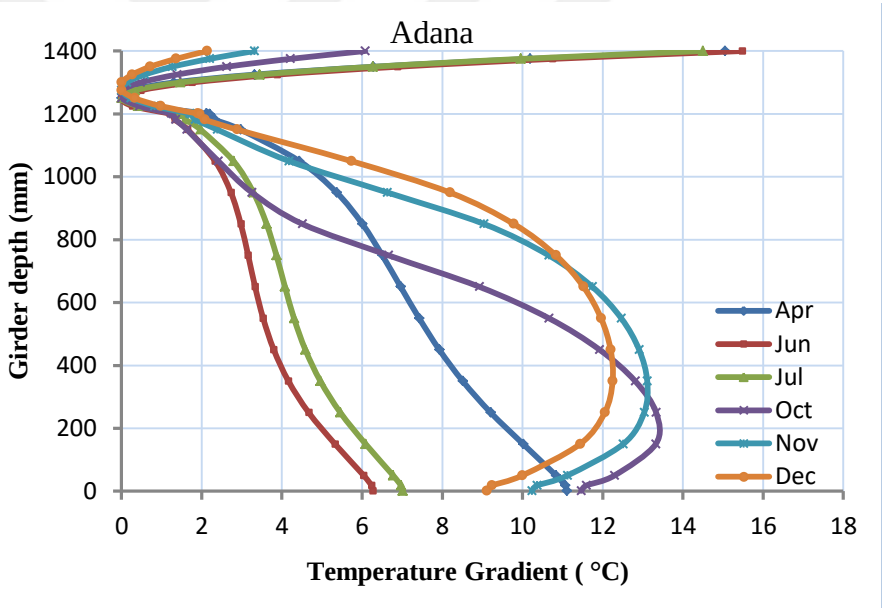

Figure 7.10 Maximum vertical positive temperature gradients in Adana.

When checking the results of the two cities notes that in hot season the maximum values of the maximum vertical positive temperature gradients occur at the top of the segment (concrete part), while in cold season the maximum value takes place in the bottom part (steel part). Where, in hot season the sun rays strike from high solar altitude angle this lead to heating of the concrete part, but in cold season the sun rays strike from the low solar altitude angle during whole day which leads to heating the steel part.

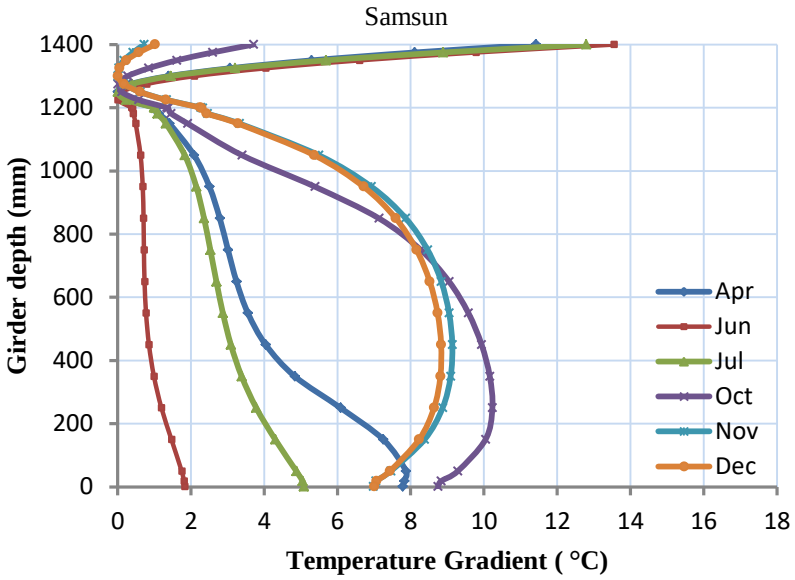

Figure 7.11 Maximum vertical positive temperature gradients in Samsun.

For Adana city, the results of the concrete part were 15.05, 15.48, 14.49, 6.08, 3.32 and 2.13 °C in six tested months respectively. In the same order, the results of Samsun city of the concrete part were 11.42, 13.55, 12.79, 3.71, 0.72 and 1.02 °C. The results of the steel part of Adana city were 11.11, 6.27, 7.01, 13.33, 13.11 and 12.25 °C in the similar sequence. The corresponding value of the steel part for Samsun city was 7.87, 1.82, 5.09, 10.23, 9.14 and 8.83 °C. Hence, in the cold season, the steel part gives the highest temperature gradient for both cities. Also, the results show that the concrete part is more stable than steel part.

Figures 7.12 and 7.13 show the maximum vertical negative temperature gradients in Adana and Samsun city. The maximum vertical negative temperature gradient showed almost similar behavior in both concrete and steel part of the segment for the two selected cities with slightly higher temperature in Adana.

For Adana city, the maximum negative temperature gradient value at concrete part was -2.61, -2.93, -3.05, -2.48,-2.21 and -1.96 °C in April, June, July, October, November and December respectively. And the value at steel part was -11.35, -11.84, -11.99, -9.98, -9.07 and -8.35 °C respectively. While, the maximum negative temperature gradient value at the concrete part for Samsun in the same order was -2.25, -2.71, -2.85, -2.32, -1.85 and -1.75 °C, and at the steel part was -10.53, -11.05, -11.33, -9.59, -7.89 and -7.49 °C respectively. The maximum difference between the

two selected cities in six months at the concrete part was 0.36 °C, and in the steel part was 1.18 °C.

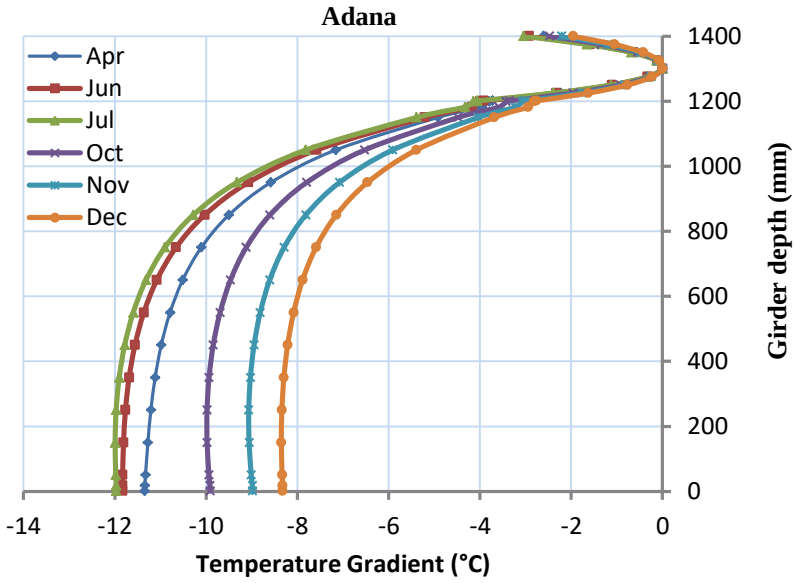

Figure 7.12 Maximum vertical negative temperature gradients in Adana.

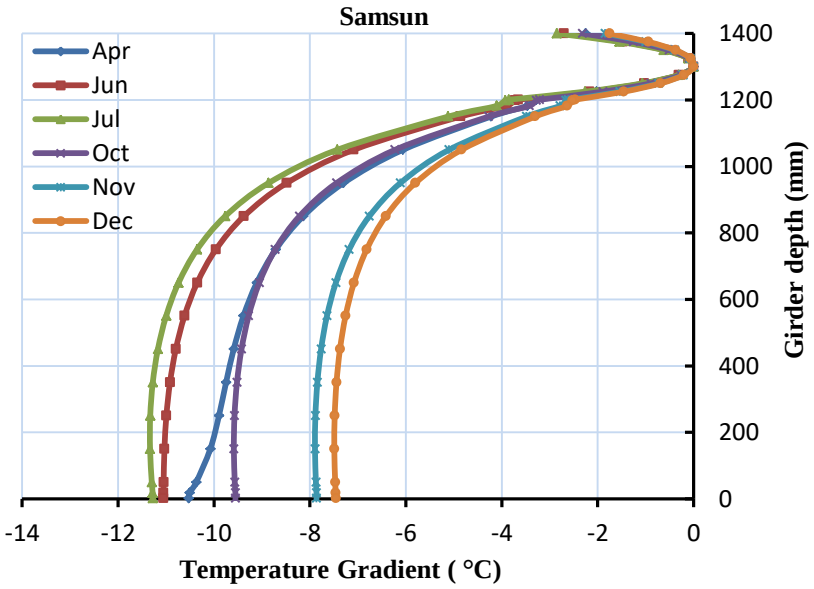

Figure 7.13 Maximum vertical negative temperature gradients in Samsun.

Generally, the zero temperature gradients occur at bottom of concrete slab for both cities in six months as shown in Figure 7.12 and 7.13. Also, from the results it is clear that the vertical gradient at the hot season (April, June, and July) was greater than the gradient at cold season (October, November and December).

7.5.2 Horizontal Temperature Gradients

Figures 7.14 to 7.17 show the maximum positive and negative lateral temperature gradients calculated along section X-X.

In general, the chart areas divided into two regions, a hot and cold region. Figures 7.14 and 7.15 illustrate that the maximum positive gradient of the lateral section for the two cities. The two cities has the same behavior, but Adana city gives the highest results in the maximum positive lateral temperature gradients than the Samsun city. Where, for the Adana city the maximum positive lateral temperature gradients in April, June, July, October, November, and December was 6.12, 4.29, 5.56, 10.05, 10.44 and 10.88 °C respectively. For the Samsun city, the corresponding values were 5.78, 4.36, 4.95, 8.85, 9.36 and 10.11 °C.

The figures of maximum positive lateral temperature gradients recorded a leap in the temperature at the north edge of the concrete slab than the other points. Where, the north edge of slab for Adana in April, June, July, October, November, and December mentioned in the previous paragraph, the corresponding values in the south edge were 0.0, 0.0, 0.0, 0.0, 1.15 and 1.53 °C respectively. In the same order, the values of the Samsun city in the south edge recorded 0.0, 0.0, 0.0, 0.98, 1.73 and 2.39 °C. So, there is a significant difference between two edges in the same slab.

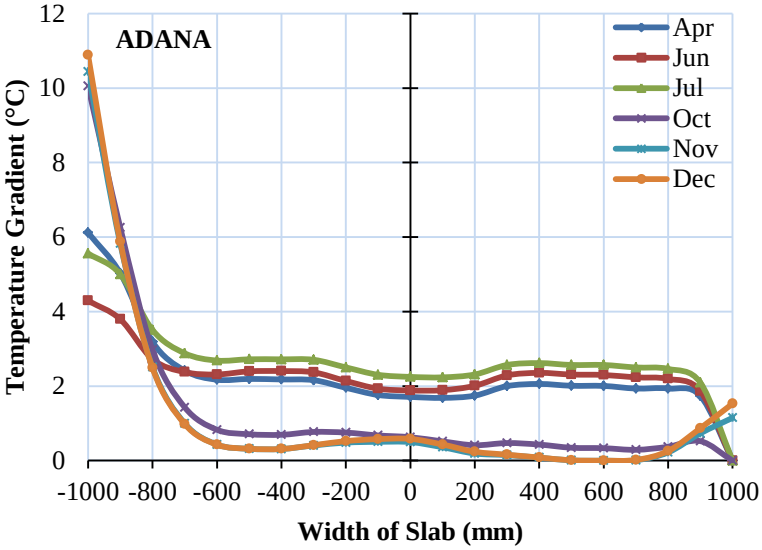

Figure 7.14 Maximum lateral positive temperature gradients in Adana.

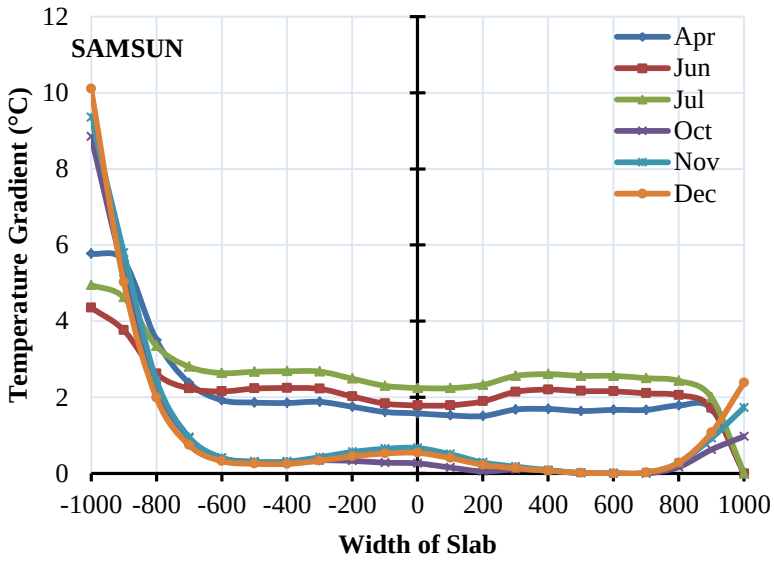

Figure 7.15 Maximum lateral positive temperature gradients in Samsun.

Figures 7.16 and 7.17 show the maximum negative lateral temperature gradients for Adana and Samsun city respectively. Where the behavior of the results for the two cities almost the same with a slight difference. The results of Adana were -4.54, -5.1, -4.73, -5.98, -5.01 and -5.12 °C in April, June, July, October, November and December respectively. The corresponding values of the Samsun city were -5.4, -5.1, -4.58, -5.7, -4.13 and -4.33 °C respectively.

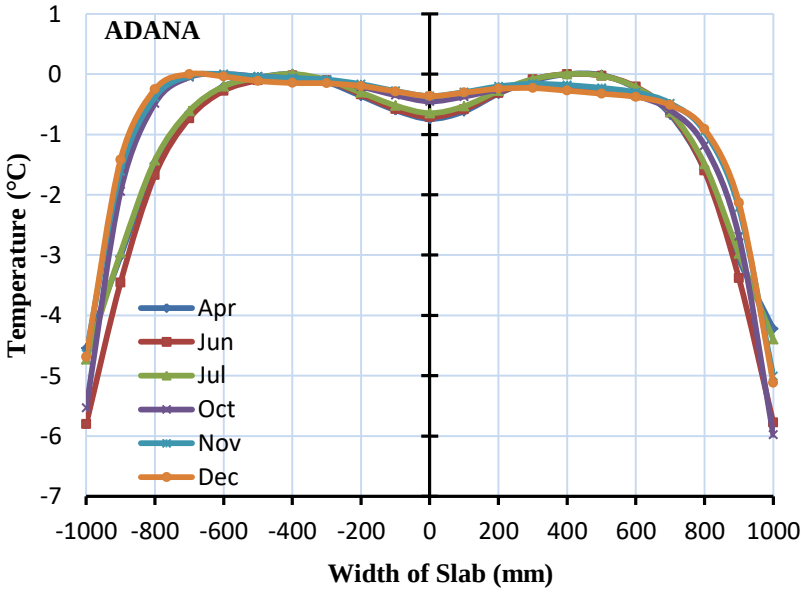

Figure 7.16 Maximum lateral negative temperature gradients in Adana.

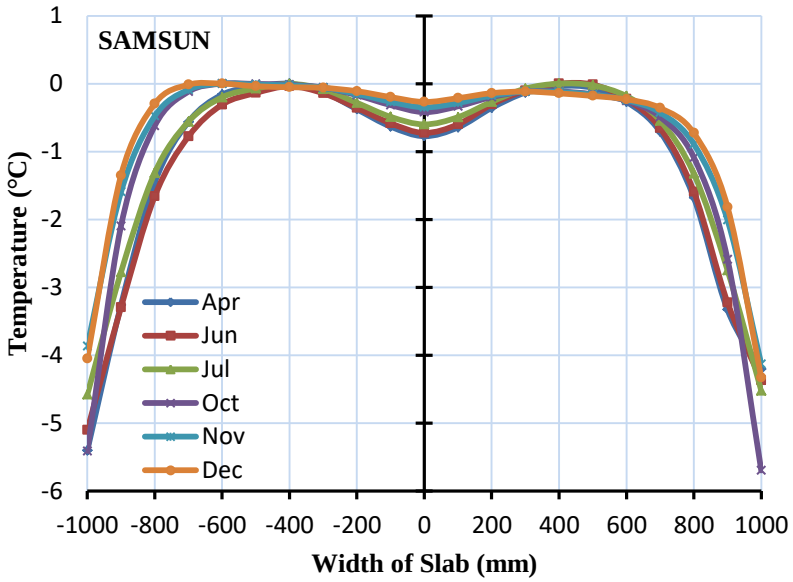

Figure 7.17 Maximum lateral negative temperature gradients in Samsun.

Figures 7.18 and 7.19 illustrate the comparison between the maximum vertical positive and negative temperature gradient for the selected cities in studied months. Figure 7.18 shows Antalya city recorded the highest maximum vertical positive temperature gradient in June which was 20.94 °C. The figure illustrates that June and July recorded the highest maximum vertical positive temperature gradient for the most cities except in Şırnak city. Samsun city recorded the lowest maximum vertical positive temperature gradient which was 13.55 °C in June.

Figure 7.19 shows the maximum vertical negative temperature gradient occur in the hot season for all cities. The maximum vertical negative temperature gradient recorded for Çorum city in July which was -12.74 °C. While the lowest maximum vertical negative temperature gradient recorded in Izmır city takes place in June which was -10.54 °C. It is clearly that the maximum vertical temperature gradient occurs in the hot season where the high intensity of solar radiations on the days and the differences between the maximum and minimum daily air temperature is high.

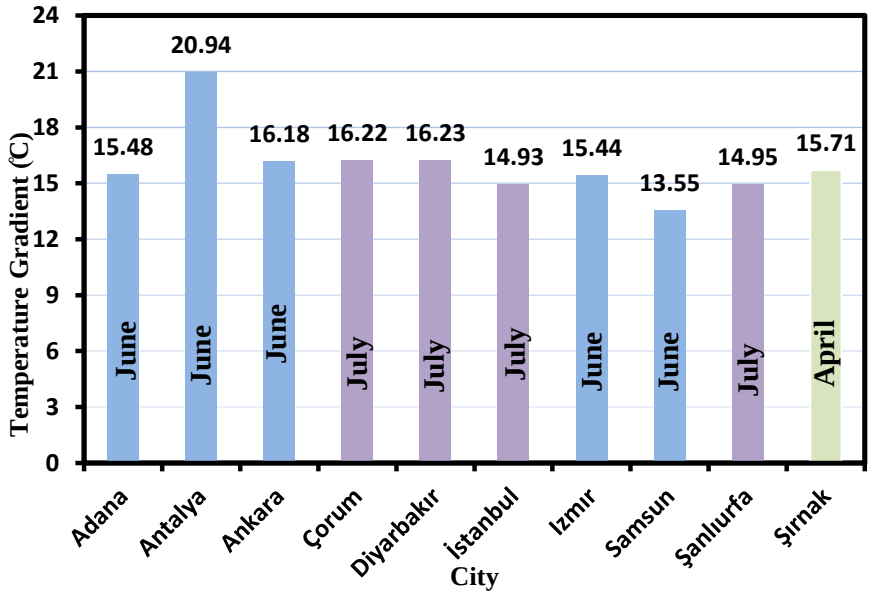

Figure 7.18 Maximum vertical positive temperature gradients for ten cities.

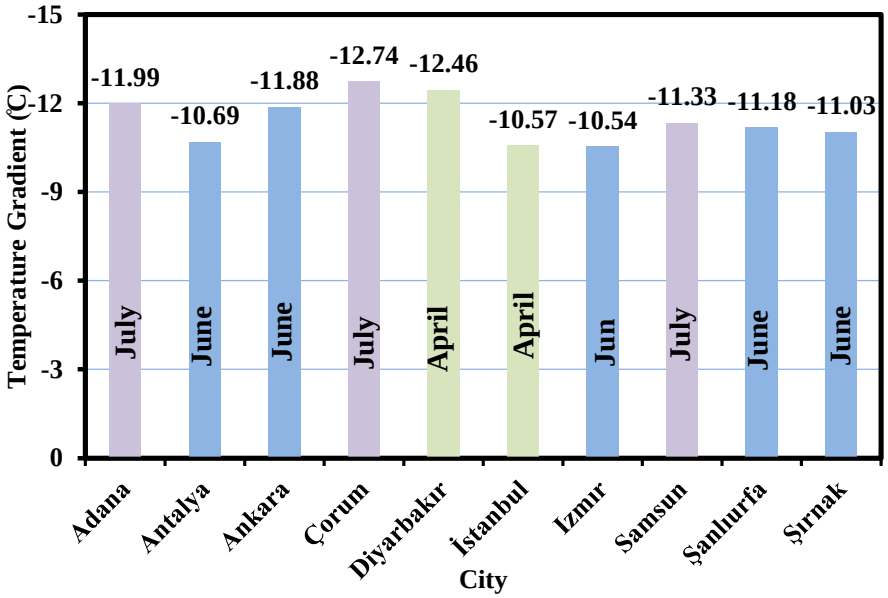

Figure 7.19 Maximum vertical negative temperature gradients for ten cities.

The comparisons between the maximum positive and negative horizontal temperature gradients for the ten cities in six months are shown in Figures 7.20 and 7.21.

Figure 7.20 shows Diyarbakır give the highest results of the maximum positive horizontal temperature gradient in December which were 11.89 °C and Şırnak was recorded the lowest result which was 9.71 °C in October.

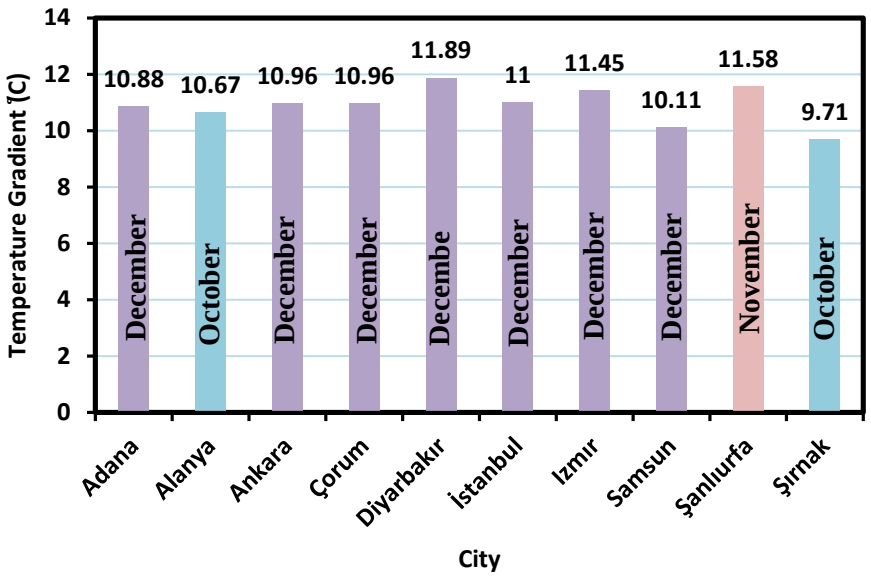

Figure 7.20 Maximum lateral positive temperature gradients.

Figure 7.21 shows the maximum negative lateral temperature gradients occurs in October for all tested cities except three cities. The maximum value recorded for Şanlıurfa city in April about -7 °C. And İstanbul city recorded the lowest value in October about -5 °C. so the maximum lateral temperature gradients generally happen in cold weather this because of the sun rays throughout the cold period strike from low solar altitude angle.

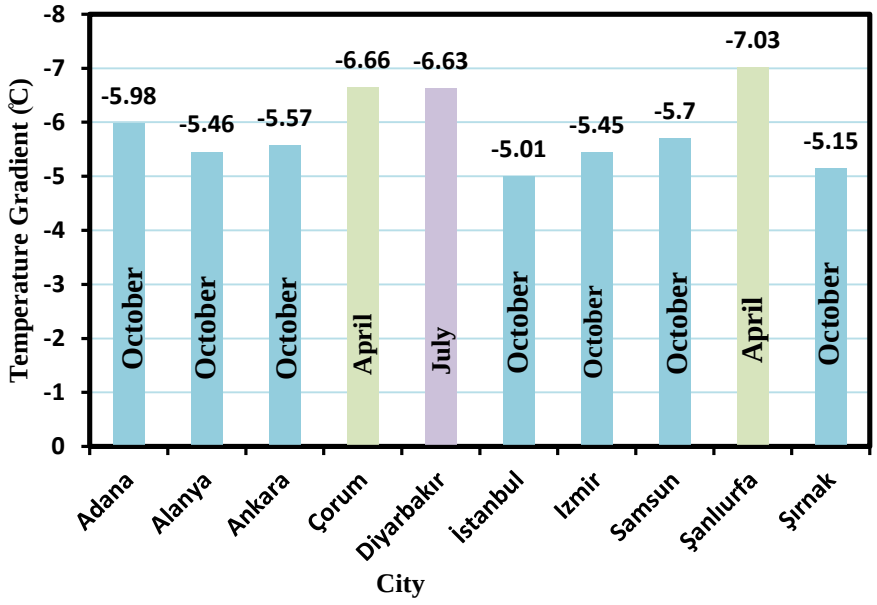

Figure 7.21 Maximum lateral negative temperature Gradients.

7.5.3 Average, Max and Min Temperature Gradients

Figures 7.22 to 7.27 show the daily variation of average, the maximum, and the minimum temperatures of T-Beam segment at 24 hours on the selected days in the six months for Adana and Samsun city.

Figures illustrated that there are three regions in the average, the maximum, and the minimum daily variation of the temperatures for two cities except in the daily maximum temperature of Adana. Where the daily temperature in June and July are the highest, then in April and October. While November and December show the lowest daily temperature. Also, the figures reflect that the average, the maximum and minimum temperature on Adana was higher than Samsun in the six months because of, Adana in a hotter region. In general, the results recorded that, the highest degree of daily temperatures was in the middle of the day because the sun is warmer.

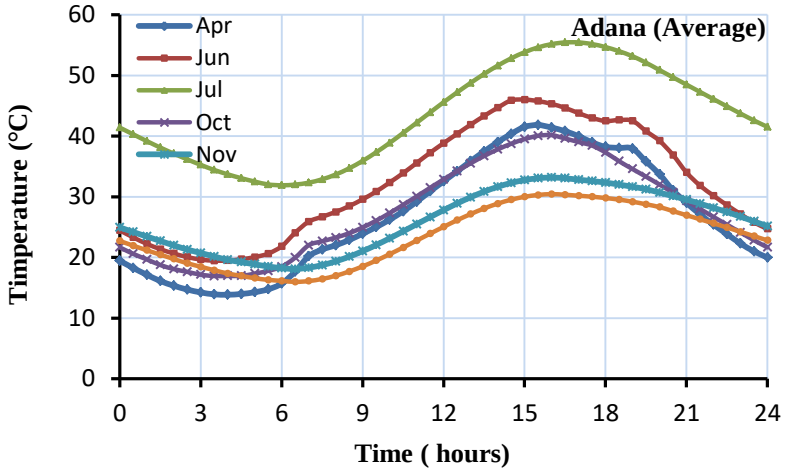

Figure 7.22 Daily variation of the average temperature in Adana.

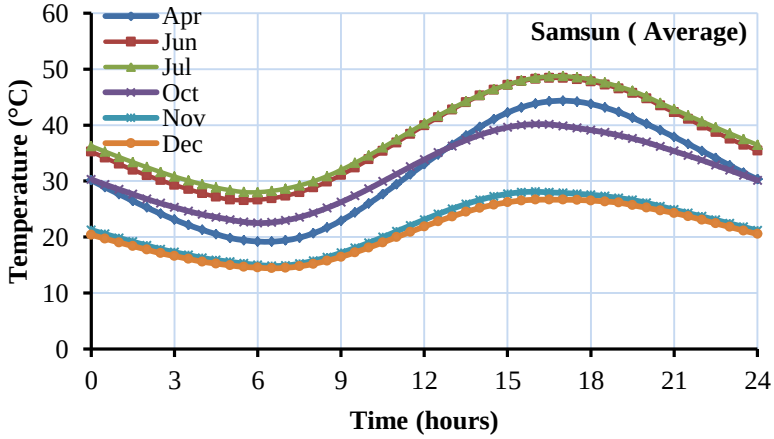

Figure 7.23 Daily variation of the average temperature in Samsun.

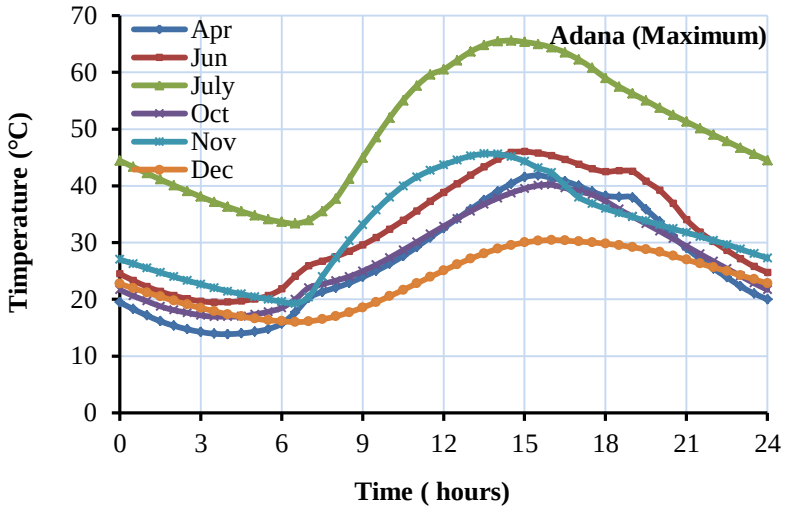

Figure 7.24 Daily variation of the maximum temperature in Adana.

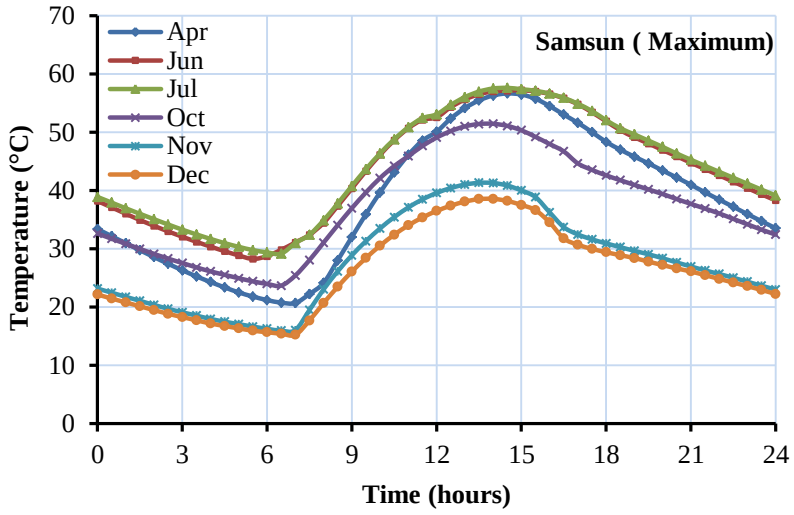

Figure 7.25 Daily variation of the maximum temperature in Samsun.

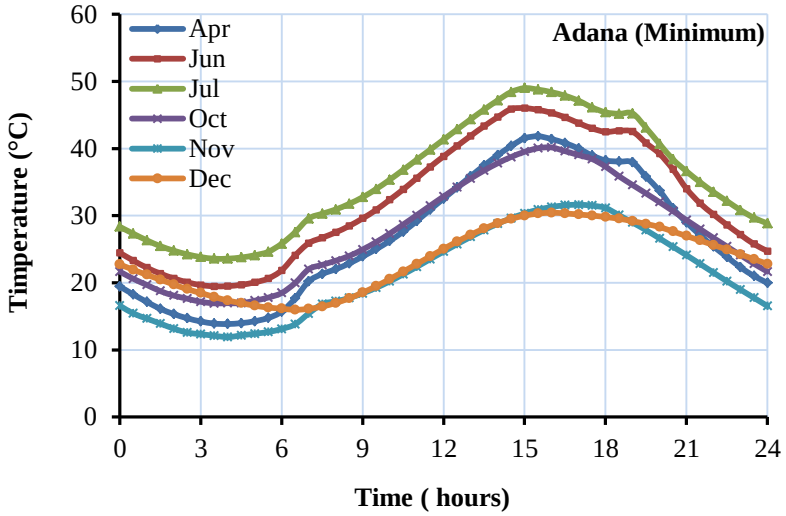

Figure 7.26 Daily variation of the minimum temperature in Adana.

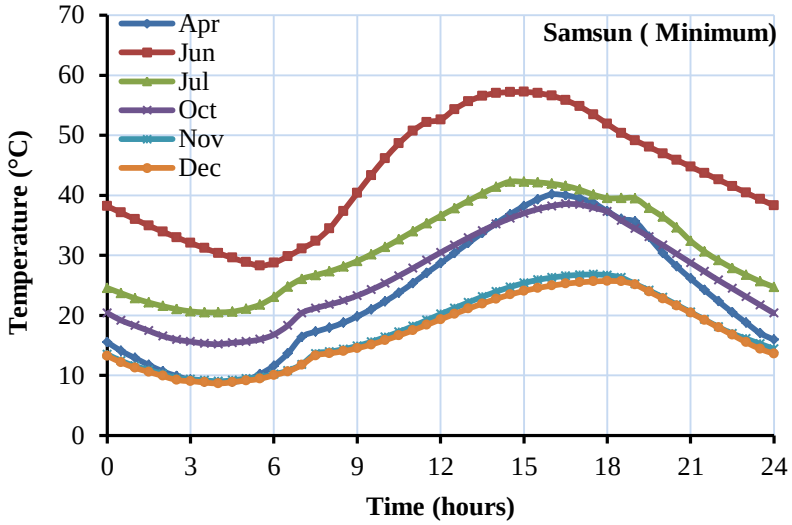

Figure 7.27 Daily variation of the minimum temperature in Samsun.

CHAPTER 8

CONCLUSIONS AND RECOMMENDATIONS

8.1 General

As one of the temporal loads that affect the long-term structural performance, temperature variation was generally one of the major foci of bridges. This thesis achieved several phases to investigate the environmental thermal loads on composite steel girders. The research presented in this thesis includes several study works starting with the experimental work in Gaziantep University, collection and analysis of data, conducting a numerical thermal model using the FE theory, conducting size and geometry parametric studies, and the evaluation of the extreme temperatures and temperature gradients for long-term (more than 50 years) for the different Turkish climate regions.

The experimental work included casting of two composite concrete-steel girder bridge segments, T-beam and I-beam. The experimental composite girder segments were instrumented with vibrating wire strain gages and thermocouples. Moreover, other sensors were installed in the site of the work to measure the long-term variation of air temperature, speed and the solar radiation intensity. The results of two segments from the collected data are analyzed according to the heat transfer fundamentals.

Three-dimensional thermo-mechanical FE models for the two segments were conducted using COMSOL finite element program. These models were verified with experimental records from the experimental composite girders. Based on the verified thermal FE model, the parametric study was performed for the effect of size of the I-Beam segment. Based on the FE model of the T-beam segment, long-term extreme temperature analysis was carried out for the seven regions of Turkey. Weather history records for about 50 years were incorporated in this study.

The followings are the most important conclusions drawn from the different study works of this research.

8.2 The Experimental Work

Based on the data collected from the strain gages, thermocouples, and the other weather sensors during the period from 21-December-2015 to 22-February-2016, the followings can be drawn:

1. The environmental data obtained from the studied period, from 21-December-2015 to 22-February-2016, show that the absolute recorded maximum and minimum air temperatures were 23.0 ℃ (18-February-2016 at 3:00 PM) and -9.9 ℃ (28-January-2016 at 3:00 AM), respectively, while the absolute maximum and minimum daily temperature differences (Max-Min) were 18.6 ℃ (25-December-2015) and 1.4 ℃ (13-January-2016), respectively. The absolute maximum recorded solar radiation intensity during the studied period was 870 W/m^2 in 10-February-2016 at 11:30 AM. Moreover, the absolute maximum recorded wind speed was 5.049 m/s in 25-January-2016 at 2:00 PM, while the minimum wind speed was 0 m/s, which occurs before sunrise and before/after one hour of sunset.

2. The temperature difference (max-min during the studied period (cold season) for the 29 thermocouples installed in steel and concrete parts of the two segments was higher in concrete than in steel. The maximum differences were recorded at the extreme edge of the concrete deck. For the T-Beam segment, the maximum difference was 15.13 ℃ at 10:00 AM and the minimum difference was 0.02 ℃ at 10:30 PM. While for the I-Beam segment, the maximum difference was 13.3 ℃ at 1:30 PM and the minimum difference was 0.00 ℃ at different times. In addition, for the T-Beam, the hourly maximum temperature recorded from the thermocouples was 36.41 ℃ in 18-February-2016 (at 2:00 PM) at the location of the thermocouple TC1, while the hourly minimum temperature was -9.39 ℃ (28-January-2016 at 4:30 AM) at the location of thermocouple TS6. Similarly, the maximum and minimum recorded temperatures in the I-beam were 36.5 and -7.3 ℃,

respectively, which were recorded on 18-February-2016 (at 2:00 PM) at IC4 and on 3-January-2016 (at 6:00 AM) at IS2, respectively.

3. Three distinct classes of days were selected to evaluate the effects of thermal loads on temperature variations in composite girders, which are the Frozen, Cold and Sunny days. The three tested days were 2-January (Frozen), 4-February (Cold), and 18-February (Sunny). The maximum hourly air temperatures recorded for the frozen, cold, and sunny days were 0.0, 13.3 and 23.0 ℃ respectively, while the minimum air temperatures recorded in the same days were -9.25, -3.2 and 4.5 ℃ respectively. The maximum hourly solar radiation intensities recorded for the frozen, cold, and sunny days were 606 W/m^2, 673 W/m^2 and 712 W/m^2, respectively.

4. For the T-Beam segment, the maximum temperatures of all thermocouples during the 24 hours of the frozen, cold, and sunny days were 5.64, 21.64 and 32.13 ℃, respectively, while the minimum temperatures were -6.28, -0.71 and 6.91 ℃, respectively. On the other hand, the maximum mean temperatures were 2.81, 20.45 and 30.87 ℃ for the frozen, cold, and sunny days, respectively, while the minimum mean temperatures were -6.76, -0.88 and 6.71℃, respectively. For I-Beam segment, the maximum hourly temperatures for all thermocouples were 5.95, 25.97 and 36.53 ℃ for the three tested days, while the minimum recorded temperatures were -5.93, 0.31 and 8.26 ℃, respectively. Similarly, the maximum mean temperatures of all thermocouple were 2.59, 18.78 and 28.69 ℃ for the frozen, cold, and sunny days, respectively, while the corresponding minimum mean temperatures were -6.09, -0.37 and 7.64 ℃ respectively.

5. The maximum vertical and lateral temperature gradients during the 24 hours of the frozen, cold, and sunny days for the two girder segments were investigated. For the T-Beam segment, the ranges of vertical temperature gradient for the three examined days were (-4.69 to 3.26 ℃), (-8.98 to 5.29 ℃), and (-9.94 to 5.99 ℃), respectively. On the other hand, the lateral temperature gradient were in the ranges of (-1.19 to 3.90 ℃), (-2.43 to 8.07 ℃), and (-2.28 to 8.12 ℃), respectively. For the I-Beam segment, the range of vertical temperature gradients for the three days were (-1.74 to 1.59 ℃), (-

1.98 to 5.68 ℃), and (-1.56 to 7.59 ℃), respectively, while their corresponding lateral temperature gradient ranges were (-2.19 to 4.79 ℃), (-3.48 to 10.55 ℃), and (-3.62 to 10.27 ℃), respectively.

6. The hourly variation of the strains measured from the two strain gages that were embedded at the central depth of the top flange of I-Beam segment. The strains were measured as the change of the strains from an initial strain reading. This reading was the strain value at the start time of the period, which is at the midnight (00:00) on the first day of 21-December-2016. During the last 10 days of December, the recorded maximum compression and tensile strains were approximately 110 and 40 micro-strains, respectively.

8.3 The Thermal Finite Element Analysis

Based on the temperature comparisons between the thermal FE analysis of and the experimental segments of the current research, the followings can be drawn:

1. The FE model of the T-Beam and I-Beam girders showed good capability to simulate the heat conduction, convection, and radiation in the girder and with the surrounding environment.

2. For the T-Beam segment and along the three selected days, good agreement was found between the predicted temperatures by the FE analysis and the experimentally recorded temperatures. Where, the maximum recorded AAEs were 1.18, 1.39 and 2.04 ℃ during the frozen, cold, and sunny days, respectively, while the minimum recorded AAEs were 0.42, 1.08 and 1.24 ℃, respectively. The maximum values of the MAE were 3.75, 5.59 and 5.59 ℃, respectively, while the minimum values of MAE were 1.29, 2.0 and 3.26 ℃, respectively.

3. The thermal FE analysis of the I-Beam segment also showed good agreement with their corresponding experimental temperatures during the three selected days. The maximum recorded AAE values were 2.01, 1.7 and 1.69 ℃ during the frozen, cold, and sunny days, respectively, while the minimum AAE values were 0.3, 1.15 and 0.86 ℃, respectively. The maximum values of MAE were 5.59, 3.88 and 4.49 ℃ for the frozen, cold, and sunny days,

respectively, while the minimum values of MAE were 0.89, 2.0 and 2.73 ℃, respectively.

8.4 The Parametric Study

Three parametric studies were carried out on the concrete-encased steel-beam girder to investigate the effect of the size of the girder using the verified FE model. In all parts of the FE parametric study, the environmental data of 5-July-2015 were used. Based on the size parametric studies using the verified FE model of the I-beam, the followings can be drawn:

1. The first parametric study investigates the combined effect of the girder depth and the thickness of its flanges and web using overall sized girders. The comparisons between the experimental size, double and triple sized girders showed that smaller girders suffer higher daily temperature fluctuation. At the central depth of the composite girder within the steel section, the daily maximum temperature difference between the three girders was 7.8 °C. The maximum vertical temperature gradient was higher for larger girders. The maximum vertical temperature gradients of the experimental, double and triple size girders were 14.0, 16.7, and 18.5 °C, respectively.

2. Another FE parametric study was directed to examine the particular effect of the girder depth. For girders with depths of 500, 1000 and 1500 mm, but with a constant thickness of web and flanges of 150 mm, the maximum daily temperature variation was only 2.1 °C, whereas the maximum difference between the maximum vertical temperature gradients of the three girders was less than 0.7 °C.

3. A third parametric study using 1500 mm deep sections with different web and flanges thickness of 150, 200, 250, and 300 mm showed that the largest share of the temperature and temperature gradient variations can be attributed to the thickness of the web and flanges of the girder. Thus, the influence of the thickness of the web and flanges on temperature variation and temperature gradient distributions is more significant than the effect of the girder depth.

8.5 The Temperature Gradients in Turkey

Ten cities were chosen from the seven different regions that compose Turkey to evaluate the long-term impact of air temperature and solar radiation on composite girders in Turkey. The maximum vertical and horizontal temperature gradients of a sized concrete-on-steel beam (T-beam) composite girder were obtained for the ten cities for six months (during the hot, moderate, and cold seasons). The analysis was conducted using the verified FE model of the current research. Only two cities of were selected to compare between the obtained results, which are Samsun and Adana. Based on this study, the followings can be drawn:

1. In the hot season, the sun rays strike from high solar altitude angle which causes a heating of the concrete part. So the maximum vertical positive temperature gradients occur at the top of the segment (concrete part). In the cold season, the sun rays strike from the low solar altitude angle during whole day which leads to heating the steel part. So the maximum vertical positive temperature gradients take place in the bottom part (steel part). In general, the concrete part is more stable than steel part because of the thermal conductivity is lower than the steel.

2. The variation in the maximum positive temperature gradient across the concrete slab was small between the two cities. However, this variation is more evident along the steel section. The vertical temperature gradients are higher in Adana than in Samsun. The maximum positive gradient values of Adana city were 15.05, 15.48, 14.49, 13.33, 13.11 and 12.25 ℃ in April, June, July, October, November, and December, respectively. On the other hand, the corresponding maximum positive gradients for Samsun were 11.41, 13.49, 12.79, 10.23, 9.14 and 8.83 ℃, respectively.

3. The distributions of the maximum negative vertical temperature gradients are similar for Adana and Samsun, with slightly higher negative temperature gradients in Adana. The zero temperature gradients occur at the bottom of the concrete slab for both cities in the six months. The vertical negative gradients in the hot season (April, June, and July) were higher than in the cold season (October, November, and December).

4. Similarly, the distributions of the maximum positive lateral temperature gradients are almost the same for both cities, but with higher gradient values in Adana. The maximum lateral temperature gradients were recorded at the northern edge of the concrete slab as the temperature of this edge is much higher than other parts of the slab. For Adana, the maximum positive lateral temperature gradients in April, June, July, October, November, and December were 6.12, 4.29, 5.56, 10.05, 10.44 and 10.88 ℃, respectively. For Samsun, the corresponding values were 5.78, 4.36, 4.95, 8.85, 9.36 and 10.11 ℃. Similar distributions were recorded for the maximum negative lateral temperature gradients, yet with smaller gradient differences between Adana and Samsun. The maximum negative lateral temperature gradients in Adana were -4.54, -5.1, -4.73, -5.98, -5.01 and -5.12 ℃ in April, June, July, October, November, and December, respectively. The corresponding values in Samsun were -5.4, -5.1, -4.58, -5.7, -4.13 and -4.33 ℃, respectively.

5. The maximum vertical temperature gradient occurs in the hot season where both the intensity of solar radiations and the differences between the maximum and minimum daily air temperature are high. The comparison between the maximum vertical positive and negative temperature gradient for the ten cities in the six months shows that Antalya city recorded the highest maximum vertical positive temperature gradient in June, which was 20.94 ℃. Samsun city recorded the lowest maximum vertical positive temperature gradient, which was 13.55 ℃ in June. The highest maximum vertical negative temperature gradient was recorded in Çorum city in July, which was -12.74 ℃, while the lowest maximum vertical negative temperature gradient recorded in Izmır city in June, which was -10.54 ℃.

6. The maximum lateral temperature gradients took place in spring or autumn (moderate seasons) or in the cold season. This because the sun rays during these seasons strike from low solar altitude angles with moderately high solar radiation intensities. The comparisons between the maximum positive and negative lateral temperature gradients for the ten cities in six months showed that these values are different among these cities. Diyarbakir showed the highest maximum positive lateral temperature gradient in December, which

was 11.89 ℃, while the lowest was recorded in Şirnak, which was 9.71 ℃ in October. The highest maximum negative lateral temperature gradient was recorded in Şanliurfa city in April and was about -7 ℃, while the lowest value was recorded in Istanbul in October and was about -5 ℃.

7. Comparisons were conducted between the daily difference between the average, maximum and minimum temperatures of the girder during the 24 hours of the selected days from the six months in Adana and Samsun. These comparisons showed that the average, maximum and minimum temperatures in Adana were higher than in Samsun in the six months. This is simply can be attributed to the higher solar radiation intensities in Adana.

8.6 Recommendations for Future Studies

According to the current survey of the literature review for this study, the recommendations for the future studies are:

1. Introducing a case study for existing composite I-steel girder bridge in Turkey, regarding the extreme weather conditions in Turkey according to the thermal effects by using the models presented in this study.

2. Investigating the thermal response of the other configurations of composite girders.

3. Investigating the fatigue effect due to the cyclic thermal loads from solar radiation and air temperature in steel and composite girders.

4. Evaluating the effect of environmental thermal loads on the dynamic properties (natural frequency) of concrete-encased steel girders.

REFERENCES

[1] Li, D., Maes, M., Dilger, W. (2004). Thermal design criteria for deep prestressed concrete girders based on data from confederation bridge, *Canadian Journal of Civil Engineering*, **31**, 813-825.

[2] Lee , J. H., Kalkan, I. (2012). Analysis of thermal environmental effects on precast, prestressed concrete bridge girders: temperature differentials and thermal deformations, *Advances in Structural Engineering*, **15**, 447-459.

[3] Chen, B., Ding, R., Zheng, J., Zhang, S. (2009). Field test on temperature field and thermal stress for prestressed concrete box-girder bridge, *Frontier of Architecture and Civil Engineering in China*, **3**, 158-164.

[4] Kim, S., Gopalakrishnan, K., Ceylan, H., Wang, K. (2010). Early-age response of concrete pavement to temperature and moisture variations, *The Baltic Journal of Road and Bridge Engineering*, **5**, 132-138.

[5] Qin, Y., Hiller, J. E. (2011). Modeling the temperature and stress distributions in rigid pavements: impact of solar radiation absorption and heat history development, *KSCE Journal of Civil Engineering*, **15**, 1361-1371.

[6] Choi , S., Cha, S.W., Oh, B.H., Kim, I.H. (2011). Thermo-hygromechanical behavior of early-age concrete deckin composite bridge under environmental laodings, *Materials and Structures*,. **1**, 1325-1346.

[7] Bentz, D.P., Stutzman, P. E., Sakulich, A. R., Wiess, W. J. (2012). Study of early-age bridge deck cracking in Nevada and Wyoming, *NISTIR Report, National Institute of Standards and Technology*, **7841**,Gaithersburg, USA.

[8] Neville , A. (2011). Properties of Concrete, Edinburgh, UK: Pearson Education

Limited.

[9] William, G.W., Shoukry, S. N., Raid M. Y. (2005). Early age cracking of reinforced concrete bridge decks, *Bridge Structures*, **1**, 379-396.

[10] Priestly, M. (1976). Design thermal gradients for concrete bridges, *New Zealand Engineering*, **31**, 213-219.

[11] Zichner, T. (1981). Thermal effects on concrete bridges, CEB Enlarged Meeting-Commission, **2**, Pavia.

[12] Ghali, A., Favre, R., Elbadry. M. .(2002). Concrete structures: stresses and deformation, London: E & FN Spon: 3rd edition.

[13] Naruoka, M., Hirai, I., Yamaguti, T. (1957). The measurement of the temperature of interior of the reinforced concrete slab of the Shigita bridge and presumption of the thermal stress, Tokyo, Japan: Japan Society for the Promotion of Science.

[14] Zuk, W. (1965). Thermal behaviour of composite bridges-insulated and uninsulated, *Highway Research Record, National Reasearch Council*, **76**, 231-253.

[15] Liu, Y., Zuk, W. (1963). Thermoelastic effects in prestressed flexural members, *PCI Journal*, **3**, 64-85.

[16] Zuk, W. (1961). Thermal and shrinkage stresses in composite beams, *ACI Journal*, **3**, 327-340.

[17] Barber, E. S. (1957). Calculations of maximum pavement temperatures from weather reports, *High Research Board Bulletin*, **168**, 1-8.

[18] Wah, T., K.irksey, R. E. (1969). Thermal charecteristics of highway bridges, *Report HR 12-4, Southwest Research Institute*, San Antonio, Texas, USA.

[19] Emerson, M. (1968). Bridge temperature movements in the british Isles, *TRRL*

Report No.228, Transport and Road Research Laboratory, Berkshire, England.

[20] Emerson, M. (1982). Thermal movements of concrete bridges, *TRRL Supplementary Report, Transport and Road Research Laborartory*, **747**, Berkshire, England.

[21] Potgieter, I. C., Gamble, W. L. (1983). Response of highway bridges to nonlinear temperature distributions, *Structural Research Series*, **505**,University of Illinois at Urbana-Champaign, Illinois, USA.

[22] Wood, J. H. (1979). In Situ thermal measurenments, from ambient thermal response of concrete bridges, *RRU Bulletin* **42**, National Road Research Board, New Zealand State Highways, Wellington.

[23] Emerson, M. (1973). The calculation of the distribution of temperature in bridges, *TRRL Transport and Road Research Laboratory*, **561**, Berkshire, England.

[24] Radolli, M., Green, R. (1975). Thermal stresses in concrete bridge superstructures under summer conditions, *Transportation Research Road*, **547**, 23-36.

[25] Will, K. M., Johnson, C. P., Matlock, H. (1977). Analytical and exerimental investigation of the thermal response of high bridges, Texas State Department of Highways and Public Transportation, University of Texas , Texas, Austin.

[26] Prakash Rao, D. S. (1986). Temperature distributions and stresses in concrete bridges, *ACI Journal*, **83**, 588-596.

[27] Emerson, M. (1980). Temperatures in bridges during the cold winter of 1978/1979., *TRRL Report*, Transport and Road Research Laboratory , **926**, Berkshire, England.

[28] COMSOL Multiphysics v4.3a, COMSOL Multiphysics users guide (2012), stockholm.

[29] AASHTO. American Association of State Highway and Transportation Officials. (2007). AASHTO LRFD Bridge Design Specifications, Washington, D.C.,USA.

[30] The Turkish State Metrological Service. Available at: http://www.mgm.gov.tr/index.aspx. Accessed by 20 December 2014.

[31] Brewanger, C., Symko, Y. (1976). Finite-element solutions for thermal stresses in steel-concrete composite bridges, **16**, no. 9, 168-175.

[32] Thepchatri, T., Johnson, C, Matlock, H. (1977). Prediction of Temperature and Stresses in Highway Bridges by a Numerical Procedure Using Daily Weather Reports, *Center for Highway Research*, 23-1.

[33] Chan, Y.T., Cheung, M. S., Beauchamp,J. C., Hachem, H. M. (1990). Thermal Stresses in Composite Box GirderBridges developments in short and medium span bridge engineering, *Canada*, **2**, 355-366.

[34] Fu, H. C., Ng, S. F, Cheung, M. S. (1990). Thermal Behavior of composite Bridges, *ASCE*, **116**.

[35] Pentas, H. A., Avent, R. R., Gopu V. K. A., Rebello, K. J. (1991). Field Study of Bridge Temperatures in Composite Bridges, 1460.

[36] Moorty, S., Roeder , C. W. (1992). Temperature-dependent bridge movements, *Journal of Structural Engineering*, **118**, 1090-1105.

[37] AASHTO. American Association of State Highway and Transportation Officials. (1992). AASHTO guide specifications: thermal effects in concrete bridge superstructures. Washington, DC, USA.

[38] Im, C. K., Chang, S. P.(2004). Estimatingextremethermalloadsin composite bridge using long-term measured data,. *Journal of Structural Engineering*, **4**, 25–31.

[39] Římal, J., Křístek, V., Kuráž, V., Jelínek, V., Kovářova, A., Zaoralová J. (2007). Thermal behavior of a composite box-girder railway bridge, *Natural hazards (optimisation of protection, interaction with structures)*, **5**,148- 187.

[40] Zhang, Tao. (2009). Thermal behavior of composite girder bridges, *IEEE*, Dalian, China, 327-330.

[41] Francesca**,** G. F. (2009). The effects of temperature variations on the long-term behaviour of composite steel-concrete beams, *Engineering Structures*, **31**, 2392-2406.

[42] Zhou, G. D., Yi, T. H. (2013). Thermal Load in Large-Scale Bridges: *International Journal of Distributed Sensor Networks*, **17**,Article ID217983.

[43] Emanue, J., Hulsey, J.(1977). Prediction of the thermal cofficient of expansion of concrete, *ACI, American Concrete Institute*, **74**, 149-155.

[44] Emanuel, J., Lewis, D. (1981). Abutment-thermal interaction of composite bridge, *ASCE American Society of Civil Engineers*, **107**, 2111-2126.

[45] Dilger, W., Beauchamp, J.C, Cheung, M., Chali, A. (1981). Field Measurements of Muskwa River Bridge, *Journal of Structural Division, ASCE* , **107**, 2147-2161.

[46] Berwanger, C. (1983) "Transient thermal behaviour of composite bridges, *ASCE American Society of Civil Engineers*, **109**, 2325-2339.

[47] Xia, Y., Xua, Y., Weia, Z., Zhub, H., Zhouc, X. (2011). Variation of structural vibration characteristics versus non-uniform temperature distribution, *Engineering Structures*, **33**,.53-146.

[48] Maher, D. R. H. (1970). The effects of differential temperature on continuous prestressed concrete bridges, *Civil Engineering Transactions*, Britain, **12**, 29-32.

[49] Priestly, M. J. (1972). Thermal gradients in bridges some design consideration,

New Zealand Engineering, **27**, 228-233.

[50] New Zealand Ministry of Works and Delevopments,(1970). Bridge design temperature gradient.

[51] Dilger, W., Ghali,A., Chan, M., Cheung, M., Maes, M. (1983). Temperature stresses in composite box girder bridges, *ASCE American Society of Civil Engineers*, **109**, 1460-1478.

[52] Elbadry, M., Ghali, A. (1986), Thermal stresses and cracking of concrete bridges, *ACI Journal*, **83**, 1001-1009.

[53] Chang, S., Im, C. (2000). Thermal behaviour of composite box girder bridges, *Institution of Civil Engineerings Structures and Buildings*, **104**, 117-126.

[54] BS 5400. British Standard institution, Steel, Concrete, and Composite Bridges-Part I& Part II (1978), Crowthorne, Berkshire, England, U.K.

[55] Au, F., Cheung, S., Tham, L. (2002). Desig thermal loading for composite bridges in tropical region, *Steel and Composite Structures*, **2**, 441-460.

[56] Stuart, S. Chen, Amjad, J. Aref, Methee, Chiewanichakorn, Il-Sang, A. (2007). Proposed effective width criteria for composite bridge girders, *ASCE American Society of Civil Engineers*, 325.

[57] Emanuel, J., Hulsey, J. (1978). Temperature distributions in composite bridges, *ASCE American Society of Civil Engineers*, **104**, 65-78.

[58] Kuehn, T., Ramsey, J., Threlkeld, J. (1998). Thermal envermental engineering. 3rd edition. Prentice Hall.

[59] AASHTO. American Association of State Highway and Transportation Officials (2007).AASHTO bridge design specification, Washington DC, USA.

[60] AASHTO. American Association of State Highway and Transportation Officials (2012). AASHTO LRFD bridge design specification Washington DC, USA.

[61] AASHTO. American Association of State Highway and Transportation Officials (2003). Standard Specification for Highway Bridges, 17th Ed, Washington DC, USA.

[62] Eurocode. European Committee for Standardization. CEN ENV 1991-1-5 (2003), General Actions- Thermal Actions, Brussels, Belgium.

[63] 108-L Temperature Probe Manual (2011). Campbell ScientificInc., Utah: USA, Logan.

[64] Solar shield for the 108-air temperature probe. Campbell ScientificInc., Utah: USA

[65] NRG#40 Maximum Wind Speed Sensor (2011), Utah: USA.

[66] CS300. Apogee Silicon Pyranometer M annual (2009), Utah: USA, Logan.

[67] Troy, T. T., Chai, H. Y. (1998). Thermal Effects on Skewed Highway Bridges Including Bearing Orientation, Alabama, May 1998.

[68] Carslaw, H. S., Jaeger, J. C.(1959). Conduction of Heat in Solids, 2 ed., C. Press, Ed., Oxford.

[69] Dilger, W. H., Ghali, A. (1980). Temperature Induced Stresses Composite Box Girder Bridges, Canada, October.

[70] Williamson, P. J. (1976). Estimation of Heat Outputs for Road Heating Installations, London.

[71] ASHRAE. American Society of Heating, Refrigerating, and Air-Conditioning Engineers (2005), ASHRAE handbook-fundamentals, Atlanta, USA.

[72] Ibrahim, A. M. (1995). Three-Dimensional Thermal Analysis of Curved Concrete Box Girder Bridges. *Concordia University Research Repository, OAI.*

[73] Duffie, J. A., Beckman, W. A. (1980). Solar Engineering of Thermal Processes,

Wiley, New York.

[74] Chapman, A. J. (1982). Fundamentals of Heat Transfer, Macmillan.

[75] Kreith, F., Kreider, J. F.(1978). Principles of Solar Engineering, McGraw-Hill.

[76] Imbsen, R.A., Vandershaf, D.E., Schamber, R.A., Nutt, R.V. (1985). Thermal Effects in Concrete Bridge Superstructures, National Cooperative Highway Research Program Report **276**, *Transportation Research Board*, Washington, DC, USA

[77] Lee, J.-H. (2012). Investigation of Extreme Environmental Conditions and Design Thermal Gradients during Construction for Prestressed Concrete Bridge Girders, *Journal of Bridge Engineering*, *ASCE*, **17**, 547-556.

[78] Threlkeld, J. (1970). Thermal Environmental Engineering, Englewood Cliff .N.J: Prentice_Hall.

[79] Hirst, M. J., Dilger, W. H. (1989). Prediction of bridge temperatures, *IABSE*, **138**, 109-120.

[80] Chen, Q (1980). Effects of thermal loads on Texas Steel Bridges, Texas: The Universityof Texas at Austin.

[81] New Zealand Ministry of Works and Delevopments (1970), Bridge design temperature gradient, New Zealand: Highway Bride Design Brief.

[82] Emanual, J., Hulsey, J. (1978). Temperature distributions in composite bridges, *Journal of Structural Division*, *ASCE*, **104**, 65-78.

[83] Elbadry, M., Ghali, A. (1983). Temperature Variation in Concrete Bridges, *ASCE*, **109**, 2355-2374.

[84] Hsieh, J. S.(1985). Solar Energy Engineering, Prentice Halls: Englewood Cliff, 1985.

PERSONAL INFORMATION

Name and Surname : Faten Ibrahim Mussa

Natioality : Iraq

Birth place and date : Misan/1975

Marial status : Single

Phone number : +90 5380670893 in Turkey

+964 770 0125915 in Iraq

Fax :

Email : faten.mussa@mail2.gantep.edu.tr

fatin.haydree@gmail.com

fatin_haydree@yahoo.com

EDUCATION

	Graduate school	**Year**
Master	University of Al-Mustansiriya	2000
Bachelor	University of Al-Mustansiriya	1997
High School	Al-Zawra High School	1993

WORK EXPERIENCE

Year	**Place**	**Enrollment**
2011-Present	University of Maysan	Lecturer
2007-2011	University of Maysan	Assistant Lecturer
2001-2007	Ministry of Housing and Construction	Engineer

PUBLICATIONS

Journals

Sallal, R. A, Faten, I. M., Nildem, T., Mustafa, Ö.(2017), Experimental and finite element investigation of temperature distribution in concrete-encased steel girders. *Structural Control and Health Monitoring*. **DOI**: 10.1002/stc.2042